Surface Effects and Contact Mechanics

IX

COMPUTATIONAL METHODS AND EXPERIMENTS

EDITORS

J.T.M. De Hosson
& C.A. Brebbia

WIT PRESS

Surface Effects and Contact Mechanics IX

NINTH INTERNATIONAL CONFERENCE ON
SURFACE EFFECTS AND CONTACT MECHANICS: COMPUTATIONAL
METHODS AND EXPERIMENTS

CONTACT AND SURFACE 2009

CONFERENCE CHAIRMEN

J.T.M. De Hosson
University of Groningen, The Netherlands

C.A. Brebbia
Wessex Institute of Technology, UK

Organised by
Wessex Institute of Technology, UK

Sponsored by
WIT Transactions on Engineering Sciences

WIT Transactions

Transactions Editor

Carlos Brebbia
Wessex Institute of Technology
Ashurst Lodge, Ashurst
Southampton SO40 7AA, UK
Email: carlos@wessex.ac.uk

Editorial Board

D **Goulias** University of Maryland, USA

K G **Goulias** Pennsylvania State University, USA

F **Grandori** Politecnico di Milano, Italy

W E **Grant** Texas A & M University, USA

S **Grilli** University of Rhode Island, USA

R H J **Grimshaw,** Loughborough University, UK

D **Gross** Technische Hochschule Darmstadt, Germany

R **Grundmann** Technische Universitat Dresden, Germany

A **Gualtierotti** IDHEAP, Switzerland

R C **Gupta** National University of Singapore, Singapore

J M **Hale** University of Newcastle, UK

K **Hameyer** Katholieke Universiteit Leuven, Belgium

C **Hanke** Danish Technical University, Denmark

K **Hayami** National Institute of Informatics, Japan

Y **Hayashi** Nagoya University, Japan

L **Haydock** Newage International Limited, UK

A H **Hendrickx** Free University of Brussels, Belgium

C **Herman** John Hopkins University, USA

S **Heslop** University of Bristol, UK

I **Hideaki** Nagoya University, Japan

D A **Hills** University of Oxford, UK

W F **Huebner** Southwest Research Institute, USA

J A C **Humphrey** Bucknell University, USA

M Y **Hussaini** Florida State University, USA

W **Hutchinson** Edith Cowan University, Australia

T H **Hyde** University of Nottingham, UK

M **Iguchi** Science University of Tokyo, Japan

D B **Ingham** University of Leeds, UK

L **Int Panis** VITO Expertisecentrum IMS, Belgium

N **Ishikawa** National Defence Academy, Japan

J **Jaafar** UiTm, Malaysia

W **Jager** Technical University of Dresden, Germany

Y **Jaluria** Rutgers University, USA

C M **Jefferson** University of the West of England, UK

P R **Johnston** Griffith University, Australia

D R H **Jones** University of Cambridge, UK

N **Jones** University of Liverpool, UK

D **Kaliampakos** National Technical University of Athens, Greece

N **Kamiya** Nagoya University, Japan

D L **Karabalis** University of Patras, Greece

M **Karlsson** Linkoping University, Sweden

T **Katayama** Doshisha University, Japan

K L **Katsifarakis** Aristotle University of Thessaloniki, Greece

J T **Katsikadelis** National Technical University of Athens, Greece

E **Kausel** Massachusetts Institute of Technology, USA

H **Kawashima** The University of Tokyo, Japan

B A **Kazimee** Washington State University, USA

S **Kim** University of Wisconsin-Madison, USA

D **Kirkland** Nicholas Grimshaw & Partners Ltd, UK

E **Kita** Nagoya University, Japan

A S **Kobayashi** University of Washington, USA

T **Kobayashi** University of Tokyo, Japan

D **Koga** Saga University, Japan

A **Konrad** University of Toronto, Canada

S **Kotake** University of Tokyo, Japan

A N **Kounadis** National Technical University of Athens, Greece

W B **Kratzig** Ruhr Universitat Bochum, Germany

T **Krauthammer** Penn State University, USA

C-H **Lai** University of Greenwich, UK

M **Langseth** Norwegian University of Science and Technology, Norway

B S **Larsen** Technical University of Denmark, Denmark

F **Lattarulo,** Politecnico di Bari, Italy

A **Lebedev** Moscow State University, Russia

L J **Leon** University of Montreal, Canada

D **Lewis** Mississippi State University, USA

S **lghobashi** University of California Irvine, USA

K-C **Lin** University of New Brunswick, Canada

A A **Liolios** Democritus University of Thrace, Greece

M **Predeleanu** University Paris VI, France

M R I **Purvis** University of Portsmouth, UK

I S **Putra** Institute of Technology Bandung, Indonesia

Y A **Pykh** Russian Academy of Sciences, Russia

F **Rachidi** EMC Group, Switzerland

M **Rahman** Dalhousie University, Canada

K R **Rajagopal** Texas A & M University, USA

T **Rang** Tallinn Technical University, Estonia

J **Rao** Case Western Reserve University, USA

A M **Reinhorn** State University of New York at Buffalo, USA

A D **Rey** McGill University, Canada

D N **Riahi** University of Illinois at Urbana-Champaign, USA

B **Ribas** Spanish National Centre for Environmental Health, Spain

K **Richter** Graz University of Technology, Austria

S **Rinaldi** Politecnico di Milano, Italy

F **Robuste** Universitat Politecnica de Catalunya, Spain

J **Roddick** Flinders University, Australia

A C **Rodrigues** Universidade Nova de Lisboa, Portugal

F **Rodrigues** Poly Institute of Porto, Portugal

C W **Roeder** University of Washington, USA

J M **Roesset** Texas A & M University, USA

W **Roetzel** Universitaet der Bundeswehr Hamburg, Germany

V **Roje** University of Split, Croatia

R **Rosset** Laboratoire d'Aerologie, France

J L **Rubio** Centro de Investigaciones sobre Desertificacion, Spain

T J **Rudolphi** Iowa State University, USA

S **Russenchuck** Magnet Group, Switzerland

H **Ryssel** Fraunhofer Institut Integrierte Schaltungen, Germany

S G **Saad** American University in Cairo, Egypt

M **Saiidi** University of Nevada-Reno, USA

R **San Jose** Technical University of Madrid, Spain

F J **Sanchez-Sesma** Instituto Mexicano del Petroleo, Mexico

B **Sarler** Nova Gorica Polytechnic, Slovenia

S A **Savidis** Technische Universitat Berlin, Germany

A **Savini** Universita de Pavia, Italy

G **Schmid** Ruhr-Universitat Bochum, Germany

R **Schmidt** RWTH Aachen, Germany

B **Scholtes** Universitaet of Kassel, Germany

W **Schreiber** University of Alabama, USA

A P S **Selvadurai** McGill University, Canada

J J **Sendra** University of Seville, Spain

J J **Sharp** Memorial University of Newfoundland, Canada

Q **Shen** Massachusetts Institute of Technology, USA

X **Shixiong** Fudan University, China

G C **Sih** Lehigh University, USA

L C **Simoes** University of Coimbra, Portugal

A C **Singhal** Arizona State University, USA

P **Skerget** University of Maribor, Slovenia

J **Sladek** Slovak Academy of Sciences, Slovakia

V **Sladek** Slovak Academy of Sciences, Slovakia

A C M **Sousa** University of New Brunswick, Canada

H **Sozer** Illinois Institute of Technology, USA

D B **Spalding** CHAM, UK

P D **Spanos** Rice University, USA

T **Speck** Albert-Ludwigs-Universitaet Freiburg, Germany

C C **Spyrakos** National Technical University of Athens, Greece

I V **Stangeeva** St Petersburg University, Russia

J **Stasiek** Technical University of Gdansk, Poland

G E **Swaters** University of Alberta, Canada

S **Syngellakis** University of Southampton, UK

J **Szmyd** University of Mining and Metallurgy, Poland

S T **Tadano** Hokkaido University, Japan

H **Takemiya** Okayama University, Japan

I **Takewaki** Kyoto University, Japan

C-L **Tan** Carleton University, Canada

M **Tanaka** Shinshu University, Japan

E **Taniguchi** Kyoto University, Japan

S Tanimura Aichi University of Technology, Japan

J L Tassoulas University of Texas at Austin, USA

M A P Taylor University of South Australia, Australia

A Terranova Politecnico di Milano, Italy

E Tiezzi University of Siena, Italy

A G Tijhuis Technische Universiteit Eindhoven, Netherlands

T Tirabassi Institute FISBAT-CNR, Italy

S Tkachenko Otto-von-Guericke-University, Germany

N Tosaka Nihon University, Japan

T Tran-Cong University of Southern Queensland, Australia

R Tremblay Ecole Polytechnique, Canada

I Tsukrov University of New Hampshire, USA

R Turra CINECA Interuniversity Computing Centre, Italy

S G Tushinski Moscow State University, Russia

J-L Uso Universitat Jaume I, Spain

E Van den Bulck Katholieke Universiteit Leuven, Belgium

D Van den Poel Ghent University, Belgium

R van der Heijden Radboud University, Netherlands

R van Duin Delft University of Technology, Netherlands

P Vas University of Aberdeen, UK

W S Venturini University of Sao Paulo, Brazil

R Verhoeven Ghent University, Belgium

A Viguri Universitat Jaume I, Spain

Y Villacampa Esteve Universidad de Alicante, Spain

F F V Vincent University of Bath, UK

S Walker Imperial College, UK

G Walters University of Exeter, UK

B Weiss University of Vienna, Austria

H Westphal University of Magdeburg, Germany

J R Whiteman Brunel University, UK

Z-Y Yan Peking University, China

S Yanniotis Agricultural University of Athens, Greece

A Yeh University of Hong Kong, China

J Yoon Old Dominion University, USA

K Yoshizato Hiroshima University, Japan

T X Yu Hong Kong University of Science & Technology, Hong Kong

M Zador Technical University of Budapest, Hungary

K Zakrzewski Politechnika Lodzka, Poland

M Zamir University of Western Ontario, Canada

R Zarnic University of Ljubljana, Slovenia

G Zharkova Institute of Theoretical and Applied Mechanics, Russia

N Zhong Maebashi Institute of Technology, Japan

H G Zimmermann Siemens AG, Germany

Surface Effects and Contact Mechanics IX

Computational Methods and Experiments

Editors:

J.T.M. De Hosson
University of Groningen, The Netherlands

C.A. Brebbia
Wessex Institute of Technology, UK

WITPRESS Southampton, Boston

Editors:

J.T.M. De Hosson
University of Groningen, The Netherlands

C.A. Brebbia
Wessex Institute of Technology, UK

*The texts of the papers in this volume were set
individually by the authors or under their supervision.
Only minor corrections to the text may have been carried
out by the publisher.*

Preface

This book contains papers presented at the Ninth International Conference on Surface Effects and Contact Mechanics held from June 9–11, 2009 in Algarve, Portugal. Previous conferences in the same series were organized in Southampton (1993), Milano (1995), Oxford (1997), Assisi (1999), Sevilla (2001), Crete (2003), Bologna (2005) and at Wessex Institute of Technology, Ashurst, UK (2007). This series of conferences is aimed at encouraging international collaboration among the participants and the exchange of new ideas. In particular the book deals with the interplay between applied physics, materials science, computational mechanics and mechanical engineering.

To an increasing degree the search is for surface modification techniques, which can increase the wear and corrosion resistance of materials. Unfortunately, there exists an almost bewildering choice of surface treatments that cover a wide range of thickness. It is worth noting here that wear resistance is a property, not of materials but of systems, since the material of the work-piece always wears against some other medium. It is its relation to its environment – e.g. lubrication, speed of sliding/rotation – that determines the wear and corrosion resistance of the material in a given construction. The characteristics of the system, e.g. whether the wear is caused by delamination or abrasion, determine which of the surface engineering methods should be chosen. The combination surface treatment and contact mechanics is an important one.

In this book various new developments are highlighted, both from an experimental and computational viewpoint. Special emphasis is given to the application of advanced theoretical and experimental approaches. Papers have been grouped into the following subject areas:

- Surface treatments
- Thick coatings
- Thin coatings
- Surface problems in contact mechanics
- Indentation and hardness
- Fatigue

- Numerical analysis
- Applications and case studies

Thanks are due to the authors for their contributions. The editors are also grateful to the members of the International Scientific Advisory Committee, and other colleagues, who helped in the reviewing process to ensure the quality of the conference and this book.

The Editors
Algarve, 2009

Contents

Section 7: Numerical analysis

Section 8: Applications and case studies

This page intentionally left blank

Section 1
Surface treatments

This page intentionally left blank

Dynamic smoothening and tribological properties of pulsed-DC sputtered DLC based nanocomposite films

K. P. Shaha, Y. T. Pei, C. Q. Chen & J. Th. M. De Hosson
Department of Applied Physics,
The Netherlands Materials Innovation Institute (M2i),
University of Groningen, The Netherlands

Abstract

Interface roughness and dynamic growth behavior of TiC/a-C nanocomposite films deposited by pulsed-DC magnetron sputtering were studied using atomic force microscopy and scanning electron microscopy. Upon increasing the intensity of concurrent ion impingement by raising the frequency of pulsed-DC sputtering, a transition from dynamic roughening to dynamic smoothening is revealed in the growth behavior of TiC/a-C nanocomposite films. Analyses of surface morphology and growth conditions imply that there is a transition of dominating growth mechanism from geometric shadowing to surface diffusion driven by impact-induced atomistic downhill flow process due to enhanced impingement of Ar+ ions, which occurs upon the change of pulse frequency from 100 kHz to 350 kHz. Also ultra-smooth TiC/a-C:H films were successfully grown on initial rough steel substrates (Sa ~ 6 nm) by pulsed-DC sputtering at 200 and 350 kHz frequency. These nanocomposite films exhibit superb toughness, wear resistance and ultralow friction.
Keywords: dynamic roughening, smoothening, nanocomposite, rough substrates, pulsed-DC sputtering.

1 Introduction

Diamond-like-carbon (DLC) is an extensively studied material due to its intriguing physical, mechanical and tribological properties [1]. DLC based nanocomposites incorporating nanosized inclusions are expected to further

improve the structural and mechanical properties of pure amorphous phases [2]. However, surface smoothness of such films becomes a crucial property for developing frictionless protective coatings. If the sliding surfaces are very rough, a high level of mechanical interlocking between surface asperities leads to high friction and wear losses (especially during the running-in period). During sputter deposition there is interplay between roughening generated by random deposition of atoms, smoothening by surface diffusion and nonlocal effects generated by shadowing. Geometrical shadowing, which results by non-normal incident flux [3], enhances growth front roughness. Without additional lateral relaxation processes, this would inevitably cause dynamic roughening i.e. an increase of surface roughness as a function of deposition time (or film thickness) [4]. A rough interface will induce columnar growth such that the column boundaries (CBs) originate at the groove networks on the growing interface and the hills become the spearheads of the columns. The CBs are potential source of failure under loading and contact sliding. The CBs may act as initiation sites for cracks and preferential cracking paths [2].

The growth mechanisms essentially govern the microstructure and thus influence the mechanical and tribological properties of these films. The substrates used in the industries are inherently rough. Thus it is of practical concern to identify the role of growth mechanisms to optimize the deposition conditions for smooth film topography. Over the last decade considerable attention has been paid to the theoretical and experimental aspects of dynamic roughening of films grown on smooth surface [5–9], whereas little attention has been paid to films grown on rough surfaces where smoothening phenomenon may occur [10–12]. Recently, we have reported the dynamic growth behavior for thick TiC/a-C films grown on smooth surface by pulsed-DC sputtering for different pulse frequencies [13]. Dynamic roughening at low pulse frequency while dynamic smoothening at high pulse frequency was observed.

In this paper, we utilize the fact that pulse frequency has a prominent effect on ion energy and ion flux bombarding at the growing film [14] to investigate the evolution of surface morphology of films grown on rough surfaces during pulsed-DC magnetron sputtering. With increasing the intensity of concurrent ion impingement by raising the frequency of pulsed DC sputtering, a transition from dynamic roughening to dynamic smoothening is revealed. Dynamic smoothening of intentionally grown initial rough TiC/a-C films at higher pulse frequency (350 kHz) has been reported. Also mechanical and tribological properties of ultra-smooth TiC/a-C:H films grown on rough steel substrates have been reported.

2 Experimental

TiC/a-C nanocomposite films were grown non-reactively on Si using close field unbalanced pulsed-DC magnetron sputtering deposition setup which has been described elsewhere [14]. It consists of two magnetrons, coupled to one Ti and one Cr target each, powered by DC power supply and two magnetrons, coupled to graphite targets, powered by pulsed-DC power supply. The substrates, located at 80 mm distant from the targets, were pulsed biased at -40 V (250 kHz

frequency). No intentional heating was applied. The substrate holder was rotated by 3 rpm to ensure a homogeneous thickness of the top layer. A 200 nm thick ductile CrTi interlayer of optimized composition and structure was employed to improve the adhesion. Various top layers were deposited for different deposition times and with different pulse frequencies to graphite targets. A rough initial top layer was grown intentionally on the interlayer for 90 min, with 100 kHz frequency and without removing the specimen from the vacuum chamber, keeping all other parameters same, growth was continued for 45 to 180 min with 350 kHz frequency. The microstructure of the films was characterized with a Philips XL-30S FEG high-resolution scanning electron microscope on fracture cross-sections and a DI NanoScope IIIa atomic force microscope was used to analyze the surface morphology. With the microscope operating in a tapping mode, using a Si tip, the film topography images with a 4 μm^2 were acquired.

TiC/a-C:H films were deposited on Ø30×6 mm discs of hardened M2 tool steel, in an argon/acetylene atmosphere, with the same setup mentioned above but replacing the two graphite targets by two Ti targets. The substrates, located at 80 mm distant from the targets, were pulsed biased at -80 V (250 kHz frequency). A ductile CrTi interlayer was deposited to improve adhesion. The substrate holder was rotated by 3 rpm to ensure a homogeneous thickness of the top layer. The pulse frequency applied to the Ti targets was varied viz. 200 kHz and 350 kHz to obtain two different TiC/a-C:H films respectively. A calibrated MTS Nano Indenter XP was employed to measure the hardness (H) and Young's modulus (E) of the films with a Berkovich indenter. In order to have reliable statistics for H and E, 20 indentations in total were configured. The maximum indentation depth for measuring H and E was defined at one tenth of the film thickness. Tribo-tests were performed using a CSM tribometer with a ball-on-disc configuration at room temperature, 0.1 m/s sliding speed (V), 5 N normal load (L) and 50% humidity. The wear depth/height of the coated disc and the counterpart (Ø6 mm ball) was in situ monitored with a resolution of 0.02 μm by a rotational variable differential transformer (RVDT) sensor during the tribo-tests, which allowed in situ measurements of the thickness of the transfer films on the surface of the counterpart. A confocal microscope was used to capture 3D images on a wear track for measuring the wear volume.

3   Results and discussions

3.1   Transition from dynamic roughening to smoothening of TiC/a-C nanocomposite films

As mentioned earlier, understanding the principal factors that govern the surface roughness is not only of fundamental importance for understanding growth mechanisms but also technologically important so as to control the roughness development of growing films. Figure 1 shows the evolution of interface morphology of various TiC/a-C films as a function of growth time. The interlayer exhibits a grainy surface morphology (Fig. 1a) with root mean square (RMS) roughness of 0.29 ± 0.01 nm. Fig. 1b shows the surface morphology of

the TiC/a-C nanocomposite film grown (on the smooth interlayer) by pulsed-DC with 100 kHz frequency. It is interesting to note the immense increase in RMS roughness from 0.29 nm to 5.94 ± 0.15 nm. This clearly indicates that during the film growth the interface experiences continuous roughening.
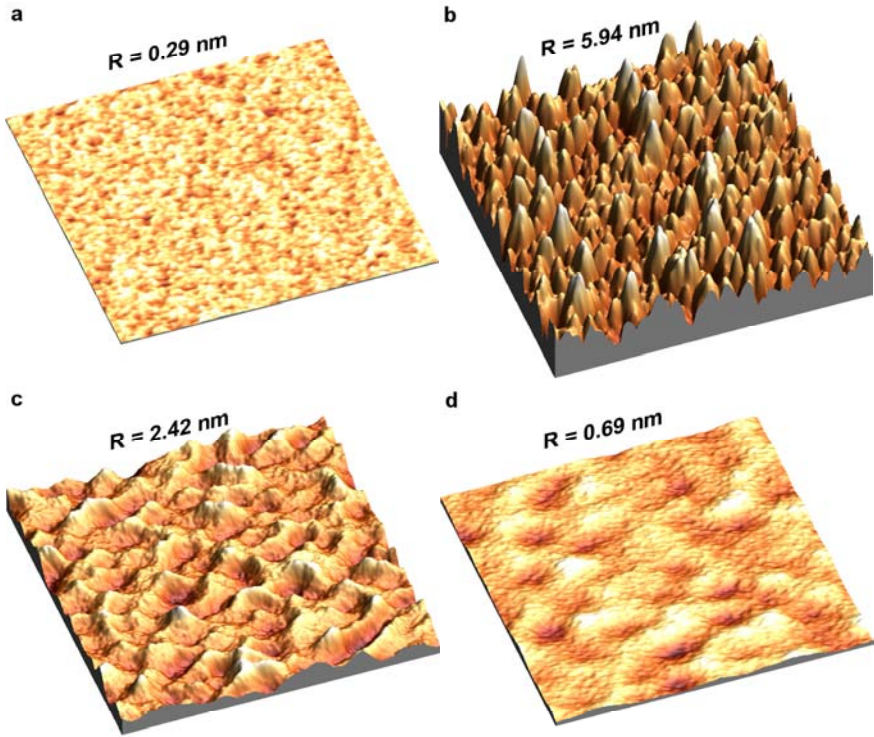
Figure 1:   AFM topography images of (a) interlayer; TiC/a-C nanocomposite films grown for (b) 90 min with 100 kHz on interlayer, (c) 45 min and (d) 180 min with 350 kHz on surface (b). The RMS roughness (R) is noted.

This rough surface (~ 6 nm RMS roughness) represent the polished substrates used in industry. To check the feasibility of dynamic smoothening effect of pulsed-DC sputtering at high pulse frequency [13] on rough surfaces, intentionally rough TiC/a-C nanocomposite films were first grown with 100 kHz (Fig. 1b) and growth was continued with 350 kHz pulse frequency for different growth time. Fig. 1c and Fig. 1d show the interface morphology of TiC/a-C nanocomposite films grown for 45 min and 180 min respectively. The interface roughness decreases from 5.94 nm to 2.42 ± 0.04 nm for 45 min and subsequently to 0.69 ± 0.02 nm for 180 min film growth with pulsed-DC 350 kHz. The rapid decrease in the surface roughness as a function of growth time, with the onset of growth with 350 kHz frequency is of great interest. This

indicates the presence of surface diffusion controlled growth. The change in pulse frequency causes a transition of dominating growth mechanism which controls the film growth.
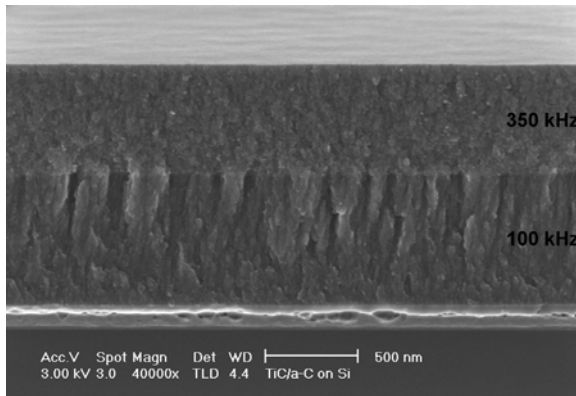
Figure 2:   Cross sectional SEM micrograph of TiC/a-C film grown first with 100 kHz for 90 min followed by 350 kHz for 180 min. An immediate transition of microstructure, from columnar to diffused, was observed with change in pulse frequency from 100 kHz to 350 kHz.

In sputter deposition, the growth dynamics are dominated by nonlocal growth effects. The primary nonlocal effect is geometrical shadowing, where taller surface features block the incoming flux from reaching lower-lying areas of the surface. The shadowing effect is active because, in sputter deposition, the incoming flux has an angular distribution. This allows the taller surface features to grow at the expense of shorter ones, leading to a competition between different surface features for particle flux. This competition, in the absence of lateral relaxation processes leads to interface roughening for films grown at low pulse frequency (100 kHz). However, pulsing the magnetrons at higher pulse frequency results in increased ion energy flux delivered to the growing film [14]. The ion flux and ion energy bombarding at the growing interface plays a crucial role in achieving the smoothening effect.

At 350 kHz frequency a high Ar+ ions and energy flux, among which 80% of ions carry 50-250 eV, was delivered to the growing film [14]. Also the plasma fills in the whole chamber ensuring continuous impingement of the growing film in a closed-field unbalanced configuration [14]. The Ar+ ions impinge more likely at the surface protrusions or hills rather than at the valleys leading to the development of growth instabilities, which is consistent with a scenario in which shadowing effects operate. As the growth progresses, the hills merge into each other at the bottom of the valleys, which is due to the preferred growth of the valley in the midst of the hills. At the final stage of the growth at 180 min, the surface becomes smoother and the peak-to-valley distance becomes smaller. It is believed that the intensive and continuous impingement with high flux and high

energy ions cause impact induced downhill flow of adatoms in the presence of top amorphous layer [13] as proposed by Moseler et al. [9]. This surface diffusion competes with the geometrical shadowing and noise induced roughening to evolve surface smoothening. However at 100 kHz the Ar+ ion and energy flux is quite low compared to 350 kHz. Also the plasma does not cover the whole chamber [14]. Under these growth conditions the surface diffusion does not provide enough lateral relaxation yielding dynamic roughening.

   Fig. 2 shows the fracture cross section of TiC/a-C nanocomposite film grown for 90 min with 100 kHz and subsequently for 180 min with 350 kHz pulse frequency. During the growth with 100 kHz frequency, the microstructure shows a severe columnar structure but at the onset of growth with 350 kHz the microstructure evolves in a dense and non columnar structure. A rough interface induces columnar growth at 100 kHz. Thus the interface structure essentially determines the microstructure of the film. And as the growth mechanisms control the interface structure during growth, the restraint of columnar structure can be attributed to change in dominant growth mechanism from geometric shadowing to surface diffusion by impact induced atomistic downhill flow.

3.2 Ultrasmooth TiC/a-C:H nanocomposite films grown on rough steel substrates

The surface topography and tribological characterization of TiC/a-C:H nanocomposite films grown by pulsed-DC at higher pulse frequencies on rough steel substrates will be described in the following. Fig. 3 shows the evolution of surface morphology of these films. The RMS roughness of the steel substrate decreases considerably from 1.37 ± 0.07 nm to 0.29 ± 0.01 nm and 0.19 ± 0.01 nm for films deposited with 200 kHz and 350 kHz respectively. The RMS roughness calculated by AFM (Fig. 3a) for steel substrates is too low as it is scanned over small area (2 μm×2 μm). So confocal microscopy was used to image the topography of the steel substrates (not shown) and the Sa value (over 290 μm×290 μm) was measured as 6 nm which is typical value for the polished industrial substrates. During the film growth the groove structure (Fig. 3a) breaks
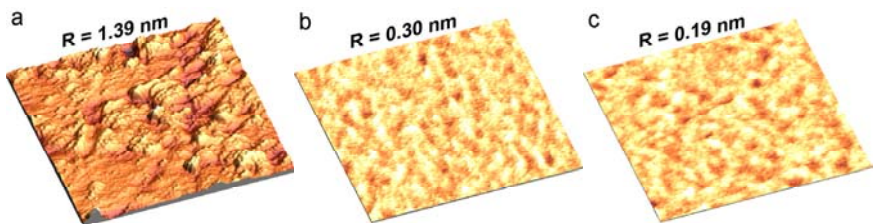
Figure 3:   AFM topography images of (a) steel substrate; TiC/a-C:H nanocomposite films grown by pulsed-DC sputtering with pulse frequency: (b) 200 kHz and (c) 350 kHz. The RMS roughness (R) is noted.
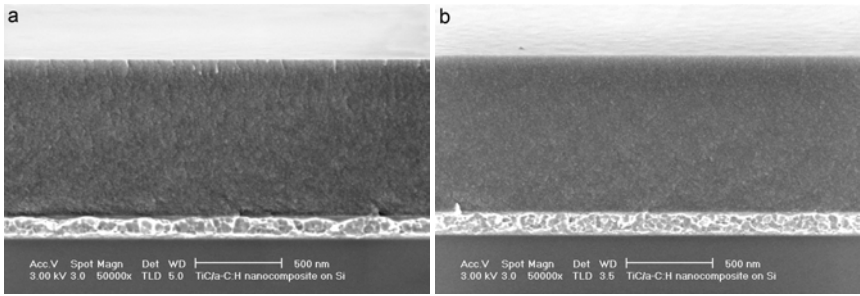
Figure 4:   Fracture cross section of TiC/a-C:H films deposited by pulsed-DC reactive sputtering of pulse frequency: (a) 200 kHz and (b) 350 kHz.

down as the hills merge at the bottom of the valleys in the presence of ion impingement and the interface experiences smoothening (Fig. 3b and 3c). Another contribution to the breaking down of grove network in reactive sputtering is filling in the grooves with carbon adatoms of high mobility [2]. Thus ultra-smooth films can be effectively grown on rough substrates with enhanced ion impingement during film growth by pulsed-DC sputtering at higher pulse frequencies.

As mentioned earlier, the interface structure essentially determines the microstructure of the films. A rough interface induces columnar structure. But the concurrent ion impingement suppresses the column formation and evolves glassy microstructure for films grown by pulsed-DC sputtering at higher pulse frequency as shown in Fig. 4. Such dense films with an amorphous microstructure exhibits a substantial toughening compared to films with columnar structure where nucleation and crack propagation is favoured at the CBs [2].

Fig. 5 shows the tribological characterization of these films. Representative graph of friction coefficient versus running laps for TiC/a-C:H film grown by p-DC 200 kHz is shown in Fig. 5a. It shows not only a low steady-state CoF (0.049), but also a quick drop in the CoF from an initially high value of about 0.18 at the beginning of sliding until the transition point where the steady state is reached. This behavior is attributed to the gradual formation of a transfer film on the counterpart surface during the early stage of a tribo-test, which makes the contact in between two basically similar hydrophobic DLC surfaces that contribute to counterpart surface during the early stage of a tribo-test, which makes the contact in between two basically similar hydrophobic DLC surfaces that contribute to self-lubrication. The interfacial sliding actually takes place between the transfer films on the ball and the surface of the film, rather than sliding between the surfaces of the counterpart and the film. To investigate further the influence of the transfer layer, the wear depth was monitored inset through an RVDT sensor. Segments with a negative slope were observed in the depth vs. lap graph, as marked by the arrows in Fig. 5a. These segments are indicative of the built-up of a transfer layer on the ball surface, rather than a real
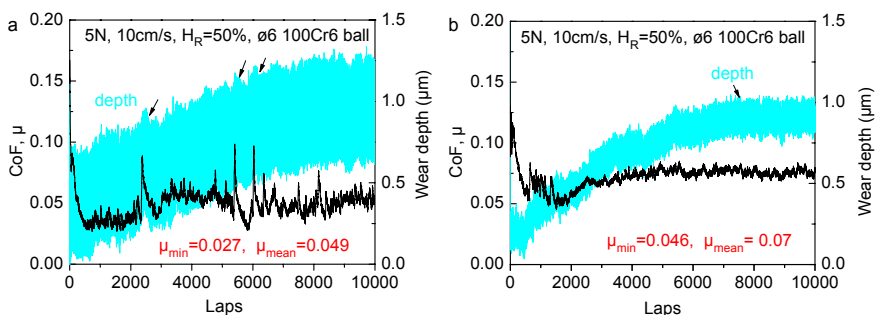
Figure 5:   Tribo-test results showing friction coefficient of TiC/a-C:H nanocomposite films on hardened M2 tool steel substrates by pulsed-DC reactive sputtering of frequency (a) 200 kHz and (b) 350 kHz.

reduction in the depth of the wear track on the films. Correspondingly, substantial drops in the CoF were detected.

Often peaks were observed in the trace. Their presence can be explained as follows: as the transfer film forms on the counterpart, the CoF cannot decrease further and therefore starts to fluctuate. It can be inferred that since the transfer film covers the ball surface in contact, the wear rate of the film decreases and leads to less wear debris. As a result, the transfer film becomes thinner during sliding until it fully breaks down, leading to a sudden rise of the CoF. Sliding at a higher CoF can generate more debris from the wear track, which in turn can provide the necessary material for the growth of a new transfer film. Thereafter, a new cycle of the dynamic friction process is repeated. Wear debris collected in front of and beside the wear scar on the ball counterpart were observed under optical microscope (not shown). Similar self-lubrication effect was observed for the film grown by pulsed-DC 350 kHz as shown in Fig. 5b. However, the steady state CoF was 0.07. The increase in CoF is mainly due to the increased hardness of the film grown at 350 kHz compared to 200 kHz. Hardness of these films was measured by nanoindentation as 16.1 and 17.1 GPa for 200 and 350 kHz respectively. During sliding (Fig. 5b), there is frequent built-up and rupture of transfer layer formed on the ball counterpart in the presence of hard abrasives. A confocal microscope was used to capture 3D images of each wear track for measuring the wear volume. Eight images of 3D profiles were captured at different positions on a wear track for statistics. A software code was programmed in MatLab to process the 3D images and to calculate the wear rate of the films. The wear rates were calculated as 5×10^{-8} and 3×10^{-8} mm^3/(N lap m) for the films grown with 200 and 350 kHz respectively.

4   Conclusions

Dynamic smoothening of DLC based nanocomposite films grown on rough substrates is revealed. It is shown that smoothening of initially rough surfaces with RMS roughness ~ 6 nm to RMS roughness < 1 nm can be effectively

achieved with pulse-DC sputtering at higher frequency. The ion flux and ion energy bombarding at the growing interface plays crucial role in achieving the smoothening effect and hence column-free microstructure. At low pulse frequencies, the film growth is dominated by geometrical shadowing effect while at high frequency surface diffusion effect due to impact induced downhill flow dominates. Ultrasmooth (RMS roughness ~ 0.2 nm), dense TiC/a-C:H films grown on rough steel substrates exhibit superb toughness, wear resistance and ultralow friction.

Acknowledgements

References

[1]   J. Robertson, *Mater. Sci. Eng*., R. 37, 129 (2002).
[2]   Y.T. Pei, D. Galvan, J.Th.M. De Hosson, *Acta Mater.,* 53, 4505 (2005).
[3]   R.P.U. Karunasiri, R. Bruinsma, J. Rudnick, *Phys. Rev. Lett*., 62, 788 (1989).
[4]   A.L. Barabasi, H.E. Stanley, *Fractal Concepts in Surface Growth*, (Cambridge Univ. Press, Cambridge, 1995).
[5]   H.N. Yang, Y.P. Zhao, G.C. Wang, T.M. Lu, *Phys. Rev. Lett.*, 76, 3774 (1996).
[6]   H. You, R.P. Chiarello, H.K. Kim, K.G. Vandervoort, *Phys. Rev. Lett.*, 70, 2900 (1993).
[7]   B.Q. Li, I. Kojima, J.M. Zuo, *J. App. Phys., 91*,4082 (2002).
[8]   C. Casiraohi, A.C. Ferrari, R. Ohr, A.J. Flewitt, D.P. Chu, J. Robertson, *Phys. Rev. Lett*, 91, 226104 (2003).
[9]   M. Moseler, P. Gumbsch, C. Casiraghi, A.C. Ferrari, J. Robertson, *Science,* 309, 1545 (2005).
[10] M.F. Gyure, J.J. Zinck, C. Ratsch, D.D. Vvedensky, *Phys. Rev. Lett*, 81, 4931 (1998).
[11] B.A. Sperling, R. Abelson, *Appl. Phys. Lett*., 85, 3456 (2004).
[12] Z.-J. Liu, P.W. Shum, Y.G. Shen, *Appl. Phys. Lett.*, 86, 251908 (2005).
[13] Y.T. Pei, K.P. Shaha, C.Q. Chen, R. van der Hulst, A.A. Turkin, D.I. Vainshtein, J. Th. M. De Hosson, *Acta. Mater.,* (submitted).
[14] Y.T. Pei, C.Q. Chen, K.P. Shaha, J. Th. M. De Hosson, J.W. Bradley, S.A. Voronin, M. Cada, *Acta. Mater.,* 56, 696 (2008).

This page intentionally left blank

The use of navy C-ring specimens to study distortion in ferritic nitrocarburized 1010 steel

C. Nan[1], D. O. Northwood[1], R. J. Bowers[1], X. Sun[2] & P. Bauerle[2]

[1]Department of Mechanical, Automotive and Materials Engineering, University of Windsor, Canada
[2]Chrysler LLC, USA

Abstract

Ferritic nitrocarburizing is being proposed as an alternative to gas carbonitriding to improve the surface characteristics of SAE 1010 plain carbon steel automotive components without producing unacceptable part distortion. Navy C-rings are specially designed specimens for the evaluation of the distortion (size and shape) that result from any heat treatment process.   In this study, gas ferritic nitrocarburizing and nitrogen cooling was used to heat treat Navy C-ring specimens of varying thicknesses (2.8 mm–19.05 mm) at temperatures ranging from 510°C to 595°C. For each combination of part thickness and heat treatment temperature, the following parameters were evaluated: size and shape distortion; XRD and OM (optical microscopy) to characterize the nature of the nitride layers formed at the surface; X-ray determination of the residual stresses in the nitride surface layers.

   The various combinations of nitrocarburizing temperature and time resulted in an expansion of the OD (Outside Diameter) dimension and a small deterioration in flatness. The ID (Inside Diameter) changed from a small expansion (+0.02%) for the thickest specimens (19.05 mm) to a small contraction (-0.02%) for the thinnest specimens (2.8 mm). The gap tends to close up as the thickness decreases from the thickest to the thinnest specimens. Microstructural differences were found in the nitrided layers formed at the different heat treatment temperatures. The residual stresses in the outer ε-nitride layers (Fe_3N) were typically tensile. On the basis of these results, preliminary recommendations are made as to heat treatment parameters to lower distortion.
Keywords: navy C-ring, ferritic nitrocarburizing, carbonitriding, dimensional distortion, residual stress.

1   Introduction

Carburizing and carbonitriding have become important and widely used processes for developing hard cases at the surface of steel parts by modifying the chemical composition of the surface with hardening species such as carbon and nitrogen [1]. Carbonitriding is generally regarded as a modified gas carburizing process, in which nitrogen is introduced into the gas carburizing atmosphere through the dissociation of ammonia, and diffuses into the austenite of steel simultaneously with carbon [2, 3]. Similar to carburizing, the austenite composition is changed and high surface hardness is produced by quenching to form martensite [4]. However, carbonitriding is performed at lower temperatures ranging between 705 and 900°C and shorter times than carburizing. The reduced process time and temperature, in addition to the ability of nitrogen to inhibit the diffusion of carbon, results in relatively shallow case depths, from 0.075 to 0.75mm [2, 4].

The nitrogen in carbonitrided steels enhances the hardenability of steel by lowering the critical cooling rate, and improves the resistance of steel to softening at slightly elevated temperatures [2]. However, high nitrogen levels can result in retained austenite after quenching because nitrogen lowers the transformation temperature of austenite, and can lead to the formation of voids or porosity when processing times are too long [2, 3]. The delayed transformation of austenite to martensite at ambient temperatures can be extremely detrimental as it results in both size and shape distortions which may cause serious assembly issues as binding or "freezing" in components with high tolerance specifications [2].

Ferritic nitrocarburizing is another surface hardening method that involves the diffusion of both nitrogen and carbon to the surface of steel while it is in the ferritic condition [5], usually at temperature range between 525 and 650°C [6]. When a steel is nitrocarburized, two different structures, known as the compound layer and diffusion region, can be developed from the surface to the core of the steel [7]. The very thin compound layer with thickness usually between 10 and 40 μm for most applications is composed of single-phase epsilon (ε) iron-carbonitride ($Fe_{2-3}(N,C)$), forming between 450 and 590°C [8]. The diffusion zone beneath the compound layer contains varying amounts of gamma prime (γ') and epsilon phase, cementite, and various alloy carbides and nitrides [8, 9]. The compound layer improves the tribological properties, wear and corrosion resistance, while the diffusion zone increases the fatigue endurance limit, particularly in carbon and low-alloy steel [5, 10]. The total thickness of the compound layer and the diffusion zone can reach 1mm [8]. Another advantage of ferritic nitrocarburizing is the minimum distortion due to the low-temperature process, no subsequent transformation from austenite to martensite occurs [6].

In the present study, gas ferritic nitrocarburizing and nitrogen cooling was performed at different heat treatment temperatures and times as well as a carbonitriding using current production practice for 1010 steel automotive components [11]. Navy C-ring specimens with varying thicknesses were used to

evaluate the size and shape distortion, the microstructure and the surface residual stresses produced by different heat treatment parameters [12].

Residual stresses are the inevitable result of thermomechanical processing of steel [13]. With its high spatial resolution and speed, excellent accuracy and nondestructive measurements, X-ray diffraction (XRD) has become an essential tool for residual stress determination. The presence of residual stress in the material causes a shift in the XRD peak angular position that can be directly measured. The depth of X-ray penetration in a material is dependent on the wavelength of the incident radiation and the mass absorption coefficient of the material. Common depths of penetration range between 10 and 20 μm [14].

2   Experimental details

The Navy C-ring specimens were cut from bar stock of hot rolled SAE 1010 plain carbon steel. The chemical composition of the steel is given in Table 1.

Table 1:   Chemical composition of SAE 1010 plain carbon steel.

Element		Wt. %	Element		Wt. %
Carbon	(C)	0.12	Aluminum	(Al)	0.052
Manganese	(Mn)	0.43	Vanadium	(V)	0.001
Phosphorus	(P)	0.008	Columbium	(Cb)	Not Detected
Sulfur	(S)	0.008	Titanium	(Ti)	0.002
Silicon	(Si)	0.03	Cobalt	(Co)	Not Detected
Chromium	(Cr)	0.03	Tin	(Sn)	Not Detected
Nickel	(Ni)	0.01	Boron	(B)	0.0003
Molybdenum	(Mo)	0.01	Calcium	(Ca)	0.0001
Copper	(Cu)	0.02	Zirconium	(Zr)	Not Detected
Plumbum	(Pb)	Not Detected	Tungsten	(W)	Not Detected

The dimensions of the Navy C-rings are shown in Figure1. According to their thickness (19.05 to 2.8 mm), the Navy C-rings were divided into five groups identified as the 1-NC to 5-NC series. Each of these groups was again subdivided into two groups. One group underwent gas ferritic nitrocarburizing and a subsequent nitrogen cooling process. The other group was heat treated using a gas carbonitriding and oil quench process. The detailed heat treatment parameters are given in Table 2. Each heat treatment process schedule was identified using the symbols *a* to *e*.

Four specified dimensions for each C-ring sample were measured using a Coordinate Measuring Machine (CMM) both before and after heat treatment. These dimensions were OD, ID, gap width and surface flatness. These results were then used to compare both size (OD, ID, gap) and shape (flatness) distortion for the different heat treatment processes.
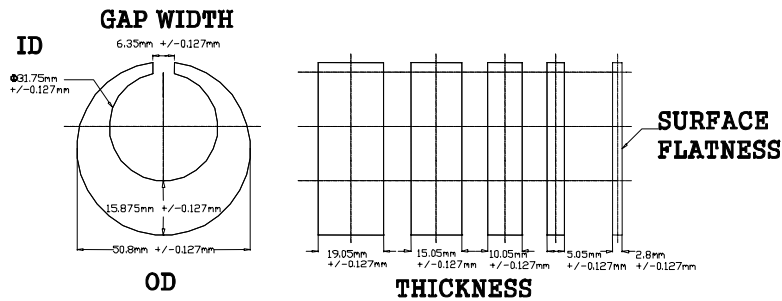
Figure 1:   Navy C-ring's geometry and distortion measurement positions.

Table 2:   Heat treatment processing matrix for navy C-ring specimens.

No.	Heat treatment schedule				
	Process 1		Process 2		Symbol
1	Gas ferritic nitrocarburizing	510ºC / 15 hrs	Nitrogen cooling	425ºC	*a*
2		540ºC / 10 hrs			*b*
3		565ºC / 5 hrs			*c*
4		595ºC / 4 hrs			*d*
5	Gas carbonitriding	850ºC / 4 hrs	Oil quench	100ºC	*e*

An XRD method was used to determine the residual stress on the surface of nitrocarburized C-ring samples. The measurement location of the residual stress was at the thickest section of the OD. The alignment of the XRD instrument was performed according to the ASTM E915 Standard [15]. The residual stresses were calculated by measuring the lattice deformations on the (302) crystallographic plane of the ε-phase (Fe_3N) using Cr target with a wavelength of 0.2291 nm. The generator voltage and current settings were 40 kV and 40 mA, respectively. The Bragg angle (2θ) was set at 165.00°. The following Ψ angles were used to ensure accurate residual stress results: 0°, ±30.00°, ±23.46°, ±11.95°, and ±7.58°. A detailed description of the XRD residual stress analysis method is given in references [13, 14, 16].

3   Results and discussion

3.1 Optical metallography

A series of micrographs for the nitrocarburized 5-NC C-ring samples are shown in Figures 2–5. The white layer is formed as a relatively uniform band at the surface. X-ray structural analysis revealed that the layer is composed predominantly of the ε phase. Beneath the white layer is the diffusion zone, which consists of a needle-like γ' phase. As shown in Figure 2, the γ' phase is mainly located near the interface of compound layer and diffusion zone. The
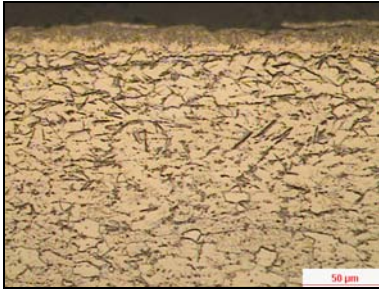
Figure 2:   Microstructure of the gas ferritic nitro-carburized sample (*a*).
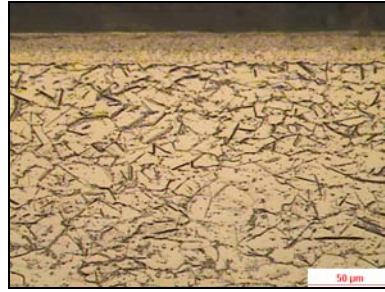
Figure 3:   Microstructure of the gas ferritic nitro-carburized sample (*b*).
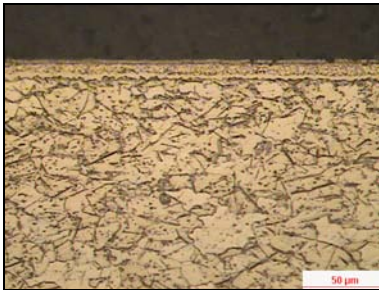
Figure 4:   Microstructure of the gas ferritic nitro-carburized sample (*c*).
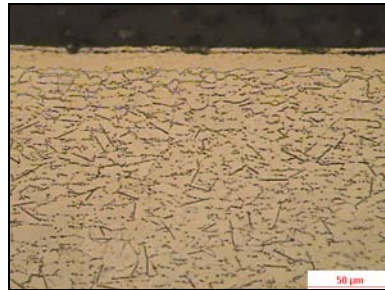
Figure 5:   Microstructure of the gas ferritic nitro-carburized sample (*d*).

penetration of γ' in the diffusion zone increased with increasing temperature, as illustrated in Figures 3–4.

3.2 Comparison of size and shape distortion

The dimensional measurements for the various C-ring sample groups were repeated on 10 identically treated C-rings, the averages of the values obtained from the individual tests were then reported as percentage dimensional changes, and are shown in Tables 3–5.

Both nitrocarburizing and carbonitriding led to a small expansion of the outside diameter, except for the carbonitrided 5-NC sample. Gas carbonitriding produced the largest OD distortion in the 1-NC series. A comparison of the OD changes resulting from the different ferritic nitrocarburizing processes is shown in Figure 6. The OD changes were similar in the same series (thickness) of specimens for the different nitrocarburizing temperatures. A comparison of the different C-ring series reveals that the OD dimensions of 1-NC and 5-NC series varied over a wider range from sample to sample and with temperature: this was

particularly true for the thinnest samples (5-NC series). The 565°C / 5 hours process resulted in the smallest OD change compared to the other temperature - time combinations.

Table 3:   OD size distortion of C-ring samples (unit: %).

Process	1-NC series	2-NC series	3-NC series	4-NC series	5-NC series
a	0.0509	0.0418	0.0472	0.0472	0.0541
b	0.0463	0.0374	0.0409	0.0360	0.0549
c	0.0438	0.0383	0.0440	0.0340	0.0380
d	0.0491	0.0393	0.0463	0.0336	0.0548
e	0.1146	N/A	N/A	0.0295	-0.0195
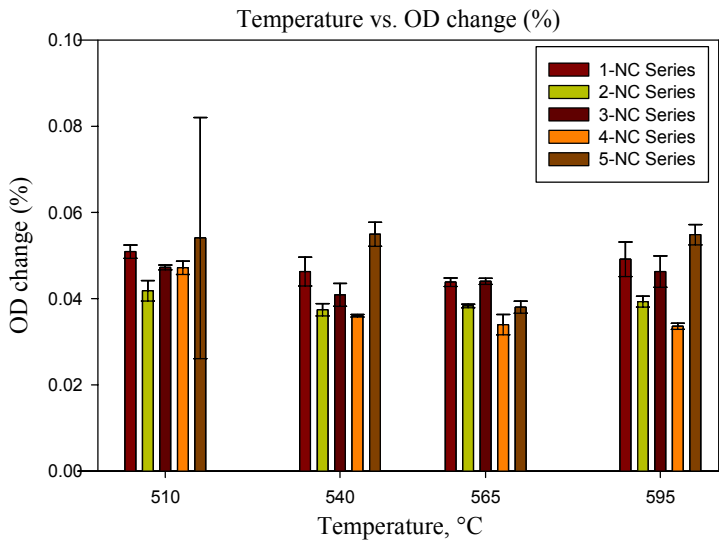
Figure 6:   OD change of nitrocarburized C-rings as a function of nitrocarburizing temperature.

Table 4:   ID size distortion of C-ring samples (unit: %).

Process	1-NC series	2-NC series	3-NC series	4-NC series	5-NC series
a	0.0203	0.0009	0.0009	-0.0216	0.0166
b	0.0248	0.0008	0.0004	-0.0087	-0.0209
c	0.0201	0.0029	0.0012	-0.0108	-0.0079
d	0.0213	-0.0038	0.0018	-0.0070	-0.0156
e	0.1565	N/A	N/A	-0.0343	-0.1230

For the ID measurements shown in Table 4, the C-rings subjected to gas carbonitriding experienced larger ID changes than those subjected to ferritic nitrocarburizing. The ID dimension after nitrocarburizing increased in the 1-NC

series, whereas it decreased in the 4-NC series. The 2-NC and 3-NC series showed smaller ID changes than the other series, see Figure 7. Similar to the OD results, the 1-NC and 5-NC series showed larger ID distortion than the other series. The ID dimension of the 5-NC series varied widely from sample to sample after 15 hours heat treatment at 510°C.
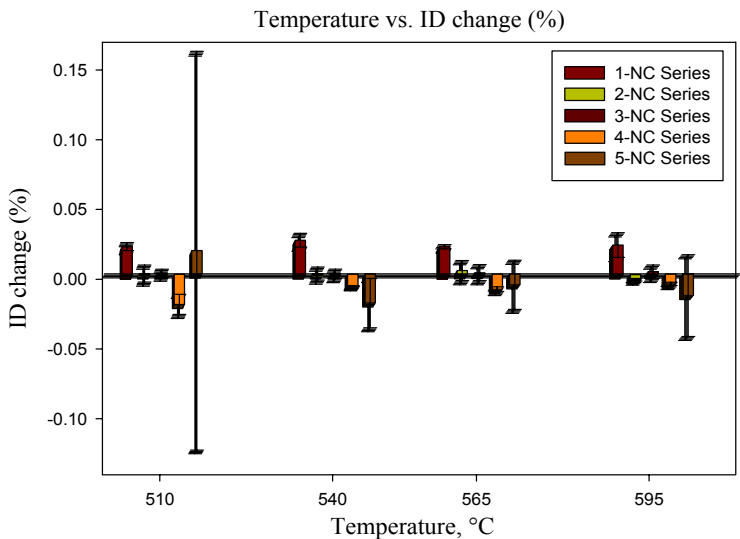
Figure 7:   ID change of nitrocarburized C-rings as a function of nitrocarburizing temperature.

Table 5:   Gap distortion of C-ring samples (unit: %).

Process	1-NC series	2-NC series	3-NC series	4-NC series	5-NC series
a	-0.0139	-0.1361	-0.2644	-0.3524	-0.3703
b	0.0798	-0.1066	-0.2528	-0.2367	-0.1820
c	0.0311	-0.0424	-0.2484	-0.2452	-0.1893
d	0.0936	-0.1173	-0.2377	-0.2030	-0.1650
e	2.4424	N/A	N/A	0.0833	-1.2482

Table 5 which is a summary of the gap distortion measurements shows that the carbonitriding resulted in a larger gap distortion in the 1-NC and the 5-NC series samples than the nitrocarburizing processes. Figure 8 shows that the gap tends to close up as the C-ring thickness decreases from the 1-NC to the 5-NC series. Nitrocarburizing at 565 °C for 5 hours led to smaller changes in gap width than other nitrocarburizing schedules.

Flatness is a geometric control in which a part surface is compared to a reference surface, usually the perfectly flat geometric counterpart of itself, to check the irregularity of the surface [17]. The flatness values in this study were

determined by scanning approximately 2100 points along the perimeter of the C-ring. The measure of flatness shows the difference between the maximum and minimum values derived from a reference surface. An example of a flatness form plot is shown in Figure 9. The small circles indicate the maximum and minimum points of deviation. The surface designated as "1-2-3-4" is the plane containing the minimum point of deviation.
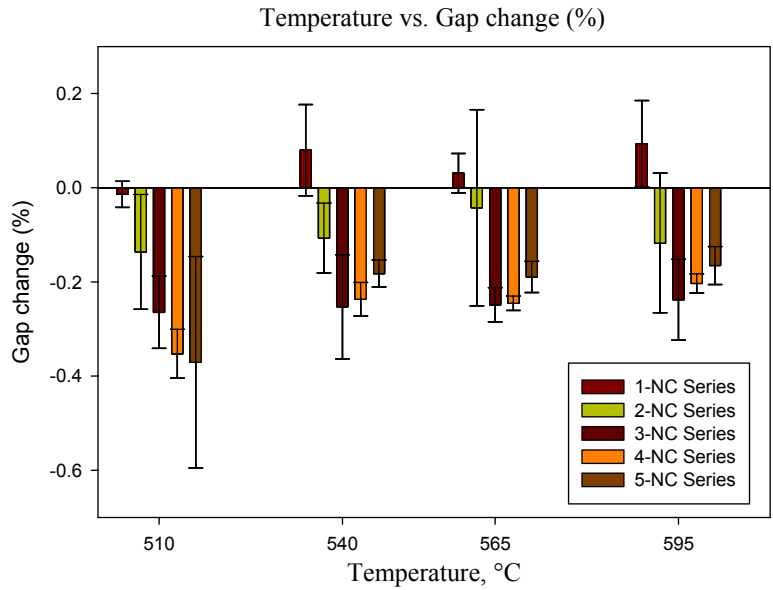
Figure 8:   Gap change of nitrocarburized C-rings as a function of temperature.
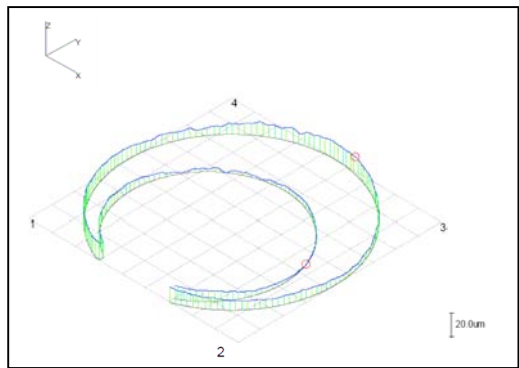
Figure 9:   Flatness measurements on nitrocarburized 1-NC sample (process d).

Table 6:   Flatness change of C-ring samples (unit: mm).

Process	1-NC series	2-NC series	3-NC series	4-NC series	5-NC series
a	-0.0045	0.0024	0.0054	0.0012	0.0002
b	-0.0013	0.0021	0.0043	0.0019	0.0067
c	0.0001	0.0023	0.0023	0.0085	0.0043
d	0.0000	0.0006	0.0038	0.0050	0.0036
e	-0.0038	N/A	N/A	-0.0034	-0.0085

The values of flatness change (mm) due to ferritic nitrocarburizing or carbonitriding are shown in Table 6. The flatness of the C-ring samples after carbonitriding was improved, which means that the difference between the maximum and minimum points of deviation was reduced compared to the sample before carbonitriding. By contrast, the nitrocarburized C-rings showed reduced flatness, except for the 1-NC series. It should be noted that the reported values of flatness are referred to the reference surface as a standard. A comparison of the flatness changes resulting from the different ferritic nitrocarburizing processes is shown in Figure 10.
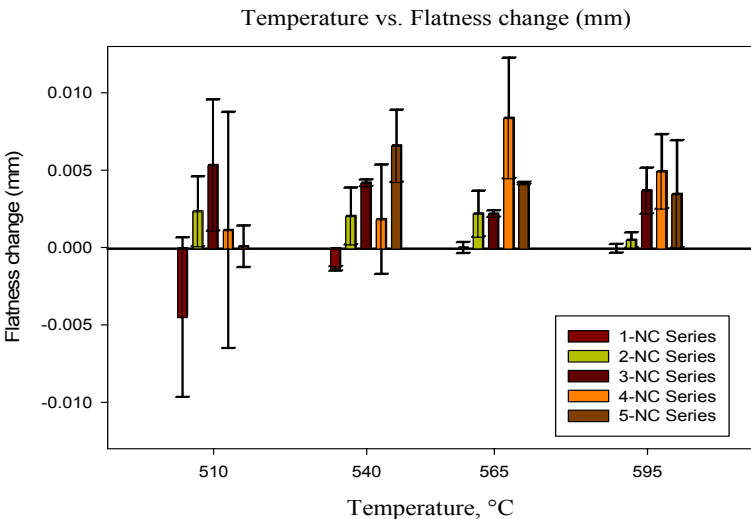
Figure 10:   Flatness change of nitrocarburized C-rings as a function of nitrocarburizing temperature.

3.3 Residual stress measurements

The results of the residual stress measurements for the 1-NC and the 5-NC series determined by XRD are given in Table 7. The nitrocarburizing process generated tensile residual stresses in the ε-nitride surface layer. This is in agreement with the findings of Kolozsva´ry [18] and Watkins et al [19].

Table 7:   Residual stress analysis of C-ring samples (unit: MPa).

Process	Normal stress of the nitrocarburized sample	
	1-NC series	5-NC series
a	86.2 ± 17.2	48.3 ± 14.5
b	101.4 ± 18.6	73.8 ± 10.3
c	140.0 ± 19.3	112.4 ± 15.2
d	103.4 ± 17.9	55.2 ± 9.7

The residual stress values versus nitrocarburizing temperatures for the 1-NC and the 5-NC series are plotted in Figure 11. The magnitude of the residual stress tends to increase with increasing nitrocarburizing temperature, reaching a maximum value at about 565°C. The main causes of the residual stresses in the compound layer are related to the volume changes during the formation of different phases and the internal stresses produced by molecular nitrogen formation within the porosity. The carbon level in the compound layer also has a significant effect on residual stress with increased carbon content producing an increased residual stress level [18]. The other point to be noted is that the residual stresses are lower for the thinner C-ring specimens (5-NC series) compared to the thicker specimens (1-NC series).
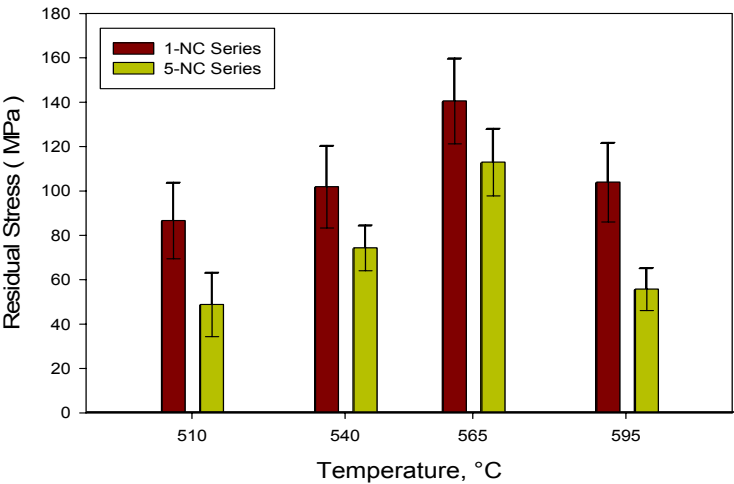
Figure 11:   Plot of the residual stress changes in the C-ring samples.

The residual stresses together with the depth of the compound layer for the 5-NC series are plotted as a function of nitrocarburizing temperature (processes *a*, *b*, *c* and *d)*, in Figure 12. As the compound layer thickness decreases, the residual stress increases. The thinner layers exhibited higher residual stress values, which may be predominantly due to the more compact nature of the thinner compound layers, and a minor effect of the complex influence of the

relaxation process during the long heat treating cycle [18]. The thickness of the compound layer is dependent on the temperature, atmosphere composition, steel grade and heat treatment time [6, 20]. Compared to the samples nitrocarburized at 510 °C and 540 °C, the thickness of the compound layer is smaller in the samples nitrocarburized at 565°C and 595 °C. This is, in part, due to the shorter heat treatment times.
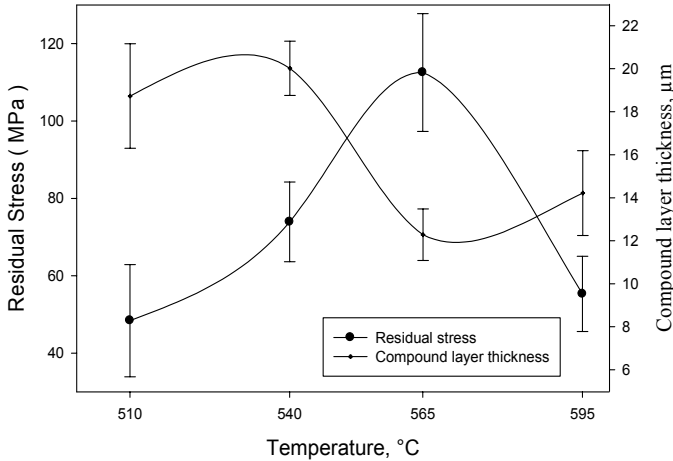
Figure 12:   Comparison of the effect of nitrocarburizing temperature on the residual stresses and compound layer thicknesses for the 5-NCC-ring samples.

4   Conclusions

1. A comparison between the ferritic nitrocarburizing and carbonitriding processes based on the variable thickness of the C-ring samples indicates that:

• In comparison with nitrocarburizing, gas carbonitriding resulted in the largest OD distortion in the 1-NC series; the largest ID changes in the 1-NC, 4-NC and 5-NC series; the largest gap distortion in the 1-NC and 5-NC series.

• The smaller dimensional changes associated with the nitrocarburizing process are attributed to the low heat treatment temperatures which are in the ferritic phase region where no transformation from austenite to martensite occurs.

2. The combination of nitrocarburizing temperature and time as well as the varying thickness of the C-rings lead to different size and shape distortions.

• Ferritic nitrocarburizing resulted in a small expansion of the OD dimension in all C-ring samples.

• Ferritic nitrocarburizing produced either a small contraction or small expansion in ID depending on temperature-time and specimen thickness. The thinner specimens, 5-NC and 4-NC series, generally exhibited a contraction in ID.

- The gap tends to close up as the thickness decreases from the 1-NC to the 5-NC series.

3. Ferritic nitrocarburizing imparted tensile residual stresses in the ε-nitride surface layers of the C-ring samples.

- A thinner compound (ε-nitride) layer gave rise to higher residual stress values.

- The tensile residual stresses in the ε-nitride layer were higher in the thicker (1-NC series) than the thinner (5-NC series) specimens.

4. The size and shape distortions can be reduced by choosing appropriate nitrocarburizing parameters. A combination of 565 °C and 5 hours led to smaller changes in OD, ID and gap, but the largest tensile residual stresses in the ε-nitride surface layers.

References

[1]   American Society for Metals Committee on Gas Carburizing, *Carburizing and Carbonitriding*, American Society for Metals: Metals Park, Ohio, pp. 1-5, 1977.

[2]   Davis, J.R., Carbonitriding (Chapter 5). *Surface Hardening of Steels: Understanding the Basics*, ed. J.R. Davis, ASM International, Materials Park, Ohio, pp. 127-134, 2002.

[3]   Dossett, J., Carbonitriding. *ASM Handbook, Heat Treating*, **4**, ASM International, Materials Park, Ohio, pp. 376-384, 1991.

[4]   Krauss, G., *Steels: Processing, Structure, and Performance*, ASM International, Metals Park, Ohio, pp. 456-460, 2005.

[5]   Bell, T., Gaseous and plasma nitrocarburizing. *ASM Handbook, Heat Treating*, **4**, ASM International, Materials Park, Ohio, pp. 425-436, 1991.

[6]   Pye, D., *Practical Nitriding and Ferritic Nitrocarburizing*, ASM International, Materials Park, Ohio, pp. 193-194, 201-202, 2003.

[7]   Çelik, A., Karakan, M., Alsaran, A. & Efeoglu, I., The investigation of structural, mechanical and tribological properties of plasma nitrocarburized AISI 1020 steel. *Surface and Coatings Technology*, **200(5-6)**, pp. 1926-1932, 2005.

[8]   Davis, J.R., Nitrocarburizing (Chapter 7). *Surface Hardening of Steels: Understanding the Basics*, ed. J.R. Davis, ASM International, Materials Park, Ohio, pp. 195-212, 2002.

[9]   Wells, A., Metallographic analysis of compound layers on ferritic nitrocarburized plain low carbon steel. *Materials Science*, **20,** pp. 2439-2445, 1985.

[10] Dawes, C., Nitrocarburising and its influence on design in the automotive sector. *Heat Treatment of Metals*, **1**, pp. 19-30, 1990.

[11] Schobesberger, P., Streng, T. & Abbas, S., Low-Distortion Heat Treatment of Thin Parts, *Industrial Heating*, **69(2)**, pp. 30-34, 2002.

[12] Boyle, E., Bowers, R.J. & Northwood, D.O., The use of Navy C-ring specimens to investigate the effects of initial microstructure and heat treatment on the residual stress, retained austenite, and distortion of

carburized automotive steels. *SAE Transactions: Materials and Manufacturing*, **116(5)**, pp. 253- 261, 2007.

[13] Ruud, C., Measurement of residual stresses*, Handbook of Residual Stress and Deformation of Steel*, eds. G. Totten, M. Howes, & T. Inoue, ASM International, Materials Park, Ohio, pp. 99-115, 2002.

[14] Pineault, J.A., Belassel, M. & Brauss, M.E., X-ray diffraction residual stress measurement in failure analysis. *ASM Handbook*, *Failure Analysis and Prevention*. **11**, ASM International, Materials Park, Ohio, pp. 484-497, 2002.

[15] ASTM E915-96 standard test method for verifying the alignment of X-ray diffraction instrumentation for residual stress measurement, *American Society for Testing and Materials*, ASTM International: West Conshohocken, PA, 2002.

[16] Walton, H.W., Deflection methods to estimate residual stress, *Handbook of Residual Stress and Deformation of Steel,* eds. G. Totten, M. Howes & T. Inoue, ASM International, Materials Park, Ohio, pp. 89-98, 2002.

[17] Meadows, J.D., *Geometric Dimensioning and Tolerancing: Applications and Techniques for Use in Design, Manufacturing, and Inspection*, CRC Press, 1995.

[18] Kolozsva´ry, Z., Residual stress in nitriding, *Handbook of Residual Stress and Deformation of Steel*, eds. G. Totten, M. Howes & T. Inoue, ASM International, Materials Park, Ohio, pp. 209-219, 2002.

[19] Watkins, T.R., England, R.D., Klepser, C. & Jayaraman, N., Measurement and analysis of residual stress in ε-phase iron nitride layers as a function of depth, *Advances in X-ray Analysis*, **43**, pp. 31-38, 2000.

[20] Sproge, L. & Midea, S.J., Analysis and control of nitriding and nitrocarburizing atmospheres. *Proc. of the 2nd Int. Conf. On Carburizing and Nitriding with Atmospheres*, eds. J. E. Morral, J. Grosch & M. Schneider, Elsevier: Cleveland, Ohio, 1995.

This page intentionally left blank

Dichromate effect on the passive layer of 316L stainless steel

M. Askarian[1], M. Peikari[2] & S. Javadpour[3]
[1]Pars Oil and Gas Company, Iran
[2]Petroleum University of Technology, Iran
[3]Shiraz University, Iran

Abstract

The resistance of a passive layer of stainless steel depends on the alloy composition and conditions in which it is generated. Chemical treatment on steel parts could improve the passive layer. In present work, the effect of passivation treatment, with immersion in a dichromate solution with concentrations 10, 20, and 40 g/l for 24 and 72 hr on the stainless steel 316L was investigated. Polarization and electrochemical impedance spectroscopy studies, conducted in NaCl 3.5%, show that 20 g/l dichromate passivation treatment for 72hr would improve corrosion resistance markedly due to the diffusion control reaction. SEM results imply that passivation treatment is advantageous to improve the smoothness. XPS analysis indicated that a stable mixture compound layer was formed and the passive film can be described by a bi-layer model (inner oxide and outer hydroxide layers).

Keywords: passive layer, 316L stainless steel, dichromate, chemical treatment, EIS, SEM, XPS.

1 Introduction

The high corrosion resistance of stainless steels is primarily due to the oxide layers formed in its surfaces, and for this reason passivation is a question of considerable technical and economical importance [1]. The protective film is normally an oxide of the metal with oxygen dissolved in the contacting solution or by an oxidizing material [4]. The resistance of the passive films is determined by the alloy composition, medium and conditions in which it is generated, causing the passivation of stainless steels to be a very complex process, not still

completely understood [1]. The presence of exogenous surface contamination, including dirt, grease, free iron from contact with steel tooling, and so forth, may interfere with the formation of the passive film. The cleaning of these contaminants from the stainless steel surface will facilitate the spontaneous passivation by allowing the oxygen uniform access to the surface. The passive film may be augmented by chemical treatments that provide an oxidizing environment for the stainless steel surface [5]. This redox system could be any oxidizing agent that forms an oxide layer on steel, such as ferric, nitrite or chromate ions [4, 6]. Stainless steel parts shall be treated in specified aqueous solutions and maintained within the specified temperature range for the specified time.

The purpose of this study is to introduce chemical treatment to enhance corrosion resistance of 316L stainless steel parts.

2 Experiment

Specimens used in this study were 316L stainless steel. The composition in wt% was 0.021% C, 17.61% Cr, 12.45% Ni, 2.29% Mo, 0.069% Si, 1.05% Mn, 0.020% S, 0.031% P, and bal. Fe. They were mounted with an exposed area to 1×1 cm^2. The surface was mechanically polished by 220 grit SiC paper followed with 320/400/800/1000 grit paper to have a comparable surface roughness. Then they were rinsed with deionized water. Passivation treatments were immersed according to the specification in table 1.

Table 1:   Specification of dichromate-passivation treatments.

Sample	Concentration (g/l)	Time (hr)
1	10	24
2	20	24
3	40	24
4	10	72
5	20	72
6	40	72

Attention shall be given to maintaining adequate volume, concentration, purity, and temperature control appropriate to the size of the stainless steel specimens to be treated.

Immediately after removal from the passivating solution the specimens were thoroughly rinsed, using spray washes [5].

The original specimen was tested as-received, without passivation treatment as reference and for comparative purposes. The corrosion properties and composition of the passive layer were studied using DC polarization and electrochemical impedance spectroscopy (EIS). Electrochemical tests were conducted using potentiostat, Model Zahner, in 3.5% NaCl solution at room temperature opening air. Saturated calomel electrode (SCE) was used as a reference electrode and platinum as an auxiliary electrode. Potentiodynamic

polarization curves were plotted from -200mV$_{SCE}$ to +200 mV$_{SCE}$ at a polarization scan rate of 0.1 mV/s; EIS measurements were performed in the frequency range from 100 mHz to 100 kHz with a logarithmic sweeping frequency of 4 steps/decade. EIS involved the imposition of a 10mV amplitude sine-wave and the measurements were carried out at the E$_{corr}$.
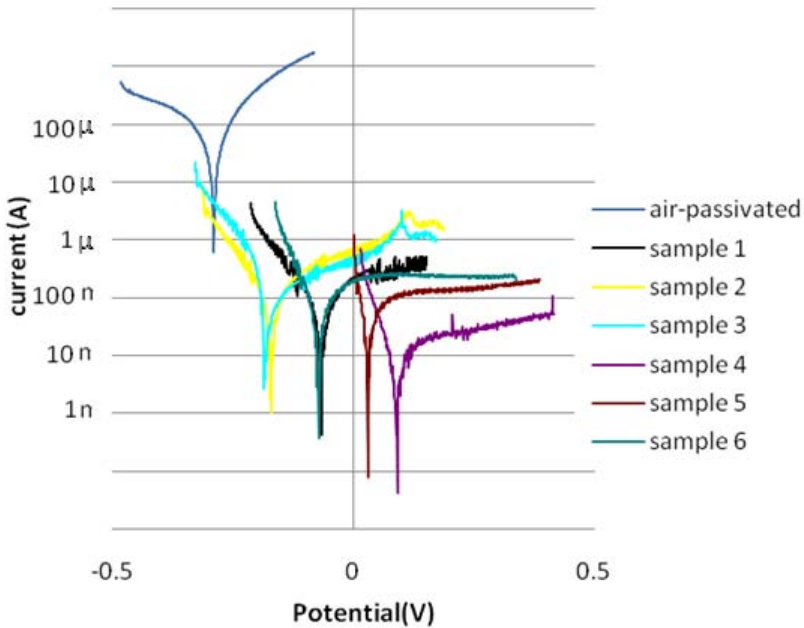
Figure 1:   Polarization curves of specimens.

    The electrochemical results for chromium-passivated specimen were compared with air-passivated indicated which passivation treatment gives superior corrosion resistance. Then the surfaces, microstructure and composition of that specimen were investigated using scanning electron microscopy (SEM), and X-ray photoelectron spectroscopy (XPS) to determine cause for this behaviour. SEM was performed using JEOL JXA-840 equipment at the voltage (15 kV). The XPS spectra were obtained with a VG Microtech electron spectrometer, model MT 500, using an Mg K$\alpha_{1,2}$ anode X-ray source (hv=1253.6 eV) with a primary beam energy of 15 kV and an electron current of 20 mA. The pressure in the analysis cabinet was maintained at 1×10^{-9} Torr throughout the measurements. The regions of interest were O$_{1s}$, Cr$_{2p}$, and Fe$_{2P}$. The concentration of each element was estimated by measuring the respective peak area in the high-resolution XPS spectrum and using elemental sensitivity factors. The specimens were analyzed by means of argon-ion sputtering on the original surface and after 30, 90 and 390 s argon-ion sputtering was carried out with primary beam energy of 5 kV and an ion density of 1 μA/cm^2, recording the corresponding XPS spectrum for each sputtering cycle.

3   Results and discussion

3.1 Electrochemical

Fig. 1 shows polarisation curves for the chromium-passivated and air-passivated specimens tested in a 3.5% NaCl solution. The E_{corr} and I_{corr} of each specimen are mentioned in table 2 [2].

Figure 2 presents Nyquist plots for chromium-passivated and air-passivated specimens tested in a 3.5% NaCl solution.
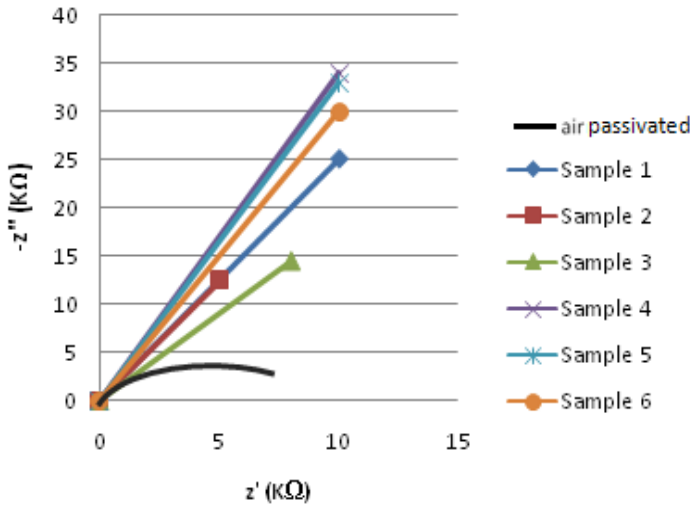
Figure 2:   Nyquist plot of samples 1–6.
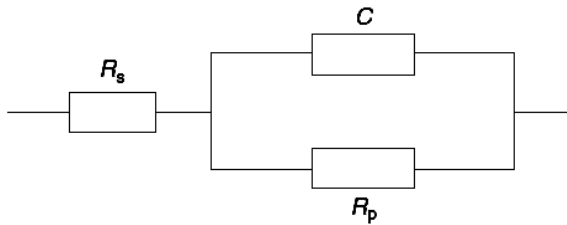
Figure 3:   Randles Simple equivalent circuit of the air-passivated sample.

EIS curves were interpreted by an equivalent circuit. Fig.3 shows Randles Simple equivalent circuit of air-passivated specimen. In this equivalent circuit R_p is the polarization resistance of the outer surface of the working electrode, C the capacity of the electrochemical double layer of the outer surface of the working electrode and R_s the ohmic resistance between the reference electrode and the outer surface of the working electrode [7,8].

The EIS curve of chromium-passivated specimen is more complicated. Imaginary impedances do not increase and capacitive semicircles do not

complete. This behaviour indicates reaction is under diffusion control. Therefore the Warburg diffusion impedance is an inevitable element in circuit. Also capacitive is replaced with CPE (constant phase element) to fit with experimental curve [7,11].

Table 2 indicates R_p obtained from equivalent circuit of each specimen. Electrochemical tests results show chromium treatment improves corrosion resistance of stainless steel. Increasing concentration of chromium and duration of immersion generally has more improving effect. However, too concentrated solution leads to a decrease in corrosion resistance relatively due to transfer into transpassive region [2, 7].
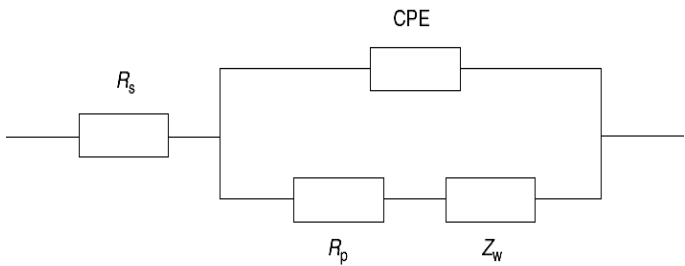
Figure 4: Equivalent circuit of the chromium-passivated samples.

Table 2: EIS and polarization tests results.

sample	(mV) Corrosion potential	Corrosion rate (nA/cm^2)	Resistance (Ω/cm^2)
Air-passivated	-289	5100	1.2×10^3
1	-68	75	2×10^5
2	-170	94	3.67×10^5
3	-157	274	8.8×10^4
4	87	10	4.5×10^5
5	29	6	5.5×10^5
6	-72	59	1.3×10^5

3.2 SEM

No visual difference was seen among the seven samples, but SEM examination indicated some slight topography changes. Figs. 5 and 6 show SEM for air-passivated and the best passivated specimen (sample No.5) respectively. The passivation treatment is advantageous to improve the smoothness [3].

3.3 XPS

XPS analysis of stainless steel surfaces treated by various chemicals can provide valuable information about passivation layer composition, and its ability to protect against corrosion.
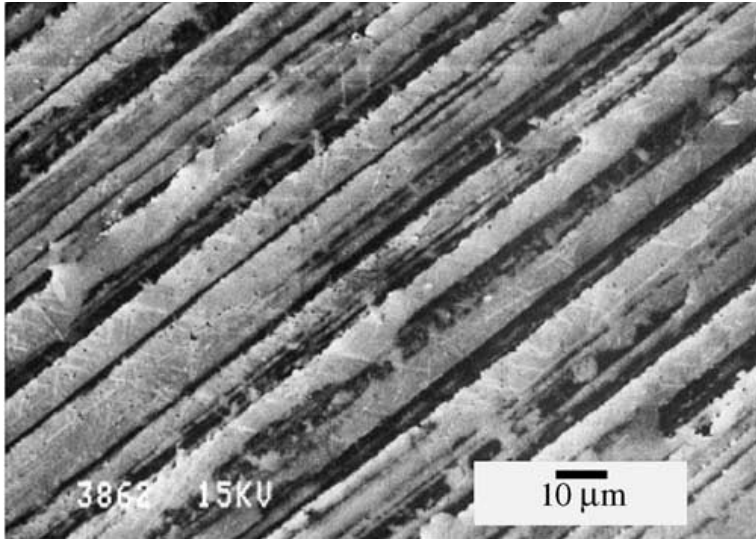
Figure 5:   SEM results for the air-passivated specimen.
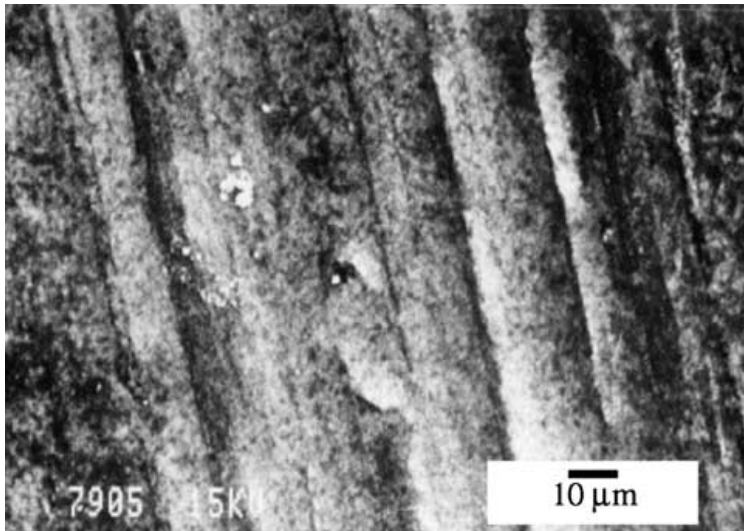
Figure 6:   SEM result for the chromium-passivated specimen.

XPS peaks of O_{1s}, Cr_{2p}, and Fe_{2p} in the passive film at different sputtering times were obtained.

The O_{1s} peaks at 530.2 eV corresponded to O^{2-} in oxide, at 531.3 eV to OH in hydroxide species, and at 532.2 eV in adsorbed water [3]. Fig.7 shows that bonding energy of the O_{1s} peaks on the surface of the passive film was 531.1 ev

to 532.3 eV, which could correspond to O in the hydroxyl oxygen (OH⁻) and oxide oxygen (O^{2-}). When argon-ions sputtering was performed, the hydroxide contributions disappear but the oxide forms increase.

The $Cr_{2p3/2}$ peak at 574.2 eV corresponded to the metallic state, at 576.2 eV corresponding to the tetravalent oxide state, at 576.7 eV corresponded to the trivalent oxide state, and at 577.2 eV corresponding to the trivalent chromium hydroxide species [3]. Fig.8 shows that the bonding energy of Cr_{2p} peak on the surface was 576 eV to 576.8 eV which could be correspond to Cr in Cr^{4+} and Cr^{3+}. Cr in the passive film was effective on improving the corrosion resistance [10].
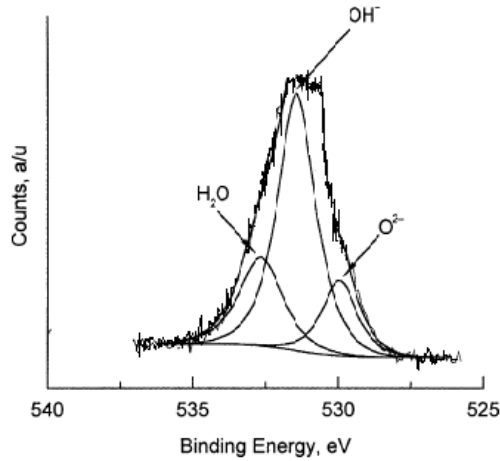
Figure 7:   O1s XPS spectra for the chromium-passivated specimen.
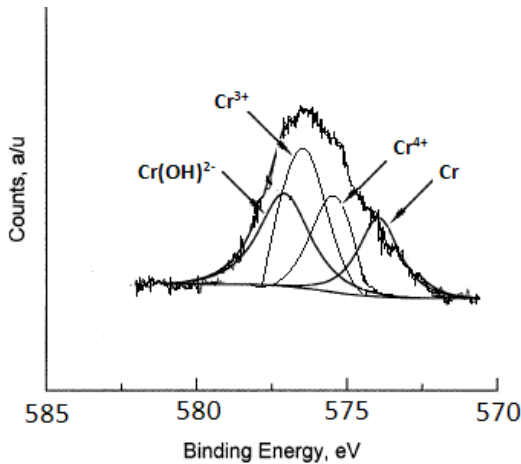
Figure 8: Cr_{2p} XPS spectra for the chromium-passivated specimen.
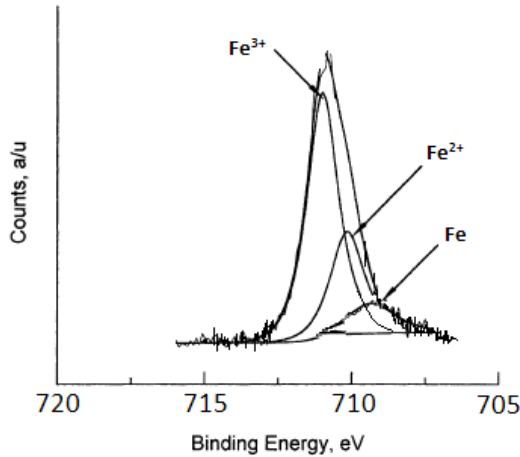
Figure 9: Fe_{2p} XPS spectra for the chromium-passivated specimen.

$Fe_{2P3/2}$ peak at 707.0 eV corresponded to the metallic state, at 709.5 eV corresponded to the divalent oxide state, and at 710.4 eV corresponding to the trivalent oxide state. Fig.9 shows that the bonding energy of the $Fe_{2P3/2}$ peak on the surface was 710.1 eV to 711.1 ev, which corresponded to Fe in Fe^{3+}, FeOOH, or $Fe(OH)_3$.

Based on Fig.7-9, the OH in the outer layer of the passive film could react directly with Cr and Fe to form FeOOH or $Fe(OH)_3$ and CrOOH or $Cr(OH)_3$ that is stable mixture layer and could promote the repassivity of passive film [10].

The atomic concentration (c_i) of the elements, as a percentage, was determined using following equation:

$$C_i = \frac{A_i / S_i}{\sum (A_i / S_i)} \times 100 \tag{1}$$

where A_i is the peak area and S_i is the sensitivity factor [9]. Fig. 10 depicts the atomic concentration of each element against the argon-ion sputtering time. Sputtering time is proportional to passive layer depth [3].

It can be observed in Fig. 10 that chromium is enriched in the surface of passive layer. Oxygen and ferrous increase with the sputtering time. The passive film can be described by a bi-layer model (inner oxide and outer hydroxide layers) [3].

4 Conclusion

- The study presented shows the differences in corrosion behaviour of 316L stainless steel after dichromate passivated. Based on this study, treating in 30g/l dichromate solution at room temperature for 72hr enhanced corrosion resistance significantly.

- DC measurements shows poor corrosion resistance behaviour of air-passivated specimen: R_p=1.2 kΩcm^2 and i_{corr}=5.1 μA/cm^2 respect to enhanced corrosion resistance behaviour of superior chromium-passivated specimen: R_p =550 kΩcm^2 and i_{corr} =0.006 μA/cm^2.
- EIS results indicated passivation treatment lead to diffusion control by considering Warburg diffusion element in equivalent circuit.
- SEM examination reveals that chromium treatment is advantageous to improve smoothness.
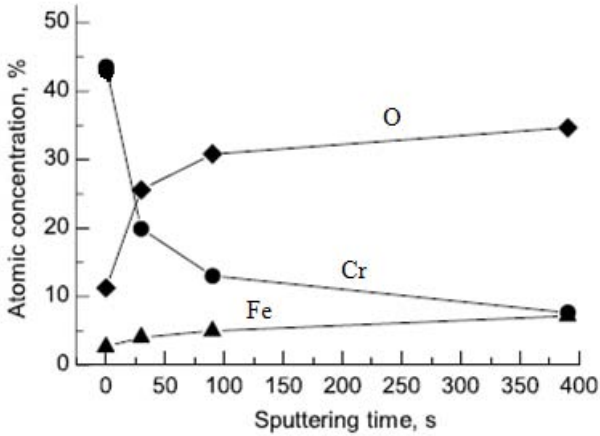
Figure 10:   Atomic concentration of oxygen, chromium and ferrous elements for the chromium-passivated specimen.

The XPS results indicated that chromium-passivation treatment was advanced in the enrichment of Cr on the surface of stainless steel. The stable mixture compounds layer was composed of the alloy elements formed in the passive film. The FeOOH or Fe(OH)$_3$, and CrOOH or Cr(OH)$_3$ could exist in the outer layer of the passive film. There existed oxides of Cr and Fe in the different layer of passive film that play important roles in improving repassivation of stainless steel. The passive film can be described by a bi-layer model (inner oxide and outer hydroxide layers).

Acknowledgements

References

[1]   C.A.C. Sequeira1, D.M.F. Santos1, J.R. Sousa2,and P.S.D. Brito , The Mechanism of Oxide Film Formation on AISI 316 Stainless Steel in

Sulphate Solution, *214th ECS Meeting*, Corrosion General Poster Session, Honolulu, No. 1598

[2] Fontana, (chapter 10), *Corrosion Engineering*, McGraw-Hill Pub., New york,1989

[3] Philippe Marcus, Florian Mansfeld, (eds). *Analytical Methods in Corrosion Science and Engineering,* CRC Press, Taylor & Francis Group, 2006

[4] R. K. Gupta, (Chapter 10) *Metal Surface Treatment and Their Chemicals,* SBP Consultant and engineering PVT. Ltd, 2003

[5] ASM A967 *Standard Specification for Chemical Passivation Treatments For Stainless Steel Parts,* 2000

[6] Tetsuo Fujii, Haruo Baba, *The Effect of Oxidizing Ion on The Passivity*, Corrosion Science (31), pp. 275-280, 1990

[7] Maryam Ehteshamzade (chapter 4), *Application of EIS in corrosion study,* Shahid Bahonar University Kerman p. , 2006

[8] SCK-CEN, Belgian Nuclear Research Centre, Boeretang Belgium, *Electrochemical impedance spectroscopy for the detection of stress corrosion cracks in aqueous corrosion systems at ambient and high temperature''* Corrosion Science (47), 125–143, 2005

[9] Y. Xingwen, C. Chunan, Y. Zhiming, Z. Derui, Y. Zhongda, *Study of double layer rare earth metal conversion coating on aluminium alloy LY12,* Corrosion. Science(43), 1283-1294, 2001

[10] X.Y. Wang, Y.S. Wu, L. Zhang, and Z.Y. Yu, *Atomic Force Microscopy and X-Ray Photoelectron Spectroscopy Study on the Passive Film for Type 316L Stainless steel*, Corrosion Science, 57(6), pg 540, 2001

[11] EG&G Princeton Applied Research, Application Note Ac-1, *Basic of ac Impedance Measurements*, New Jersey, 1992

Section 2
Thick coatings

This page intentionally left blank

Metallic laser clad coatings:
on the processing-microstructure-property relationships

V. Ocelík, U. de Oliveira & J. Th. M. De Hosson
Department of Applied Physics, Materials innovation Institute,
University of Groningen, The Netherlands

Abstract

A thick metallic coating that is resistant against high loading impact, severe wear and corrosion at high temperatures can be produced through the laser clad method. This work introduces the Orientation Imagining Microscopy based on electron backscatter diffraction in a scanning electron microscope as a very powerful instrument for studying relationships between processing parameters and the microstructure of individual laser tracks and final coatings formed by overlap. The study has been performed on thick (~1mm) Co-based coatings prepared by a 2 kW CW Nd:YAG laser cladding on 42CrMo4 steel substrate using substantially different laser beam scanning speeds.

OIM provides new insights into the microstructure of laser clad coatings and yields very useful information concerning the directional grow of individual grains, the solidification texture and the shape of solidification front during laser cladding. Strong correlations between these parameters and laser cladding speed as well as the presence of internal interfaces with the sharp microstructural and mechanical properties changes are presented and discussed.

Keywords: laser cladding, microstructure, orientation imaging microscopy.

1   Introduction

Laser cladding is an advanced hard facing technology that can deposit a hard layer with a controlled thickness onto the selected area of a metallic substrate. It has a low energy input and causes less distortion of the component as compared

to conventional welding base processes. A detailed description of laser cladding process and its characteristics has been presented in the literature [1–3].

Processing windows have been studied intensively during last two decades to define technological regimes that produced thick and defect free coatings with a required thickness. It was found, that the laser cladding process is technologically a quite robust procedure. Laser power P, laser beam scanning speed S and powder feeding rate F (or combinations thereof) are the main technological parameters that control the laser cladding with the powder blowing technique [4-6]. Rapid solidification in the surface layer is the characteristic feature for the laser cladding process and in some conditions the coatings formed by cooling rates higher than 10^3 K/s show very fine, non-equilibrium or even amorphous microstructures. Moreover, the recently developed fiber laser with a nominal power exceeded 5-10 kW provides a possibility to form laser clad coatings at even higher processing speeds and cooling rates [7, 8].

However, the relations between the processing parameters and the final microstructure and properties of laser clad coatings were studied only scarcely [9, 10] and it was mainly focused to the relation between processing speed, secondary dendrite spacing, hardness and wear resistance of Co-based alloys.

The modern Orientation Imagining Microscopy (OIM) technique [11] which combines advantages of Scanning Electron Microscopy (SEM) observations with the information about crystal/grain orientations typical for transmission electron microscopy (TEM) observation may be the very efficient method to study complicated microstructures formed during the laser cladding and fast solidification associated to it. This work is the first attempt to study systematically microstructure of the individual laser tracks and laser clad coatings using OIM.

The Eutroloy 16012 powder was selected for this work because of wide use of Stellite type Co-based alloys in laser coatings applications for hardfacing, wear and corrosion resistance at elevated temperatures. These coatings are extensively used for hardfacing valves, shafts and many other industrial components [3]. The wear resistance of this type alloys and their laser clad coatings is attributed to the high hardness of chromium rich M_7C_3 carbides [12] and to the formation of an oxidation protective layer at high temperatures [6]. The microstructure of rapidly cooled Stellite type alloys with carbon content lower than ~2 wt% is simply characterized as hypoeutectic structure containing face-centered cubic (fcc) Co rich primary dendrites (α-cobalt based solid solution) surrounded by an interdendritic eutectic with W, Cr and Co carbides. It results in a relatively strong electron back scattering diffraction (EBSD) signal originated from α-Co dendrites and interdendritic eutectic component [13]. Due to the coherence between the fcc phase in primary dendrites and in eutectic, the fine dendritic microstructure is not manifested on low magnification OIM scans.

2   Experimental

A 2 kW Nd:YAG Rofin Sinar CW20 high power laser source was used to prepare all single laser tracks or continuous coatings. The laser beam with

wavelength of 1.06 μm was focused 16 mm above the substrate surface forming the circular beam spot size of 3 mm in diameter with a Gaussian distribution of energy density inside the beam on the treated surface. Side powder cladding set-up [6] was used in which the powder is delivered by carrier gas (Argon) from a side against the cladding hill using the commercial powder nozzle (IWS Dresden) mounted under angle 35º to the surface normal. Four different laser beam scanning speeds S = 1, 2.5, 7.5 and 15 mm/s were used to vary the solidification rate. Different laser power and powder feeding rates from intervals 600-1750 W and 21-250 mg/s, respectively, were used to achieve the laser tracks with a similar height and width for all four different scanning speeds.
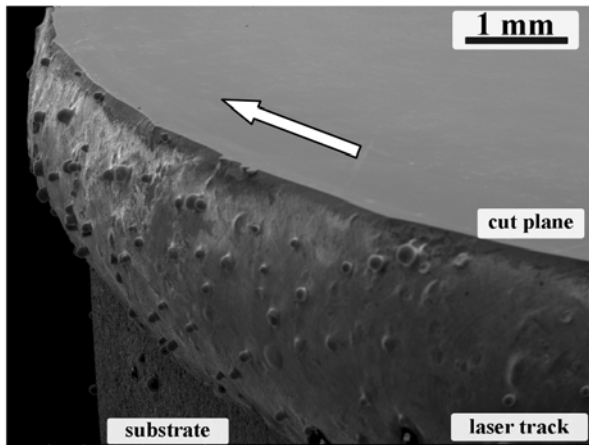
Figure 1:   SEM image of laser clad sample cut in direction perpendicular to substrate bar axes and almost parallel to cladding direction. The arrow indicates direction of substrate movement during laser cladding.

All laser clads were deposited on the substrate consisting of 42CrMo4 steel bar with diameter of 25 mm. The bar was horizontally mounted into a rotation clamp to rotate bar around its axis. The rotation speed at the bar surface actually represents the laser beam scanning speed during the laser cladding. At the same time the substrate bar was slowly moving in the direction of bar axis, to create the laser track in a form of coil at the bar surface. During the clad of single laser tracks this axial movement was set to perform a displacement of one laser track width after each single rotation. To create the laser coatings this displacement has been set to 2/3 of the single laser track width after each rotation to form coatings with 33% laser tracks overlap. The advantage of such arrangement is that the cutting of the bar in an appropriate plane perpendicular to the bar axis allows to observe the microstructure in planes almost parallel to the cladding direction, slowly moving from one to the other side of laser track. Figure 1 demonstrates this on the sample with a single laser track. Samples cut surfaces were subjected to the standard metallographic procedure that started with

grinding on grind papers (180, 300, 500, 800 and 1200), continued with polishing in diamond particles suspensions (9, 6 and 3 µm size) and finished with a long time (~2 hours) polishing in Struers OP-U suspension. This procedure results in an excellent EBSD signal coming from the laser clad area as Kikuchi patterns easily indexed by fcc Co crystal data. TSL back scatter diffraction system installed inside Philips XL30 FEG scanning electron microscope was used to collect OIM data. The samples were mounted in the scanning electron microscope so that the sample normal is at 76 degree with respect to the electron beam direction. The diffraction image formed on the phosphorous screen by diffracted backscattered electrons is digitized and transmitted to the computer. The orientation of the crystal lattice at each predetermined sample surface point is then automatically determined in coordinate system connected with the sample. The arrays of indexed points used in the present experiments were hexagonal networks with y and x increments equal to 3 µm. Between 260k and 520k lattice orientations were determined in each observation using automated indexing regime [14].

3   Results and discussion

3.1 Grains structure

Figure 2 shows the typical OIM image collected from Eutrolloy 16012 single laser track on its transversal cross-section. This Image Quality (IQ) map consists from about 520k points.
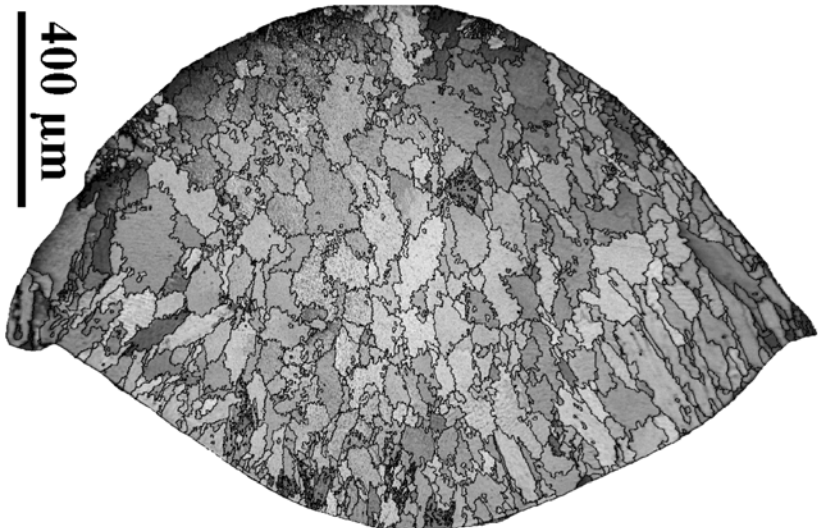
Figure 2:   Typical OIM image quality map with grain boundaries on perpendicular cut of single laser track made at laser beam scanning speed 1 mm/s.

The grey intensity of individual points corresponds to IQ parameter that reflects the quality of Kikuchi pattern for that particular point and number of detectable Kikuchi lines in it. In some grains one could recognize slight variations in grey intensity due to the presence of small dendrites (size ~4 µm) in the microstructure that results in higher quality Kikuchi pattern than interdendritic space between them. Grain boundary lines presented in Fig. 2 were constructed electronically using the condition that the grain boundary between two scanned points exists when the crystal misorientation angle between these two points exceeds 5 degrees. This figure demonstrates few advantages of OIM technique in comparison with standard SEM observations. The size and shape of the grains could be easily detected and statistically investigated due their digital character of OIM maps. The average grain size diameter calculated from data in Fig. 2 is 88 µm. The grain diameter size is spread from 20 to 180 µm and grains are or equiaxial or only slightly elongated in directions pointing from their bottoms to a point at the top of laser track hill.

However, a completely different picture appears when the longitudinal cut in the middle of the laser track shown in Fig. 2 is observed as Fig. 3 clearly demonstrates.
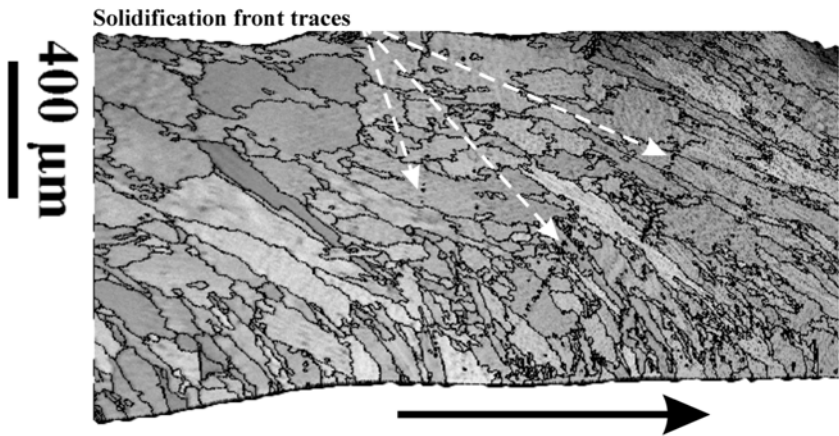
Figure 3:   OIM image quality map with grain boundaries on transversal cut in the middle of single laser track made at laser beam scanning speed 1 mm/s. Black arrow indicates the substrate movement direction during cladding.

The average grain shape aspect ratio is about 0.4, much smaller than on transversal cut. Moreover, the IQ map in Fig. 3 clearly shows the traces of solidification front in the form of group of small black objects on parabolic lines that witness low qualities of EBSD patterns. This is the manifestation of impurities and oxides segregation at such a low laser cladding speed that results in marking of the solidification front shape in a particular moment of laser cladding process. Majority of the grains in the central and lower part of the laser

track are strongly elongated in the direction locally perpendicular to the shape of solidification front. It is inherent to expect, that these directions of grains elongation correspond to the direction of their growing, because the main heat transfer during solidification is realized in direction perpendicular to the solidification front. We may conclude here that the grain size and their shape information from only transversal cut observation are not satisfactory for description of the microstructure formed during laser cladding process. More complete picture is offered by observation of longitudinal cross section.

3.2 Influence of laser beam scanning speed

Figure 4 summarizes the grain size and grain shape observations from transversal and longitudinal cross-sections for all four laser beam scanning speeds.
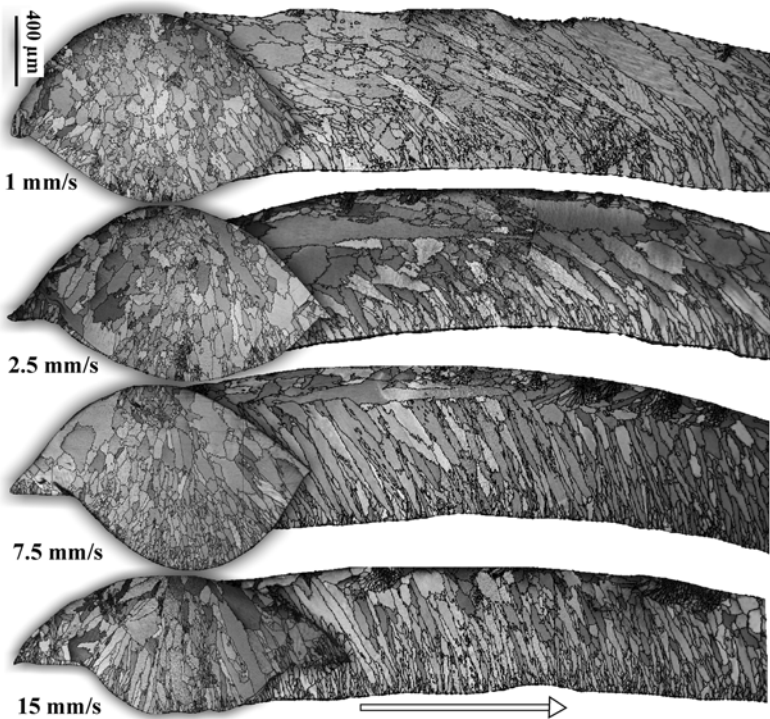
Figure 4: Image quality figures with grain boundaries from transversal (left) and longitudinal (right) cuts of single laser tracks formed at four different laser cladding speeds.

Transversal cross sections show a gradual increase of number of elongated grains with increasing laser beam scanning speed. However, this increase is not induced by a higher presence of elongated grains in the microstructure but it is a simple consequence of gradual change of the average angle between the long

axis of elongated grains and the cladding direction, represented in Fig. 4 by an arrow. To collect quantitative data how this angle changes with the cladding speed we performed the following procedure. First, each detected grain in the longitudinal microstructures from Fig. 4 was replaced by an ellipse that fits this grain shape. In the second step only those grains that shown corresponding ellipse shape ratio (ratio between short and long ellipse axis) lower than 0.3 were separated from the microstructure. Finally, the average angle between the long axes of ellipses represented these grains and cladding direction was calculated for each cladding speed together with the average grains shape ratio. This procedure is explained in the insert of Fig. 5 where an example of the selection of elongated grains is shown for microstructure formed at 15 mm/s scanning speed. Corresponding ellipses, which fit individual elongated grains, are also visible. There is also one example of an angle between the long axis of one grain and the cladding direction shown. The average values were calculated as a statistical mean value from all elongated grains for each scanning speed separately.
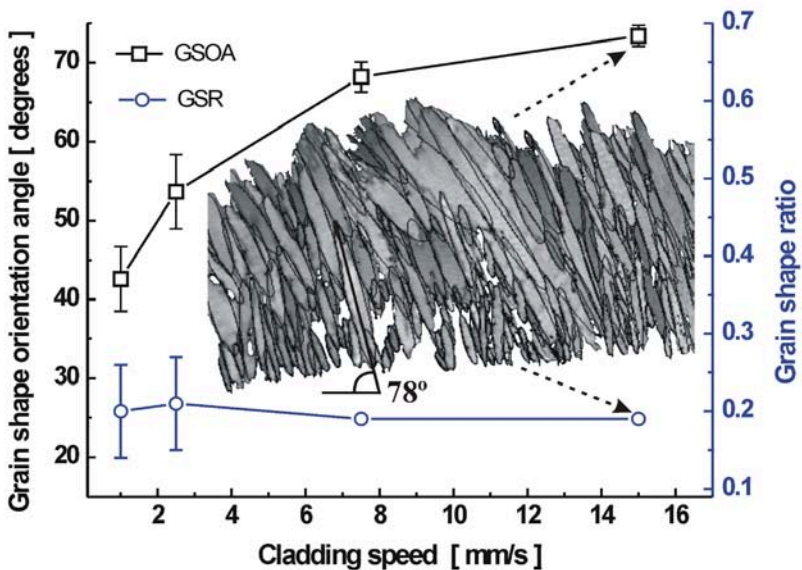
Figure 5:   Example of selected elongated grains from longitudinal cut at 15 mm/s cladding speed (insert) and results of statistical study of grains orientation angle and grains shape ration as a function of cladding speed.

Graphs in Fig. 5 show the dependence of average grain shape orientation angle and grain shape ratio on the laser beam cladding speed. While the grain shape ratio seems to be not dependent on the scanning speed; keeping its value around 0.2 for all scanning speeds, the average grain shape orientation angle

substantially increases from 43º to 74º with increasing cladding speed. At the same time the variation of this average angle decreases substantially from 10% at cladding speed of 1 mm/s to 2% at cladding speed of 15 mm/s.

3.3 Solidification texture

The OIM data contains information about the crystal orientation for each point of SEM scanned surface. Therefore it is easy not only to construct grain boundaries but also to study texture in observed microstructures [15]. However, EBSD signal has to be collected from large number of grains. The presence of strong texture inside the laser clad Co based coatings was already concluded by Olivera et al. [16] when measuring the internal microstrains by diffraction of synchrotron radiation. To prove the hypothesis that grains are elongated due to their growth in a direction perpendicular to the solidification front we studied the texture of microstructures formed by different laser beam velocity. Our OIM observations on longitudinal cross-section confirmed the strong solidification texture for all four laser beam scanning speeds. It is the fiber type of texture, when one <100> direction in fcc cubic crystal has a preferable orientation in a coordinate system fixed to the sample whereas others two <100> directions are free. This type of texture often results from directional solidification that prefers the crystal grow in [100] direction for fcc structures [17].
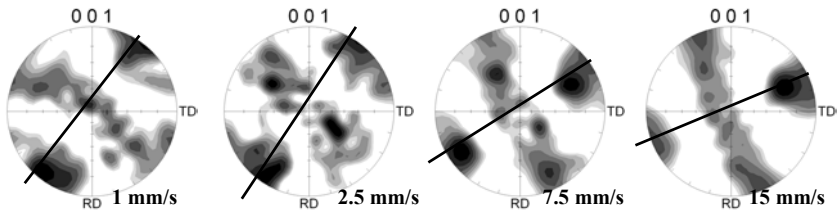
Figure 6:   The fibre solidification texture detected by OIM observations on longitudinal cross-sections strongly corresponds to the grain orientation angle.

The Figure 6 demonstrates this situation in the form of (001) pole figures. There is a strong tendency for clustering in one direction while two others form a band crossing the pole figure in its centre. Rolling Direction (RD) in these pole figures represents actually the cladding direction of our samples. It is not surprising that angles measured between the preferable orientation and RD direction correspond to the grain shape orientation angles presented in Fig.5 for all laser beam scanning speeds. This confirms that grains on longitudinal cross-section are elongated in [001] direction and this direction tends to be perpendicular to the shape of solidification front. However, the OIM texture study performed on the transversal cross-sections [13] did not confirm such a strong texture as shown in Fig.6. Simple explanation is hidden in 3D dimensional character of the solidification front shape.

3.4 Internal interfaces due to the laser tracks overlap

Here we present OIM observations performed on coatings prepared by overlap of individual laser tracks. Figure 7 shows at the top OIM image quality map and grain boundaries on the transversal cut of coating prepared at laser beam scanning speed of 15 mm/s. An overlap of 5 individual laser tracks may be recognized on this transversal cross-section. The longitudinal cross-sections made at different planes are shown on the bottom part of Fig. 7.
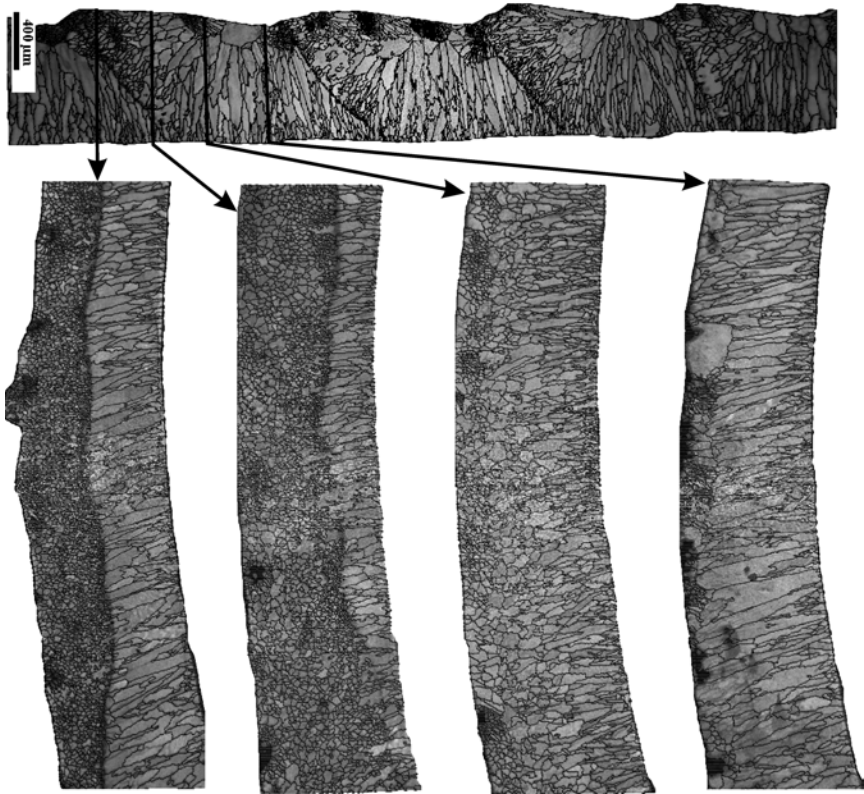
Figure 7:   OIM image quality maps with grain boundaries on transversal (up) and 4 longitudinal (bottom) cuts performed at marked positions trough laser clad coating.

Two longitudinal cuts that intersect track overlap boundary show a very sharp change of characteristic grain size directly on this boundary. The presence of such microstructural boundary inside the coating could be less desirable from the point of view of the local sharp change of functional properties of the coating [16]. A comparison of different laser cladding shows that such a sharp microstructural interface is most pronounced in the coating prepared with the highest laser beam scanning speed, e.g. 15 mm/s.

3.5 Microhardness profiles

Figure 7 summarizes the vertical Vickers' hardness profiles measured with indenter load of 4 N on single laser tracks and coatings prepared with all laser beam scanning speeds. It is interesting to note, that for the single laser tracks made at higher scanning speeds (7.5 and 15 mm/s) the hardness of the substrate at Heat Affected Zone (HAZ) is substantially higher than the hardness of the coating itself. This is consequence of hardening ability of the substrate steel material. Higher cooling rates associated with faster scanning speeds lead to a higher amount of martensite resulting in higher hardness inside HAZ. The laser beam scanning speed influences the hardness inside laser tracks only slightly. Hardness of coatings is substantially higher than hardness of individual laser tracks made with the same laser beam scanning speeds that is probably raised by precipitation hardening presented during thermal cycling when laser tracks overlap occurs. The same thermal treatment leads to the substantial decrease of hardness inside HAZ, where a decomposition of martensite occurs.
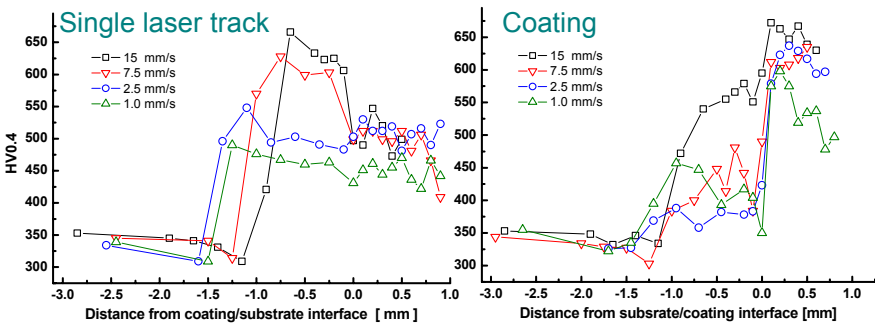
Figure 8:   Vickers' microhardness profiles measured on single laser tracks (left) and coatings prepared by different laser beam scanning speeds.

4   Conclusions

Orientation Imaging Microscopy provides new insights into the microstructure and texture of thick metallic laser clad tracks and coatings. Cobalt based laser tracks prepared by different laser beam scanning speeds contains relatively large, strongly elongated grains with a strong solidification fibre texture. The direction of this texture together with grain shape orientation strongly depends on cooling rate, e.g. laser beam processing speed.

Conclusions about microstructural features that are based only on a transversal cut of laser track may be misleading. The longitudinal cross-section at the centre of the laser track provides much more information concerning the grain size, the grain shape and the solidification texture of the microstructure formed during laser cladding.

The possibility for a direct observation of the shape of solidification front at low laser beam scanning speeds has been discovered due to the sensitivity of OIM technique towards impurity phases segregated at the solid/liquid interface.

Formation of thick Co-based coatings via the overlap of individual laser tracks introduces sharp microstructural discontinuities that are more pronounced in coatings made at higher speeds. The laser track overlap may also substantially change the functional properties not only inside the coatings but also inside the heat affected zone.

Acknowledgement

References

[1]   Steen W.M., *Laser Materials Processing*, 3-rd edition, Springer-Verlag London Limited: London, 408p, 2003.

[2]   Toyserkani E., Khajepour A. & Corbin S., *Laser cladding*, CRC Press: London, 260p, 2005.

[3]   Ion J.C., *Laser Processing of Engineering Materials*, Elsevier Butterworth-Heinemann: Amsterdam, 556p, 2005.

[4]   Yellup J.M., Laser cladding using the powder blowing technique. *Surface and Coatings Technology,* **71(2)**, pp. 121-128, 1995.

[5]   Oliveira de U., Ocelík V. & De Hosson J.Th.M., Analysis of coaxial laser cladding processing conditions. *Surface & Coatings Technology,* **197(2-3),** pp. 127-136, 2005.

[6]   Ocelík V., Oliveira de U., de Boer M. & De Hosson J. Th. M., Thick Co-based coating on cast iron by side laser cladding: Analysis of processing conditions and coating properties. *Surface & Coatings Technology,* **201(12)**, pp. 5875-5883, 2007.

[7]   Nowotny S., Scharek S. & Schmidt A., Advanced laser technology applied to cladding and buildup. *Welding Journal,* **86(5),** pp. 48-51, 2007.

[8]   Partes K., Seefeld T., Sepold G. & Vollertsen F., High efficiency laser cladding at elevated processing speed. *Proc. Of the ICALEO 2005 conference on Laser Materials Processing,* Eds. A. Ostendorf, A. Hoult & Y.F. Lu, Miami (FL), USA, October 31 - November 3, pp. 621-627, 2005.

[9]   Frenk A., Henchoz N. & Kurz W., Laser cladding of a cobalt-based alloy: Processing parameters and microstructure. *Z. Metallkd.* **84(12),** pp. 886-892, 1993.

[10] Frenk A. & Kurz W., Microstructural effects on the sliding wear resistance of a cobalt-based alloy. *Wear,* **174(1-2),** pp. 81-91, 1994.

[11] Dingley D.J., The development of automated diffraction in scanning and transmission electron microscopy (Chapter 1). *Electron Backscattered diffraction in Materials Science,* ed. A.J. Schwartz, M. Kumar & B.L. Adams, Kluwer Academic/Plenum Publishers: New York, pp. 1-16, 2000.

[12] Davis J.R., ASM Handbook. *Properties and Selections: Nonferrous Alloys and Special-Purpose Materials,* ASM International: Material Park, OH, Vol.2, 446p, 1990.

[13] Oliveira de U., Laser treatment of alloys: processing, microstructure and structural properties, PhD Thesis, University of Groningen, 128p, 2007.

[14] Wright S.I., Fied D.P. & Dingley D.J., Advanced software capabilities for automated EBSD (Chapter 13). *Electron Backscattered diffraction in Materials Science,* ed. A.J. Schwartz, M. Kumar & B.L. Adams, Kluwer Academic/Plenum Publishers: New York, pp. 141-152, 2000.

[15] Rajan K., ibid, (Chapter 3), pp. 31-38.

[16] Oliveira de U., Ocelík V. & De Hosson J.Th.M., Microstresses and microstructure in thick cobalt-based laser deposited coatings. *Surface & Coatings Technology,* **201(14)**, pp. 6363-6371, 2007.

[17] Kurz W. & Fisher D.J., Fundamentals of Solidification, Trans Tech Publications Ltd: Switzerland, 245p, 1986.

Heat treating of the antifriction deposited layers by thermal spraying

A. V. Petrica[1] & L. Milos[2]
[1] *"Eftimie Murgu" University, Resita, Romania*
[2] *"Politehnica" University, Timisoara, Romania*

Abstract

The first section of the paper presents the thermal spraying technology of the deposited layers. The X-ray diffraction analysis and the electron-scan microscopic analysis of these layers leads to the conclusion that the obtained microstructure does not reduce the anti-friction quality of these layers. The temperature of these layers during processing is relatively lower in relation with the temperatures used in the heat treatments. The second part of this paper presents the results obtained after a heat treatment of these layers. The same analysis after the heat treatment shows the appearance of some compounds that significantly improve the anti-friction property of these layers.

Keywords: thermal spraying, anti-friction layers, X-ray diffraction, electron-scan microscopically analysis, heat treatment.

1   Introduction

From the microstructural point of view the thermally sprayed layers must have some stability to the temperatures that were reached during the exploitation, for preserving the functional characteristics. Thus, the heat treatment of these layers before the exploitation could confer a higher stability. Also, a heat treatment that changes the initial microstructure of the sprayed layers could lead to improve the exploitation performances of these layers. The basic quality of the Babbitt casting alloys is the anti-friction property, obtained grace to the presence of the SnSb and Cu_3Sn crystals in the eutectic. The thermal spraying procedures can be a solution for the partial or total replacement of the boundary layer to some pieces. The Babbitt layer deposited by thermal spraying must keep the same

functional characteristics in relation with the previous layer. So, the microscopic and the X-ray diffraction analysis can prove this aspect in a good manner.

2 Experimental samples

The appendix material used, its chemical composition and the parameters of the procedure recommended by the manufacturer of the wire are inserted in tables 1 and 2. The dimensions of the samples for the microscopic and the X-ray diffraction analysis were 20/25 mm (fig. 1). The final thickness of the layer was obtained after four passes and it is of 3 mm.

Table 1:   The chemical composition of the appendix material used to thermal spraying by flame and wire.

Type of wire	Chemical composition, [%]				Wire diameter, [mm]
	Sn	Sb	Cu	Pb	
Sprababbitt A	87,75	7,5	3,5	0,25	3,2

Table 2:   The parameters used in thermal spraying with flame and wire procedure.

Rotation, [rot/min]	Spraying distance, [mm]	Oxygen and acetylene pressure, [bar]	Wire speed, [cm/s]	Compressed air pressure, [bar]	Angle of spraying, [°]	Layer temp., [°C]
200	100 – 120	2	2	3,65	max. 45	80 – 100

Figure 1:   Macroscopic image of the sample, deposited layer – Babbitt.

3 The X-ray diffraction analysis

The purpose of this analysis was to find the nature of the microstructural constituents for the used appendix material. Also we followed the evolution of possible structural changes in the case of some heat treatments performed on the deposited layers.

The experiments were made off with the DRON 3 X-ray difractometer using the characteristic radiation Kα of molybdenum ($\lambda = 0,71$ Å). The parameters of the equipment were: $U_{acc} = 40$ KV and I = 30 mA. The speed of the detector was 2°/min for the recordings made off in $2\theta = 7...55°$ angular domain, and $(1/2)°$/min for the recordings made off in $2\theta = 30...41°$ angular domain.

The diffraction spectrums obtained by these analysis are presented in figures 2 and 3. The values for these analyses are inserted in tables 3 and 4.

Table 3:   The values for the non-heat treated sample.

Pick no.	Angle 2θ	d [Å]	(hkl)	Phase
1	13,95	2,92	(200)	Sn (Sb, Cu)
2	14,50	2,81	(101)	Sn (Sb, Cu)
3	19,65	2,08	(220)	Sn (Sb, Cu)
4	20,35	2,01	(211)	Sn (Sb, Cu)
5	24,85	1,65	(301)	Sn (Sb, Cu)
6	27,75	1,48	(112)	Sn (Sb, Cu)
7	28,20	1,45	(400)	Sn (Sb, Cu)
8	28,45	1,44	(133)	Sb_2O_4
9	31,55	1,30	(035)	Sb_2O_4
10	31,85	1,293	(420)	Sn (Sb, Cu)
11	34,25	1,205	(312)	Sn (Sb, Cu)
12	37,75	1,097	(431)	Sn (Sb, Cu)
13	39,85	1,041	(332)	Sn (Sb, Cu)
14	40,45	1,026	(440)	Sn (Sb, Cu)
15	42,35	0,982	(441)	Sn (Sb, Cu)
16	44,90	0,929	(512)	Sn (Sb, Cu)
17	47,20	0,886	(323)	Sn (Sb, Cu)
18	49,50	0,848	(413)	Sn (Sb, Cu)

Table 4:   The values for the heat treated sample.

Pick no.	Angle 2θ	d [Å]	(hkl)	Phase
1	13,25	3,077	(200)	SnSb
2	14,00	2,91	(200)	Sn (Sb, Cu)
3	14,55	2,803	(101)	Sn (Sb, Cu)
4	18,90	2,162	(220)	SnSb and ε – Cu_3Sn (002)
5	19,70	2,075	(220)	Sn (Sb, Cu) and ε – Cu_3Sn (2.12.0)
6	20,40	2,005	(211)	Sn (Sb, Cu)
7	23,20	1,765	(222)	SnSb
8	24,05	1,704	(310)	Sb_2O_4
9	24,80	1,653	(301)	Sn (Sb, Cu)
10	26,85	1,529	(400)	SnSb
11	27,75	1,480	(112)	Sn (Sb, Cu)
12	28,20	1,457	(400)	Sn (Sb, Cu)
13	28,50	1,442	(133)	Sb_2O_4
14	30,12	1,366	(420)	SnSb and ε – Cu_3Sn (083)
15	31,50	1,307	(035)	Sb_2O_4
16	31,90	1,292	(420)	Sn (Sb, Cu)
17	33,20	1,242	(422)	SnSb and ε – Cu_3Sn (2.26.1)
18	34,40	1,200	(312)	Sn (Sb, Cu)
19	37,90	1,0293	(431)	Sn (Sb, Cu)
20	39,95	1,039	(332)	Sn (Sb, Cu) and ε – Cu_3Sn (174)
21	40,70	1,021	(440)	Sn (Sb, Cu)
22	42,45	0,980	(441)	Sn (Sb, Cu)
23	43,12	0,966	(620)	SnSb
24	45,00	0,927	(512)	Sn (Sb, Cu)
25	45,40	0,920	(622)	SnSb and ε – Cu_3Sn (5.21.1)
26	47,20	0,887	(323)	Sn (Sb, Cu)
27	49,55	0,847	(413)	Sn (Sb, Cu) and ε – Cu_3Sn (0.8.5)
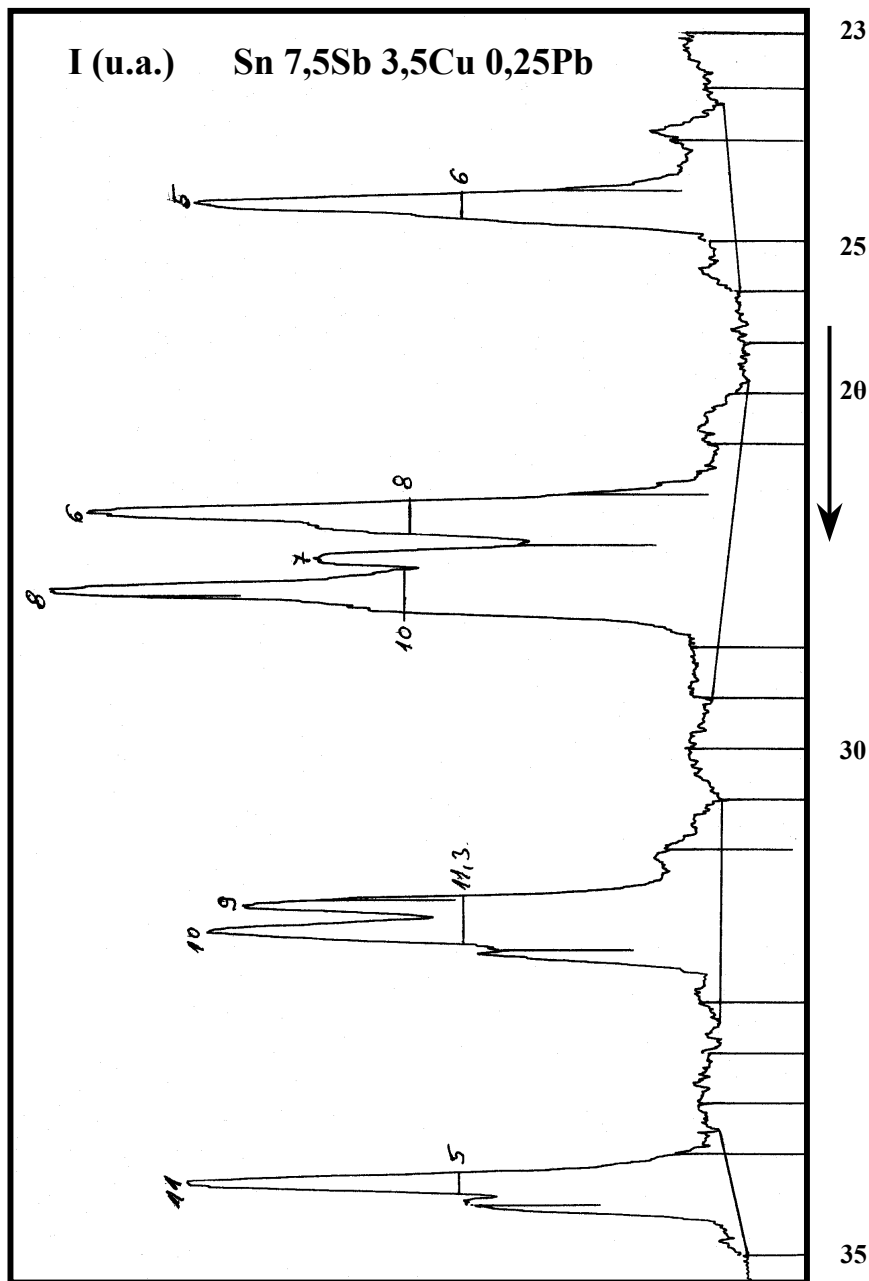
Figure 2:   The partial spectrum of diffraction characteristic to the non-heat treated deposited layer.
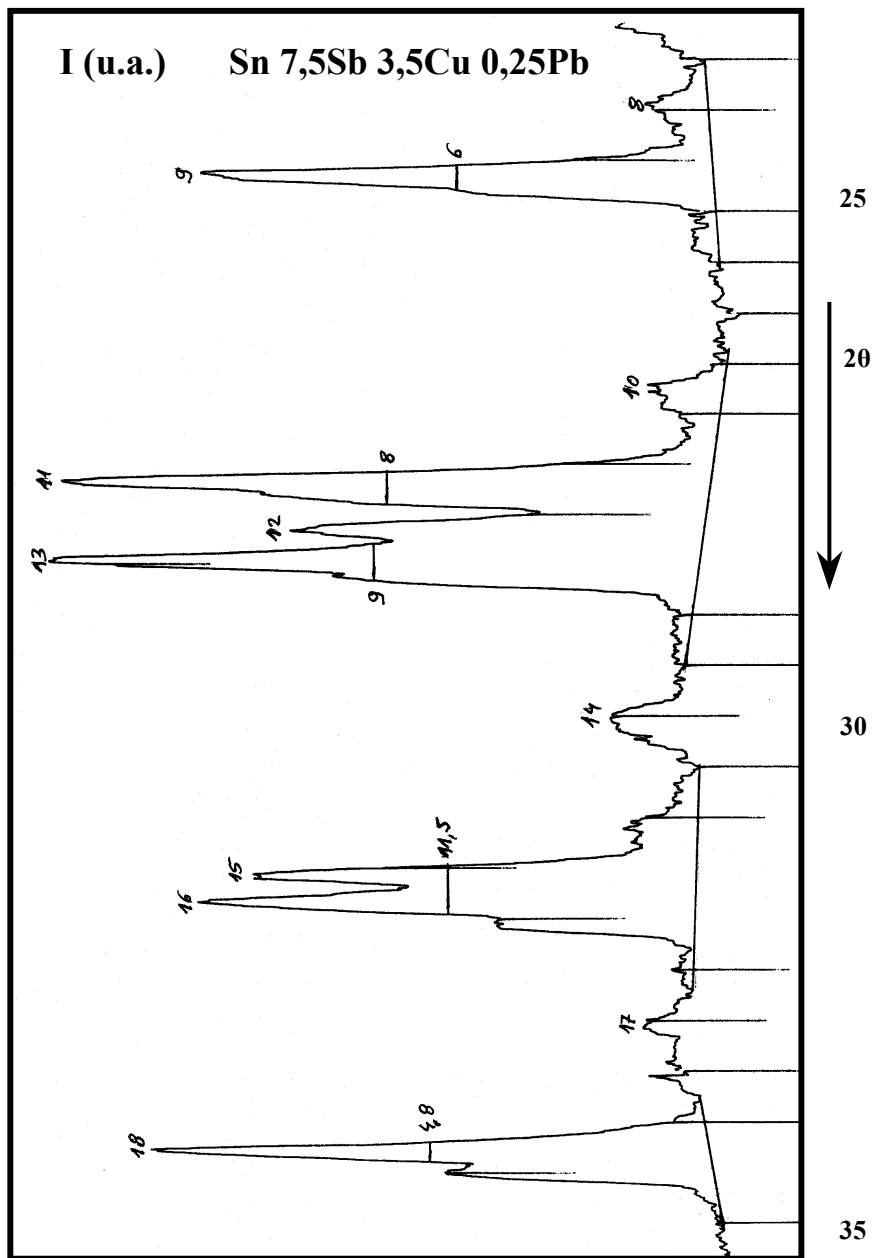
Figure 3:   The partial spectrum of diffraction characteristic to the heat treated deposited layer.

Two types of samples were analyzed. The first sample was non-heat treated, and the second sample was heat treated as follows: 150°C heating temperature, one- hour time keeping, cooling in the furnace.
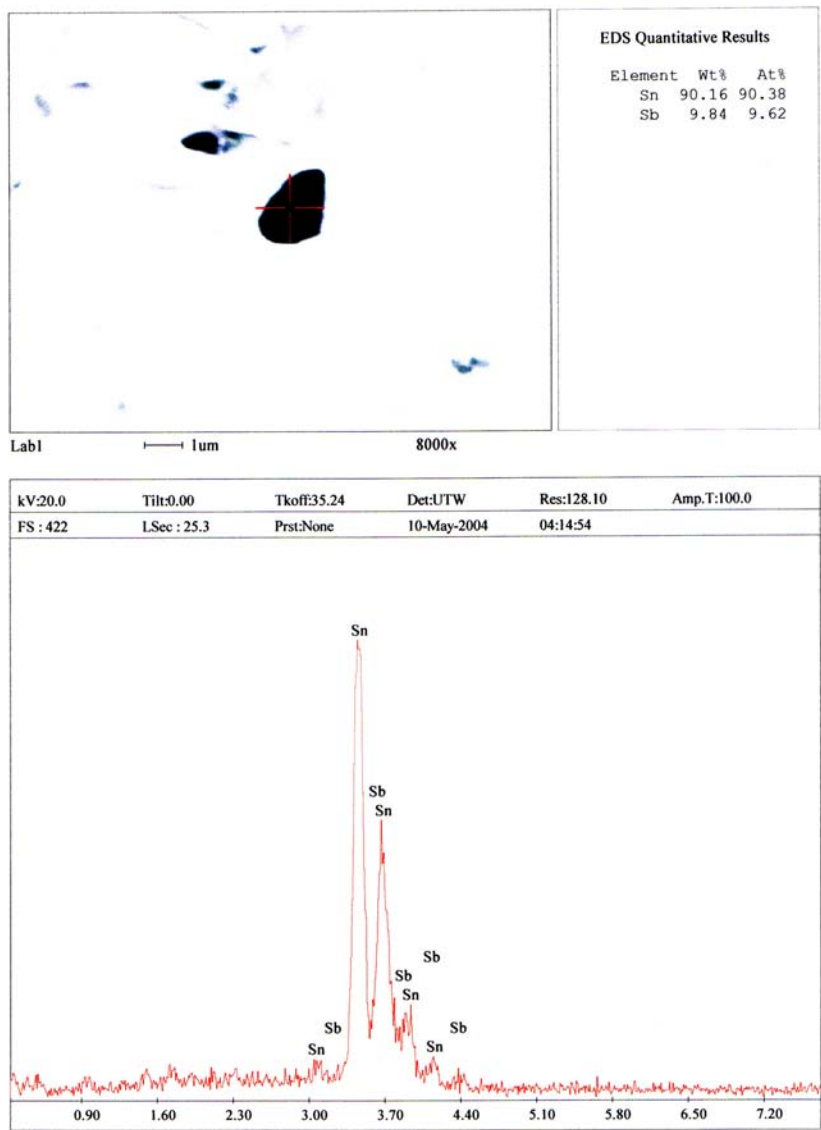
Figure 4:   The quantitative chemical analysis to the deposited layer – SnSb compound.

The following aspects are pointed out:

- ✓ The occurrence of the Sb and Cu solid solution in Sn;
- ✓ The occurrence of the Sb oxide (pick no. 8 and 9) – to the non-heat treated sample;
- ✓ The absence of the SnSb crystals and Cu_3Sn needles – to the non-heat treated sample;
- ✓ After the heat treatment the structure of the deposited layer is significantly modified by the occurrence of the SnSb and Cu_3Sn compounds.

4   The microscopic analysis

This analysis became necessary after the X-ray diffraction analysis, which pointed out the occurrence of the SnSb and Cu_3Sn compounds after a heat treatment.

In the 4th figure we presented the chemical quantitative analysis of the compound from the image. One can remark only the presence of Sn and Sb, the compound tends to have a regular shape like the SnSb compounds from the molten state. It is obvious that the colour of this compound is different from the colour of the basic metallic matrix, due to the BSE (back scattered – electron) analysis. The small quantity of this compound it's maybe the result of a short time keeping (1 hour) at the 150°C temperature.

5   Conclusions

- In the non-heat treated Babbitt layers the SnSb and Cu_3Sn crystals are not present;
- The X-ray diffraction analysis of the heat treated Babbitt layers points out the occurrence of these compounds;
- The quantitative microscopic analysis attests the occurrence of the SnSb compound;
- The detection of the Cu_3Sn compound is more difficult to achieve because of the shape of this compound (acicular, in the case of molten Babbitt) and because of its small dimension.
- The occurrence of these compounds in the structure of the Babbitt layers deposited by thermal spraying contributes to the improvement of the basic quality of these layers, namely the anti-friction property.

Reference

[1] Petrica A., *Contributions to the increase of the availability of the boring type pieces*, Doctor's degree thesis, September 2004, "Politehnica" University of Timisoara.

This page intentionally left blank

The influence of the spraying angle on properties of thermally sprayed HVOF cermet coatings

Š. Houdková, F. Zahálka & M. Kašparová
ŠKODA VÝZKUM s.r.o., Czech Republic

Abstract

The tribological properties of the surfaces of parts, namely their wear resistance and friction properties, are in many cases decisive for their proper function. To improve surface properties, it is possible to create hard, wear resistant coatings by thermal spray technologies. Using these versatile coatings it is possible to increase the lifetime, reliability and safety of parts. For proper function of the surface treatment it is necessary to find and keep the optimal condition and parameters during preparation, deposition and further processing of the sprayed part. The spraying angle is one of the deposition parameters that influence the quality of thermally sprayed coatings. According to the theory, with decreasing spraying angle the process deposition efficiency decreases, whereas the porosity of coatings increases, being a cause of aggravated microstructure and mechanical properties. In this paper, the microstructure together with the basic mechanical properties and wear of WC-Co and Cr_3C_2-NiCr HVOF sprayed coatings were investigated in dependence of the spraying angle. For each coating, the marginal spraying angle that can be used without a significant decrease of the coating's quality was identified. With respect to the change in coating properties as well as to process deposition efficiency, the maximum 30° diversion from a normal spray direction is recommended in the case of WC-Co and 15° diversion in the case of Cr_3C_2-NiCr.

Keywords: thermal spraying, coating, HVOF, spraying angle, cermet, WC-Co, Cr_3C_2-NiCr.

1   Introduction

The tribological properties of the surfaces of parts, namely their wear resistance and friction properties, are in many cases decisive for their proper function. To improve surface properties, it is possible to create hard, wear resistant coatings by thermal spray technologies. Using these versatile coatings it is possible to increase the lifetime, reliability and safety of parts. Thermal spraying is an expanding area within the technology of surface engineering. It is a process that involves the deposition of molten or semi-molten droplets of powder onto a substrate to form a coating. A wide range of materials can be thermally sprayed for a variety of applications ranging from gas turbine technology to the electronics industry. For the creation of hard, wear and corrosion resistant coatings the most suitable materials are ceramics and hard metals. For spraying ceramics, which need to be melted under very high temperatures, plasma spraying is the technology used. For hard metals, the best way is to use the HVOF technology that was developed for spraying hard metals to get the high-quality coatings. In high velocity oxy-fuel (HVOF) thermal spraying, oxygen and fuel gas flow at high pressures and flow rates with internal combustion produces very high particle velocities with relatively low temperatures compared with other thermal spray processes, such as air or vacuum plasma spraying [1]. As a result, HVOF has a capability for producing dense coatings with low degrees of decomposition, which are well bonded to the substrate. As a line-of-sight process, HVOF has application limitations with respect to part geometry, particularly in coating small internal diameters. It is often not possible to realize a perpendicular spraying angle. This can lead to significant changes of coating properties. In the literature the influence of the spray angle was studied in terms of microstructure, hardness, surface roughness and deposition efficiency [2–5]. It is generally considered, that spraying at angles of up to 45° guaranties a successful application with only a marginal loss of coating quality. To verify these statements for particular coating materials, the investigation of spray angle influence on deposition processes and coating properties was provided for HVOF TAFA JP-5000 sprayed WC-17%Co and Cr_3C_2-25%NiCr coatings. This study can provide fundamentals to determine the tolerance to which coatings exhibit reproducible properties.

2   Experimental

The coatings were sprayed using TAFA JP-5000 spraying equipment onto grit-blasted carbon steel EN 10025-90 using spray parameters that were previously optimized at a spray angle of 90° [6]. The basic spraying parameters are summarized in Table 1.

Table 1:   Spraying parameters.

Coating	Powder	Eq. ratio	Carrier gas	Barrel length	Spraying distance
WC-Co	FST K-674.23	0.8	Argon, 414 kPa, 8 sl/h	150 mm	380 mm
Cr_3C_2-NiCr	1375VM	0.8	Argon, 345 kPa, 8 sl/h	150 mm	360 mm

Five different spray angles were used to spray the samples: 90°, 60°, 75°, 45°and 30°. For each spraying angle, a different number of passes was applied to reach similar coating thicknesses of all samples.

2.1 Microstructure

The WC-15%Co powder for HVOF spraying consists of hard particles of WC, surrounded by a tough Co matrix. Due to oxidation during the deposition process, part of the WC decomposes to W_2C and W, producing CO and CO_2. Together with the oxidation process, dissolution of W and C in the Co matrix takes place. As a result of rapid solidification of droplets after the impact, the matrix includes amorphous or fine-grained structures, which could later give rise to precipitation of W or so called η phases (in particular Co_3W_3C and Co_6W_6C). Decarburization and formation of brittle η phases is an undesirable effect leading to a loss of the tough Co matrix. The presence of the above mentioned phases in HVOF sprayed WC-Co coatings were described in literature many times [7, 8].

The Cr_3C_2-25%NiCr coating's microstructure includes beyond hard Cr_3C_2 carbides, NiCr matrix, Cr_2O_3, originated from the oxidation process during spraying, and also lower carbides Cr_7C_3 and $Cr_{26}C_6$ with a hardness lower than the initial Cr_3C_2, originated from the decarburization process similarly to WC-Co. Due to the dissolution of carbides in the matrix, the concentration of C and Cr in the matrix of the coating is higher compared to the powder material. It enables the melted droplets to solidify as a quasi-amorphous or nano-crystallic structure. Other nano-crystallic phases, with a grain size around 10 nm, formed of Ni and Co, appear in the coatings microstructure as a result of rapid solidification [8, 9].
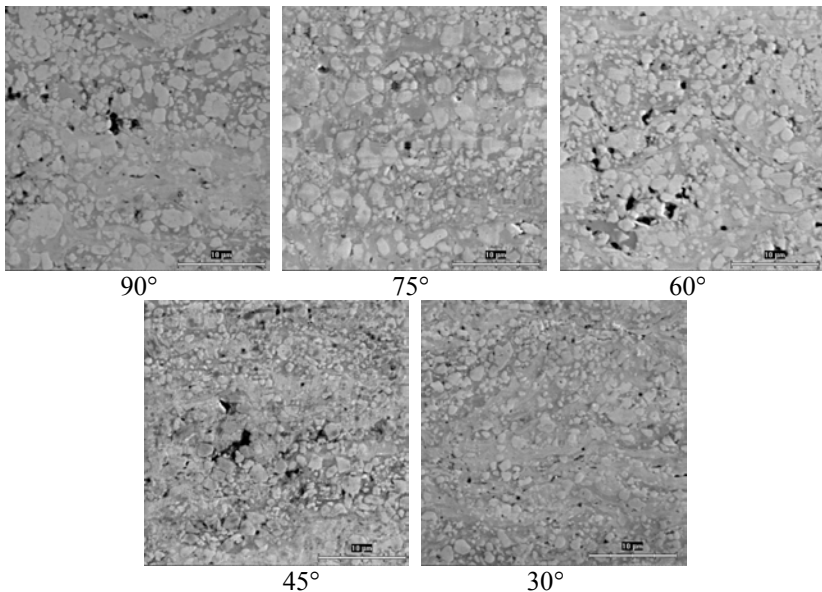
Figure 1:   Microstructure of WC-Co coatings.

The influence of the spray angle on the coatings microstructure was studied by optical microscopy and SEM, in two directions (longitudinal and transversal) to the direction of spraying.

The microstructure of all studied WC-Co coatings is homogenous, without cracks or unmelted particles. Just a minor amount of porosity is included in the coating; the carbide distribution in the matrix is uniform. No obvious influence of spray angle was observed. In the case of Cr_3C_2-NiCr coating, the microstructure is without visible changes up to the spray angle 75°. Coatings sprayed at 60° and lower showed longitudinal and lateral cracks, also on the substrate-coating boundary. Only negligible changes in porosity were observed for both coatings, in contradiction to expected effect of shielding [10] and results of Tillmann *et al.* [3] study, focused on APS WC-Co and Cr_3C_2-Nicr coatings. Moreover, the amount of porosity in the coatings sprayed under 30° is lower than in the coatings sprayed under 60° and 45°.

2.2 Hardness and microhardness

The hardness HR15N was measured on the surfaces of the coatings according to EN ISO 6508-1, microhardness HV0,3 was measured on coatings cross sections in both directions - longitudinal and transversal – to direction of spraying according to EN ISO 6507-1.

As expected, the hardness and microhardness of WC-Co coating was higher compared to Cr_3C_2-NiCr coating. The surface hardness of both coatings showed decrease in values for 75° spray angle, followed by unexpected increase for 60° spray angle. After that, the HR15N values decreased together with the spray angle. No measurement of surface hardness in dependence on spray angle was found in available literature.

The microhardness results showed continuous decrease with decreasing spray angle, which is in correlation with results of Strock *et al.* [2]. Tillmann *et al.* [3] did not find any dependence between microhardness and spray angle. The hardness and microhardness results are shown in Figure 2 and 3.
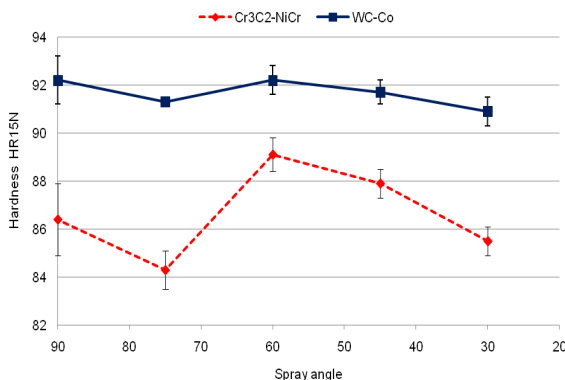
Figure 2:   Surface hardness of the coatings.

2.3 Residual stress

Residual stress correlations were made using so-called Almen strip test method. The method is based on the measurement of deflection of coated thin metal strip. The measurement is only qualitative, the value of stress cannot be directly determined [11, 12].

Generally, HVOF coatings tend thanks to high impact velocities of droplets to have compressive residual stress, which is beneficial for their properties. In our case, compressive residual stress appeared only at WC-Co coating, while tensile residual stress occurred at Cr_3C_2-NiCr coating. The tensile stress component increased with spray angle decreasing from 90° for both coatings, although at 30°spray angle the level of tensile stress slightly decreased. The increasing in the tensile stress level with decreasing spray angle is observed also by Strock *et al.* [2]. The level of the coatings residual stress is shown in Figure 4.
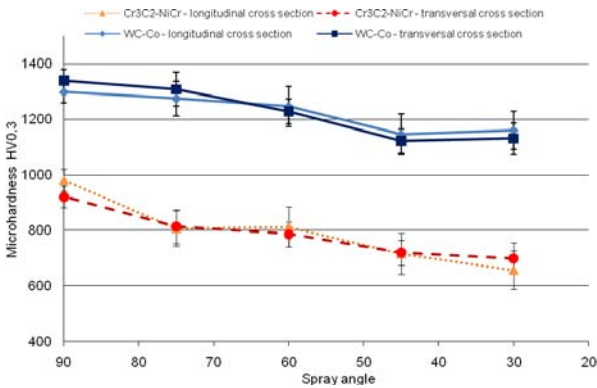
Figure 3:   Microhardness of the coatings.
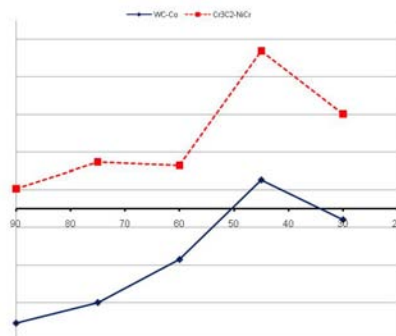
Figure 4:   The level of residual stress.

2.4 Indentation fracture toughness

The resistance of coatings against the fracture spreading of brittle materials can be measured by Vickers indentation method. The technique of indentation fracture toughness measurement, described in detail by Ponton and Rawlings [13], can be successfully used for evaluation of thick brittle coatings [14–16]. In this case, the model of Lawn and Swain [17] was used to determine the number of K_{Ic}. The results of measurement are displayed in Figure 5.

The resistance of WC-Co coating against the fracture spreading expressed by KIc decreased together with spray angle decreasing from 90°, with a slight increase at 60°. The tendency is similar to the tendency of superficial hardness HR15N (see Fig. 2). The Cr_3C_2-NiCr behaved as more brittle compared to WC-Co. The cracks were much longer and scatter of the results was much higher. No significant dependence of KIc on spray angle was observed. Either the spray angle does not influence the Cr_3C_2-NiCr cracking behavior, or, more probably, the dependence is under the resolution limits of the used method.
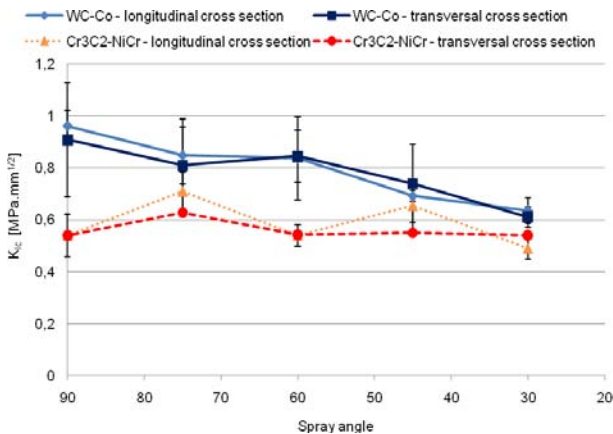
Figure 5:   Indentation fracture toughness of the coatings.

2.5 Surface roughness

The surface roughness measurement was done in both directions, longitudinal and transverse, to the direction of spraying. For both coatings, the surface roughness expressed by Ra decreased with spray angle decreasing from 90°, with the exception of 30° sprayed WC-Co coatings, where the slight increase could be noticed. In both cases, the surface roughness in longitudinal direction is gently higher compared to Ra in the transversal direction. For APS sprayed coatings, Tillmann *et al.* [3] present opposite tendency.

The technological conclusion is that there is no need to increase the machining allowance in the case of off-angle sprayed coatings.

2.6 Specific density

Specific density of the coatings was measured by the method, based on the Archimedes law. The differences in values for each coating material represent the different amount of porosity in the coatings. The results are shown in Figure 7. The density measurement, with respect to the measurement error, does not exhibit any clear dependence on the spray angle. A sudden increase of density for coatings sprayed at 30°, correlating with the result of microstructure evaluation, is interesting.
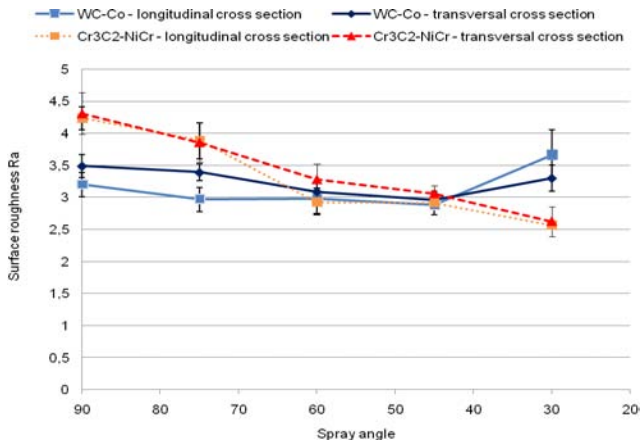
Figure 6:   Surface roughness Ra values.
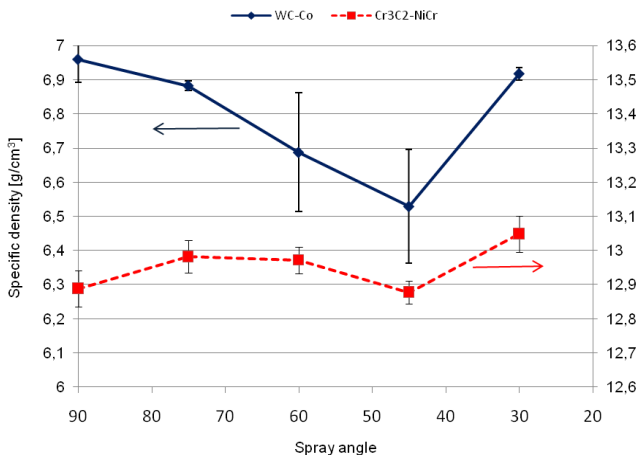
Figure 7:   Density of the coatings.

2.7 Deposition efficiency

The deposition efficiency of spraying process was determined according to EN ISO 17836. From the measured results (Figure 8) it is clearly visible, that the deposition efficiency is strongly dependent on the spray angle. The deposition efficiency is one of the main parameters that affect the economy of the thermal spray process. From this point of view it is noticeable that the process of spraying is not very effective even for 90° spray angle (only 40% deposition efficiency).

2.8 Wear

Wear resistance of coating was tested by Dry Sand/Rubber Wheel test according to ASTM G-65. The principle of the method enables to evaluate the tree-body abrasive wear under the low-stress condition. The wear is characterized by the wear rate, calculated from the coating volume loss and the abrasive distance.
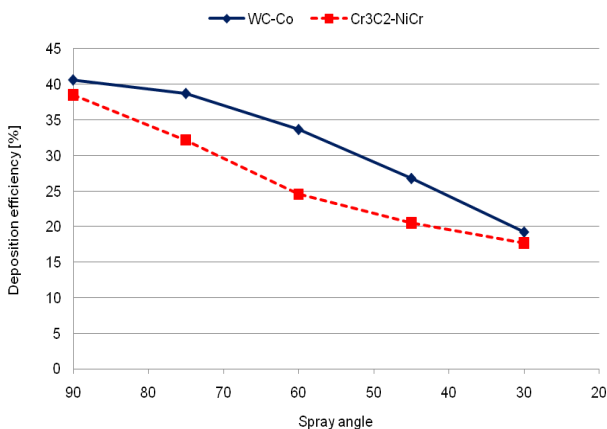
Figure 8:   Deposition efficiency.

The WC-Co coating is approximately 5 times more wear resistant compared to Cr_3C_2-NiCr coating (Figure 9). Both coatings met the expectation of decreasing the wear resistance with decreasing spray angle. For WC-Co coating, the difference between the wear rate of coatings sprayed at 90°, 75° and 60° was very small and their wear resistance can be considered equal. The coatings, sprayed at the lower spray angles, especially 30°, had significantly worse wear behavior. For Cr_3C_2-NiCr coating, the equal wear behavior can be observed for coatings sprayed under 90°a 75° spray angle. Theoretical models [17] predict the wear rate to be dependent on materials hardness: $1/H$ for tough materials and $1/H^2$ for brittle materials. Such a clear dependence was not confirmed in our measurements. The results of the Dry Sand Rubber Wheel test are in contradiction with results of Strock et al. [2], who found an opposite dependence

in the fretting wear test. In spite of lower hardness and lower compressive residual stress, the off-angle WC-CoCr coatings exhibited less wear than 90° coatings. He explained this unexpected behavior by more uniform distribution of phases across the surface at off-angle coatings that was not observed in our case. The contradiction can also be caused by differences between wear conditions of the fretting and the abrasive wear test.
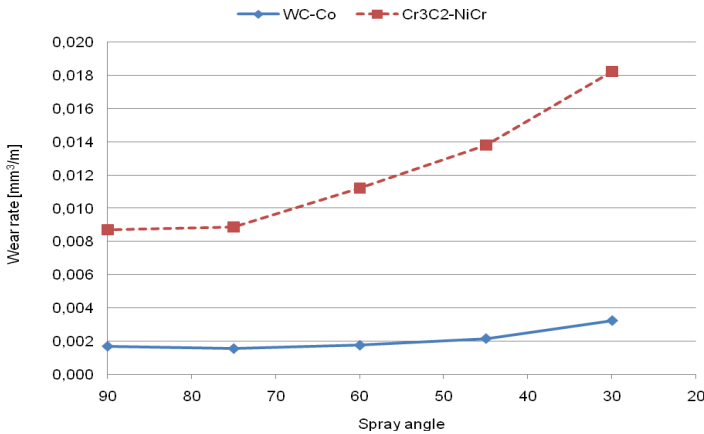
Figure 9:   Wear rate.
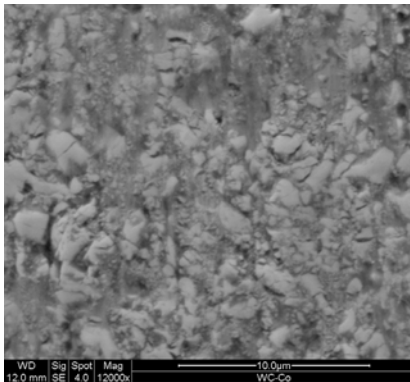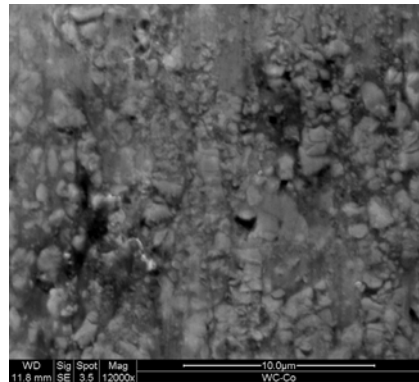
90°	30°

Figure 10:   Wear track of WC-Co coatings after the Dry Sand/Rubber Wheel test.

The mechanism of wear was studied using SEM. The micrographs of the worn surface match the wear rate results. The wear mechanism of perpendicularly sprayed coating can be characterized by the gradual loss of metal matrix followed by decrease in carbide-matrix cohesion and pull-off the carbides. The coatings, sprayed at lower angles, exhibit massive wear

represented not only by pull-off the carbides, but also by pull-off parts of whole splats. Such a behavior indicates low intersplat cohesion in the coating.

3   Summary and conclusion

The evaluation of the spray angle influence on physical, mechanical and technological parameters of the HVOF hard metal coatings showed a significant dependence of the coating properties on the spray angle. During the results' analyses some interesting correlations occurred. The trend of the surface hardness measurements and the indentation fracture toughness of WC-Co coating are almost similar. The results of microhardness and residual stress measurement are conformable to each other, but not to surface hardness and indentation fracture toughness, although it could be expected. The explanation could be in the load range, used for the measurement. Microhardness with the load of 300 g is measured within one splat, while surface hardness with the load of 15 kg includes information from several splats as well as the indentation fracture toughness (200 kg). Surface hardness indentation fracture measurements take place on the same microstructure "scale" and are influenced by the same coating's microstructure features: pores, oxides, splat boundaries etc., while the microhardness measurement is closer to the measurement of a bulk material.

The properties of WC-Co coatings sprayed at 30° are surprising in general. Contrary to expectation its microstructure, density, microhardness, residual stress and surface roughness are better compared to the coating sprayed at 45°. For Cr_3C_2-NiCr coating the same effect was observed only for the density and the residual stress.

However, whatever thee mechanical and physical properties of coatings sprayed at 30° are, no increase in their wear resistance was observed. It is caused probably by a low intersplat cohesion, or a low adhesion of coating to the substrate connected with imperfect spreading and emplacement of droplets to the originating coatings microstructure during spraying at low angles. This hypothesis would be necessary to confirm by test of adhesive/cohesive strength.

Based on the measured data, using the spray angle up to 60° for WC-Co HVOF coating, and up to 75° for Cr_3C_2-NiCr HVOF coating can be recommended. These coatings are fully acceptable both from the functional and the economical point of view.

Acknowledgement

References

[1]   Smith, E. B., Power, T. J., Barber, T. J., United Technology Research Centre Report, East Hartford, CT, (1991), p.91
[2]   Strock, E., Ruggiero, P., Reynolds, D., The effect of off-angle spraying on the structure and properties of HVOF WC/CoCr coatings, Proc. of

International Thermal Spray Conference 2001,   May 28-30 2001, Singapore, 671- 676, 2001

[3] Tillmann, W. Vogli, E., Krebs, B., Influence of the spraying angle on characteristics for atmospheric plasma sprayed hard material base coatings, Proc. Of International Thermal Spray Conference 2008, June 2-4 2008, Maastricht, 235-240, 2008

[4] Smith, M. F., Neiser, R. A., Dykhuizen, R. C., An investigation of the effects of droplet impact angle in thermal spray deposition, Proc. Of 7th National Thermal Spray Conference 1994, June 20-24, 1994, Boston, 603-608, 1994

[5] Leigh, S. H., Berndt, C. C., Evaluation of off-angle thermal spray, Surface and Coatings technology, 89, 213-224, 1997

[6] Houdková, Š., Enžl, R., Fiala, P., Bláhová, O., Mechanical properties of HVOF coatings, Proceedings of University of West Bohemia 2001, 5, 73-83, 2002

[7] Schwetzke, R., Kreye, H., Microstructure and properties of tungsten carbide coatings sprayed with various high velocity oxygen fuel spray system, Journal of Thermal Spray Technol. 8, 433-439, 1999

[8] Berger, L.-M., Chemistry of carbide-metal composites for preparation of HVOF sprayed coatings, Papers, Materials Week 2001, Int. Conf. on Adv. Mater., their Processes and Applications, 1- 4 October 2001, München, 10, 2001

[9] Zimmermann, S., Kreye, H., Chromium carbide Coatings produced with Various HVOF Spray Systems, Proc. of the 9th National Thermal Spray Conf., Cincinnati, 147-152, 1996

[10] Davis J. R., Davis & Associates, Handbook of Thermal Spray Technology, ASM International, 2004

[11] SAE J442 Revised Dec. 2001: Test Strip, Holder, and gage for Shot Peening

[12] SAE J443 Revised Jan. 2003: Procedures for Using Standard Shot Peening Test Strip

[13] Ponton, C. B., Rawlings, R. D., Materials Science and Technology, 5, 865-872, 1989

[14] Li, H., Khor, K. A., Cheang, P., Young's modulus and fracture toughness determination of high velocity oxy-fuel-sprayed bioceramic coatings, Surface and Coatings Technology, 155, 21-32, 2002

[15] Brantnrer, H. P., Pippan, R., Prantl, W., Local and global fracture toughness of flame sprayed molybdenum coatings, Journal of Thermal Spray Technology, 12, 560-571, 2003

[16] Giolli, C., Scrivani, A., Rizzi, G., Borgioli, F., Bolelli, G., Lusvarghi, L., Failure mechanism for thermal barrier coating systems, Proc. Of International Thermal Spray Conference 2008, June 2-4 2008, Maastricht, 460-467, 2008

[17] Lawn, B. R., Swain, M. V., Journal of Mater. Science, 10, 113-122, 1975

[18] Hutchings, I. M., Abrasive and erosive Wear: Wear by Hard Particles, in Wear Fundamentals for Engineering, Elsevier, 1999,

This page intentionally left blank

Section 3
Thin coatings

This page intentionally left blank

Modification of rubber surface with DLC thin films for low friction and self lubrication

X. L. Bui, Y. T. Pei, E. D. G. Mulder & J. Th. M. De Hosson
Department of Applied Physics,
The Netherlands Materials Innovation Institute (M2i),
University of Groningen, The Netherlands

Abstract

Thin films of hydrogenated diamond-like carbon (DLC) have been deposited on hydrogenated nitrile butadiene rubber (HNBR) via magnetron-enhanced plasma chemical vapor deposition (ME-PCVD). Pre-deposition plasma treatment of HNBR substrate is proven to be crucial for the improvement of film performance due to enhanced interfacial adhesion. Moreover, enhancement of concurrent ion impingement via magnetron sputtering of graphite in poisoning condition raises further the adhesion and hardness of the films. The columnar structure and the crack network developed during deposition enhance the flexibility of DLC thin films and exhibit strain tolerance up to 5%. After unloading from 50% strain stretch, thin DLC films of ~300nm thickness still adhere very well on the rubber substrates and no spallation or delamination is observed. The thin DLC film on 400V plasma treated HNBR rubber exhibits very low coefficient of friction of 0.175 under dry sliding against ø6mm steel ball (compared to >1 of uncoated HNBR rubber). After tribotests even at high normal load of 3N, almost no damage can be seen on the films. Such tribological property is even better than that of 1μm thick DLC or Me-DLC coated rubbers.
Keywords: DLC film, rubber substrate, magnetron sputtering, flexibility, tribology.

1   Introduction

Rubbers are widely used in various engineering applications. Nonetheless, rubbers exhibit very high friction when sliding against other materials. It is known that contact rubber seals are the major source of friction of lubrication

systems or bearings, which may take 50-70% of the total friction loss. The high friction of rubbers is due to the adhesion-prone of rubber to the counterpart, the ploughing of asperities of harder counterpart (steel, glass, etc.) on the rubbers surface and the so-called "hysteresis" that relates to the viscoelastic nature of rubbers [1]. Besides the high friction, wear of rubbers is usually severe and mostly relates to adhesive and abrasive wear. So far, there are two solutions that can be used to reduce the friction and to enhance the wear resistance of rubber components: lubrication and coating. As to the first solution, oil or grease is applied to improve the surface lubricity of rubbers. However, it has drawbacks such as the degradation of lubricants and environmental pollution problems. For the second solution, a layer of an appropriate wear-resistant material is coated on the working surfaces of rubber components in order to protect the rubbers from wear and to reduce the friction. The development of advanced deposition methods makes the coating solution very promising. To coat rubbers, two problems have to be considered: (1) The deposition temperature must not exceed the maximum working temperatures of various rubber materials; (2) The use of chemical substance, especially the toxic ones, in cleaning rubbers before deposition should be limited to prevent pollution. For a good performance, a coating deposited on rubbers should have (1) strong adhesion to rubber substrates, (2) sufficient flexibility to adapt large strain of rubbers under applied loads and (3) good wear resistance and low friction. According to these criteria, efforts in finding appropriate coatings for rubbers lead to diamond-like carbon (DLC) and DLC-based thin films, which have been well investigated and industrialized for decades but mostly used on stiffer substrates such as metallic alloys or Si-wafers [2].

Several deposition techniques such as RF-plasma deposition [3,4], filtered-arc deposition [5,6], femtosecond-pulsed laser deposition [7] have recently been applied to deposit DLC films on various kinds of rubbers. In general, the coefficient of friction (CoF) of DLC coated rubbers was reported to be much lower than uncoated ones (by more than 2 times). However, the loads applied in these works were usually lower than 2N (with ø6 mm 100Cr6 steel ball counterparts) since at higher loads the films were damaged after a few rotation revolutions. Also, the microstructure of these DLC-coated rubbers has not been well investigated. Recently, we deposited metal-doped DLC (Me-DLC) via reactive magnetron sputtering on rubbers [8,9] and successfully decreased the coefficients of friction from more than 1 of uncoated rubber to less than 0.22 for coated ones (1N load, ø6mm 100Cr6 steel ball counterpart). Especially, under high normal load of 5N, the films were still functional after the tests of 10000 revolutions with coefficients of friction less than 0.24. It has been revealed that, due to high coefficients of thermal expansion (CTE) of rubbers, a segmented structure composed of crack network and patches is formed in thick DLC-based films and the size of the film patches is mainly depending on the difference in the CTEs between the films and rubbers and the temperature variation during deposition [10]. The crack network is in fact beneficial for the enhancement of film flexibility. We also recognized that thick DLC film (1 μm or thicker) may not be necessary for a good tribological performance of coated rubbers since

wear of DLC film under "soft" contact due to the very low modulus of rubbers is negligibly small. The most critical issues that determine the performances of DLC-coated rubber are the interfacial adhesion and film flexibility.

In this work, we deposit a thin layer (about 300 nm) of DLC on HNBR rubber by sputtering of graphite targets in Ar/C_2H_2 plasma. For enhancement of film adhesion, plasma pre-deposition treatment of HNBR and its influence on the performance of the coated rubber are investigated. In addition, a simple and effective method for removal of the wax on rubber surfaces is introduced.

2   Experimental

Black hydrogenated nitrile butadiene rubber (HNBR) sheet of 2 mm thickness was used as substrate in this study. The commercial HNBR sheet has oil contamination and a thin wax layer on the surfaces, likely from the rolling process. The HNBR substrates of 40×40 mm² size were first cleaned by soap in an ultrasonic cleaner then rinsed carefully with demineralized water. Thereafter, wax removal was carried out in ultrasonic tank with hot demineralized water (80-90°C). This washing process with hot water was repeated three times. After that the HNBR substrates were dried in a centrifugal machine and then heated up to 120°C for 15 min in order to evaporate all absorbed water. The substrates were cooled down in ambient air to room temperature before being loaded into the deposition chamber. The instrumental modulus of HNBR rubber, determined by the method described in [8], is 15.2 MPa and its surface roughness is 0.35 µm measured after wax removal using laser confocal microscope.

Plasma etching pre-treatment of rubber substrates and deposition of DLC films were carried out in a Teer UDP400/4 closed-field unbalanced magnetron sputtering system, which was configured of four magnetrons evenly distributed along the round chamber of 400 mm diameter with two graphite targets opposite to each other (the other two magnetrons were off-power). HNBR substrates were etched in 250 kHz pulsed-DC Ar plasma for 20 min at different bias voltages (-200V, -300V and -400V). The deposition process followed immediately after the plasma etching pre-treatment. DLC films were deposited for 23 min by sputtering two graphite targets (99.9%) of 249×133mm² size in Ar/C_2H_2 plasma. The current applied on the graphite targets was fixed at 0.8 A each, corresponding to an average voltage of 480V and average power of 384W. The gas flow rate was set at Ar/C_2H_2 = 15/10 sccm and the process pressure of 3×10^{-3} mbar was kept constant during deposition via throttle control. The HNBR substrates clamped 80 mm apart from the graphite targets were biased with pulsed DC (250 kHz, 75% duty cycle) at -200V and the sample holder was rotated at a speed of 5 rpm during the deposition. The maximum deposition temperature of 102±2°C was measured in situ with a surface thermometer (model 574CM, PTC instruments, Los Angeles, USA) laid in a cup holder that was fixed at the same position as the HNBR substrates on the sample holder.

The surface morphology and wear track of coated rubber after tribotests were characterized with scanning electron microscope (SEM) (Philips FEG-XL30). The film flexibility is estimated via stretch test with a tensile stage inside the

SEM. The coated rubber sheets were glued onto ø30 mm polished M2 steel discs for tribotests. The tests were performed at 20~23°C on a CSM tribometer with ball-on-disc configuration. The counterpart was ø6 mm 100Cr6 steel balls of hardness HRC 60-62. All the tribotests were carried out at sliding velocity of 10 cm/s and a constant humidity of 35±1% kept with a humidity regulator.

3   Results and discussion

Fig. 1 shows the effect of pre-deposition treatment on the surface morphology of HNBR rubber. Before wax removal, the surfaces of the rubber are almost fully covered by a layer of wax (Fig. 1a), which could not be removed in the previous step (ultrasonic cleaning with soap). After wax removal using hot water, no wax blots can be seen but a powdery morphology observed (Fig. 1b). The plasma treatment of rubber substrates further removes the contaminants (at molecule level) and modifies the surface morphology of the rubber. As seen in Figs. 1c and 1d, pitted areas are formed on the rubber surface due to plasma etching. The density of pitted areas is proportional to the voltage applied during plasma treatment. After -400V plasma etching, a large amount of finer fillers resulted from partially etching are exposed on the surface and the original rubber "skin" was fully peeled off.
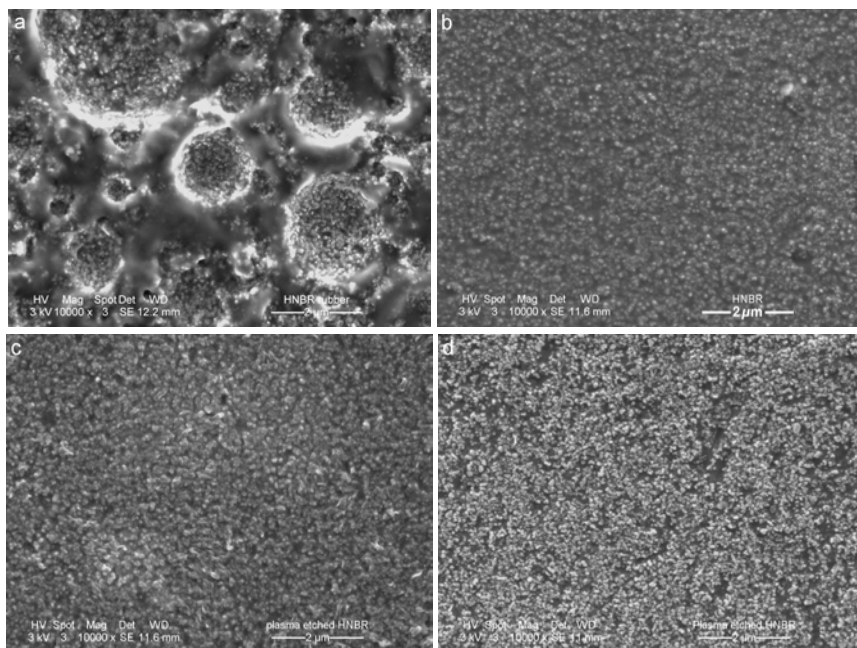
Figure 1:   Surface morphology of HNBR substrates: (a) before and (b) after wax removal by hot water; after further etching treatment for 20 min with -200V Ar-plasma (c) and -400V Ar-plasma (d), respectively.
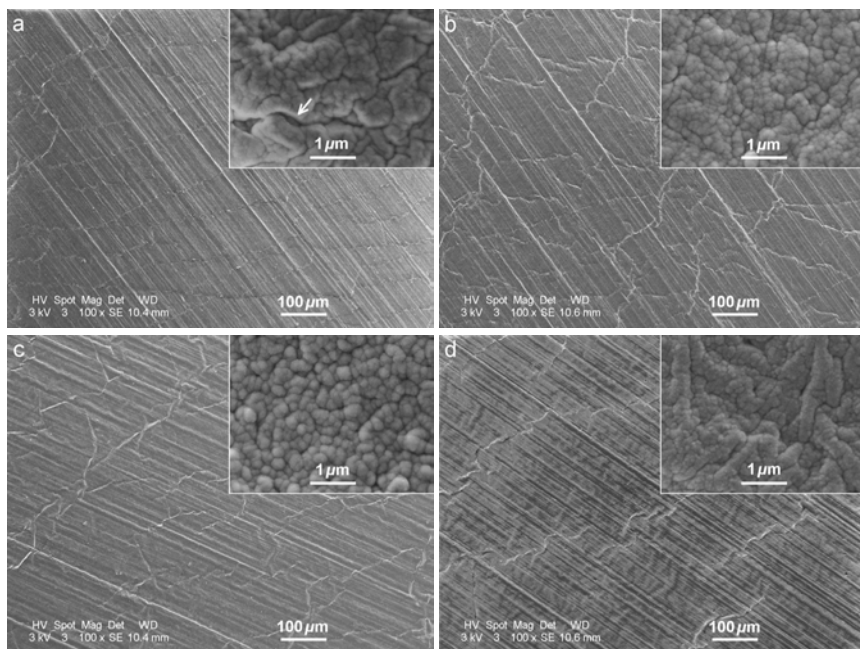
Figure 2:   Crack network and surface morphology of DLC films on HNBR substrate pre-treated differently: (a) without plasma treatment; etched for 20 min in -200V Ar-plasma (b), -300V Ar-plasma (c) and -400V Ar-plasma (d), respectively.

The surface morphology of DLC film coated HNBR substrates with different regimes of plasma pre-treatment is shown in Fig. 2, with inset of high magnification view. The overview shows random crack networks formed in all the DLC films, as well as dense and coarse rolling scratches originated from fabrication of rubber sheet. These crack networks are different from the ones previously observed on 1 μm thick Me-DLC films deposited on HNBR rubber under the same bias voltage of -200V [10]. The differences concern two aspects: (1) The cracks are not open and (2) no clear segmented structure is seen. It has been proven that the formation of open cracks and segmented structure of films on HNBR is directly related to the large difference in the CTE of HNBR (230×10^{-6} K^{-1}) and DLC films (2.3×10^{-6} K^{-1}) and the squeeze between the film segments during cooling down from the deposition temperature to room temperature. Therefore, such differences can be attributed to the lower deposition temperature controlled in this study and smaller film thickness (280-360 nm versus 1 μm in Ref. [10]), thus lower stresses in the thin DLC films. From Fig. 2, it can be seen that the film on the rubber substrates pre-treated in higher voltage plasma has less dense cracks in comparison with that on untreated rubber. The main reason considered is the temperature difference of the substrates prior to and under deposition. The starting temperature of the substrate was 21°C with no treatment and 29°C, 49°C and 85°C right after plasma etching at substrate

voltage of -200V, -300V and -400V, respectively. During the onset of deposition, the temperature of the substrates gradually increased to the steady deposition temperature of 102°C due to ion impingement. Apparently, a smaller increase of temperature during the onset of deposition results in lower tensile stress in the growing film and thus less cracks. In this sense, pre-deposition heating of rubber substrates close to the deposition temperature is helpful to reduce the density of crack network. On the other hand, crack network is beneficial for flexibility and release of the compressive stress built up in a film during cooling after deposition.

At high magnification, it can be seen that the DLC film on -400V Ar-plasma pre-treated HNBR substrate (inset of Fig. 2d) has the densest and finest morphology with domains of worm-like shapes, likely attributed to the strong etching effect on the substrate. The fine and dense feature of film morphology is the result of finer fillers exposed on rubber surface after plasma treatment (Fig. 1d) and smaller thermal mismatch resulted from the smallest temperature difference. The morphology of the films on -200V and -300V plasma pre-treated HNBR substrates (inset of Figs. 2b and 2c) is similar, with coarser and well defined columns characterized by dome head compared to that of the film on -400V plasma pre-treated substrate. The DLC film on untreated substrate (inset of Fig. 2a) exhibits micro-gaps (marked with an arrow), which divide the film into micro-domains. This probably relates to the highest thermal stress built up in the growing film due to the largest temperature difference during the onset of deposition.
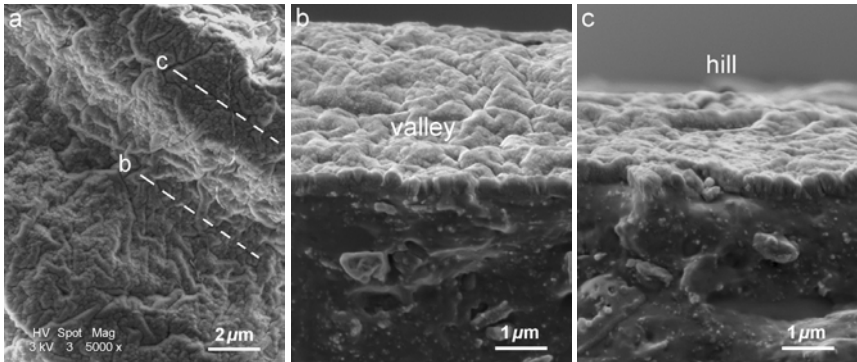
Figure 3:   (a) Surface morphology of DLC film deposited on -400V Ar-plasma pre-treated HNBR; fracture cross section of the DLC film coated HNBR along a valley (b) and a hill (c).

The thickness of DLC films is not very homogeneous as examined at the fracture cross sections of the coated rubbers. Due to the rolling scratches formed on the rubber surfaces during manufacturing, the concave (the "valley") and convex (the "hill") areas are easily recognized after film deposition. As seen in Fig. 3a where the location of representative cross sections of DLC coated rubber is marked, the film on the valley (thickness of about 280 nm) is thinner than that

on the hill (thickness of about 360 nm), as shown in Figs. 3b and 3c. It is attributed to the shadowing effect. All thin DLC films deposited in this study have columnar structure (like the one shown in Fig. 3). As investigated in our previous work [8], due to rough morphology and high CTE of rubbers, DLC and DLC-based films typically have columnar structure when deposited on rubber substrates unless ion impingement of high intensity is used.

To examine the interfacial adhesion strength and flexibility of DLC films on HNBR substrates pre-treated differently, tensile tests (stretch) and in situ SEM observation were performed. When the coated rubber is stretched, the strain tolerance of the columnar structure and existing cracks may compensate the applied strain at the beginning of the test. When the strain is beyond 5%, new cracks initiate and propagate perpendicular to the stretch direction. The amount of cracks increases with increasing strain. Fig. 4 shows the morphology of DLC coated rubbers (untreated and -400V plasma pre-treated) stretched to 20% and 50% strain, and after unloading from 50% strain. At 20% strain (Figs. 4a and 3d), considerable amount of new cracks form and open. These cracks together with the cracks parallel to the stretch direction formed due to the Poisson's shrinkage of rubber divide the DLC film into rectangular segments.

At high strain of 50%, new generations of cracks form and separate the segments further (Figs. 4b and 3e). Also, the opening of the cracks is widened as stretch goes on. At higher strains (>50%), the number of such cracks does not considerably increase but only continuous widening of existing cracks is observed. It is recognizable that the crack spacing in the film deposited on untreated rubber is much larger than that of film on plasma pre-treated one at the same levels of strain (compare Fig. 4a with 3d and 3b with 3e, respectively). It has been proven that, under tensile condition, the interfacial shear strength of a film/substrate system is inversely proportional to the crack spacing [11]. Therefore, it can be concluded that DLC film on -400V Ar-plasma pre-treated HNBR has stronger adhesion than that on untreated HNBR. After being unloaded from 50% strain, no delamination or damage can be observed on the films. However, the cracks generated during stretch can be easily recognized in the film on untreated HNBR substrate (Fig. 4c), due to residual opening. In contrast, it is hard to observe these cracks in the film on the pre-treated substrate (Fig. 4f). It is clear that, at 50% strain, the cracks in the film on untreated HNBR are much wider (~10 μm, Fig. 4b) compared to that of film on the pre-treated rubber (<5 μm, Fig. 4d). In addition, a few tiny chips of DLC film are formed and delaminated from untreated HNBR substrate after unloading (Fig. 4c). In view of tribology, these open cracks worsen the performance of films since they are the cause of wear debris generated due to impact of counterpart with the sharp edge of crack banks during sliding [9]. The results of stretch tests confirm that the DLC films reported here have good flexibility since they can adapt the deformation of the rubber substrate up to 5% strain without crack generation. At high strain of 50%, the films exhibit no spallation, indicating a strong adhesion to the plasma-treated HNBR substrate. It should be noted that DLC films deposited on steel substrates are heavily cracked and already peeled off at 4% strain [12].
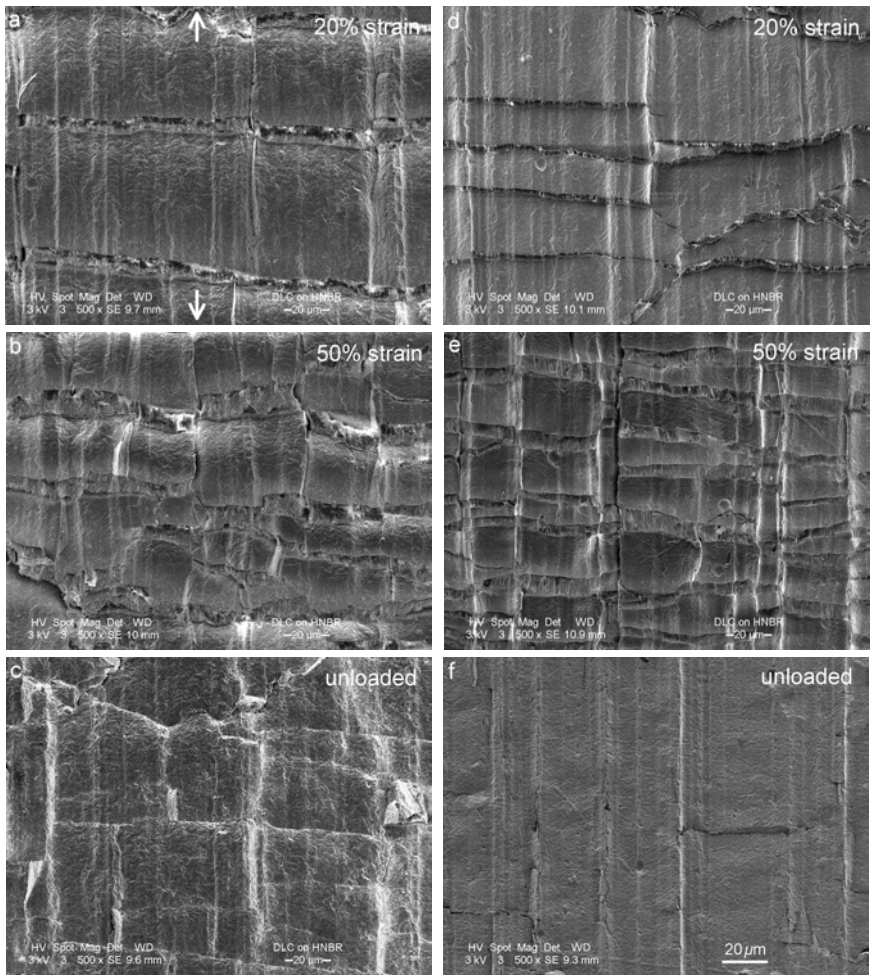
Figure 4:   Morphology of DLC film deposited on untreated (left column) and
             -400V Ar-plasma pre-treated HNBR (right column) after being
             stretched to 20% strain (a,d), 50% strain (b,e) and unloaded from
             the maximum strain (c,f). A pair of arrows indicates the stretch
             direction.

The CoF of DLC films deposited on untreated and -400V Ar-plasma pre-
treated HNBR substrates are shown in Fig. 5. The CoF of uncoated HNBR
rubber (>1) was measured in our previous work [8] and not included here. At 1N
load, the CoF of two DLC films is very low. By the end of the tests, it is 0.175
for the film deposited on -400V plasma pre-treated HNBR and is about 0.18 for
the films on untreated HNBR. Such low CoFs are mainly attributed to the
chemical inertness of DLC film that prevents adhesion onto the contact surface
of the counterpart, rather than its graphitization. Surface graphitization of DLC

films on rigid substrates (like metals, Si, etc.) is considered as one of the major mechanisms operating for ultralow CoF [13,14]. However, it does not work in the case of softer substrates such as rubber because the contact stress (<10 MPa) is not high enough to induce the process of graphitization [10]. At the end of tribo-test, the CoF of films on untreated rubber slightly increase, whereas that of the film on -400V plasma pre-treated rubber is almost constant. At a high applied load of 3N, the CoF is higher compared to that measured at 1N load. Also, the increase in the CoF of the films on untreated rubber can be easily recognized, especially, at the stage after 6000 laps. This is an indication of partial film damage or formation of wear debris (see Fig. 6b); but the film is still functional since the CoF of these films is still low (about 0.22) at the end of the tests and exhibits no sudden increase in the whole course of tests. On the contrary, the CoF of the film on -400V plasma pre-treated HNBR does not considerably increase and maintains at a lower value of about 0.2 till the end of the test.
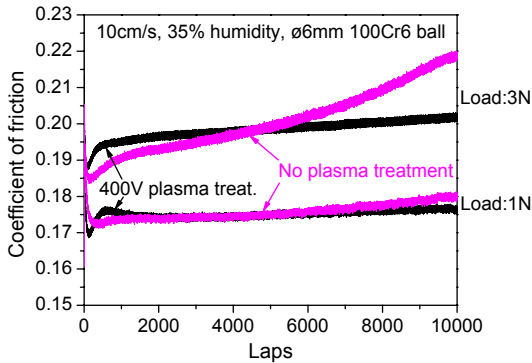
Figure 5:   Coefficient of friction of DLC films deposited on untreated and -400V Ar-plasma pre-treated HNBR substrates, with tribo-test condition indicated.

Fig. 6 shows wear track on DLC film coated HNBR rubbers after tribotest. In the case of DLC film on -400V plasma pre-treated HNBR (Fig. 6a), the wear track is hardly visible except the increased density of random micro-cracks observed under close inspection, so that two dashed lines are added to indicate the borders of the wear track for a better view. The generation of micro-cracks on the wear track is attributed to the large localized bending deformation of the rubber substrate at the high normal load of 3N to adapt the spherical geometry of the counterpart. In fact, almost no wear is observed on the track. Only tiny polished spots of micrometric size are observed, as marked by an arrow in the inset. For the films on untreated (Fig. 6b) HNBR substrates, the wear tracks are obvious, with dense bright dots and many cracks within and beside the wear track. Tensile-type (arc-shaped) Hertzian cracks of regular spacing form within the wear track, concave towards the sliding direction of counterpart ball. Forward chevron cracks nucleate at the borders of the wear track. All these cracks hardly form at 1N load and are attributed to the large deformation of

rubber substrate at higher load and especially poorer adhesion of DLC film on untreated or weak plasma pre-treated HNBR on one hand. The less dense structure of straight column characterized by dome head on top view may cause an easy propagation of cracks through the column boundary on the other hand, in comparison with the curved worm-like microstructure of DLC film on -400V Ar-plasma pre-treated HNBR. The bright dots are micro-chipping, the source of wear debris (see the inset of Fig. 6b). Indeed, wear of DLC film is evident as the original growth features are fully worn out. This explains the increase in the CoF of these two films after 6000 laps as seen in Fig. 5. In comparison with thick DLC films that were totally damaged after a few testing laps under the same testing conditions (3N load and ø6mm steel ball) [4], the thin DLC films in this study exhibit superior tribological properties, especially the film deposited on -400V plasma pre-treated HNBR. Such excellent performance is attributed to the enhanced adhesion, good flexibility, refined microstructure and adequate hardness of thin DLC films, via proper plasma treatment of rubber surfaces.
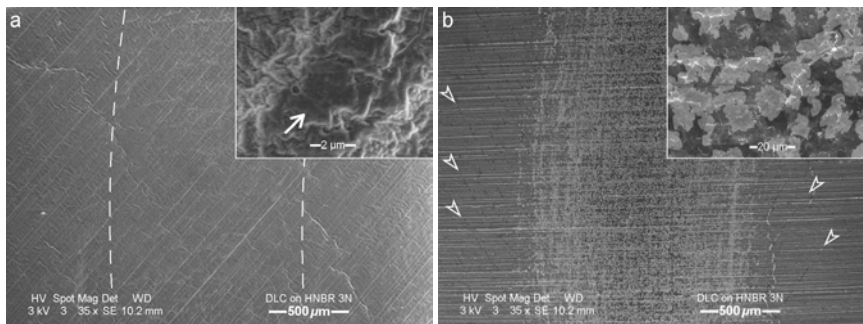
Figure 6:   Wear track of DLC film coated HNBR after tribotest under 3N load: (a) -400 V Ar-plasma pre-treated HNBR and (b) untreated HNBR. The hollow arrows indicate the chevron cracks beside the wear tracks.

4   Conclusion

Thin DLC films have been deposited on rough HNBR rubber by sputtering of graphite targets in C_2H_2/Ar plasma. Hot water and plasma treatment are proven to be very effective and environment-friendly in removal wax and other contaminants on rubber surface. Plasma treatment modifies the film morphology due to: (1) modification of the rubber morphology and (2) changing the temperature at which the deposition starts. The network of cracks and columnar structure make the DLC films flexible. Plasma pre-treatment of the rubber substrate enhances the interfacial adhesion. After stretched to 50% strain and unloading, the DLC films still adhere very well on the rubber substrates and no spallation or delamination was observed. The thin DLC film deposited on -400V plasma pre-treated rubber exhibits very low CoF (0.175 at 1N load and 0.20 at 3N load), suitable for industrial applications. The wear resistance of this film is

very good, no damage but only mildly polished tiny spots can be seen on the "hill" positions. Such tribological behavior is even better than that of 1μm pure DLC or Me-DLC coated rubbers.

Acknowledgements

References

[1]   B.N.J. Persson, J. Phys. Condens. Matter. 18 (2006) 7789
[2]   A. Matthews, S.S. Eskildsen, Diamond Relat. Mater. 3 (1994) 902
[3]   T. Nakahigashi, Y. Tanaka, K. Miyake, H. Oohara, Tribol. Int. 37 (2004) 907
[4]   Y. Aoki, N. Ohtake, Tribol. Int. 37 (2004) 941
[5]   H. Takikawa, N. Miyakawa, S. Minamisawa, T. Sakakibara, Thin Solid Films 457 (2004) 143
[6]   N. Miyakawa, S. Minamisawa, H. Takikawa, T. Sakakibara, Vacuum 73 (2004) 611
[7]   S. Yoshida, M. Okoshi, N. Inoue, J. Phys.: Conference Series 59 (2007) 368
[8]   Y.T. Pei, X.L. Bui, X.B. Zhou, J.Th.M. De Hosson, Surf. Coat. Technol. 202 (2008) 1869
[9]   Y.T. Pei, X.L. Bui, X.B. Zhou, J.Th.M. De Hosson, J. Vac. Sci. Technol. A 26 (2008) 1085
[10] X.L. Bui, Y.T. Pei, J.Th.M. De Hosson, Surf. Coat. Technol. 202 (2008) 4939
[11] D.C. Agrawal, R. Raj, Acta Metall. 37 (1989) 1265
[12] H.W. Choi, K-R. Lee, R. Wang, K.H. Oh, Diamond Relat. Mater. 15 (2006) 38
[13] Y. Liu, A. Erdemir, E.I. Meletis. Surf. Coat. Technol. 86-87 (1996) 564
[14] Y.T. Pei, D. Galvan, J.Th.M. De Hosson. Acta Mater. 53 (2005) 4505.

This page intentionally left blank

Computational evaluation of interfacial fracture toughness of thin coatings

M. Bielawski & K. Chen
Institute for Aerospace Research, National Research Council, Canada

Abstract

A computational method to evaluate fracture toughness of single- and multi-layered coatings using first-principles density functional theory (DFT) calculations was proposed. This method was first applied to calculate elastic properties and fracture toughness K_{IC} of single crystalline TiC and several transition metal nitrides with cubic structure, such as TiN, CrN, ZrN, VN and HfN. After comparison with known experimental data and other DFT results, the reliability of present calculations was favourably confirmed. Next, DFT was applied to calculate the ideal work of adhesion W_{ad}, Young's modulus E and interfacial fracture toughness K_{IC}^{Int} for bi-layer combinations of five transition metal nitrides in (100) and (110) surface orientations. For the analyzed coatings, the following trends were observed: $E(100) > E(110)$, $W_{ad}(100) < W_{ad}(110)$ and $K_{IC}^{Int}(100) < K_{IC}^{Int}(110)$, demonstrating that it is the W_{ad} that plays a decisive role in determining interfacial fracture toughness of these materials. All interfaces formed with TiN in the (110) orientation showed the best combination of adhesion and interfacial fracture toughness.
Keywords: thin coatings, first-principles calculations, elastic properties, fracture toughness, interfacial fracture toughness.

1   Introduction

Erosion-resistant (ER) coatings are used to protect compressor components of land and airborne gas turbines from destructive effects of dust and sand particles suspended in the inflowing air. As particulate dry erosion can significantly impact component life and aircraft safety, attempts were made to develop advanced erosion-resistant coatings for compressor components of gas turbine engines [1–4]. Despite years of effort, high-performing ER coatings capable of

extending service life of compressor blades by about a factor of ten or more are still sought after. To achieve top performance of erosion-resistant coatings, new materials and new design approaches are being developed [5, 6]. Typically, ER coatings are complex systems, produced using either physical or chemical vapour deposition (PVD or CVD), and consisting of many layers (at the micro and nano scale) of different materials, usually nitrides or carbides of transition metals. The principal damage mechanism for ER coatings is brittle fracture, with crack morphology predominantly controlled by the kinetic energy of impacting particles [7–11]. In the case of small impact velocities, the contact is essentially elastic, and the resulting fracture is in the form of axially symmetric cone cracks starting at the periphery of the contact area. With increased velocities, when plastic deformation occurs, lateral and radial cracks start from the edge of the plastic zone around the impact area. This effect is more pronounced in the case of angular (as oppose to spherical) particles [8]. In actual erosion conditions, under multiple particle impacts, many types of cracks are produced, which leads to material removal when the cracks interlink and propagate to the free surface. In the case of multilayer coatings, developing cracks may reach the interface of individual layers and cause local delamination, leading to an accelerated loss of coating. These mechanisms clearly point to fracture properties as the critical factors in determining erosion resistance of hard and brittle materials [5–9]. In particular, interfacial fracture toughness appears to be one of the key parameters in determining performance of multilayered ER coatings.

Since the traditional methods of developing protective coatings through trial-and-error experimentation are time-consuming and costly, extensive modelling and simulation efforts are underway to speed up these developments. However, the materials data needed for the computer models are not easily available. In particular, limited experimental data exist on the fracture toughness of thin films and there are virtually no data on interfacial fracture toughness for thin multi-layer coatings. Therefore, developing computational methods that could allow an evaluation of fracture properties of candidate erosion materials would benefit both experimental and modelling efforts.

Density functional theory (DFT) was previously used to calculate elastic constants, electronic structure and adhesion properties of many materials [12–18]. Recently, the DFT calculations were extended to evaluation of mechanical properties of structural materials and protective coatings [19–25]. In the present approach, DFT calculations were applied to obtain elastic properties, surface energy and ideal work of adhesion for single crystals of several transition metal nitrides and carbides, leading to the calculation of fracture toughness and interfacial fracture toughness of these materials. To simplify DFT calculations, it was assumed that cracks propagate under Mode I loading in an elastic regime. Since fracture toughness of TiC and TiN is relatively well known, these materials were first used to test our approach. Then, DFT calculations were expanded to include directional properties of investigated materials. In this context, the results of DFT calculations of elastic and fracture properties for transition metal nitrides with cubic structure such as TiN, CrN, ZrN, VN and HfN, and their coherent interfaces in (100) and (110) orientations, are reported.

2   Calculation procedure

The Vienna *ab initio* simulation package (VASP) [26] using projector augmented wave (PAW) method [27], based on DFT with the generalized-gradient approximation (GGA) [28] was utilized to calculate the total energy E_{tot} for the investigated cubic structures of TiC, TiN, CrN, ZrN, VN and HfN. From the total energy, the elastic constants C_{11}, C_{12} and C_{44} were derived and Young's modulus E calculated, according to procedure described elsewhere [18].

To obtain Young's modulus along a specific direction, elastic compliances S_{11}, S_{12}, and S_{44} were first calculated according to the following formula [29]:

$$s_{11} = \frac{C_{11} + C_{12}}{(C_{11} - C_{12})(C_{11} + 2C_{12})} \tag{1}$$

$$s_{12} = \frac{-C_{12}}{(C_{11} - C_{12})(C_{11} + 2C_{12})} \tag{2}$$

$$s_{44} = \frac{1}{C_{44}}. \tag{3}$$

Then, Young's modulus in the direction of unit vector [hkl] was calculated [29]:

$$\frac{1}{E_{hkl}} = s_{11} - 2(s_{11} - s_{12} - \frac{1}{2}s_{44})(h^2k^2 + k^2l^2 + l^2h^2). \tag{4}$$

For elastic coefficient evaluations, the integration in the Brillion zone of *ab initio* DFT calculations was done using Monkhorst Pack 17×17×17 k-points of bulk unit cell. For each of the calculations, the Hellman-Feynman forces were calculated to fully relax the atomic coordinates in the models. The planewave cut-off energies were ~450 eV in total energy calculations and the convergence of the total energy calculations was ~10^{-5} eV.

Fracture toughness K_{IC}, interpreted as a critical stress intensity factor, was calculated from the formula given by Ohring [30]:

$$K_{IC} = \sqrt{4\gamma \cdot E}, \tag{5}$$

where γ is surface energy calculated from the Boettger formula [31]:

$$\gamma = (E_{slab}^N - N \cdot \Delta E)/2, \tag{6}$$

where E_{slab}^N is the total energy of an N-layer slab, and ΔE the incremental energy determined by $(E_{slab}^N - E_{slab}^{N-2})/2$. For these calculations, a series of slab models in (100) orientation and with variable number of layers were generated. It was observed that a critical thickness of 11 layers was enough to achieve the convergence and stable surface energy. In order to prevent interactions between the slab and its periodic images, a vacuum region of at least 1 nm was included in all supercell models.

Calculations of interfacial fracture toughness K_{IC}^{Int} were performed using a formula similar to eqn. (5), by substituting surface energy γ by interfacial debonding energy γ_d [30]. Further, for the purpose of this research, the debonding energy of an interface was assumed to be equal to a thermodynamic (ideal) work of adhesion W_{ad} [20]. In addition, to accommodate for interface

anisotropy, orientation-dependent Young's modulus E_{hkl} was used in these calculations. Thus, the interfacial fracture toughness K_{IC}^{Int} between two materials along a specific direction [hkl] was calculated from the following formula:

$$K_{IC}^{Int} = \sqrt{4W_{ad} \cdot E_{hkl}} \; . \tag{7}$$

Calculations for every pair of materials were performed assuming that the material with the larger Young's modulus was on top of the stack, corresponding to approaching the interface from that side, i.e. giving the upper bound estimation of the interfacial fracture toughness for the given pair of materials.

The work of adhesion W_{ad} was determined through DFT calculations as the difference in total energy between the interface and its isolated surfaces, using the following equation [32]:

$$W_{ad} = (E_{s1}^{tot} + E_{s2}^{tot} - E_{s1+s2}^{tot}) / A , \tag{8}$$

where E_{S1}^{tot} and E_{S2}^{tot} are the total energy of slab 1 and slab 2, E_{S1+S2}^{tot} is the total energy of the interface system consisting of slab 1 and slab 2 separated by the distance χ, and A is the interface area. The interface separation χ, usually expressed in units of lattice constant a_0, is a parameter in the calculation for the work of adhesion. DFT calculations as per eqn. (8) were performed for a series of χ distances and the calculated values of W_{ad} were plotted vs. χ to reveal the minimum, corresponding to the binding (debonding) energy. Two orientations (100) and (110) between nitride pairs have been selected as the interfaces. Since the analyzed nitrides have different lattice parameters, a coherent interface was modelled by assuming an average lattice parameter between the two nitrides [20].

3 Results and discussions

DFT calculations were applied to obtain elastic properties for several transition metal nitrides with cubic structure such as TiN, CrN, ZrN, VN and HfN. Table 1 shows the calculated lattice parameters a_0 and elastic coefficients C_{11}, C_{12} and C_{44} for the selected nitrides. The respective numbers were compared to known theoretical and experimental results for TiN and VN. A good agreement between the current calculations, and other DFT calculations and experimental measurements was observed.

The calculated elastic compliances S_{11}, S_{12}, S_{44} and direction-dependent Young's modulus E_{hkl} for investigated nitrides are listed in Table 2, together with other DFT calculations for TiN and VN. After comparison with literature data, it was found that the current DFT calculations are in good agreement with existing DFT results, thus confirming the reliability of the present approach.

From Table 2, a clear trend of $E(100) > E(110)$ for all five transition metal nitrides can be observed. This trend on Young's modulus indicates that the bond strength in the [100] direction is stronger than that along the [110], which in turn may affect deformation behaviour and mechanical properties of these materials. It is interesting to note that for $E(100)$, HfN and VN nitrides show larger values than TiN, while in the (110) orientation, it is the TiN that holds the largest value of Young's modulus, indicating that the bond strength of TiN in the (110)

orientation is stronger compared to that of (100). In both directions, the weakest material in terms of the bond strengths was CrN, as indicated by the lowest E values.

Table 1:   Lattice constants a_0 and elastic coefficients C_{11}, C_{12} and C_{44} for selected nitrides together with other DFT calculations [15, 16] and experimental measurements [33, 34].

	a_0 (Å)	C_{11} (GPa)	C_{12} (GPa)	C_{44} (GPa)
TiN	4.255, 4.27 [15] 4.26 [16], 4.26 [33]	591, 604 [15] 706 [16], 625 [34]	144, 136 [15] 138 [16], 165 [34]	160, 162 [15] 175 [16], 163 [34]
VN	4.121, 4.128 [15] 4.229 [16], 4.13 [33]	631, 636 [15] 752 [16], 533 [34]	170, 162 [15] 183 [16], 135 [34]	133, 126 [15] 121 [16], 133 [34]
CrN	4.124	406	88	75
ZrN	4.609	583	109	115
HfN	4.530	628	115	120

Table 2:   Elastic compliances S_{11}, S_{12}, S_{44} and Young's modulus E in (100) and (110) orientations for selected nitrides along with other DFT calculations [15].

	S_{11} ($10^{-12}m^2N^{-1}$)	S_{12} ($10^{-12}m^2N^{-1}$)	S_{44} ($10^{-12}m^2N^{-1}$)	$E(100)$ (GPa)	$E(110)$ (GPa)
TiN	1.87 1.81 [15]	-0.37 -0.3 [15]	6.26 6.17 [15]	534 554 [15]	432 439 [15]
VN	1.79 1.75 [15]	-0.38 -0.4 [15]	7.53 7.94 [15]	559 570 [15]	387 373 [15]
CrN	2.67	-0.48	13.31	374	226
ZrN	1.82	-0.29	8.72	548	339
HfN	1.69	-0.26	8.32	593	358

The DFT-calculated fracture toughness K_{IC} and surface energy γ for TiC, TiN, CrN, ZrN, HfN and VN coatings are listed in Table 3. Again, a very good agreement between the current calculations, other DFT data and experimental measurements was observed, further confirming the reliability of present DFT calculations.

From Table 2 and 3, it can be noted that materials with the largest values of Young's modulus such as HfN and VN at (100) orientation may not necessarily have the largest fracture toughness K_{IC}. As HfN shows the largest $K_{IC}(100)$ value of 2.14 MPa·m$^{1/2}$, VN is the second lowest with only 1.44 MPa·m$^{1/2}$. A similar example can be found at (110) direction. The important factor here is the surface energy γ. As indicated by eqn. (5), only coatings with a reasonable combination of E and γ can reach high fracture toughness. Not surprisingly, CrN with the

lowest E value and very low γ (in both directions) yielded the lowest fracture toughness among the investigated materials.

Table 3:   Fracture toughness K_{IC} and surface energy γ in (100) and (110) orientations for TiC and selected nitrides with other DFT calculations [12, 13] and experimental measurements [35–37].

	K_{IC} (100) (MPa·m$^{1/2}$)	γ (100) (J/m^2)	K_{IC} (110) (MPa·m$^{1/2}$)	γ (110) (J/m^2)
TiC	1.71 1.70 [36], 1.55 [37]	1.69 1.67 [13], 1.71 [12]	-	-
TiN	1.67 1.76 [35]	1.312	2.16	2.700
VN	1.44	0.922	1.77	2.030
CrN	1.24	1.029	1.48	1.859
ZrN	1.89	1.635	1.90	2.668
HfN	2.14	1.932	1.97	2.724

Table 4 lists the calculated ideal work of adhesion W_{ad} and interfacial fracture toughness K_{IC}^{Int} along the [100] and [110] direction for all 10 coherent interfaces of the five investigated nitrides.

Table 4:   Ideal work of adhesion W_{ad} and interfacial fracture toughness K_{IC}^{Int} in the (100) and (110) interfaces of selected transition metal nitrides.

	W_{ad}(100) (J/m^2)	K_{IC}^{Int}(100) (MPa·m$^{1/2}$)	W_{ad}(110) (J/m^2)	K_{IC}^{Int}(110) (MPa·m$^{1/2}$)
HfN/TiN	3.47	2.87	6.08	3.24
VN/TiN	2.99	2.59	5.68	3.13
ZrN/TiN	3.23	2.66	5.84	3.18
HfN/VN	3.11	2.71	5.55	2.93
VN/ZrN	3.36	2.74	5.81	3.00
HfN/ZrN	3.49	2.88	5.82	2.89
TiN/CrN	3.47	2.72	5.79	3.16
VN/CrN	2.66	2.44	5.60	2.94
ZrN/CrN	2.93	2.54	5.52	2.74
HfN/CrN	3.19	2.75	5.51	2.81

Evidently, the work of adhesion values along the [110] direction are larger than those along the [100], i.e. W_{ad} (110) > W_{ad} (100), although Young's moduli (as shown in Table 2) follow the opposite trend E(100) > E(110). Besides, Table 4 shows that the general trend for interfacial fracture toughness follows K_{IC}^{Int}(110) > K_{IC}^{Int}(100). Comparison of trends for K_{IC}^{Int} with those for E indicates that W_{ad} is not fully determined by pure bond strength. Otherwise both

trends would be identical. It is speculated that the atomic density and packing sequence on that interface may be another factor in controlling W_{ad}. Illustration of trends in ideal work of adhesion W_{ad} and interfacial fracture toughness K_{IC}^{Int} in the (110) direction is shown in Figure 1 for all interfaces formed by the five transition metal nitrides. Similar relationships can be also observed in the (100) direction. Thus, it may be concluded that the ideal work of adhesion W_{ad} plays a decisive role in controlling the interfacial fracture toughness of investigated materials.
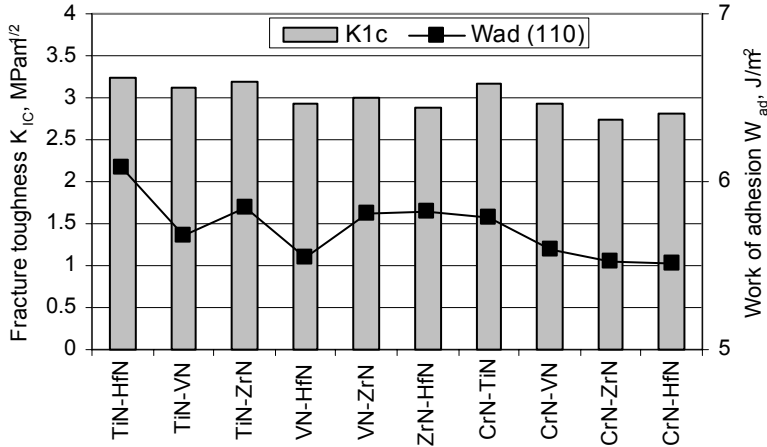
Figure 1:   Trends in ideal work of adhesion W_{ad} and interfacial fracture toughness K_{IC}^{Int} in the (110) interfaces formed by TiN, CrN, VN, HfN and ZrN.

It should be noticed from Table 4 that in both directions, W_{ad} achieved the largest value on the interfaces of HfN/ZrN, HfN/TiN and TiN/CrN. However, the largest K_{IC}^{Int} values were obtained for HfN/TiN, ZrN/TiN, TiN/CrN and VN/TiN interfaces in the (110) orientation. Overall, the best combination of adhesion and interfacial fracture toughness was obtained for all interfaces formed with TiN in the (110) orientation. It can be also noticed from Tables 3 and 4 that on any given orientation, fracture toughness K_{IC} of any nitride is always lower than interfacial fracture toughness K_{IC}^{Int} of any bi-layer combination. Thus, multi-layered coatings fabricated from these nitrides will have interfaces relatively more resistant to fracture, making them suitable candidates for erosion-resistant applications.

4   Conclusions

Density functional theory (DFT) calculations have been applied to investigate fracture toughness and interfacial fracture toughness of TiN, CrN, ZrN, VN and HfN, targeted as erosion-resistant coatings for aerospace applications. DFT

calculations were performed in (100) and (110) surface orientations. The following conclusions were drawn for the investigated materials.

Only coatings with a reasonable combination of E and γ can reach high fracture toughness. The largest fracture toughness was obtained for HfN (2.14 MPa·m$^{1/2}$) in (100) orientation and for TiN (2.16 MPa·m$^{1/2}$) in (110) orientation. The lowest fracture toughness, in both orientations, was obtained for CrN.

Ideal work of adhesion W_{ad} and interfacial fracture toughness K_{IC}^{Int} along the [100] and [110] direction for all 10 coherent interfaces of the five investigated nitrides were calculated. Overall, the best combination of adhesion and interfacial fracture toughness was obtained for all interfaces formed with TiN in the (110) orientation.

For the analyzed coatings, the following trends were observed: $E(100) > E(110)$, $W_{ad}(100) < W_{ad}(110)$ and $K_{IC}^{Int}(100) < K_{IC}^{Int}(110)$, demonstrating that it is the W_{ad} that plays a decisive role in determining interfacial fracture toughness of these materials.

In any given orientation, fracture toughness K_{IC} of any nitride was always lower than interfacial fracture toughness K_{IC}^{Int} of any bi-layer combination. Thus, multi-layered coatings fabricated from these nitrides will have interfaces more resistant to fracture, making them suitable candidates for erosion-resistant applications.

Acknowledgement

Reference

[1]   Paramesvaran, V.R., Immarigeon, J.P. & Nagy, D., Titanium nitride coating for aero engine compressor gas path components, *Surf. Coat. Technol.*, **52**, pp. 251-260, 1992.

[2]   Paramesvaran, V.R., Nagy, D., Immarigeon, J.P., Chow, D. & Morphy, D., Erosion resistant coatings for compressor applications (Chapter 13.0). *Advances in High Temperature Structural Materials and Protective Coatings,* ed. A.K. Koul, V.R. Paramesvaran, J.P. Immarigeon & W. Wallace, Publication from National Research Council of Canada: Ottawa, pp. 262-281, 1994.

[3]   Tabakoff, W., Protection of coated superalloys from erosion in turbomachinery and other systems exposed to particulate flows, *Wear*, **233-235**, pp. 200-208, 1999.

[4]   Klein, M. & Simpson, G., The development of innovative methods for testing a Russian coating on GT T64 gas turbine engine compressor blades, *Proc. of the ASME Turbo Expo*, CD-ROM peer -reviewed, ASME: Vienna, pp. 1-6, 2004.

[5] Bielawski, M. & Beres, W., FE modelling of surface stresses in erosion-resistant coatings under single particle impact, *Wear,* **262**, pp. 167-175, 2007.

[6] Hassani, S., Bielawski, M., Beres, W., Martinu, L., Balazinski, M. & Klemberg-Sapieha, J.E., Design of hard coating architecture for the optimization of erosion resistance, *Wear*, **265**, pp. 879-887, 2008.

[7] Finnie, I., Some reflections on the past and future of erosion, *Wear*, **186-187**, pp. 1-10, 1995.

[8] Field, J.E. & Hutchings, I.M., Surface response to impact (Chapter 7). *Materials at High Strain Rates*, ed. T.Z. Blazynski, Elsevier: London and New York, pp. 243-293, 1987.

[9] Evans, A.G., Impact damage mechanics: solid projectiles (Chapter 1), *Treatise on Materials Science and Technology: Vol. 16 Erosion*, ed. C.M. Preece, Academic Press: New York, pp. 1-67, 1979.

[10] Ruff A.W. & Wiederhorn, S.M., Erosion by solid particle impact (Chapter 2). *Treatise on Materials Science and Technology: Vol. 16 Erosion*, ed. C.M. Preece, Academic Press: New York, pp. 69-126, 1979.

[11] Gachon, Y., Ienny, P., Forner, A., Farges, G., Sainte Catherine, M.C. & Vannes, A.B., Erosion by solid particles of W/W–N multilayer coatings obtained by PVD process, *Surf. Coat. Technol*., **113**, pp. 140-148, 1999.

[12] Dudiy, S.V. & Lundqvist, B.I., First-principles density-functional study of metal-carbonitride interface adhesion: Co/TiC(001) and Co/TiN(001), *Phys. Rev*. B, **64**, pp. 45403-45417, 2001.

[13] Arya, A. & Carter, E.A., Structure, bonding, and adhesion at the TiC(100)/Fe(110) interface from first principles, *J. Chem. Phys*., 118, pp. 8982-8996, 2003.

[14] Chen, K., Zhao, L. & Tse, J., *Ab initio* study of elastic properties of Ir and Ir_3X compounds, *J. Appl. Phys*., **93**, pp.2414-, 2003.

[15] Lazar, P., Redinger & J. Podloucky, R., Density functional theory applied to VN/TiN multilayers, *Phys. Rev. B*, **76**, pp. 174112-174121, 2007.

[16] Wolf, W., Podloucky, R., Antretter, T. & Fischer, F.D., First-principles study of elastic and thermal properties of refractory carbides and nitrides, *Philos. Mag. B*, **79**, pp. 839-858, 1999.

[17] P. Ravindran, L. Fast, P.A. Korzhavyi, B. Johansson, Density functional theory for calculation of elastic properties of orthorhombic crystals: Application to $TiSi_2$, *J. Appl. Phys*., **84**, pp. 4891-4904, 1998.

[18] Chen, K., Zhao, L., Rodgers, J. & Tse, J.S. Alloying effects on elastic properties of TiN-based nitrides, *J. Phys. D: Appl. Phys*., **36**, pp. 2725-2729. 2003.

[19] Hu, Q.M. & Yang, R., Mechanical properties of structural materials from first-principles, *Curr. Opin. Solid. St. M*., **10**, pp. 19-25, 2006.

[20] Chen, K. & Bielawski, M., Interfacial fracture toughness of transition metal nitrides, *Surf. Coat. Technol*., **203**, pp. 598-601, 2008.

[21] Ding, Z., Zhou, S. & Zhao, Y., Hardness and fracture toughness of brittle materials: A density functional theory study, *Phys. Rev. B*, **70**, pp. 184117-6, 2004.

[22] Medvedeva, N.I. & Freeman, A.J., Cleavage fracture in Ti_3SiC_2 from first-principles, *Scripta Mater.*, **58**, pp. 671-674, 2008.

[23] Chen, K. & Bielawski, M., *Ab initio* study on fracture toughness of $Ti_{0.75}X_{0.25}C$ ceramics, *J. Mater. Sci.*, **42**, pp. 9713–9716, 2007.

[24] Aouadi, S.M., Structural and mechanical properties of TaZrN films: Experimental and *ab initio* studies, *J. Appl. Phys.*, 99, pp. 53507-6, 2006.

[25] Chen, K. & Zhao, L., Elastic properties, thermal expansion coefficients and electronic structures of $Ti_{0.75}X_{0.25}C$ carbides, *J. Phys. Chem. Solids.*, **68**, pp. 1805-1811, 2007.

[26] Kresse, G., Furthmuller, J., Efficiency of ab-initio total energy calculations for metals and semiconductors using a plane-wave basis set, *Comput. Math. Sci.*, **6**, pp. 15-50, 1996.

[27] Kresse, G. & Joubert, J., From ultrasoft pseudopotentials to the projector augmented-wave method, *Phys. Rev. B*, **59**, pp. 1758-1775. 1999.

[28] Perdew, J.P., Chevary, J.A., Vosko, S.H., Jackson, K.A., Pederson, M.R., Singh, D.J. & Fiolhais, C., Atoms, molecules, solids, and surfaces: Applications of the generalized gradient approximation for exchange and correlation, *Phys. Rev. B*, **46**, pp. 6671-6687, 1992.

[29] Nye, J. F., *Physical Properties of Crystals*, Oxford University Press: Oxford, 1993.

[30] Ohring, M., *The Materials Science of Thin Films*, Academic Press: San Diego, pp. 561-570, 1992.

[31] Boettger, J.C., Nonconvergence of surface energies obtained from thin-film calculations, *Phys. Rev. B*, **49, pp.** 16798-16800, 1994.

[32] Siegel, D.J., Hector Jr., L.G. & Adams, J.B., First-principle study of metal-carbide/nitride adhesion: Al/VC vs. Al/VN, *Acta Materialia*, 50, pp. 619-631, 2002.

[33] Pearson, W.B., *A Handbook of Lattice Spacings and Structures of Metals and Alloys*, Pergamon Press: Oxford, 1967.

[34] Kim, J.O., Achenbach, J.D., Mirkarimi, P.B., Shinn, M. & Barnett, S.A., Elastic constants of single-crystal transition-metal nitride films measured by line-focus acoustic microscopy, *J. Appl. Phys.*, 72, pp. 1805-1811, 1992.

[35] Karimi, A., Wang, Y., Cselle, T. & Morstein, M., Fracture mechanisms in nanoscale layered hard thin films, *Thin Solid Films*, **420–421**, pp. 275–280, 2002.

[36] Maerky, C., Guillou, M.-O., Henshall, J.L. & Hooper, R.M., Indentation hardness and fracture toughness in single crystal $TiC_{0.96}$, *Mater. Sci. Eng. A.*, **209**, pp. 329-336, 1996**.**

[37] Warren, R., Measurement of the fracture properties of brittle solids by hertzian indentation, *Acta Metallurgica*, **26**, pp. 1759-1769. 1978.

Section 4
Surface problems in
contact mechanics

This page intentionally left blank

The analysis of the state of a turned surface with the use of its image

A. Zawada-Tomkiewicz & B. Storch
Koszalin University of Technology, Poland

Abstract

This paper presents the influence of cutting parameters on the machined surface in turning. Machined surface geometrical features were analyzed in the aspect of four different tool geometries. The analyzed machined surfaces possessed definitely unlike features. The tool with rounded cutting wedge created a machined surface in a form of a thread. For the greater tool nose radius the machined surface was smoother and contained fewer features of the thread. In wiper geometry the machined surface was burnished by the additional radii. In modified geometry, in a form of artificial wear, the machined surface was very smooth with visible material side flow. The aspect of the machined surface creation was discussed for each different geometry. The machined surface after turning was analyzed with the use of surface image data. Turned surface images were indicated dependent on feed rate and tool geometry.
Keywords: turning, tool geometry, machined surface, image analysis.

1   Introduction

Machined surfaces consist of irregularities and defects, such as tool marks and scratches. After turning the resultant surface is created by two-way interaction between the surface and the tool wedge. All the turned surfaces contain the dominant feed component disturbed by vibrations, tool wear and cutting parameters [5, 6]. The use of turning as a finishing process is often limited by surface quality requirements.

The developments in cutting tool materials and geometries have significantly increased the potential for industrial applications of turning as a finishing process. To achieve high surface quality, a good understanding of the effects of process parameters on surface quality is necessary [2, 3].

Surface quality in turning is affected by many factors. One of the most important is tool nose radius. A large nose radius distributes the cut along a greater length, providing better heat dissipation. A large nose radius ensures also better parameters of surface finish. The idea of greater nose radius was applied in the creation of the wiper geometry. Wiper inserts feature additional radii behind the tool nose that are kept in contact with the workpiece after the initial cut. This burnishes peaks and results in a smoother surface finish. Increase of feed per revolution for wiper geometries enables the achievement of the same surface finish as with a standard radius turning insert with a small feed. Wiper geometries require large depths of cut and high feed rates to work correctly [1].

For non-wiper geometries the low roughness can be achieved only at low feed rates. But a very small feed rate led to more material side flow on the machined surface and to a deterioration of the surface quality [6]. The improvement in surface roughness in such circumstances was achieved by applying a tool at a certain degree of wear [3, 7, 8]. For finishing operation of turning the artificial wear land on the tool nose was introduced with the patent of Borys Storch (1998). The increased contact zone and strengthening of tool corner were achieved by avoidance of the first initial phase of accelerated wear. For tool with modified geometry the linear increment of wear land was observed with improvement in surface finish parameters [4, 7].

The main aim of the study was the assessment of the machined surface produced in turning, keeping different cutting conditions and then the comparison of machined surfaces with the use of optical imaging. The surface was illuminated with different lightings and the mechanisms of the creation of these surfaces were revealed. The replication of the tool tip profile on the machined surface was explored. The machined surface images confirmed the variability of the surface with the great impact of the cutting tool geometry.

2   Experimental details

2.1   Material specification and specimen preparation

In this study, steel C45 (EN 10250-2:2001) with 137 HB was used as workpiece material. It was selected because of its wide range of applications in industry. Workpieces were received as cylindrical bars with an initial diameter of 26 mm.
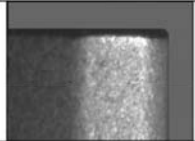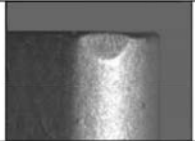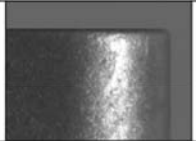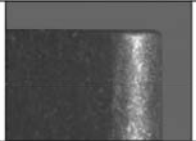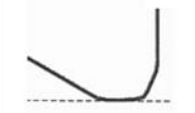
2.2   Turning tools and the procedure of the turning process

Cutting parameters were selected according to the tool manufacturer recommendations. The insert type and feed rate were determined as process variables. Four constructions of cutting tool geometry were considered in this study, which were described as wiper geometry, modified geometry and rounded tool nose featuring two different radii (Table 1). Tool nose geometry was considered as a key factor affecting insert strength and machined surface finish. Using a large nose radius makes the cut to be distributed along a greater length, providing better heat dissipation and improving tool life. Two different tool nose

radii were applied - 0.8 mm and 0.4 mm (Insert 3 and Insert 4). The wiper geometry (Insert 1) features additional radii behind the tool nose that are kept in contact with the workpiece after the initial cut. The modified geometry in a way of artificial wear on the tool nose (Insert 2) increases the contact zone and strengthening of tool corner by avoidance of first initial phase of accelerated wear.

Table 1:   Turning tool geometries.

Insert 1 – wiper TNMX 160408WF	Insert 2 – modified TNMG 160408 PF $KE_{artificial}$=0.02 mm	Insert 3 – rounded TNMG 160408 PF	Insert 4 – rounded TNMG 160404 PF

Before each experiment, the workpiece was turned with a new tool to preserve the same starting conditions. Feed rate was chosen to be 0.1, 0.2 and 0.3 mm/rev with cutting speed of 100 m/min and depth of cut equal to 1.0 mm.

2.3 Surface roughness measurements

After the process of turning the measurements of surface roughness were performed. The surface roughness was measured using the optical method with the use of surface roughness Taylor-Hobson CC16000 instrument with 59x lens and stylus profilometer HOMMELWERKE T2000E. The cut-off and sampling length for optical measurement was taken as 0.388 mm and stylus measurement was taken as 0.8 mm. On each specimen, nine surface roughness measurements were made along the machined surface and an average of these values was taken as a response variable.

For rounded cutting nose the machined surface after turning was the result of kinematic-geometrical pass of the tool.

For wiper tool geometry, additional radii smothered the traces after each pass of the turning tool. In this way the created machined surface after turning was also initially burnished. The shapes of machined surface profiles were combined in Figure 1. For wiper geometry the main shape of turned surface was almost lost. For other geometries the feed component was easier to explore. The machined surface for modified geometry looks the most promising because it is reflective and fine.

Images of ordinate values of the surfaces, combined in Figure 2, show the distribution of irregularities. In this presentation the machined surface for wiper

geometry is significantly different from other surfaces for all the feed rates. It is a set of flat overlapping surfaces. The small deep holes can be distinguished between the surfaces. The machined surface for modified geometry is the smoothest.

When the rounded cutting tools were applied, then the vertical parameters were strictly associated with feed rate. Only for small feed rate the surface roughness Ra parameter was smaller than 2 μm. For wiper and modified geometry of the tool the mean roughness of the machined surface for all the feed rates was not greater than 2 μm. The machined surface for modified geometry for all the feed rates indicated the features of being reflective and smooth.
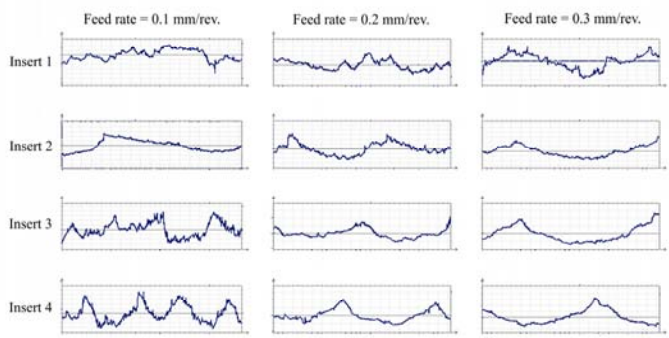
Figure 1: The shape of machined surface profile (CC16000) – ordinate values (vertical axis) in a function of 388 μm definition length (horizontal axis).
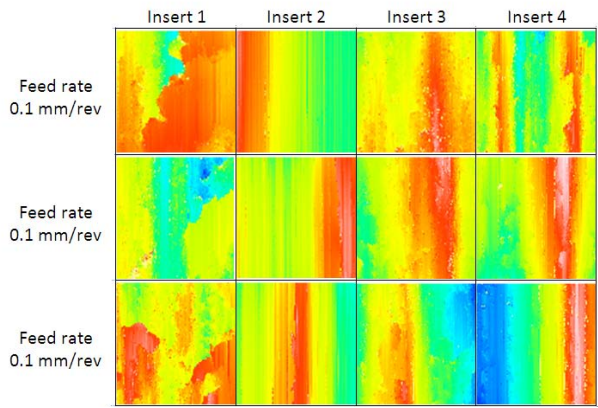
Figure 2: The shape of machined surface (CC16000) – ordinate values $150 \mu m^2$.

2.4 Measurement system for optical imaging

The vision system for turned surface observation was based on a computer with a frame-grabber card, a digital camera, lenses, a stand for a camera with movable worktable and a lighting system (Figure 4a). Four different ways of observing the machined surface were proposed (Fig. 4b, 5).
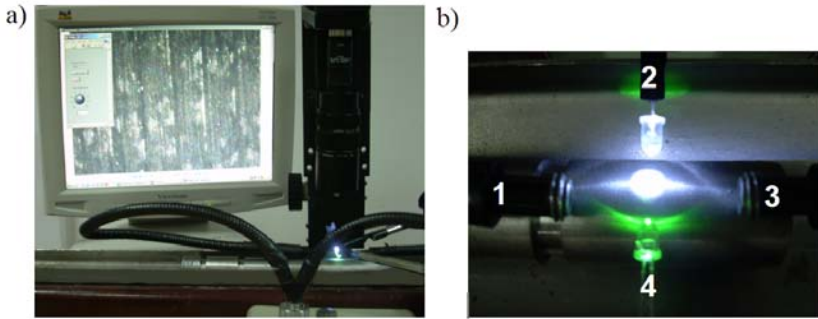
Figure 3:   Surface roughness Ra parameter after the turning operation – T2000E with definition length of 0.8 mm.
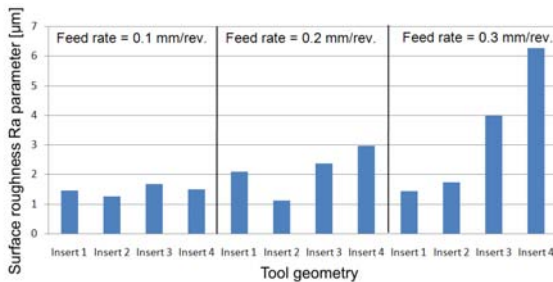
Figure 4:   a) Vision system for machined surface image acquisition, b) lighting configuration for the surface illumination.

Figure 5:   Machined surface image (Fig. 4b): two-sided lighting with the use of halogen – (1-3). One-sided lighting with the use of blue LED – (2), one-sided lighting with the use of green LED – (4). Four-sided lighting with the use of halogen and LED – (1-2-3-4).

The main way of illumination of machined surface after the turning process was the two-sided lighting system based on a halogen white light. It revealed the main shape of irregularities, which were directional with periodic marks after the tool run (Fig 5a). Irrespective of the direction of lighting, the illumination of the surface along the traces presented a texture, which was weak and full of small pale dots (Fig. 5b, 5c). Utilisation of all the sources of lighting, presented in Figure 5d, was almost without an impact on the machined surface image in relation to two-sided one. It was because the halogen two-sided lighting created the dominant image texture. In this way this kind of surface illumination was applied for further analysis.

3 Images of machined surface after turning

Machined surfaces after turning were illuminated to expose their features (Table 2). The smoothest and the most reflective was the machined surface achieved when the modified cutting point was used. When the feed rate was small then the surface features revealed the feed marks like after the grinding. For greater feed rates the machined surface was still very smooth and reflective but tool run left more and better visible burrs. They are perfectly visible as light unequal ribbons set parallel along the traces.

Some disturbances are visible in uniform texture after the use of wiper geometry. Additional radii increased the contact length and cutting traces were smeared out over the surface. Darker spots reveal pits. In these regions the access for the light to the valleys was difficult because of steep slopes of the valleys.

Table 2:   Machined surface image after turning.

For rounded cutting points the machined surface features were the reflection of cutting tool geometry. When the feed rate was grater, the diversification of machined surfaces was more noticeable. For the small tool nose radius the machined surface image was characterised by a lot of light regions. Because of the two-sided lighting the slopes in a thread-like surface were perfectly

distinguished. Only the bottom of the valleys, where the penetration of the light was difficult, was slightly darker.

For the cutting tool featuring greater tool nose radius the machined surface with the increase of feed rate showed less subsurfaces exposed to light. It contained a lot of smooth valleys between irregular remains after the tool pass. The features of this surface can in this way be located between the features of the surface for modified geometry and the surface created by the tool featuring the small tool nose radius.

4   Final conclusions

The paper considers the turned surface for different cutting parameters. Feed rate and tool geometry were the variables of the system. Three feed rates and four different tool wedge geometry were applied. The features f machined surfaces were distinguished and compared for the same cutting parameters.

When the wiper geometry tool wedge was applied, the machined surface was significantly different from the other surfaces. This surface was not typical for turned surface because the machined surface was also burnished by additional radii. These surfaces ware characterised by small roughness. Three-dimensional surface data revealed a lot of heterogeneities and discontinuities. In machined surface optical images these features were visible as dark ragged regions.

The other tool geometries (modified geometry, rounded cutting points with great and small tool nose radii) created directional machined surface, typical for turning operations. The comparison of surface roughness parameters and optical images enabled for the three geometries to be described more general. For the smallest tool nose radius the machined surface revealed the features of thread. It was rough and very directional. The increase of the tool nose radius made the decrease in surface roughness parameters. The machined surface was smoother. By applying tool with modified geometry in a way of artificial wear, the tool nose radius increased even more significantly. This new tool created machined surface of the smallest vertical parameters, very smooth and reflective.

References

[1] Grzesik W., Wanat T.*: Surface finish generated in hard turning of quenched alloy steel parts using conventional and wiper ceramic inserts, *International Journal of Machine Tools & Manufacture* 46, pp.1988–1995, 2006.
[2] Kukielka L.: *The principals of engineering research* (in Polish), PWN Warszawa 2002.
[3] Storch B., *The issues of edge phenomena and monitoring in single-point turning* (in Polish), Technical University of Koszalin Press, Monograph 124, 2006.
[4] Storch B.: *Geometry of cutting part* (in Polish), Patent no. PL 173536 B1, WUP Vol. 03, 1998.
[5] Thiele J.D., Melkote S.N.: Effect of cutting edge geometry and workpiece hardness on surface generation in the finish hard turning of AISI 52100 steel*, Journal of Materials Processing Technology* 94, pp. 216-226, 1999.

[6] Zawada-Tomkiewicz A., Storch B.: Introduction to the Wavelet Analysis of a Machined Surface Profile, *Advances in Manufacturing Science and Technology*, Vol. 28, No 2, pp. 91-100, 2004.

[7] Zawada-Tomkiewicz A., Storch B.: Efficiency of turning process with the use of modified cutting points (in Polish). *Cutting. High productivity.* Editorship of Cichosz P. Wroclaw University Press, Vol. 1, pp. 205–212, 2007.

[8] Zawada-Tomkiewicz A., Storch B.: The Application of Image Processing Techniques in the Tool Wear Estimation, *Computational Methods in Contact Mechanics VI*, WIT*PRESS* Southampton, pp. 201-210, 2003.

Comparative analysis of the machined surface image after the process of burnishing rolling

A. Zawada-Tomkiewicz & B. Storch
Koszalin University of Technology, Poland

Abstract

In this paper the machined surface after burnishing rolling was analyzed with the use of image data. The burnished surfaces were regarded as the post process after the turning. The effect of turning parameters on the machined surface image after the burnishing rolling process was demonstrated. The roughness peaks after burnishing rolling were flattened and the quality of the workpiece surface was improved. The surface texture after the burnishing rolling was indicated to be dependent on the previous process and possessed some features of turning. Surface images confirmed the complexity of all the stages of the manufacturing process forming the surface layer.
Keywords: burnishing rolling, machined surface, image analysis.

1 Introduction

The use of turning as a finishing process is often limited by surface quality requirements. Low roughness can be achieved only at low feed rates. Moreover, tool wear leads to deterioration in the surface [10–12]. A finishing operation can increase feed rates and prolong the tool life of the cutting tool.

Burnishing process offers an attractive post-machining alternative due to its chipless and relatively simple operations. Burnishing process is a cold working technique. Surface enhancement can be achieved by compressing the surface layer of the workpiece with a highly polished and hardened roller. When the applied burnishing pressure exceeds the yield strength of the material, the asperities of the surface will deform plastically and spread out permanently to fill the valleys [1–3, 5, 6, 8].

When combined with turning, burnishing rolling provides a manufacturing alternative to other finishing operations. The roughness peaks are flattened and

the quality of the workpiece surface is improved. The surface is smoothed out and because of the plastic deformation the surface becomes work hardened, the material being left with a residual stress distribution that is compressive on the surface [8, 9].

The aim of the study was the investigation of the impact of the preparation of turned surfaces on the finishing process of burnishing rolling. The turned surface parameters and texture were indicated to determine the course of burnishing rolling and the burnished surface features. Optical imaging was used for burnished surface features identification and analysis. The machined surface images after burnishing rolling were compared taking into consideration the process before.

2 Experimental procedure

2.1 Preparation of machined surfaces for burnishing rolling

Nine turned surfaces were prepared for burnishing rolling. Cutting parameters were selected according to the tool manufacturer recommendations. Four constructions of cutting tool geometry were considered, which were described as wiper geometry, modified geometry and rounded tool nose featuring two different radii. More detailed analysis is described in [13].

2.2 Burnishing rolling procedure

Burnishing tools were designed for the purpose of experimental tests. Figure 1 shows a schematic representation of the burnishing tool mounted on the lathe machine TUB32. The head was mounted in a tool holder. The Rafan NUGH 14–27 head was equipped with three rollers. Each roller was built to possess the same features. It was 24 mm long with head entrance and exit featuring 2º along 5 mm decrease [7, 8].

The workpiece was fastened in a three-jaw chuck. The burnishing parameters were selected according to the initial parameters of the machined surface after
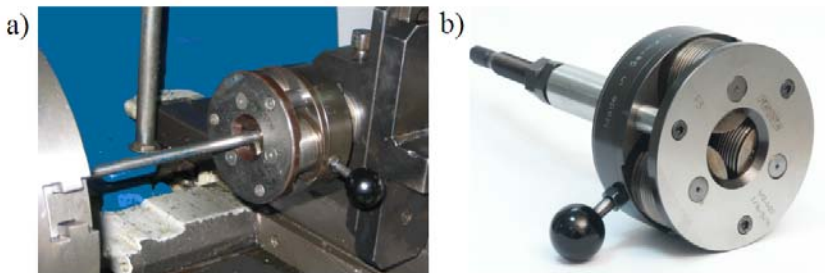
Figure 1:   a) A photograph of the burnishing rolling tool and b) detailed view of the burnishing rolling tool assembly.

the turning process. The three burnishing depths were chosen in dependence on the Rt parameter. It was accordingly 6 μm, 8μm and 10 μm.

A calibration process was conducted and then the burnishing depth was set up. The feed rate in burnishing was forced in relation to the rotation angle of roller axis to workpiece axis. In this way the machined surface was burnished several times. It was multi-pass burnishing rolling.

Table 1:   Summary of burnishing parameters.

Burnishing rolling parameters	Values
Burnishing rotational speed (rev/min)	14
Burnishing initial diameter (mm)	25
Number of burnishing rollers	3
Burnishing depth (μm)	6, 8, 10

2.3 Surface roughness measurements

Measurements of surface roughness were performed before and after burnishing rolling. The surface roughness was measured using the stylus method with the use of surface roughness HOMMELWERKE T2000E instrument. The cut-off and sampling lengths for each measurement were taken as 0.8mm. On each specimen, nine surface roughness measurements were made along the machined surface and an average of these values was taken as a response variable.

Burnishing process improved the surface roughness. For rounded cutting nose geometry the machined surface after turning was the result of kinematic-geometrical pass of the tool. The burnishing process smoothed the surface significantly to the mean roughness of 0.85 μm when the burnishing depth was small.

For wiper tool geometry, additional radii smothered the traces after each pass of the turning tool. In this way the created machined surface only after turning was initially burnished. Applying burnishing rolling process for such a surface was in a way the repetition of the burnishing. The surface roughness parameters were only slightly smaller (20%).

For modified turning tool geometry in a way of artificial wear the mean roughness of the machined surface after burnishing rolling decreased significantly (60%). The machined surface after turning indicated the features of being reflective and very smooth. The burnishing process left these features unchanged. Still, after burnishing rolling only this surface was reflective and received the smallest value of Ra parameter (0.61μm).

The greater burnishing depths caused the change in surface roughness parameters. The change in feed rate from 0.2 to 0.3 mm/rev. caused the increase in surface roughness Ra parameter to be respectively 1.65 μm and 1.85 μm. The maximum roughness was almost the same around 6 μm for the Rt parameter and 4μm for the Rz parameter.
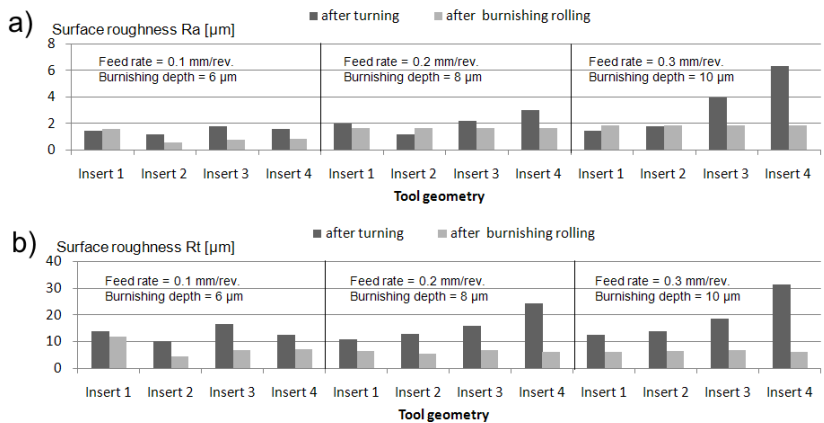
Figure 2: Surface roughness for the Ra and Rt parameters after turning and burnishing rolling for various tool geometries (Insert 1 – wiper geometry, Insert 2 – modified geometry, Insert 3 – rounded tool nose featuring 0.8 mm radius, Insert 4 – rounded tool nose featuring 0.4 mm radius).
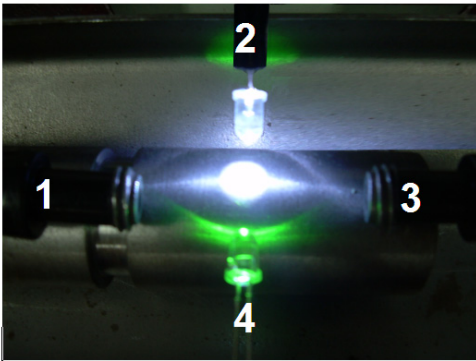
Figure 3: Lighting configuration for the surface illumination. For burnished surface illumination two lighting systems were applied: two-sided lighting with the use of halogen – (1-3) and four-sided lighting with the use of halogen and LED – (1-2-3-4).

3 Images of the machined surface after burnishing rolling

The vision system for turned and burnished surface observation was based on a computer with a frame-grabber card, a digital camera, lenses, a stand for a camera with movable worktable and a lighting system (Figure 3).

Surface image observation needs the interpretation of colour. HLS model defines perceptual colour space by hue, lightness and saturation components [4]. Hue, dominant wavelength, defines the colour itself. Lightness, total power,

indicates the level of illumination. Saturation, purity, indicates the degree to which the hue differs from a neutral grey.

Combination of HLS components in Figure 4 for rounded cutting tool featuring nose radius 0.4mm and feed rate 0.3mm/rev. enables the selection of images for the detailed analysis.
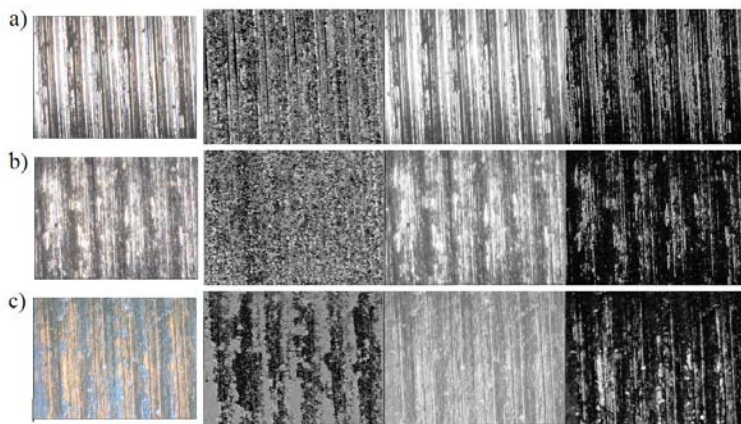
Figure 4:   Machined surface image and its HLS representation: a) after turning with two-sided lighting; b) after burnishing rolling with two-sided lighting; c) after burnishing rolling with four-sided lighting.

The lightness component and the original image are very similar when printed out in gray. This component can be omitted in analysis. The hue component for two-sided lighting is omitted as well because it contains noise-like dispersed colour. Additional illumination caused ordering in a hue component. The interpretation of this component for four-sided lighting is covered by this paper. Saturation component is very similar for both ways of illumination and is discussed only for four-sided lighting.

4   Analysis of the burnished surface images

Images of machined surface after burnishing rolling, when illuminated with two-sided lighting, show the features after the previous process, i.e. turning (Table 2). Feed rate and tool geometry can easily be indicated. Under this illumination the roll marks are also visible. The material plastic deformation process depends on the burnishing parameters. It is clear, however, that the initial state of the surface quality contributes to the final aspect of the part surface. The analysis highlights only the geometrical aspect of surface.

When the burnished surface is visualized under the two-sided lighting, then the feed marks are clearly visible. They are not as sharp as for turned surface but still recognizable. The texture of the image is blurred like after the low-pass

filter. The images show several patches, which are light in colour. They testify to the levelling of the surface. These light spots are well lighted mirror surface parts which were particularly well burnished. Dark spots indicate the places on the surface where the penetration of light was difficult. They show the shadowed valleys after the tool pass in turning and pits left by cold-working burnishing.

Table 2:   Machined surface image after burnishing rolling under two-sided lighting.

	Insert 1	Insert 2	Insert 3	Insert 4
Feed = 0.1 mm/rev. Burnishing depth = 6 μm				
Feed = 0.2 mm/rev. Burnishing depth = 8 μm				
Feed = 0.3 mm/rev. Burnishing depth = 10 μm				

Table 3:   Machined surface image after burnishing rolling under four-sided lighting.

	Insert 1	Insert 2	Insert 3	Insert 4
Feed = 0.1 mm/rev. Burnishing depth = 6 μm				
Feed = 0.2 mm/rev. Burnishing depth = 8 μm				
Feed = 0.3 mm/rev. Burnishing depth = 10 μm				

When the machined surface is illuminated by additional lightings located in such a way that the light penetrates the surface along the traces, then other features of burnished surface are revealed (Table 2). Under this illumination the feed marks are barely visible. The machined surface looks very flat.
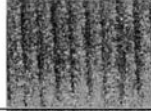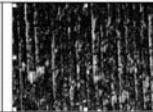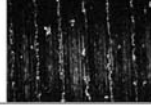
The machined surface is distinctly different for the Wiper geometry. Pattern of developed dark and light spots is sharply outlined. For all feed rates, the light sheet covers the dark background. Randomly scattered dark pits point out at places where steel was not burnished. When the feed rate was smaller the dark

spots were greater and the number of them was smaller. Increasing of feed rate caused the need of grater force and the depth of burnishing was greater. The number of pits was grater and their shape was more elongated. It is clearly visible the geometrical change of the machined surface in relation to turned surface.

For the modified geometry, the whole burned surface image is covered with fine dark points. When the feed rate is greater than for the machined surface after burnishing rolling the protruded rest of material along cutting traces is pressed. The groove interior is visible. The light is capable of penetrating the irregularities because they are not self shadowed and steep. Plastic burrs are sharply outlined. They occur periodically accordingly to feed rare value.

Table 4:   Machined surface image after burnishing rolling under four-sided lighting – hue and saturation components.

For the tool geometry in a shape of rounded cutting nose, the machined surface image after the process of burnishing rolling revealed the fine and uniform texture. Well distinguished plastically deformed surface fill most of the field of view. Plastically changed places stretch along the hills leaving

undeformed material in valleys, on which the tool marks can be observed. It looks like as if the roller surface was spreading the material of the surface along the traces leaving some parts still untouched. Comparing the burnished surface with the turned one, gentler surface with blurred edges can be developed.

Analysis of colour components revealed additional features of burnished surface (Table 4). When the burnishing depth is small, then the distribution of colour (hue component) on the surface illuminated in the same way is similar. When the burnishing depth is greater, then the images show very different pattern of colour. For the modified tool, the small points create regular pattern. For wiper geometry the grey patches spread over an area of black and white noise. With increasing of burnishing depth the patches become less elongated and smaller. For rounded cutting tools, the hue component of the image underlines the irregularity of the burnished surface. Dark grey spots show the places when the changes in colour appear. When the burnishing depth and nose radius are greater, then regularity of the pattern is greater.

Saturation component shows how pure the colour is. White pixels indicate the places with colour. For wiper geometry, when the burnishing depth is small, then the dark image of saturation presents only threads and dots of colour. When the burnishing depth is greater than the threads are shorter and the dots are united. The image has more developed texture and in this way it can be described as being more colourful – contains more diversified fine patterns. For modified tool geometry, the increase of burnishing depth causes greater underline of undeformed material in a form of long white thin lines and more visible band of burrs. For rounded cutting tools the white threads are of different lengths but occur in feed rate interval. Increase of burnishing depth caused the increase of white thread lengths which often appear in groups.

5   Final conclusions

Burnishing rolling process caused for the turned surface to be more predictable in roughness parameters but very complex in image description. To simplify the task, the additional way of illumination of the surface was proposed with the consideration of colour components.

The proper illumination of the surface firstly was to reveal the features of turning parameters on the surface images after burnishing rolling and then to indicate the parts of machined surface still unchanged after burnishing and finally describe irregularities identified on the burnished surface image.

The effect of smoothing on the roughness peaks was described for a turned surface after burnishing rolling. A comparison between images of burnished surface was shown in Tables 1-3 when the same lighting conditions were preserved. The burnishing rolling has plastically deformed and removed the turning tool marks leading to smoother surface appearance. However, burnishing condensed the surface to a depth which was not sufficient to smooth out all the irregularities in the surface.

References

[1]   Ahmed R., Sutcliffe M.P.F., Identification of surface features on cold-rolled stainless steel strip, *Wear* 244, pp. 60-70, 2000.

[2]   El-Axir M.H., An investigation into roller burnishing, *International Journal of Machine Tools & Manufacture* 40, pp. 1603-1617, 2000.

[3]   El-Tayeb N.S.M., Low K.O., Brevern P.V., Influence of roller burnishing contact width and burnishing orientation on surface quality and tribological behaviour of Aluminium 6061, *Journal of Materials Processing Technology* 186, pp.272-278, 2007.

[4]   Foley J.D., van Dam A., Feiner S.K., *Computer Graphics—Principles and Practice*, Addison-Wesley, 2nd edition, 1996.

[5]   Klocke F., Liermann J., Roller Burnishing of Hard Turned Surfaces, *International Journal of Machine Tools & Manufacture* 38, No 5-6, pp. 419-423, 1998.

[6]   Korzynski M., Modelling and experimental validation of the force-surface roughness relation for smoothing burnishing with a spherical tool, *International Journal of Machine Tools & Manufacture* 47, pp. 1956-1964, 2007.

[7]   Kukielka L., *The principals of engineering research* (in Polish), PWN Warszawa 2002

[8]   Patyk S., Patyk R., Kukiełka L., *Problematic of parts technological quality forming in burnishing rolling process*. Conference proceedings TON 2008.

[9]   Sonka M., Hlavac V., Boyle R., *Image processing, analysis and machine vision*, PWS Publishing at Books/Cole Publishing Company, 1999.

[10] Storch B., *The issues of edge phenomena and monitoring in single-point turning* (in Polish), Technical University of Koszalin Press, Monograph 124, 2006.

[11] Zawada-Tomkiewicz A., Storch B., Classifying the wear of turning tools with neural networks, *Journal of Materials Processing Technology* 109, pp. 300-304, 2001.

[12] Zawada-Tomkiewicz A., Storch B. The Application of Image Processing Techniques in the Tool Wear Estimation, *Computational Methods in Contact Mechanics VI*, WIT*PRESS* Southampton, pp. 201-210, 2003

[13] Zawada-Tomkiewicz A., Storch B. The analysis of the state of turned surface with the use of its image. *Ninth International Conference on Surface Effects and Contact Mechanics Computational Methods and Experiments*, WIT*PRESS* Southampton, 2009

This page intentionally left blank

Evaluation of material friction properties using the "Block-on-Ring" apparatus

M. Kašparová, F. Zahálka & Š. Houdková
Department of Thermal Spraying, ŠKODA VÝZKUM Ltd.,
Czech Republic

Abstract

One of the tribological tests for the evaluation of friction properties is introduced in this paper. The test, named "Block-on-Ring", is in accordance with the standard ASTM G-77 and in ŠKODA VÝZKUM Ltd. is realized on the VRS-3 renovated apparatus. The measurement is as follows: the flat surface of the sample is pressed against the cylindrical surface of a rotating wheel of the rotor material. Arbitrary oil is fed to the material contact surface and the increasing temperature is detected using a thermocouple. The friction force is recorded using the strain-gauge dynamometer. The test is performed in a number of periods and always after one expiration time the wear track formed in the sample is measured and evaluated. The final results are the summary of the partial results of the long-standing tests and are used for the preliminary detection of the friction behavior of individual material couples.

Keywords: friction force, coefficient of friction, block-on-ring, ASTM G-77, wear.

1   Introduction

Friction properties rank among many important material properties, which characterize the tribological behavior of materials that are in a sliding contact. Because of the sliding between two or more machine parts friction arises. Friction is the resistance to motion during sliding or rolling what occurs when one solid body moves tangentially over another one with which it is in contact. Then, the resistive tangential force, which acts in a direction directly opposite to the direction of motion, is called the friction force. There are two main types of friction: dry friction and fluid friction. If the solid bodies are loaded together and

a tangential force is applied, the value of the tangential force that is required to initiate the motion is the static friction force. It may take a few milliseconds before the relative motion is initiated at the interface. The tangential force required to maintain the relative motion is known as the kinetic or dynamic friction force. The static friction force is higher than the kinetic friction force, as Bhushan [1] showed. The science called "tribology" deals with the main friction problems. A large part of tribology science solves the following questions: surfaces interface, adhesive wear and lubrication of machine units. It is evident that in addition to the friction, wear also occurs. Vocel *et al.* [2] mentioned that friction without wear may occur if the hydrodynamic lubrication of function surfaces occurs and the compact lubricant layer is spread between two contact bodies. Friction and friction characteristics are advantageously measured using laboratory tribo-tests. Complete tests are described in the related Standards. For example, the pin-on-disc test is specified in the ASTM G-99 [3], the block-on-ring test in the ASTM G-77 [4], the four-ball test in the ASTM D5183-95 [5] and in the ASTM D4172-94 [6], etc.
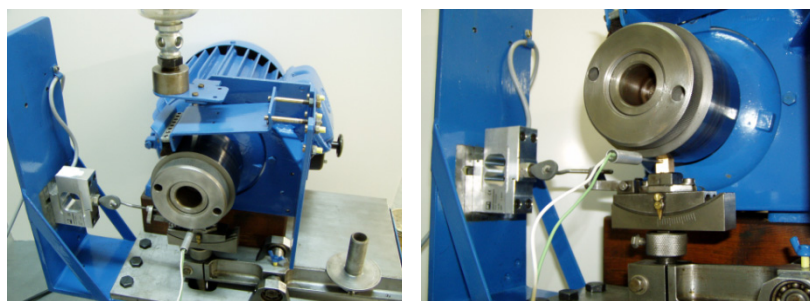
Figure 1: Block-on-ring method, VRS-3 apparatus.

2 Experimental

2.1 "Block-on-Ring" method

In ŠKODA VÝZKUM Ltd. the friction properties are evaluated using the "Block-on-Ring" apparatus, see fig.1. This apparatus, called VRS-3, was put out of operation for a long time but at present it has been renovated and it is used for the evaluation of the material friction properties. The apparatus development is described in the company annual reports [7–9]. The test is generally characterized in such a way that against the flat surface of the sample (block) the cylindrical surface of the rotating wheel of the rotor material (ring) is pressed. Arbitrary oil is fed to the material contact surfaces and increasing temperature is detected there using the thermocouple. The friction force is recorded using the strain-gauge dynamometer. The test can run in a number of periods and always after one expiration time the wear track formed in the block-sample is measured and evaluated. One of the disadvantages of this apparatus is the constant velocity of the ring sample. Because of that it is impossible to change the speed of the ring rotation and to record the statistic coefficient of friction.

By means of the renovated apparatus it is possible to measure a dynamic friction coefficient in lubricated conditions, thermal changes in the material contacts, the wear coefficient, the actual load of a sliding couple in the contact surfaces and it is possible to monitor the waveform of the friction force during the test running. To determine the coefficient of friction, eqn (1) in [4] is used:

$$f = \frac{F_t}{F_n} \tag{1}$$

and after substitution to eqn (1), according to [7,8]:

$$f = \frac{F_t}{(\frac{m * g * b}{a}) + k} \tag{2}$$

where:
Ft   is the friction force in the contact surface [N]
F_n is the normal force in the contact surface [N]
m   is load [kg]
g   is acceleration of gravity [m/s^2]
a, b   is the length of the laver arm [m]
k   is the constant of the measuring apparatus [-]

The technical parameters of the apparatus are listed in table 1. The actual load is determined using eqn (3) according to [7]:

$$G = \frac{F_n}{S\phi} \tag{3}$$

where:
G   is actual load [MPa]
$S_\varnothing$ is the "average" surface of the wear scar [mm^2]

Table 1:   Technical parameters of the VRS-3 apparatus.

Engine revolutions	1400 [r/min]
Circumferential speed	7,33 [m/sec]
Service voltage	380/220 V; 50 Hz
Total power	0,85 kW

For the experiment, the nominal load 3,5 MPa of the tested samples and 500 km sliding distance was used. The total distance was divided into six cycles. The first cycle was the running-up step and its length was one kilometer. Each of the further five steps was one-hundred kilometers long. To determine the wear coefficient of the block sample, eqn (4) was used according to [7]:

$$k = \frac{V_m}{G} \tag{4}$$

where:
k   is the wear coefficient [mm^3/km.MPa]
V_m is the volume loss of the block sample [mm^3]

For the determination of the volume loss of the block sample, eqn (5), which is stated in ASTM G-77 [4], is used (fig.2). The scar width is normally measured by the magnifying glass with an accuracy of measurement of 0,1 mm, using light microscopy (for small widths of the wear scars) or using the profilometer "Mitutoyo SJ-201P" by measuring the profile of the wear scars (fig.3).

$$V = \frac{D^2 * t}{8}(\theta - \sin\theta) \tag{5}$$

where:

t   is the block width [mm]
r   is the radius of the ring [mm]
D   =2r = diameter of the ring [mm]
b   is the average scar width [mm]
θ   is the sector angle in radians
d   is the scar depth [mm]

As a result, eqn (5) can be written as follows:

$$V = \frac{D^2 * t}{8}\left[2\sin^{-1}\frac{b}{D} - \sin\left(2\sin^{-1}\frac{b}{D} \right) \right] \tag{6}$$
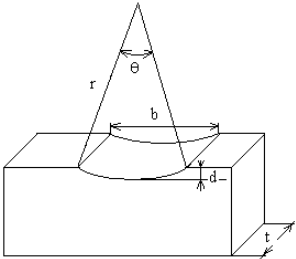
Figure 2:   Schematic diagram of the volume loss of the block sample [4].
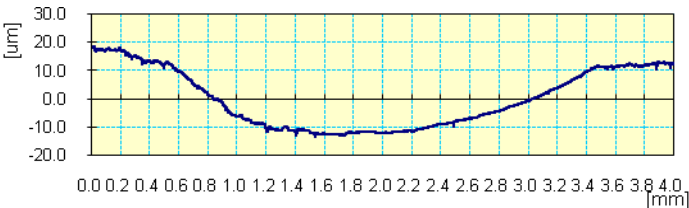
Figure 3:   The wear scar profile.

2.2 Experimental material

For the experimental measurement using VRS-3 apparatus two samples of the thermally sprayed coatings were chosen: one kind of cermet coating on the base of WC-carbide (further in the text sample A only) and one kind of self-fluxing alloy on the base of NiCr (further in the text sample B only). The WC-base

coatings are commonly used as a protector against different types of wear up to approx. 500°C. The NiCr-alloys coatings are characterized by good corrosion and wear properties and they are serviceable up to approx. 850°C. Surface hardness of the WC-sample is 67 HRC and of the NiCr-sample is 57 HRC. These both coatings were thermally sprayed by high pressure high velocity oxygen fuel systems in ŠKODA VÝZKUM Ltd., Pilsen, CZ. The used spray parameters are the intellectual property of the company. The coatings were deposited on the test ring pieces of EN 10025-90 low-carbon steel. As the block the "stanit" tin-based babbitt was chosen. The "stanit" tin-based babbitt is one of many kinds of tin-compositions on the base Sn-Sb-Cu. Its chemical composition is given in table 2.

Table 2:   Chemical composition of the "stanit" tin-based Babbitt.

Stanit	Sb (%)	Cu (%)	Ni (%)	Pb (%)	Sn (%)
	9-11	2-4	0,4-1,0	max.1	84,5-86,5 + 0,5-1,1 Cd

Table 3:   Surface roughness of sample A, sample B and the stanit.

Material	Sample A	Sample B	Stanit
Ra [μm]	1,10E-01±1,55E-02	2,84E-01±2,07E-02	3,20E-01±5,00E-02

2.3 Surface roughness

Tribological characteristics depend on the surface roughness of the sliding materials. If the comparing tests between several different materials are required it is preferable to compare sliding couples of the same surface roughness. The surface roughness was measured using SJ-201P Surftester and the Ra parameter was measured. The results are summarized in table 3.

2.4 Lubricants

The "Block-on-Ring" method facilitates to use many kinds of lubricants in a fluid stage. The lubricants, mostly oils, are injected into the surface contact of the samples (for the VRS-3 apparatus the lubricant presence is essential because it is not constructed for measuring in dry friction conditions). Oils include natural organics consisting of animal fat, vegetable oils, mineral fractions, synthetic organics and mixtures of two or more of these materials. It is mentioned in [1] that the main aim of the lubricants is the decreasing in friction losses, wear and noise level and increasing in absorbing and corrosive resistance. Currently in the industrial market many types of liquid lubricants are offered. From this large offer it is necessary to select the suitable lubricant for the practical application where moving parts with a sliding contact will work. Main tribological components in practical applications are e.g.: bearings, seals, cams, piston rings, electrical brushes, cutting and forming tools, etc. For the experiment the turbine deeply refined TSA 32 oil (in accordance with the ISO 6743 Standard) was chosen. This oil is characterized by the outstanding oxidative stability and antirust performance to protect turbines from rust and corrosion in

severe conditions. It is suitable for steam turbines and water turbines, pumps and valves. The viscosity of the lubricant at temperature 40°C is 28,8 - 35,2 mm^2/sec. The thermal stability and its using are possible up to temperature 140°C. During the experiments the lubricant supply to the sliding contact was 0,002675 dm^3/hours. This amount of lubricant is sufficient for the boundary friction.

3   Results of the measurements

The waveforms of the friction force and the temperature are the primary results of the friction test. By means of the Labview software the waveforms are displayed on the screen of the laboratory PC, see fig.4, and the measurements values are saved to the Excel program simultaneously.
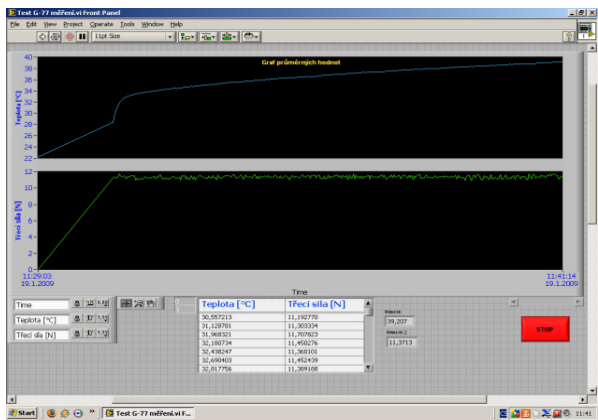
Figure 4:   Registration of the friction force and the temperature.

Because of the values saving in the Excel program it is possible to calculate the average values of the friction force. The average friction force was calculated in each of the test steps and the average values were recorded in the graph, see fig.5. The coefficient of friction was calculated from the friction force and the results are recorded in the graph, see fig.6. It is evident that the friction force and the coefficient of friction vary for both tested samples. The varying of the friction values conforms to the materials characteristic properties and to the properties of the used lubricants. The lubricants with properly selected additives are able to create the compact viscous layer between sliding surfaces, which prevents the sliding materials from being in full relative contact. Hu *et al.* [10] targeted the research on the investigation of the minerals oils and of several types of dispersed nano-particles and their effect on the coefficient of friction and on the wear of the sliding parts. They found several types of nano-particles which decrease the coefficient of friction and the wear very significantly. The similar research with other nano-particles was also done by further authors, for example Liu *et al.* [11], Batter *et al.* [12], Zhao *et al.* [13] and Wu *et al.* [14]. They mainly studied the influence of the load on the wear in the lubricated environment with different nano-particles additives.
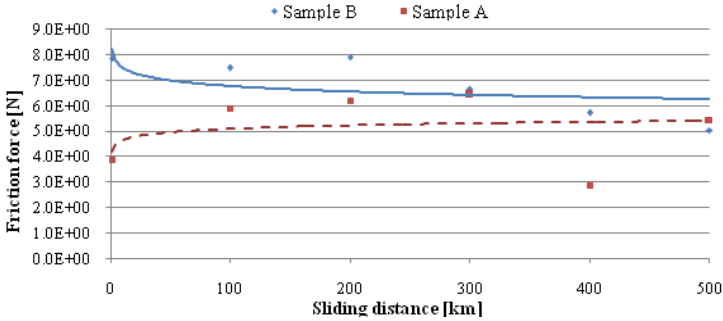
Figure 5:   Dependence of the friction force on the sliding distance.
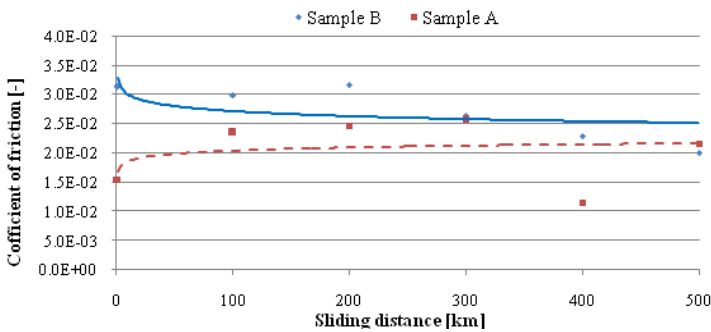
Figure 6:   Dependence of the coefficient of friction on the sliding distance.

In fig.7 the coefficient of wear of the "stanit", in fig.8 the cumulative volume loss of the "stanit" and in fig.9 the actual load of sliding materials couples are recorded. The coefficient of wear decreases markedly. In the first running-up step the coefficient of wear is the highest. Then it decreases and varies for the Sample A in the range 2,1E-06 – 1,1E-05 and for the Sample B in the range 4,5E-06 – 2,2E-05. The values of the actual load of the sliding materials couple decrease as well but the downtrend is smooth in this case. The actual load is dependent on the wear of block sample because of the increasing sliding area between the sliding materials. The larger the contact surface, the lower load presses on the sliding couple. During sliding with the sample B the cumulative wear of the stanit block is visibly higher, see fig.8. It could be ascribed first to the higher roughness of the sample B (NiCr-alloy) and second to the specific properties of NiCr-alloy material. In [15] it is mentioned that the roughness characteristics of the surface have a significant influence on the number of junctions forming, as well as on the ratio of the real area of materials contact to the apparent area of materials contact. Junctions are the points in which the actual contact occurs. The sum of the individual contact areas of these junctions is generally called the real area of the contact. Because of that, during sliding
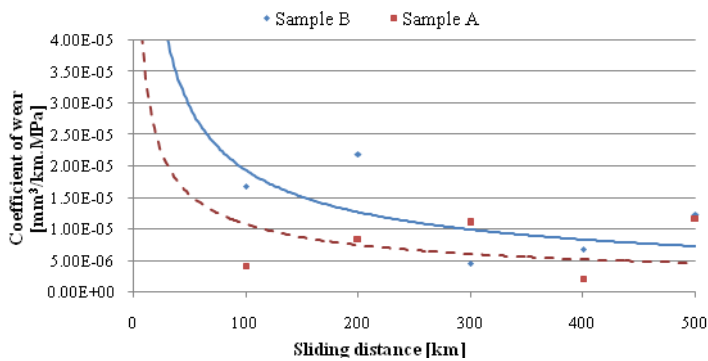
Figure 7: Coefficient of wear of the "stanit".
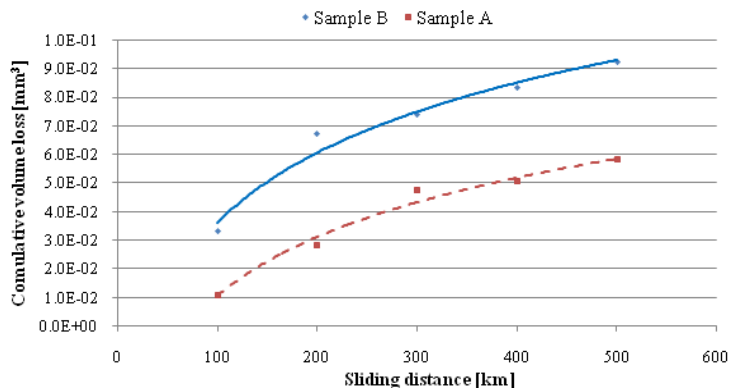
Figure 8: Cumulative volume loss of the "stanit".
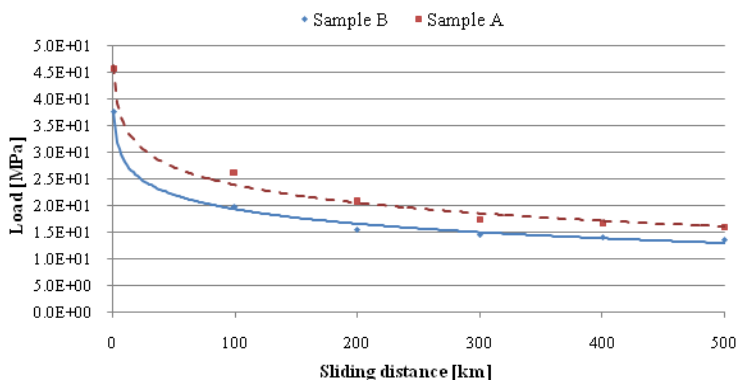
Figure 9: The actual load of the sliding material couples.
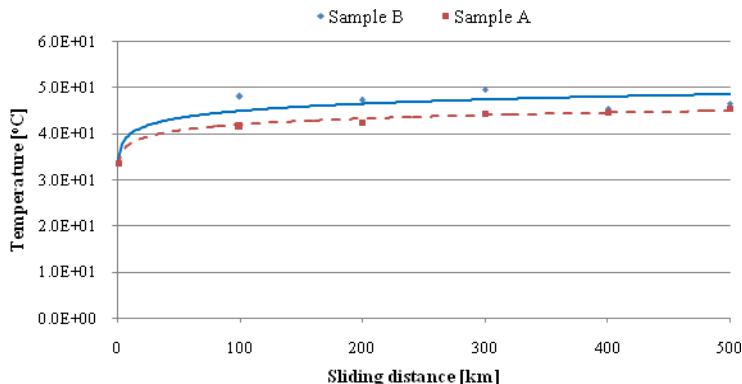
Figure 10:   The temperature of the sliding material couples.

using the "block-on-ring" method the surface disturbing of the ring and block sample due to creation of the micro-welded joins between sliding parts may occurs. The wear debris that are then formed detach from the ring and block surface and are carried by the lubricant to the sliding contact. Wear debris released in such away can act then as an abrasive medium and abrade the materials in the sliding contact. Further important factor is the temperature. During the sliding test the temperature in the materials contact increases as the results of the friction. It is possible to record the temperature using the thermocouple, which is placed close to the materials contact. More accurately, the thermocouple is placed in the slight hole in the block sample. The hole is drilled to the deep of two millimeters and it is placed approximately in one millimeter under the sliding surface. The results of the temperature registration are recorded in fig.10. The temperature was identical for both sliding parts and its increasing was very slow.

4   Conclusion

The main aim of this paper was to introduce the "block-on-ring" tribology test, which is used in ŠKODA VÝZKUM Ltd, Pilsen CZ. The apparatus for this sliding test was designed in accordance with the ASTMG-77 Standard [4]. The found-out results was showed that using the "block-on-ring" test the friction force, the dynamic coefficient of friction, the temperature in the contact area, the actual load, the coefficient of wear and the cumulative volume loss of the block sample can be recorded and measured. The friction force is recorded using the strain gauge dynamometer and using the Labview software the waveform can be displayed on the PC screen. The sliding distance and the load can be arbitrarily changed. Using the block-on-ring test it is possible to bring the laboratory condition nearer to the real practical conditions and applications because of the possibility of using any fluid lubricants, loads and test durations.

Acknowledgement

References

[1] Bhushan, B., *Introduction to tribology*, published by John Wiley and Sons, New York, pp. 207-209 and pp. 544-557, 2002

[2] Vocel, M., Dufek, V. et al., *Friction and wear of machine parts*, SNTL – publisher of technical literature, Praha, pp. 28-30, 1976

[3] ASTM G99 – 05, Standard Test Method for Wear Testing with a Pin-on-Disk Apparatus, ASTM International, West Conshohocken, PA, www.astm.org

[4] ASTM G77 – 05, Standard Test Method for Ranking Resistance of Materials to Sliding Wear Using Block-on-Ring Wear Test, ASTM International, West Conshohocken, PA, www.astm.org

[5] ASTM D5183-95(1999)e1, Standard Test Method for Determination of the Coefficient of Friction of Lubricants Using the Four-Ball Wear Test Machine, ASTM International, West Conshohocken, PA, www.astm.org

[6] ASTM D4172-94(2004), Standard Test Method for Wear Preventive Characteristics of Lubricating Fluid (Four-Ball Method), ASTM International, West Conshohocken, PA, www.astm.org

[7] Kašparová, M, *Evaluation of friction properties of steel materials and of thermal sprayed coatings together with stanit tin-babbitt counterpart*, internal report of ŠKODA VÝZKUM Ltd., 2006

[8] Kašparová, M, *Methodology of materials friction properties measured on VRS-3 apparatus using "Block-on-Ring" method*, internal report of ŠKODA VÝZKUM Ltd., 2008

[9] Zahálka, F., *Apparatus for evaluation of sliding properties*, internal report of ŠKODA VÝZKUM Ltd., 2005

[10] Hu, Z.S., Dong, J.X., Chen, G.X. & He, J.Z., Preparation and tribological properties of nanoparticle lanthanum borate, *Wear*, **243(1-2)**, pp. 43-47, 2000

[11] Liu, G., Li, X., Lu, N. & Fan, R., Enhancing AW/EP property of lubricant oil by adding nano Al/Sn particles, *Tribology Letters*, **18(1)**, pp. 85-90, 2004

[12] Battez, A.H., Rico, J.E.F., Arias, A.N., Rodriguez, J.L.V., Rodriguez, R.Ch. & Fenandez, J.M.D., The tribological behavior of ZnO nanoparticles as an additive to PAO6, *Wear*, **261(3-4)**, pp. 256-263, 2006

[13] Zhao, Y., Zhang, Z. & Dank, H., A simple way to prepare bismuth nanoparticles, *Materials Letters*, **58(5)**, pp. 790-793, 2004

[14] Wu, Y.Y., Tsui, W.C. & Liu, T.C., Experimental analysis of tribological properties of lubricating oils with nanoparticle additives, *Wear*, **262(7-8)**, pp. 819-825, 2007

[15] Bayer, R.G, Mechanical wear prediction and prevention, published by Marcel Dekker, INC., New York, pp. 11-20, 1994

Section 5
Indentation and hardness

This page intentionally left blank

Identification of elasto-viscoplastic material properties from indentation testing using an inverse method

G. Rauchs & J. Bardon
Laboratoire de Technologies Industrielles,
Centre de Recherche Public Henri Tudor, Grand Duchy of Luxembourg

Abstract

A combination of finite element modelling with gradient-based numerical optimization is used to determine the material parameters of a mechanical constitutive law from indentation testing by minimizing a cost function, quantifying the difference between load versus displacement-into-surface curves obtained from experiments and from finite element modelling. The required gradients of the cost function are calculated through a sensitivity analysis based on the direct differentiation method. Approximate correlation or cosine matrices will be calculated for assessing parameter correlation and used for designing load histories, which improve the parameter correlation in indentation testing. Finally, experimental indentation curves from metallic materials will be analyzed using the inverse method. The impact on material parameter identification of indenter tip size and of the incorporation of residual imprint data, obtained by white light interferometry, into the objective function will be monitored.
Keywords: indentation testing, finite element modelling, numerical optimization.

1   Introduction

Depth-sensing indentation and nanoindentation testing is being used for determining some material properties, such as Young's modulus and hardness following methods developed by Oliver and Pharr [1]. A rigid indenter is pushed into a specimen and the displacement-into-surface is recorded as a function of the applied load. Computational inverse methods have been developed for material parameter identification, either based on neural networks (Huber and

Tsakmakis [2]) multiple response surface analysis (Hamasaki *et al.* [3]) or on numerical optimization (Constantinescu and Tardieu [4], Bolzon *et al.* [5], Rauchs [6]), which offer the possibility to determine material parameters of mechanical constitutive laws in addition to those found through standard experimental procedures. The inverse methods may be used in combination with the finite element method for determining material parameters, both for the case of simple tests, such as uniaxial tension (Mahnken and Stein [7]), and especially in the case of highly inhomogeneous, multiaxial stress fields, such as the indentation test or in the case of local damaging of the specimen. In optimization-based methods, the material parameters are determined by minimizing an objective function, quantifying the difference between load versus displacement-into-surface curves obtained from experiments and from finite element modelling. Most often, gradient-based optimization algorithms are used because they offer the potential for fast parameter identification, and the required gradients of the cost function can easily be calculated in a fast and reliable way through a sensitivity analysis based on either direct differentiation or adjoint-state methods. Some material parameters are difficult to determine, such as viscosity parameters (Constantinescu and Tardieu [4], Klötzer *et al.* [8]), or the separation of isotropic and kinematic hardening (Huber and Tsakmakis [2]) and the reliability of the results is poor because of strong parameter correlation. This stems from the fact that in indentation tests, some physical phenomena inherent to the constitutive laws may not affect the experimental curves in a significant or distinguishable way, as shown in Chen *et al.* [9]. In addition to this, the experimental data resulting from indentation testing, i.e. load and displacement-into-surface, are integrals of stress and strain, respectively, whereas the material constitutive law is based directly on stress and strain. In the present paper, the spherical indentation test is modelled by an axisymmetric finite element model for obtaining the objective function and the sensitivities with respect to the material parameters necessary for the material parameter identification algorithm. After presenting the material constitutive law, the computational framework and the sensitivity analysis based on direct differentiation, the investigation of material parameters of the aluminium alloy Dural will be presented, and the influence of experimental residual imprint measurements on parameter identification assessed.

2   Elasto-viscoplastic law

In the following, tensors, matrices and vectors are characterized by boldface letters, unless index notation is required for a clearer representation. A neo-Hookean hyperelastic law is used, which relates the Kirchhoff stress $\mathbf{S}$ to the left Cauchy-Green elastic deformation tensor $\mathbf{B}_e$, defined through the elastic deformation gradient $\mathbf{F}_e$, obtained from the standard multiplicative elastic-plastic decomposition of the deformation tensor $\mathbf{F}$. The hyperelastic constitutive law, with the elastic Lamé constants ν and λ, the determinant of the elastic deformation gradient J and the second order identity tensor $\mathbf{I}$ reads

$$\mathbf{S} = \mu(\mathbf{B}_e - \mathbf{I}) + \lambda \ln J \mathbf{I}. \tag{1}$$

Plastic hardening with an associative flow rule is considered, including non-linear isotropic and nonlinear kinematic hardening. The evolution of the yield limit K_y is described through a non-linear isotropic hardening law, with

$$K^y = \sqrt{\frac{2}{3}}\left(Y + R\left(1 - \exp(-\beta s)\right)\right), \tag{2}$$

where s is the plastic arc length, Y is the initial uniaxial yield stress, and R and β are the nonlinear isotropic hardening parameters. The back-stress, $\boldsymbol{\alpha}$, and the plastic strain, $\boldsymbol{\varepsilon}_p$, are related through the kinematic hardening evolution using the Armstrong-Frederick law with the non-linear kinematic hardening parameters H_{kin} and b.

$$\dot{\boldsymbol{\alpha}} = \sqrt{\frac{2}{3}}H_{kin}b\dot{\boldsymbol{\varepsilon}}_p - b\dot{s}\boldsymbol{\alpha}. \tag{3}$$

In order to include viscoplasticity into the constitutive equations in a simple and efficient manner, the yield condition differs from the consistency condition. The yield condition f reads, with the deviatoric projection operator $\mathbf{P}$,

$$f = \left\|\mathbf{P} : (\mathbf{S} - \boldsymbol{\alpha})\right\| - K^y, \begin{cases} f < 0, & \text{elastic} \\ f \geq 0, & \text{viscoplastic} \end{cases}, \tag{4}$$

For viscoplasticity, the consistency condition reads

$$f' = \left\|\mathbf{P} : (\mathbf{S} - \boldsymbol{\alpha})\right\| - K^y - \sqrt{\frac{2}{3}}(\dot{s}\eta)^{\frac{1}{m}}, \tag{5}$$

where η is the viscosity and m is the viscosity exponent.

3 Stress update equations

In the following, the state at the beginning of the time increment is characterized by the prefix [0], the state at the end of the increment by [1]. The time integration of the constitutive equation is performed through an operator split: an elastic predictor step followed by an inelastic corrector step. In the elastic predictor step, no inelastic deformation takes place and the deformation gradient $\mathbf{F}$ is modified by $\Delta\mathbf{F}$, whereas in the inelastic corrector step the deformation gradient $\mathbf{F}$ remains unchanged and inelastic deformation takes place. The elastic predictor step gives the trial state, labelled by the prefix [Tr],

$$^{Tr}\mathbf{B}_e = \Delta\mathbf{F}\,^0\mathbf{B}_e\Delta\mathbf{F}^T, \tag{6}$$

with

$$\Delta\mathbf{F} = {}^1\mathbf{F}^0\mathbf{F}^{-1}. \tag{7}$$

The predictor of the back-stress of the elasto-viscoplastic constitutive law is calculated similarly to eqn (6). The inelastic corrector leads to the stress and internal variable update equations used in the direct deformation finite element code. In order to simplify the notations, we introduce a generalized directional derivative, similar to a Gateaux-differential, which designates derivatives with respect to time or with respect to a material parameter κ. Such a differential of a tensor $\mathbf{X}$ is written as

$$\left[\mathbf{X}\right]^{\Diamond} \tag{8}$$

The linearization of the Kirchhoff stress at the end of the increment gives a relationship in the following form

$$\left[{}^{1}\mathbf{S}\right]^{\Diamond} = \partial^{1}\mathbf{S} + \mathbf{D}^{mat} : \left[\frac{\partial \Delta \mathbf{u}}{\partial^{1}\mathbf{x}}\right]^{\Diamond}, \tag{9}$$

where $\mathbf{D}^{mat}$ is the consistent constitutive tensor, derived from the stress update equations. The first term on the right hand side regroups the explicit sensitivities of the material parameter and the sensitivities of the stress at the beginning of the increment. It is important to notice that this term is only active in the sensitivity analysis and vanishes for the linearization used in the Newton-Raphson iteration, which is a linearization with respect to the displacement increment, $\Delta \mathbf{u}$, upon which the state variables at the increment start do not depend.

4 Sensitivity analysis

Sensitivity analysis is performed using the direct differentiation method, which is presented in Rauchs [6], for example, because of its conceptual simplicity. Starting from the basic equilibrium equation of non-linear finite element analysis and using the element shape function N^{A}, the current position vector ${}^{1}\mathbf{x}$ and integrating over the body in the current configuration, the discretized form is obtained:

$$\int_{\Omega} \frac{\partial N^{A}}{\partial^{1}\mathbf{x}} {}^{1}\boldsymbol{\sigma} d\Omega - \mathbf{f}^{A,ext} - \mathbf{f}^{A,con} = 0, \tag{10}$$

where $\mathbf{f}^{A,ext}$ is the external nodal load and $\mathbf{f}^{A,con}$ is the contact nodal load at nodes on the contact boundary. The derivative of eqn (10) with respect to a material parameter κ yields

$$\left[\int_{\Omega} \frac{\partial N^{A}}{\partial^{1}\mathbf{x}} {}^{1}\boldsymbol{\sigma} d\Omega\right]^{\Diamond} - \left[\mathbf{f}^{A,con}\right]^{\Diamond} = 0. \tag{11}$$

In case of conservative external nodal loads, the sensitivity of the second term in eqn (10) vanishes. Replacing the Cauchy stress, $\boldsymbol{\sigma}$, by the Kirchhoff stress, $\mathbf{S}$, using the sensitivity of the Kirchhoff stress specific to the constitutive law,

eqn (9), and performing some lengthy mathematical developments, which can be found in Rauchs [6], for example, eqn (11) becomes

$$
\int_\Omega \frac{\partial N^A}{\partial^1 \mathbf{x}} \left(-\left[\frac{\partial \Delta \mathbf{u}}{\partial^1 \mathbf{x}} \right]^\Diamond \frac{{}^1\mathbf{S}}{{}^1 J} + \mathbf{D}^{mat} : \left[\frac{\partial \Delta \mathbf{u}}{\partial^1 \mathbf{x}} \right]^\Diamond \right) d\Omega
$$
$$
+ \int_\Omega \frac{\partial N^A}{\partial^1 \mathbf{x}} \left(-\left[{}^0\mathbf{F} \right]^\Diamond {}^1\mathbf{F}^{-1\ 1}\mathbf{S} + \partial^1 \mathbf{S} \right) d\Omega + \left[\mathbf{f}^{A,con} \right]^\Diamond = 0 \tag{12}
$$

where the first integral contains terms depending on the sensitivity of the displacement increment and the second integral contains only terms known at the beginning of the increment. With the sensitivity of the displacement gradient interpolated through

$$
\left[\frac{\partial \Delta u_m}{\partial^1 x_n} \right]^\Diamond = \frac{\partial N^B}{\partial^1 x_n} \left[\Delta u_m^B \right]^\Diamond, \tag{13}
$$

the two integrals can be further condensed into

$$
\left(\mathbf{K}^{AB} + \mathbf{K}^{AB,con} \right) \left[\Delta \mathbf{u}^B \right]^\Diamond + {}^\kappa \mathbf{V}^A = 0, \tag{14}
$$

with

$$
K_{im}^{AB} = \int_\Omega \frac{\partial N^A}{\partial^1 x_j} \left(D_{ijmn}^{mat} - I_{mj} \frac{{}^1 S_{in}}{{}^1 J} \right) \frac{\partial N^B}{\partial^1 x_n} d\Omega \tag{15}
$$

and

$$
{}^\kappa \mathbf{V}^A = \int_\Omega \frac{\partial N^A}{\partial^1 \mathbf{x}} \left(-\left[{}^0\mathbf{F} \right]^\Diamond {}^1\mathbf{F}^{-1\ 1}\mathbf{S} + \partial^1 \mathbf{S} \right) d\Omega + \mathbf{K}^{AB,con} \left[{}^0\mathbf{x} \right]^\Diamond, \tag{16}
$$

in which repeated capital indices stand for the summation over all the nodes coupled to node A through solid continuum elements. $\mathbf{K}^{AB,con}$ is the contact stiffness matrix. In the frictionless case considered here, the contact force sensitivity depends on geometric quantities only. It should be noted that the differential of ${}^0\mathbf{x}$ is known from the previous increment or the boundary conditions, respectively. Therefore, ${}^\kappa \mathbf{V}^A$ contains only known entities and can be calculated explicitly. By summing up eqns (15) and (16) over all connected nodes, the global stiffness matrix and pseudo-load vector can be constructed.

After resolving the sensitivities of the displacement increment, $\Delta \mathbf{u}$, the update of the sensitivities of the state variables is done in a postprocessing step. As the use of Oldroyd rates in the constitutive formulation gives a compute-efficient fully consistent linearization of the stress update equations, the same stiffness matrices may be used in direct deformation modelling and in the direct differentiation sensitivity analysis. Therefore, the latter one is performed at the end of each time increment, after convergence of the non-linear state variable update through the Newton-Raphson iteration. In the direct differentiation calculation, each increment is treated in three stages:
1. Calculation of the pseudo-stiffness matrix and pseudo-load vector from eqns. (14) and (16).

2. Solution of eqn (14), which is a linear equation, for each material parameter to obtain the unknown displacement increment derivatives.

3. Back substitution of the displacement increment derivatives to obtain the updated derivatives of geometry and the state variables at the end of the increment.

5   Numerical optimization procedure

For the indentation test, the objective function to be minimized by a numerical optimization algorithm is made up of the difference between the experimental and modelled displacement-into-surface, h and h', respectively, which are a function of the independent load P:

$$\Xi = \frac{1}{2} \sum_{k=1}^{N} \left[h\left(P^k\right) - h'\left(P^k\right) \right]^2 . \tag{17}$$

A gradient-based optimization algorithm requires the derivative of the objective function with respect to a material parameter κ, given as

$$\frac{\partial \Xi}{\partial \kappa_i} = \sum_{k=1}^{N} \left[h\left(P^k\right) - h'\left(P^k\right) \right] \frac{\partial h\left(P^k\right)}{\partial \kappa_i} . \tag{18}$$

The Hessian matrix is then

$$\frac{\partial^2 \Xi}{\partial \kappa_i \partial \kappa_j} = \sum_{k=1}^{N} \left[\frac{\partial h\left(P^k\right)}{\partial \kappa_i} \frac{\partial h\left(P^k\right)}{\partial \kappa_j} + \left[h\left(P^k\right) - h'\left(P^k\right) \right] \frac{\partial^2 h\left(P^k\right)}{\partial \kappa_i \partial \kappa_j} \right] . \tag{19}$$

As the second term of the sum is known to adversely affect convergence, this term is neglected, and the approximated Hessian labelled as H'. The minimization algorithm iteratively calculates the material parameters using standard Gauss-Newton algorithm. Additional experimental data can be included through mapping the residual imprint remaining after complete load removal, Bolzon et al. [5]. The objective function will be extended by a term comprising the differences of experimental and modelled imprint. For quantifying the residual imprint, the total vertical displacement, h^{res} (r^l) of the contact surface at a set of M fixed radial locations r^l, with respect to a chosen reference point, for example the imprint centre, called r^0, is used, and an aggregate objective function takes the form:

$$\Xi' = \frac{1}{N} \Xi + \frac{1}{2M} \sum_{k=1}^{M} \left[\left(h'_{res}\left(r^l\right) - h'_{res}\left(r^0\right) \right) - \left(h_{res}\left(r^l\right) - h_{res}\left(r^0\right) \right) \right]^2 . \tag{20}$$

In practice, the state variable history is calculated by solving the direct deformation problem using the finite element method. Subsequently, the derivative of h is calculated by linear update, as described above. The objective function minimization is performed through the overall optimization loop. In the present study, the system response considered is the displacement-into-surface, which has the same order of magnitude as the residual imprint. Therefore, no scaling factor needs to be introduced in eqn (20), apart from the scaling with respect to the number of data available for each term, N and M.

From uniaxial tension/compression tests for material parameter identification of elasto-plastic materials in Mahnken and Stein [7], it was found that the compressive cycle is necessary for uniquely determining isotropic and kinematic hardening parameters. In the absence of a compressive cycle with reverse plastic flow, it is not possible to separate kinematic from isotropic hardening. In case the Hessian matrix is available, correlation or cosine matrices can be calculated and used to visualize the material parameter correlation. The cosine matrix indicates if the different sensitivities are co-linear. Even if the approximated Hessian matrix in eqn (19) does not include terms with the second order derivatives, it can give an indication of the parameter correlation. In fact, H' is equivalent to the Hessian matrix if the objective function is exactly zero and as such it should give a sufficient information about parameter correlation in indentation testing. The cosine matrix of the Hessian matrix in eqn (19) is defined according to Forestier *et al.* [10], without summation over double indices, as

$$c_{ij} = \frac{H'_{ij}}{\sqrt{H'_{ii} H'_{jj}}}.$$

(21)

The total correlation between material parameters is quantified by the correlation factor, k, defined as

$$k = \sqrt[72]{\prod_{i,j=1, i \neq j}^{9} c_{ij}}.$$

(22)

6   Finite element model

The finite element model of the indentation test consists of an axisymmetric model discretizing both the indenter and the specimen as flexible bodies. The spherical indenter has a tip radius of 5 μm and the overall shape is a cone with an opening angle of 60 degrees. Quadratic elements with displacement degrees of freedom have been used. Contact constraints are fulfilled by using C^2-continuous quadratic node-to-segment contact elements with a modified C^2-continuous logarithmic barrier potential according to Kloosterman [11]. Instead of an augmented Lagrangian contact algorithm, a similar algorithm with intermediate loops has been used, where the penalty parameter is increased from one intermediate loop to the next. The motivation is to have an explicit form of the contact tractions, unlike the augmented Lagrangian algorithm, where the contact tractions are calculated iteratively in the intermediate loops, which then have to be performed in the sensitivity analysis as well. At the end of each intermediate loop, an extrapolation according to Dussault [12] is performed in order to improve convergence. A line search method is included into the Newton-Raphson iteration loop in order to improve overall convergence.

The finite element calculations are performed under load control, because most nanoindenters operate in this mode and the noise on load is usually smaller than that on the displacement measurements. Computations of the indentation test showed that at indentation loads, mesh locking becomes an issue. This

problem was overcome by the use of nine-noded fully integrated quadratic elements. However, it should be noticed that such elements require larger computing times.

7 Results

In the first place, the correlation factor, k, has been calculated to assess parameter correlation in parameter identification based on nanoindentation testing. It was found that a hold period is crucial for reducing the parameter coupling between viscosity parameters on the one hand and elastic and plastic material parameters on the other hand, reducing k from 0.98 to 0.66 for a single load cycle. Inclusion of residual imprint data, according to eqn (20), provided some decoupling between the elastic parameter and the plastic parameters, reducing k to 0.52. However, the parameters within these three groups of material parameters, i.e. elastic, plastic and viscous, remained nearly fully coupled. It was somewhat striking to note that with the hysteresis produced during reloading in a second load cycle, no uncoupling between isotropic and kinematic hardening parameters was monitored, whereas in Huber and Tsakmakis [2], this hysteresis can be used successfully for parameter identification in neural network-based parameter identification.

In a last stage, material parameter identification was performed using true experimental nanoindentation curves. The material under investigation was an aluminium alloy, Dural, where unfortunately only a limited number of material parameters from tensile testing is available. Three indenter tip radii where used: 5μm, 10 μm and 50 μm, and the indenters are labelled R5, R10 and R50, respectively. It should be noted that these are nominal radii. In the finite element models, measured radii have been used.

Table 1:   Material parameters identified from first load cycle.

Parameter	R5	R5 err	R10	R10 err	R50	R50 err
E (MPa)	60462	3.8%	72634	4.0%	80860	3.2%
ν (-)	0.37	9.7%	0.24	11.9%	0.40	1.7%
Y (MPa)	228	12.6%	77	67.3%	745	6.6%
R (MPa)	143	24.7%	673	17.0%	189	79.2%
β (-)	28.0	5.2%	7.1	9.4%	7.8	49.0%
H_{kin} (MPa)	169	5.0%	479	14.3%	741	120.2%
b (-)	31.2	15.4%	7.4	9.9%	8.5	40.1%
η (MPa s)$^{1/m}$	1.6E+08	146.7%	7.0E+06	67.3%	1.9E+07	39.6%
m (-)	4.3	15.6%	3.2	6.8%	2.0	12.6%
Σ (MPa)	624	1.2%	1468	11.8%	2045	70.4%

In table 1, the material parameters identified from input data made up of the first load cycle only are given. A comparison with the only reliable material parameter available, the Young's modulus of 73000 MPa, shows that the indenters R5 and R50 give erroneous results whereas indenter R10 gives a very

accurate value of the Young's modulus. Residual imprint measurements indicate that the shapes of the indenters R5 and R50 significantly deviate from the assumed spherical shape. The Poisson's ratio, assumed to be around 0.3 for metals, is also determined quite reliably. However, the indenter R50 gives poor values for the plastic material parameters, as even the yield stress Y lies above the strength of Dural, which is approximately 500 MPa. It can be realized that Σ, the weighted sum of Y, R and H_{kin}, representing the maximum hardening stress, is identified with very little scatter. The hardening exponents β and b are high for all indenters, especially for R5, and will produce nearly full hardening after only small amounts of plastic deformation. The viscosity η exhibits large scatter and is therefore unreliable. In fact, as viscosity plays a role in indentation testing because of the high compressive stresses occurring in indentation testing, the viscosity parameter should be considered as no more than numerical parameters used for introducing the right amount of creep deformation found in indentation testing, but irrelevant in room temperature applications.

Table 2:   Material parameters identified from the two-cycled load history.

Parameter	R5	R5 err	R10	R10 err	R50	R50 err
E (MPa)	58593	2.9%	72281	3.4%	70812	1.1%
ν (-)	0.38	28.1%	0.25	14.8%	0.49	0.3%
Y (MPa)	325	7.7%	66	58.9%	688	6.2%
R (MPa)	113	14.6%	739	1.7%	33	132.2%
β (-)	15.6	19.8%	6.7	27.4%	5.6	53.7%
H_{kin} (MPa)	126	22.8%	488	6.6%	52	80.5%
b (-)	18.8	28.5%	7.4	21.0%	5.2	52.2%
η (MPa s)$^{1/m}$	3.3E+07	88.4%	9.7E+06	37.8%	7.6E+04	77.8%
m (-)	4.3	12.8%	3.1	6.1%	4.0	64.7%
Σ (MPa)	627	2.7%	1536	5.4%	799	7.7%

Table 3:   Material parameters identified from the two-cycled indentation test, with and without residual imprint data, for nominal tip radius of 10 μm.

Parameter	R10i	R10i err	R10	R10 err
E (MPa)	45924	7.5%	72281	3.4%
ν (-)	0.39	20.0%	0.25	14.8%
Y (MPa)	507	2.6%	66	58.9%
R (MPa)	439	23.7%	739	1.7%
β (-)	1.1	7.2%	6.7	27.4%
H_{kin} (MPa)	400	31.7%	488	6.6%
b (-)	1.6	24.5%	7.4	21.0%
η (MPa s)$^{1/m}$	1.7E+06	56.7%	9.7E+06	37.8%
m (-)	6.8	25.5%	3.1	6.1%
Σ (MPa)	1546	10.0%	1536	5.4%
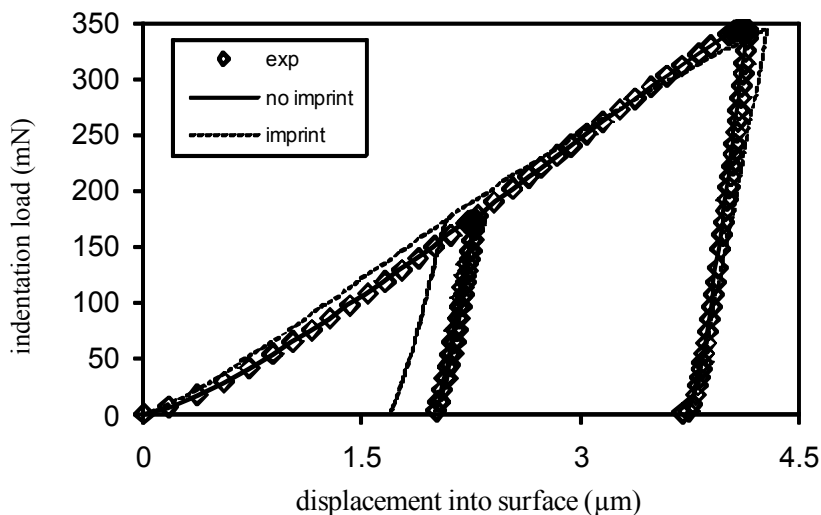
Figure 1:   Indentation curves for indenter tip radius of 10 μm: experimental (symbols), computed from parameters identified from load curves only (solid line) and from load curve and imprint data (dotted line).

In table 2, material parameters identified from the full load history comprising two consecutive load cycles, with the second peak load being twice the first load peak, are shown. No major improvement over the parameters presented in table 1 are visible, with the largest change being found in the viscosity. A more prominent change in material parameters takes place if residual imprint data are included into the objective function according to eqn (20), see table 3. Here, one can see that on the one hand, the Young's modulus deteriorates, whereas the yield stress increases. The hardening exponents β and b are also much lower. It can be seen in Fig.1 that the indentation curve obtained from the parameters identified with residual imprint data does not fit well with the experimental indentation curves, unlike the indentation curves obtained from indentation curve data only.

The situation is completely different for the modelled residual imprint, where pile-up takes place for experimental input including residual imprint measurements, whereas sink-in occurs in the absence of imprint data, which is in contradiction to the experimental residual imprint data, as depicted in Fig.2. It is known that the ratio between yield stress and Young's modulus determines whether pile-up or sink-in occurs, which is a fundamental aspect of each specific material. This is a clear indication that the yield stress found without imprint data is much too low, the value determined with imprint data seems much more appropriate from the point of view of pile-up. However, this value lies above the strength given by the manufacturer. It should be noted that the residual imprint data of the centre of the imprint have been removed from the objective function

because they do not fit the measured residual displacement into surface from the indentation curve. The absence of data points between 3 and 7 µm in radial direction stems from the fact that white light interferometry does only yield data for surfaces whose inclination with respect to the horizontal lies below a magnification-dependent threshold, 25° in our case, leading to a large blind spot in case of deep imprints. It has to be said that the residual imprint measurements are highly affected by experimental scatter, either caused by surface defects like scratches, or by polycrystalline anisotropic deformation taking place.
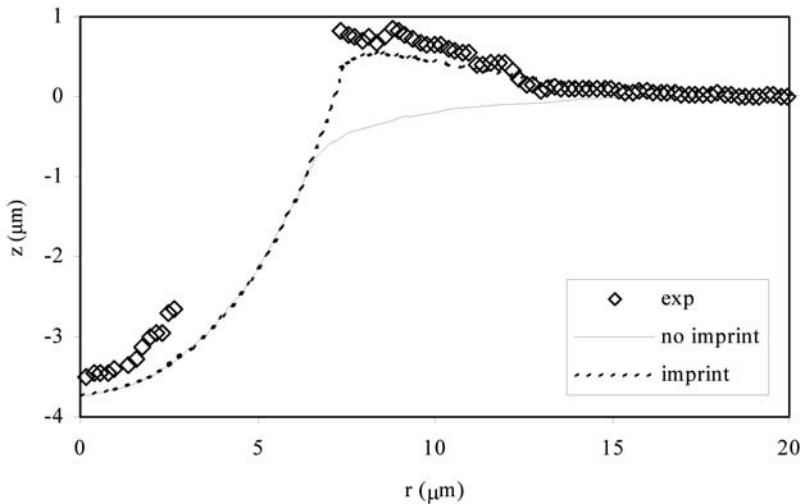
Figure 2:   Residual imprint profiles for indenter tip radius of 10 µm: experimental (symbols), computed from parameters identified from load curves only (solid line) and from load curve and imprint data (dotted line).

To resume, the identification of material parameters from nanoindentation testing coupled to an inverse method is not very reliable in the current form, with the exception of the Young's modulus, where quite reliable results with very low scatter may be obtained. Progress has to be made for determined the plastic material parameters, and a more efficient use of residual imprint data may be required for achieving more reliable results. Another issue is the influence of surface roughness on the indentation curves, as stated in Klötzer *et al.* [8], which has a significant impact on the initial part of the indentation curve, because surface asperities are less stiff than the modelled, perfectly flat specimen surface.

References

[1]   Oliver, W.C. & Pharr, G.M., An improved technique for determining hardness and elastic modulus using load and displacement sensing indentation experiments, *J. Mater. Res.* 7, pp. 1564-1583, 1992.

[2]   Huber, N. & Tsakmakis, Ch., Determination of constitutive properties from spherical indentation data using neural networks. Part II: Plasticity with nonlinear isotropic and kinematic hardening. *J. Mech. Phys. Solids*, **47**, pp. 1589–1607, 1999.

[3]   Hamasaki, H., Toropov, V.V., Kazuhiro, K. & Yoshida F., Identification of Viscoplastic Properties for Lead-Free Solder by Microindentation Experiments, FE Simulation and Optimization, *J. Japan Soc. Tech. Plast.* **46**, pp. 397-401, 2005.

[4]   Constantinescu, A. & Tardieu, N., On the identification of elastoviscoplastic constitutive laws from indentation tests. *Inverse Problems in Engineering*, **9**, pp. pp. 19–44, 2001.

[5]   Bolzon, G., Maier, G. & Panico, M., Material model calibration by indentation, imprint mapping and inverse analysis. *Int. J. Sol. Struct.*, **41**, pp. 2957–2975, 2004.

[6]   Rauchs, G., Optimization-based material parameter identification in indentation testing for finite strain elasto-plasticity. *ZAMM*, **86**, pp. 539–562, 2006.

[7]   Mahnken, R. & Stein, E., Parameter identification for viscoplastic models based on analytical derivatives of a least–squares functional and stability investigations. *Int. J. Plasticity*, **12**, pp. 451–479, 1996.

[8]   Klötzer, D., Ullner, Ch., Tyulyukovskiy, E. & Huber N., Identification of viscoplastic material parameters from spherical indentation data. Part II: Experimental validation of the method, *J. Mater. Res.* **21**, pp. 677-684, 2006.

[9]   Chen, X., Ogasawara, N., Zhao, M. & N. Chiba, N., On the uniqueness of measuring elastoplastic properties from indentation: The indistinguishable mystical materials. *J. Mech. Phys. Solids*, **55**, pp. 1618–1660, 2007.

[10] Forestier, R., Chastel, Y. & Massoni, E., 3d inverse analysis model using semi–analytic differentiation for mechanical parameter estimation. *Inverse Problems in Eng.*, **11**, pp. 255–271, 2003.

[11] Kloosterman, G., *Contact Methods in Finite Element Methods*. PhD thesis, University of Twente, 2002.

[12] Dussault, J.-P., Numerical stability and efficiency of penalty algorithms. *SIAM J. Num. Anal.*, **32**, pp. 296–317, 1995.

Surface ruggedness processing of cylindrical Cu-Zn wire with wet blasting

M. Yamashita[1], J. Fukuoka[1], K. Yamashita[1], Y. Fukuzawa[1]
& M. Ogata[2]
[1]Department of Mechanical Engineering,
Nagaoka University of Technology, Japan
[2]Macoho Co., Ltd, Japan

Abstract

To reduce the machining cost and energy, the higher removal rate has been required on the wire cut electrical discharge machining (WEDM) method. Some experimental trials have been applied to improve the machining properties on the WEDM using the coated and/or the rugged wire materials. As the appropriate technology has not been established on the rugged wire machining method, the expected results have not been obtained yet. In this paper, we propose a new method of the wet blasting technology that was designed and made by ourselves. In this method the ZrO_2 abrasives were exhausted from the three nozzles with the compressed water jet on the feeding wire surface. The cylindrical Cu-Zn wire surface was deformed and the rugged shapes depended on the compressed air pressure, the abrasive size and shape, and the feeding speed of wire electrode material. The relation between the wet blasting condition and the formed ruggedness shape was discussed. In addition, the mechanical properties of the rugged wire were investigated by the tensile test.
Keywords: wire cut electrical discharge machining, wet blast, cemented carbide.

1   Introduction

On the wire electrical discharge machining (WEDM) method, to obtain better discharge machining properties of removal rate and surface roughness, many experimental trials have been carried out. Some researcher reported that when the discharge machining was carried out with the rough surface of the workpiece or tool electrode, the electrical discharge delay time became shorter than the

smooth surface [1]. The removal rate could be improved within a few percent [2–4]. In these reports, the effect was discussed with the difference of surface roughness level. Recently, we have succeeded in making the new machining machine of constant rugged surface on the wire tool electrode. This is called the wet blasting method.

The electric discharge machining characteristic improves by using the wire that gives the ruggedness by the wet blasting method [5]. The reason is that it becomes difficult for the wire to be broken, and the electrical discharge machining by a high current becomes possible. On the WEDM, two dimensional complex arbitrary shapes were made by the controlled system that was attached onto the machine with the feeding wire. The discharged point on the wire surface moved with the constant speed and dispersion accordance with the machining direction.

To obtain the precise shape, the vibration motion must be avoided. The wire was pulled with a moderate tensile force between the tension roller. Considering the used condition of wire on the WEDM, the rugged creator must be impressed on the whole surface constantly and continuously. The mechanical properties of rugged wire must be bigger than the pulled force. When the discharge occurred at a high current condition, the wire was melted at the local region and elongated to breaking point. The authors have reported before that the broken limit current value expanded bigger zone using the rugged wire [6].

In this paper, to clarify the effects of the wet blasting method as a new machining technology of rugged surface on Cu-Zn wire, the machining condition and the mechanical strength was investigated with a variation of experimental factors.
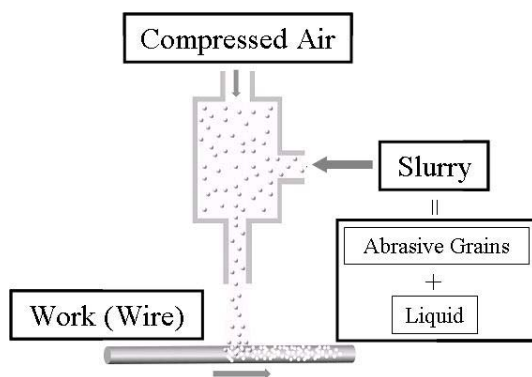
Figure 1:   Wet blasting method.

2   Experimental method

Figure 1 shows the outline of the wet blasting method. It is composed of the slurry box in which the abrasives and the liquid was mixed, air compressor and jet nozzle. The mixed abrasives and liquid was exhausted by the compressor air

to the jet nozzle. Figure 2 shows the outline of the wet blasting device used in this research. To deform the all wire surface constant condition the jet nozzles were arranged every 120° as shown in Fig. 3. The ruggedness could be detailed on all the wire surface area as shown in Fig. 4. The machining conditions were controlled by the following factors: (1) the compressed air pressure, (2) the size and shape of abrasive, and abrasive density, and (3) the wire feed speed. It is considered that the ruggedness and distribution of the deformed crater would be controlled by these experimental factors. Table 1 shows the wet blasting conditions. In this experiment, ZrO_2 powder was selected as the abrasive. The abrasives were filtered to the size region of 60 to 130 μm. As the Cu-Zn wire of ϕ 0.2 was used normally on the WEDM method, it was selected to the workpiece.
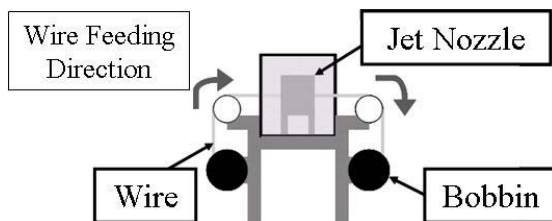
Figure 2:   Schematic drawing of the wet blasting device.
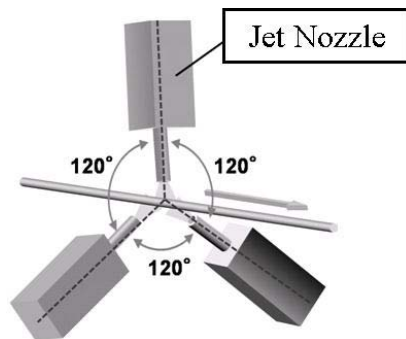
Figure 3:   Triangularly arranged jet nozzles.
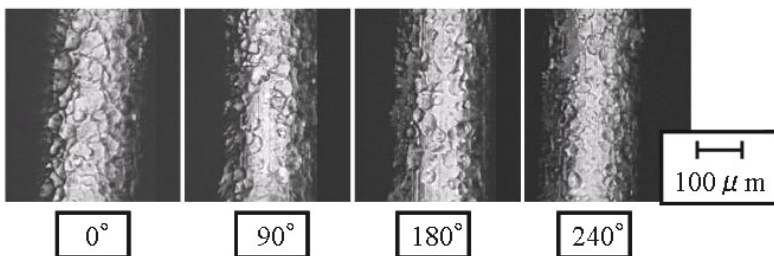
Figure 4:   The images of all ruggedness wire surface.

3 Results and discussions

3.1 Influence of the wet blasting condition on the rugged surface shape

3.1.1 Wire feed speed
The effects of the feeding speed of wire electrode on the rugged shape of the wire were investigated. The wet blasting condition used for this experiment is shown in Table 1. The rugged surface shape of the wire was observed with the light microscope. The results are shown in Fig. 5.

The ruggedness of the deformed area by abrasive decreased with increasing the feeding speed of wire electrode material. On a fast feeding speed condition, the rugged crater could not cover the entire deformed surface. It indicated that the exhausted ZrO_2 abrasive could not collide with the feeding wire surface under high speed motion.

3.1.2 Compressed air pressure
To confirm the effects of the compressed air pressure on machining the rugged crater shape, the experiment was carried out using the condition of Table 2. The compressed air pressure changed from 0.1 to 0.4 MPa under the wire feeding speed of 250mm/min. The observation results using the microscope on the rugged surface are shown in Fig. 6. The indentation height was estimated with the focus depth method. The difference depth from the bottom to the raised part of the indentation was measured, show in Fig. 7. Figure 8 shows the measurement results on each compressed air pressure.

On the lower pressure condition of 0.1MPa, a few shallow craters could be observed. On the other hand, with higher pressure condition, over 0.2MPa, many clear-cut craters could be observed on each deformed surface. Many types of creator shape and size were recognized on each machined condition. The mean crater depth became large with increased compressed air pressure. However, the deviations of indentation length values were so large that it was difficult to discuss the dependency of pressure over the 0.2MPa. The abrasive diameter range spread over a wide area from 63 to 126 μm. The rugged crater shape and size was changed with the following on the collision direction and the abrasive size. As the collusive energy was controlled by the mass and velocity of abrasive, the deviation of the abrasive size and the impact direction with the wire affected the rugged crater size and shape. The mechanism is summarized in Fig. 9.

3.2 Machining condition of the whole rugged surface

Considering the EDM processing, it is assumed that better machining properties would be obtained under dispersed discharge generation condition. When many rugged craters were impressed on the surface of the wire, the probability of the discharge generation would be increased. The electrical discharge is assumed to occur in the concentrating area in the electric field. The electrical discharge is distributed to this area uniformly. The rugged crater must be deformed on the whole wire surface. To machine the constant rugged crater on the tool wire

Table 1:   Wet blasting conditions.

Experiment No.	1-1	1-2
Wire feed speed [mm/s]	50, 150, 250	250
Compressed air pressure [MPa]	0.3	0.1, 0.2, 0.3, 0.4
Abrasive substance	Globular ZrO_2	
Abrasive diameter [μm]	63 ~ 126	
Abrasive density [vol.%]	10	
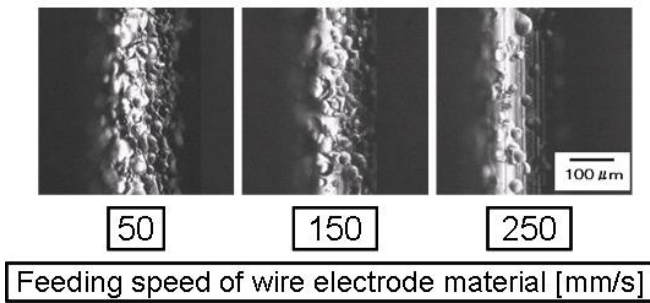
Figure 5:   The images of the rugged wire surface with respective feeding speed.
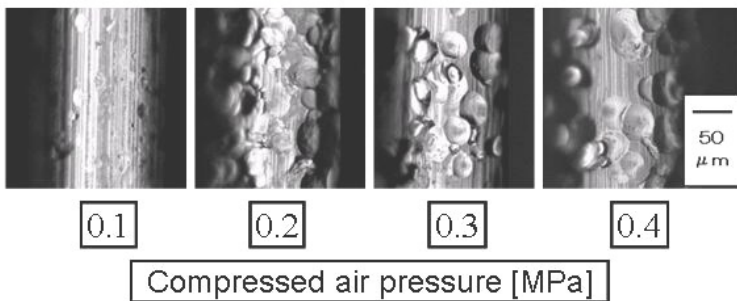
Figure 6:   The images of rugged wire surface with respective compressed air pressure.

electrode, the experimental factors of the abrasive size, constituent of the ZrO_2 abrasives in the machining water and the compressed pressure were investigated. In this experiment, the abrasive density of 20 vol.% was selected, as mentioned, the fine rugged crater couldn't be detailed on the feeding speed of 250 mm/s and the abrasive density of 10 vol.%. The experimental feeding speed of wire electrode material is 250 mm/s in consideration of productivity. But, when the feeding speed of wire electrode material was 250, the ruggedness could not be given to the whole wire surface. Consequently, the feeding speed of wire electrode material of 200 mm/s and the abrasive density of 20 vol.% was selected. The other conditions were selected as follows. The compressed air pressure is 0.2 and 0.4 MPa that is higher than 0.1 MPa. Abrasive has a diameter of 106–126 μm and 45–75 μm. Table 2 shows these wet blasting conditions. An unprocessed wire was called normal.
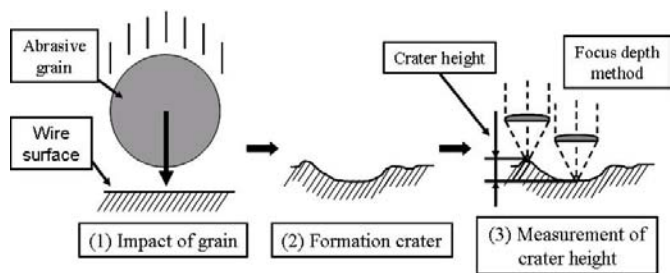
Figure 7:   Schematic illustration of crater formation process and measurement of the crater height.

Compressed air pressure [MPa]
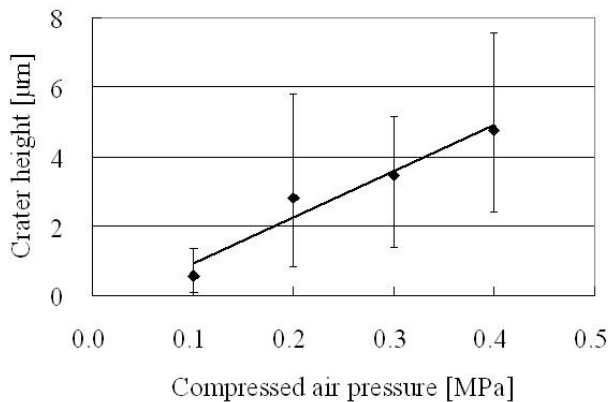
Figure 8:   Relationship between compressed air pressure and crater height.

The surface of the rugged wire was observed with the laser microscope, and the results are shown in Fig. 10. The deviations of indentation over the length were too large to discuss. In this experiment, surface roughness of rugged wire is discussed by the surface roughness Ra, the result are shown in Fig. 11. Surface roughness Ra is calculated from the surface profile measured by the laser microscopy. As a result, there is not so much deviation on each pressure point.

The surface roughness Ra of the rugged surface was increases by the compressed air pressure. The diameter of the indentation increases when the abrasive diameter is large and the distribution of the ruggedness changes. It appeared that average rugged crater depth was related to the compressive pressing under the conditions.
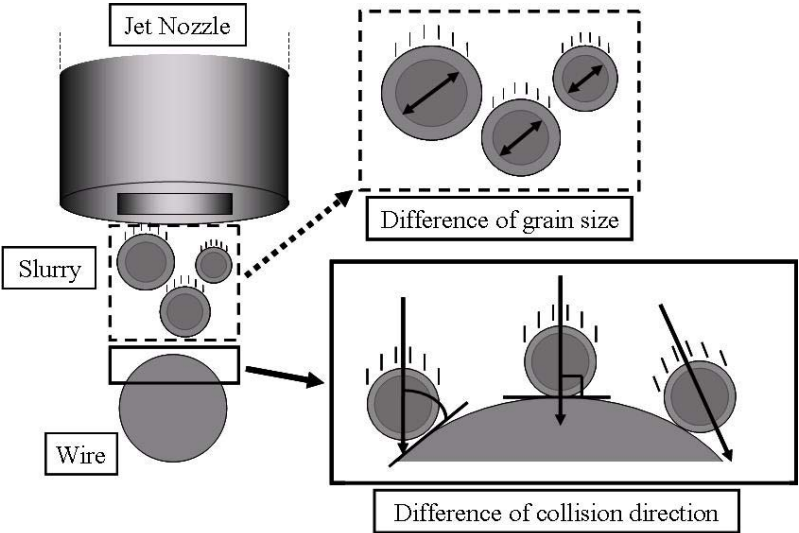
Figure 9:   Disturbances in crater height control.

Table 2:   Wet blasting condition with various wire feed speed and compressed air pressure.

Wire name	PB02L1	PB04L2	PB02A	PB04A
Wire feed speed [mm/s]	200			
Compressed air pressure [MPa]	0.2	0.4	0.2	0.4
Abrasive substance	Globular ZrO_2			
Abrasive diameter [μm]	$106 \sim 126$		$45 \sim 75$	
Abrasive density [vol.%]	20			

3.3 Mechanical properties of ruggedness wire

After the wet blasting machining, the mechanical properties of the wire would be varied with the generation of work hardening, residual stress and the stress

concentration on the rugged area. If the tensile strength of the rugged wire became less than the pulling stress, the wire could not be applied for WEDM process. In this paper, the tensile strength of the rugged wire was investigated. It was well-known that almost all the breakage occurred out of the gage length area on the tensile test of thin wire. More than 90%, the failure was detected around the chuck zone. It indicated that many specimens were needed to evaluate the accurate tensile strength value of wire. In this experiment, the tensile test is carried out with the Instron type tensile machine as shown in Fig. 12. The following conditions were selected: gauge length of 10 mm, and crosshead speed of 1mm/min. The new chucking system was designed with the O-ring. The estimated wires were PB02A and PB04A and normal wire. Using the O-ring as the chucking attachment material, the breakage position was detected at the centre of gage length at least more than 10% with small deviation. Figure 13 shows the breaking stress and the breaking strain obtained from the tensile test. Fracture pattern of the pulled out wire is observed with the light microscope, and the result is shown in Fig. 14.
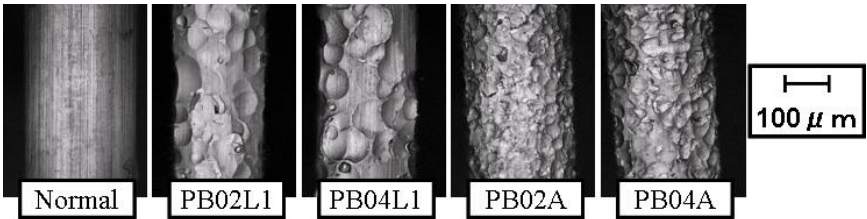
Figure 10: The image of rugged wire surface with respective compressed air pressure and abrasives diameter.
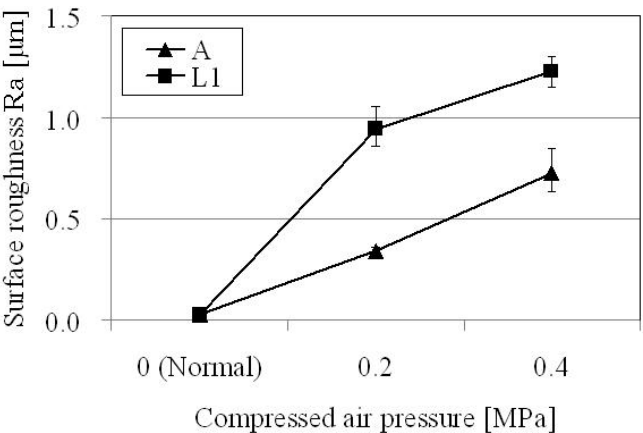
Figure 11: Relationship between compressed air pressure and surface roughness Ra.

The fracture stress and the strain of the rugged wire decreased with increasing the compressed air pressure. The fracture pattern of normal wire showed the ductile fracture with the necking, but on the rugged wire it turned to the shear type failure. It was assumed that on account of the work hardening and the residual stress, the tensile strength of rugged wire became smaller than the normal wire. However, tensile strength of a rugged wire was enough higher than the pulled stress on the WEDM machine of 300 to 400 MPa.

In addition, the shear fracture was observed on the rugged wire as shown in Fig. 14. As the breakage generated from the damage surface zone, it indicated that the rugged crater was deformed on the limited thin surface area. It was considered that the rugged surface was impressed constantly and continuously without large residual stress by the wet blasting method on the thin Cu-Zn wire.
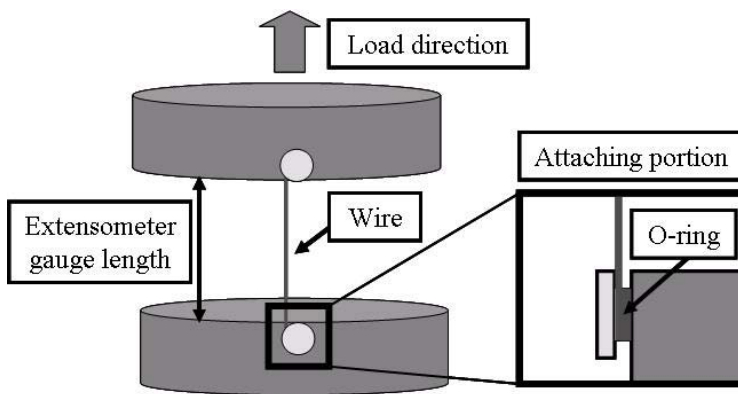
Figure 12:   Schematic drawing of the tensile test.
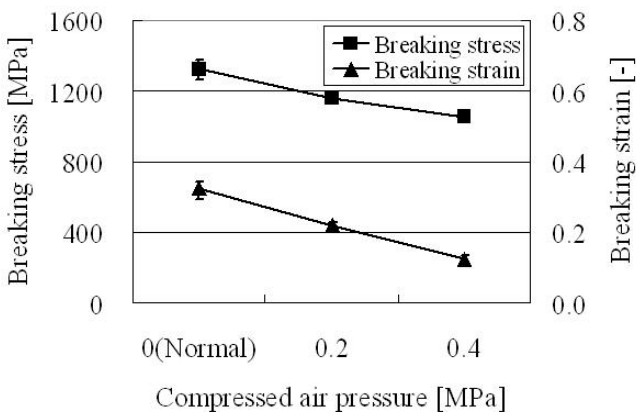
Figure 13:   Fracture stress and strain obtained from tensile test.

4   Conclusion

The new wet blasting method was proposed for making the rugged surface on the Cu-Zn wire. The effects of the machining conditions for making the rugged crater were investigated. The mechanical properties of the rugged wire were also discussed. The results were summarized as follows.

(1) The ruggedness can be impressed on the whole surface of the thin wire by the proposed wet blasting method.
(2) The size and distribution of the rugged craters can be controlled by changing the blast processing conditions.
(3) The breaking stress and strain of the rugged wire is smaller than the normal wire. The shear fracture occurred on the rugged wire for the tensile test.
(4) On the rugged wire, the stress concentration and residual stress of the damaged surface was not so large.
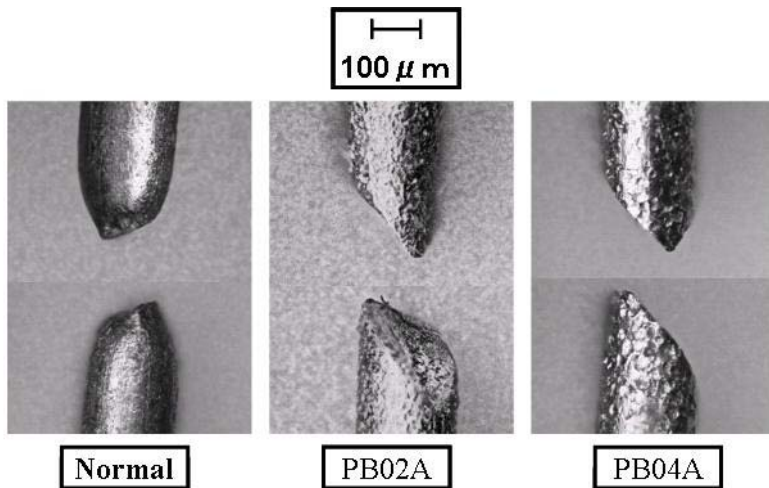
Figure 14:   The image of the wire breakage region.

References

[1] Ichiro ARAIE, Sadao SANO, Masanori KUNIEDA, Effect of Electrode Surface Profile on Discharge Delay time in Electrical Discharge Machining, Journal of Electrical Machining Engineers, 41(97), pp. 61-68, 2007.
[2] Masahiko FUKUI, Natsuo KINOSHITA, Develop of the Wire Electrode under Wire EDM (1st Report), Journal of Electrical Machining Engineers, 16(32), pp. 25-36, 1983.
[3] Masahiko FUKUI, Toshiharu TAKAHASHI, Natsuo KINOSHITA, Hisao ORIMO, Research on wire EDM. Surface treated wire electrodes and their characteristics of electric discharge., Journal of Electrical Machining Engineers, 21(42), pp. 8-21, 1988.

[4] J. Prohaszka, A. G. Mamalis, N. M. Vaxevanidis, The effect of electrode material on machinability in wire electro-discharge machining, Journal of materials Processing Technology, 69, pp. 233- 237, 1997.

[5] Jumpei FUKUOKA, Masahide YAMASHITA, Ken YAMASHITA, Yasushi FUKUZAWA, Masayoshi OGATA, Influence of Surface Condition of Wire Tool Electrode on Wire Electrical Discharge Machining Properties, Proceedings of 2008 Annual Meeting of the Japan Society for Precision Engineering, pp393-394, 2008.

[6] Jumpei FUKUOKA, Masahide YAMASHITA, Ken YAMASHITA, Yasushi FUKUZAWA, Masayoshi OGATA, Electrical Discharge Machining Properties of Wire EDM with Rugged Wire Tool Electrode, Proceedings of 2008 Annual Meeting of JSEME, pp29-32, 2008.

This page intentionally left blank

Section 6
Fatigue

This page intentionally left blank

External surfaces affected by free hydrogen in metastable austenitic stainless steels

Y. Katz
Negba, Beer Sheva, Israel

Abstract

Malfunction in service of contact components due to fretting fatigue enhanced mainly by the environmental interaction provided incentives to broaden and deepen the understanding of this complex time-dependent process. Metastable austenitic stainless steels affected by solid solution free hydrogen interaction, deserves further elaboration and input. In fact, the aforementioned systems combine both materials and aggressive environment that suppose to be candidates for important applications in future energy technology. As such, the whole issue of tribology turns out to be a major design topic in terms of structural integrity and service life considerations. Fretting fatigue driving force includes in addition to the remote load also the environmental interaction effects. By considering the deformation/environment interaction in metastable austenitic stainless steels at least two origins of damage are recognized, namely, sequential events connected to phase stability and hydrogen embrittlement aspects. Materials were selected from the AISI 300 group of austenitic stainless steels in general, with special attention to the relatively stable AISI 316L steel. Hydrogen was provided either by electrolytic cathodic charging or by high temperature/pressure gaseous charging. Following the current information, regarding fretting fatigue, life degradation due to internal/external hydrogen has been established. Thus, the present study is centered on tracking surface modification activated by environmental interaction confined to the near surface hydrogen affected layer. For this purpose, global and local findings were gathered in a bottom-top methodology. Standard and novel techniques were utilized including nano indentation, scratch tests and acoustic emission tracking that enabled visualization and measurements. Experimentally based, the study emphasized the local approach in contrast to the macroscopic contact mechanics approach. On a local resolution a dislocation model has been attempted, which facilitated advanced analysis as related to wear, damage evolution and near surface behavior assessment.

Keywords: austenitic stainless steel, hydrogen interaction, fretting fatigue, surface modification, localized approach.

1   Introduction

Macro scale fretting fatigue in general [1] and in metastable austenitic stainless steel affected by hydrogen environment or in hydrogen pre-charged specimens in particular has been addressed by Kubota et al. [2]. The study established the destructive effects of hydrogen either on the fatigue strength or on the total service life. This unique cyclic deformation/environment interaction emphasized here the significant role of the environment, on top of the solely remote cyclic load parameter that accentuate transitions in the friction or wear behaviour [1,3]. Considering the role of near surface characterization affected by the environment some brief background regarding metastable austenitic stainless steel and hydrogen interaction seems to be in order. Since hydrogen/deformation interactions consist of many facets with broad implications, the wide range of intrinsic/extrinsic variables resulted in enormous number of sometimes-controversial findings and/or interpretations. Thus, the study is intentionally restricted to some relevant key-points. Regarding hydrogen/deformation interaction effects, a summary of hydrogen embrittlement (HE) will be addressed. An additional section intends to focus on small volume research activities as confined to nanoscale probing and fine features observations. In fact the current investigation is aimed to clarify the potential of such new avenues for analyzing highly localized flow and fracture events. The advances in nano-mechanical characterization followed by arguments regarding its relevancy to hydrogen/deformation interactions are described. In this context nano-mechanical methodology become promising in advancing tribological contact topics with attention to high resolution localized imaging information. As a background, insights as relates to HE included activities in single crystals and polycrystalline systems by utilizing global and local approaches. Nevertheless, in the current study special emphasis is paid to nano-mechanical testing engaging with tribology aspects. Clearly nanoscale contact methodology enabled additional options that can assist in cyclic evaluation supported also by nanoscratch tests information. For example, nano-indentation can extend the meaning of single point contact, providing from nano load-displacement curves, the contributions of yield excursions information to local dislocation dynamic models. Beside dislocation nucleation, the resistance of dislocations arrangement below a single contact point was explored. At this juncture the local stress field can be estimated with implications on damage evolution, failure criterion leading to transition in friction coefficient. Refinements of plastic displacement can clarify the threshold wise behaviour resulting from reversible events that were established by nanomechanical testing [4,5].

2   Material and experimental procedures

Second phase aspects have been investigated in metastable austenitic steels while considering austenitic decomposition enhanced by hydrogen interaction. In fact, the whole AISI300 material class is unstable below the Md temperature even with no hydrogen. Moreover, hydrogen with or without a remote mechanical field can result in first order martensitic transformation. Studies in AISI 304L,

316L and 310 stainless steels that covered a relatively wide range of phase stability have defined the important role of second phases in shaping the mechanical degradation degree [6–8]. Standard mechanical tests were applied supplemented by X-ray diffraction and Mossbauer spectroscopy analysis. Austenite decomposition was tracked with attempt to explore the transformation reaction. Only briefly, these global tests were conducted on AISI 304L, 316L and 310 martensitic stainless steels with characterization efforts as related to both, the bulk and the surface. Issues like surface relief, delayed micro cracking and local strains were all included. The nanomechanical tests were conducted mainly on the 316L system. Specimen preparations involved electro chemical following mechanical polishing. Specimens were then electrochemically hydrogen charged in 1MNaOH for 4-6h prior to testing. Charging current densities ranged from 10 to 500 mA/cm^2. Nanoindentation tests of the 316L surfaces were conducted to a prescribed load of 1000 μN by Hysitron nano-indentation instrument utilizing a 90^0 conical indenter with 400 nm tip-radius of curvature. An approximate spacing of $5\mu m$ in two dimensions was maintained for adjacent indent, in microstructure consistent of grain size of 50-100 μm. This allowed at least 5-10 consecutive indents to be within the same grain. For completeness, tests were performed prior to hydrogen charging, at different time stages namely, instantly after charging and one day after charging. Load-displacement of nanoindentation curves were supplemented by Atomic Force Microscopy (AFM) observations that enabled also measurements of indentation induced slip traces. Beside the important information of yield excursions; more was achieved by nano-scratch tests enhancing plastic deformation of fine-features. Scratch tests were performed with the Micro-Mechanical Tester (MMT) using a 90° conical indenter with $1\mu m$ radius of the tip curvature. A typical test included the following steps. The indenter was driven into the surface with the horizontal and the vertical displacements increasing at the rates of 1 μm/s and 7 nm/s. With the prescribed scratch length of 200 μm the resulting normal force increased from 0 to 40-50 mN, depending on the local surface inclination. The maximum penetration depth scaled up to 1.5 μm. With the Scanning Electron Microscopy (SEM) an overview of scratch grooves were taken at different magnifications. Based on the recorded load vs. horizontal distance, loads corresponding to selected scratch segments could be estimated. For comparison of the hydrogen effects, scratch segments corresponding to nearly normal loads were selected. Again, the AFM provided quantitative measures of localized plastic deformation in addition to early cracks formation. Measurements by AFM of localized slip became a quantitative characterization based on surface slip height and spacing that enables to assess the localized strain. This methodology can provide interpretation of interfaces stress failure, namely pile-up considerations or plastic instability via slip band or void instability.

3   Experimental results

Global findings indicated that 304L, 316L and 310 austenitic stainless steels, differ in the phase stability degree. Considering hydrogen interaction even with

no thermomechanical driving force, martensitic transformation occurred. Previous activities [6–8] have adopted also quantitative programs. For example, X-ray diffraction and Mossbauer spectroscopy were aimed to determine the austenite decomposition products resulting from thermo-mechanical driving force with and with no hydrogen interaction or even from both. As such, the decomposition phase reaction was established in addition to the near surface affected layer thickness under specific gas fugacity or specific crack-tip environment conditions.

$$\gamma \rightarrow \varepsilon' + \alpha'$$
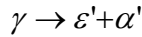
Where γ is the austenitic phase and ε' and α' are the closed packed hexagonal and body centered martensitic phases respectively. The quantitative X-ray and Mossbauer analysis in terms of phase's volume fraction remained highly consistent and slight differences were experimentally dependent (Fig. 1 and 2).
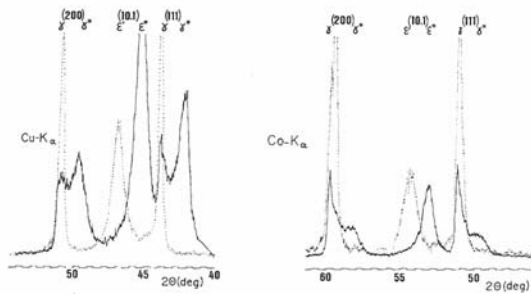
Figure 1:   X-ray diffraction, 304L for different penetration power (a) charged 100min at 60 mA/c2 (b) charged 180min at 100 mA/c2.

Information regarding the near surface affected layer is highly important regarding contact wear. In addition, sequential events either instantaneous or delayed were explored. Here, events like localized plastic displacement, surface relief, microcrack nucleation and debonding were characterized. For example, in relatively low fugacity of hydrogenated AISI 304L, an affected layer of 1.14μm was established. Microscopic examinations in this material revealed pseudo expanded phases, namely ε^* and γ^* due to hydrogen uptake that transformed to ε' and γ' causing significant surface relief. Internal friction studies supported this behavior [9]. Finally, it became apparent that both, increased martensitic α' volume fraction and multiaxial stress state accentuated the near surface degradation due to internal stress field including the critical gas release stage causing surface modification and even micro cracks nucleation beside delayed fracture. In 316L the nano indentation tests resulted in reproducible displacement excursions at an average load of 200 μN for non-charged samples. These were attributed to plastic initiation. Prior to the excursion load, no residual deformation exists, namely typical mechanical response that is still in the elastic regime. There was a slight difference in the average excursion load for tests

performed in different areas of the same specimen. This was attributed to a grain orientation difference or localized pre-existing dislocations; nevertheless the average yield load was near 200μN. In contrast, instantaneously after hydrogen charging the yield initiation occurred at higher values of 650 to 700 μN with an elapsed time of 35 min, the initiation load decreased to values of 300 to 350 μN. However, after one day, values returned back to approximately 200μN (Fig. 3).
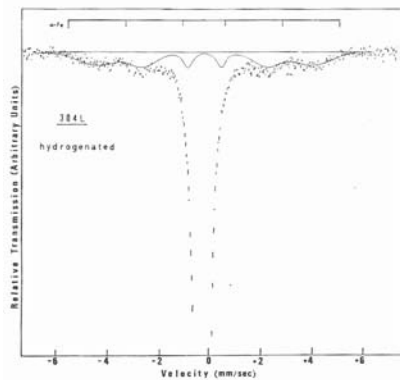
Figure 2:   Mossbauer transmition spectrum of 5μm thin foil computed spectrum-solid line.
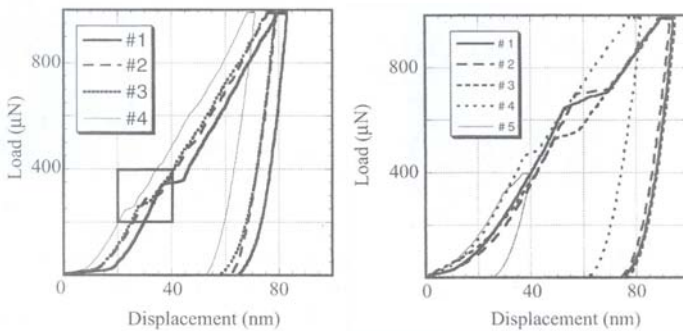
Figure 3:   Nano indentation, load-displacement curve (left) no charged (right) charged. #1-4 time increase.

Supplementing nano indentation curve analysis with AFM measures of normal indentation revealed induced slip features that were also achieved by nano scratch tests probing the hydrogen-affected surface. Here to mention that non-charged specimen were probed as well for comparative study. A comparison of quantitative measures indicated greater localization of slip with hydrogen. It is also worth noting that even with the more widely spaced slip bands, the amount of slip band upset implies a greater local plastic strain (Fig. 4).
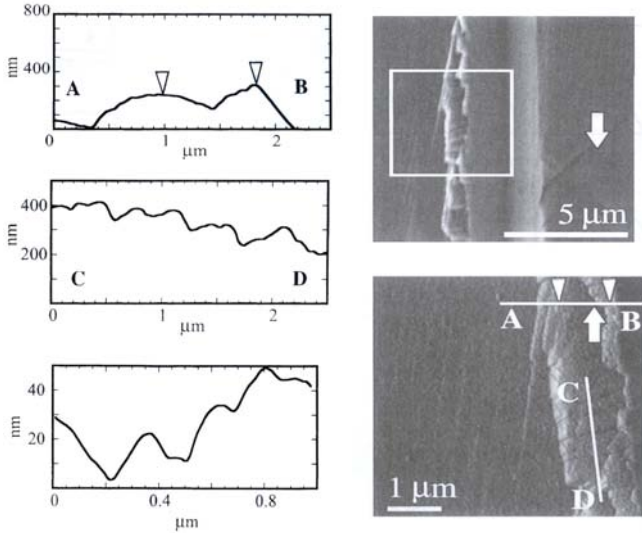
Figure 4: Plastic deformation features (left) AFM micrograph showing slip steps (right) SEM and AFM micrograph near nano scratch.

A determination of such surface strains has been described for fatigue induced surface slip [10,11] in titanium, iron and copper. In the iron case, as cyclic work hardening occurred, it became apparent that enhanced localized plasticity may occur under hardening conditions. This is not uncommon as fatigue induced persistent slip bands in copper and γ' cutting in superalloy are classic examples of localization. For the scratch tracks, smaller indenter pile-up was measured in the hydrogen case. This is consistent with a more highly work hardening material compared to the non-charged case. Such effects of hydrogen on hardening in stainless steels have already been established [12]. This might lead to either decohesion along boundaries and slip planes or to plastic instability through stress or strain elevation with the enhancement of hydrogen interaction

4 Discussion and conclusions

Summarizing briefly the experimental findings; first, nano-indentation revealed major changes in load-displacement behavior after hydrogen charging. It seems that the initial yield increase is related to the hydrogen uptake resulting as such in stress or strain gradients. However, the time dependent stress decay is caused by the hydrogen outgassing. The hydrogen behavior can lead to misunderstanding of the exact meaning of the current reversible cycle. This apparently reversible process involves the end result of surface modification. The impact on the near surface depends on the surface condition and the hydrogen charging fugacity. Nano displacements can develop to intensive damage so important in the assessment of wear transitions of fretting behavior. Beside surface modification as mentioned already the specific contribution of hydrogen

embrittlement aspects deserves special attention in terms of enhanced localized flow and fracture mechanisms. At this juncture it becomes apparent that nano tests methodology suggests further option into fundamental engagement as related to fretting fatigue. Nano resolution suggests connectivity to basic concepts of dislocation emission and dynamics to be translated to local stress fields. The remarkable contribution that might be achieved by nano tests as related to fundamental topics of tribology is striking. Nano-indentation representing the case of a single-point contact situation promises an experimental engagement and analysis of asperities contact wear effects. Clearly such activities open avenues for simulations assisted by dislocations based models via stress/strain field analysis. In specific materials systems, further complexities like surface morphology and statistical characteristics can be attempted in explaining contact transitions. As already been addressed by Kramer et al. [4,5], nano indentation served as powerful experimental facility exceeding more than damage description. As such, providing better understanding of the role of fatigue, micro-plasticity partition and initial methodology to include statistical aspects in damage evolution. Coming back to the deformation/environment case in metastable austenitic stainless steel systems, the hydrogen interaction affects the plastic deformation characteristics completely. This was confirmed experimentally on global and local scales. In fact, localized slip is enhanced by hydrogen uptake. In addition, martensitic transformation beside embrittlement factor involves dramatic changes at near surfaces that were defined quantitatively. Thus, implication on wear become feasible as confirmed in fretting fatigue findings. Accordingly, the following is summarized. On top of intensive activities in deformation/hydrogen embrittlement in austenitic stainless steels, including fracture mechanics methodology [13–19], nano tests have been supplemented. The extension has involved nano-indentation and micro scratch tests and other small volume effects at surfaces. Due to measured surface modification the case of fretting fatigue became highly relevant. With no surprise the findings of fretting fatigue or fretting wear tests confirmed reduction in fatigue life by hydrogen gas environment or in hydrogen pre-charged material. The potential contribution of nano tests in exploring contact wear micromechanisms could be illustrated in AFM measurements and plasticity transitions caused by hydrogen interaction. Particularly the introduction of dislocation-based models becomes possible. Hydrogen remains an aggressive environment affecting damaged sites (pitting), from identified - affected layers up to reduces fracture resistance. These sequential events at least influence strongly a fretting contact, not only in wear transition term but also in the number of cycles for fracture. In a consistent fashion the wide sense of mechanical degradation caused by hydrogen, affect also fretting fatigue behaviour. Expansion tendencies due to hydrogen transformation (in the order of 6%) in direction parallel to the external surface are contracted by hydrogen free material under layer. Such sequential events give rise to significant internal stresses consequently the following is concluded;

    (1)   Metastable austenitic stainless steels interaction with hydrogen involves ample facets including the structural integrity aspects of fretting fatigue

and contact wear degradation. This becomes as such a direct and central design concern.

(2) Searching for fundamental origins affecting contact wear, near-surface small volume probe study provided important information as related to tribological contact understanding.

(3) Particularly in AISI 316L stainless steel nano tests indicated in the load-displacement curves to explore dislocations activity particularly in comparative study including local load displacement curves.

(4) In addition, micro scratch tests revealed plastic displacements, surface perturbations, delamination and micro cracking. Such sequence of events indicated that variations in fretting fatigue with hydrogen are inevitable.

(5) Utilizing nano-tests in order to study fretting fatigue opens new and important avenues engaging not only in solely mechanical driving force but also in the role of environmental effects.

(6) In the investigated system of metastable AISI 316L stainless steel, phase stability aspects, hydrogen embrittlement combine to enhanced surface modification layer, delamination and micro-cracking.

(7) The current investigation alluded to the powerful contributions assisted by nano-tests including micro probe visualization and measurement potential in contact wear basic engagement and evaluation.

(8) The issue of threshold wise behavior needs further studies that have to be seen.

Acknowledgements

References

[1] Y. Kondo and M. Bodai, Study of fretting fatigue crack initiation mechanism based on local stress at contact edge, JSME, series A,63, pp 669-676,1977.

[2] M. Kubolta, N. Noyama, M. Fuerta, C. Sakae and Y. Kondo, Effect of hydrogen gas environment on fretting fatigue, J. Soc. Mat Sci. Japan, 54, pp. 1231-1236, 2005.

[3] P. Blau, Friction and wear transitions of materials, Park Ridge NJ Noyes pub.1989

[4] D.E. Krammer, H. Huang, J. Robach, J. Nelson, A. Wright, D. Bahr and W.W. Gerberich, Yield strength predictions from plastic zone around nano-contact. Acta Mater 47, pp. 333-343, 1999.

[5] D.E. Krammer, K.B. Yoder and W.W. Gerberich, Phil, Mag, 81A, p.2033, 2001.

[6]   H. Mathias, Y. Katz and S. Nadiv, Hydrogenation gas release effects in austenitic steels: Quantitative study, Melat-Hydrogen Systems, T.N. Veziroglu ed. Pergamon Press, Oxford, 225-249 1982.

[7]   Y. Katz, H. Mathias and S. Nadiv, The mechanical stability of austenite in maraging steel, Metall Trans. 14A pp. 801-807 1983.

[8]   Y. Katz, H, Mathias and S. Nadiv, Stability of austenitic stainless steels - micro aspects transformation, Suppl. Trans. Jap, Inst. Metals. 17, pp. 381-386 1976.

[9]   V.G. Gavriljuk, H. Hannien, A.V. Tarasenko, A.S. Tereschenko and Ullakko, Acta. Metall. Meter, 43, p.559, 1995.

[10] S. E. Harvey, P. G. Marsh and W. W. Gerberich, Acta Acta. Metall. Meter, 42, p.3493, 1994.

[11] A. Alush, A. Busiba and Y. Katz, Fatigue crack initiation stage in polycrystalline copper, ECF12, M. W. Brown, E. R. de los Rios and M. G. Miller, Eds. pp.253-258, EMA, pub, U.K, 1998.

[12] D.P.Abraham, C.J. Alstetter, Metall. Trans. 26A, p.2859, 1995.

[13] W.W. Gerberich, R.A. Oriani, M.J. Lii, T. Chen and T. Fockeke, The necessity of both plasticity and brittleness in fracture thresholds of iron. Phil. Mag. 63A, 363-76, 1991.

[14] K. Sieradzki, Theory of environmental effects on transgranular fracture, in Chemistry and Physics of Fracture. Eds. R.M. Latansiaa and R.H. Jones. Nato Asi Series E, Martinus Nijhoff Pub, Dordrecht, pp. 219-252, 1987.

[15] Y. Katz, N. Tymiak and W.W. Gerberich, Nanomechanical probes as new approaches to hydrogen/deformation interaction studies, Engin. Frac. Mecha. 68 pp. 619-646, 2001.

[16] S. H. Chen, Y. Katz and W. W. Gerberich, Crack-tip strain fields and fracture micro-plasticity in hydrogen induced cracking of Fe-3wt%Si single crystals, Phil. Mag. A63 pp. 131-155, 1991.

[17] M.J. Lii, X.F. Chen, Y. Katz and W.W. Gerberich, Dislocation modelling and acoustic emission observations of alternating ductile/brittle events in Fe-3wt% Si crystals, Acta Metall. 28, pp. 244-53, 1990.

[18] X.F. Chen, Y. Katz and W.W. Gerberich, On the directional dependency of micro-plasticity for {100} cleavage in Fe-Si single crystals, Ser. Metall. 24, pp. 1125-30, 1990.

[19] C. W. Tien, C. J. Altstetter, CDI 92, T. Magnin, J. M. Gras, Eds, Les Editions De Physique, Les Ulis, France, 1993, p 356.

This page intentionally left blank

Numerical and experimental study of the fatigue of threaded pipe couplings

J. Van Wittenberghe, P. De Baets, W. De Waele & S. Van Autrève
Laboratory Soete, Faculty of Engineering Ghent University, Belgium

Abstract

Threaded pipe couplings are used in the oil and gas industry as an alternative to welding and in applications where pipes should be frequently coupled and uncoupled as is the case for drill pipes. To maintain a sealed and secure connection while being subjected to external variable loads, they are commonly preloaded by using threaded connections with a conical shape. In this study a series of finite element analyses of conical threaded API Line Pipe couplings is carried out to quantify the influence of its contact parameters (coefficient of friction, preload and taper angle). In the assembled pipes, small sliding of the thread contact surfaces is still possible due to elastic deformation under external loads. This means that the contact zones of the threads can change under load, which complicates the analysis of the couplings. It was found that the coefficient of friction between the threads had a significant influence on this sliding. The shape of the threads inherently causes local stress concentrations, which can in turn initiate fatigue cracks. To validate the results of the finite element simulations, both static and dynamic tests were carried out on an API Line Pipe coupling. The preloading of the connection was carried out on a torque machine and an experimental fatigue test was carried out on a four-point bending test setup. Strains measured by strain gauges on the connections are in good agreement with the strains predicted by the finite element simulations. Fatigue cracks appearing emanated from the root of the last engaged thread of the male part of the connection, which is the region with the highest stress concentration factor in the numerical model.

Keywords: threaded connection, pipe coupling, finite element analysis, coefficient of friction, experimental testing.

1   Introduction

Threaded pipe couplings are commonly used in the oil and gas industry as an easy-to-assemble alternative for welding e.g. in risers and in applications where pipes should be frequently coupled and uncoupled as is the case for drill pipes. They consist of a male and a female part called respectively 'pin' and 'box'. Fatigue failure of threaded pipe couplings is an important problem. Although much research has been done in this field, its frequency of occurrence is still excessive. In the case of drill strings, it was reported by Vaisberg *et al.* [1] that up to 73% of all drill string defects were caused by fatigue cracks. Fatigue failure is caused by cyclic loads that appear in drill strings during drilling operations. Risers are underwater pipelines that connect oil wells in the seabed to oil rigs. They are subjected to cyclic loads by displacement of the rig, waves, tides and currents, which can induce vibrations in the riser.

It is essential for the couplings, first of all, to maintain a secure connection between the different pipes of the pipeline or string, which does not loosen under the influence of external loads and vibrations. Secondly, they should provide a good sealing to prevent the coupling from leaking. To achieve this, the connections commonly have a conical shape that enables them to be preloaded. This preload is attained by applying a certain torque to the coupling. The torque value is different for every connection type and size and is commonly referred to as the 'make-up torque'. The combination of the make-up torque together with external loads and the geometry of the threads results in a complex stress distribution over the connection. Local stress concentrations at the thread roots can initiate fatigue cracks, in time causing the connection to fail. According to Griffin *et al.* [2], the highest stress concentration under axial load can be expected at the last engaged thread (LET) of the pin. Newport and Glinka [3] showed that this is because the load is distributed unevenly over the threads of the connection and the thread carrying the highest load is the LET of the pin. In order to improve the fatigue strength of a threaded connection, these stress concentrations and the load distribution over the threads should be studied.

Both global and local connection parameters can have an influence on the load and stress distribution over the connection. It is known from Newport and Glinka [3] that the thread type has an influence on the stress concentration factor in the root of the threads since a thread acts like a notch and has a stress raising effect on the local stress. Assanelli *et al.* [4] showed that the load distribution over the threads can be changed by altering the taper angle of the pin or box, creating a small mismatch.

Despite the make-up torque, small sliding of the thread contact surfaces is still possible due to elastic deformation under external loads. This means, the contact zones of the threads will change under load, which complicates the analysis of the couplings. In the present study it was found that the contact behaviour of the mating surfaces of the connection, and in particular the coefficient of friction (COF), has a significant influence on this sliding. A series of finite element analyses was carried out on a model of an API Line Pipe connection to quantify the influence of the coefficient of friction, the number of

make-up turns and the taper angle. To validate the presented results make-up and fatigue tests were carried out.

2   Finite element modelling

2.1   General practice

It is general practice to model threaded connections using 2D axisymmetric models, as can be seen in [2] and [4-6]. The advantage of this approach is the reduced calculation time compared to full 3D models. In addition to this, due to their complexity, full 3D models have a tendency to be more unstable and to diverge from a stable solution more easily. The disadvantage of the 2D axisymmetric models is that they neglect the helical shape of the threads and the runout region. However, it was shown by Chen and Shih [7] in the analysis of bolts and later by Zhong [8] for threaded pipe connections, that the results of 2D axisymmetric models are in good agreement with the results of full 3D models.

There is a general consensus on using elastic-plastic material models since local stresses exceed the material's yield strength even in the make-up stage. For the coefficient of friction, however, very different values are used. Bahai *et al.* [9] assumed frictionless sliding. ISO 10407-1 [10] gives a coefficient of friction between 0.06 and 0.14, mentioning a typical value of 0.08 when thread compounds are used. Recently Santus *et al.* [11] measured a value of 0.15 for a drill pipe joint even when thread compound was applied. As will be shown further, this variation of the COF has a significant influence on the performance of the connection. Since the coefficient of friction depends on the surface conditions of the threads and the thread compounds used, special attention has to be paid when choosing a value for the COF in a finite element model.

2.2   API line pipe model

In the present study 2D axisymmetric finite element analyses (FEA) were carried out using the software package ABAQUS®. The model consists of an API Line Pipe threaded connection with a nominal size of 4" according to API 5B [12]. The pipe body has an outside diameter of 114.3 mm and wall thickness of 6 mm, the box has a length of 114.3 mm and an outside diameter 132.1 mm. An elastic-plastic material model for API Grade B steel is used, which has a minimum yield strength of 241 MPa and minimum tensile strength of 413 MPa according to the API 5L specifications [13]. In the elastic region a Young's modulus of 208 GPa and Poisson coefficient of 0.3 is used.

Part of the model of the API Line Pipe connection is shown in Figure 1. The model consists of a section of the pin and a section of a half box. The body of the pin extends over a length of 100 mm to the left to exclude boundary effects (not shown in the figure). Figure 1 also shows the resulting von Mises stresses from an analysis of the standard API Line Pipe connection. The analysis is done in two steps.
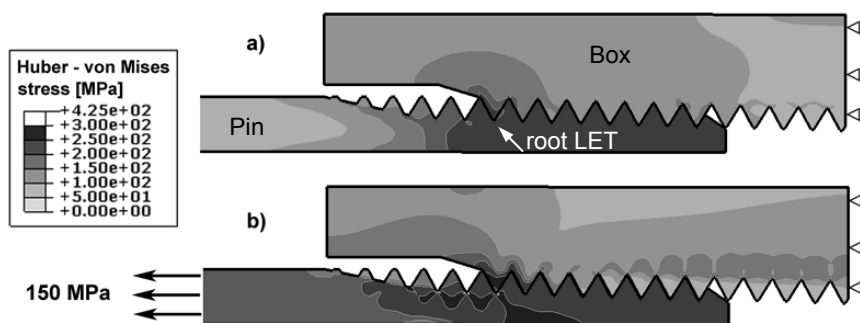
Figure 1:   Von Mises stress distribution for a standard 4" API Line Pipe connection: a) at make-up; b) with an additional external tensile stress of 150 Mpa.

During the first step, the make-up is modelled by applying an initial overlap between the male and female part of the connection and then bringing them into contact. The size of the overlap corresponds to the specified number of make-up turns. In the pin the make-up causes a compressive hoop stress which can be very high and even exceed the material's yield strength.

Once the make-up step is completed, an additional external axial tensile stress is applied at the left end of the pin. The pull-out strength of this type of connection is 373 kN (Clinedinst [14]), which corresponds with a uniform axial tensile stress of 183 MPa in the pipe body. Since the modelling of thread pull-out is not of interest and does not correspond to a service condition, a maximum applied tensile stress of 150 MPa was chosen.

As can be seen in Figure 1 the highest stress appears in the LET of the pin as can be expected from Griffin *et al.* [2]. This will also be the region where a fatigue crack is most likely to initiate.

2.2.1 Coefficient of friction

Once a certain external tensile stress is exceeded, the threads will start to slide over each other creating an opening between the threads. This means the gas or liquid inside the pipes will find their way out through the helical path created by the thread opening. It is obvious that such a leak is undesirable. From Figure 2 it can be seen that the opening is highly dependent on the coefficient of friction μ between the threads. The opening is defined as the perpendicular distance between the thread flanks, and varies between 0.03 mm when $\mu = 0.16$ and 0.41 mm for the frictionless situation, at an external tensile stress of 150 MPa. The opening increases slowly from 0 to a value of approximately 0.025 mm, and when a certain limit stress S_L is reached, the threads start to slide and the opening increases significantly. It can be seen from the graph that the limit stress increases with increasing COF and that paths of the opening during sliding are parallel for the different COF's.

Based on the simulations, an empirical correlation was found for the limit stress S_L and the opening O:

$$S_L = 124 + \mu \cdot 169 \; [\text{MPa}] \tag{1}$$
$$O = 0.014 \, (S - S_L) + 0.025 \quad [\text{mm}] \quad \text{for} \; S > S_L \tag{2}$$

With S the externally applied tensile stress in the pin body.

If during fatigue loading, the maximum cyclic stress exceeds the limit stress, there is a possibility for fretting fatigue cracks to initiate from the threads contact surface.

2.2.2 Load distribution over the threads

When the threads start to slide, the contacting surfaces of the threads will decrease, increasing the resulting contact pressure. The load distribution over the threads, however, is not affected by this pressure change and is the same for the different COF's. The load distributions for an external tensile stress of 100 MPa and 150 MPa as a percentage of the total load is given in Figure 3. Thread nr. 1 corresponds to the LET of the pin.

Note that at an external stress of 100 MPa the LET carries 47% of the total load. With a higher external stress applied, the LET will start to bend, transmitting part of its load to the other threads. This way the tooth load decreases to 36% at a tensile stress of 150 MPa.
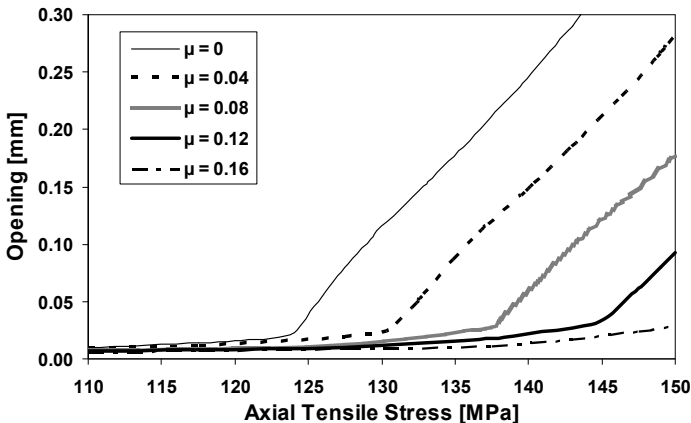
Figure 2:   Influence of the coefficient of friction on the thread opening.

2.2.3 Number of make-up turns

According to the API 5B specifications [12], the connection should be made up in such a way that the end of the box recess (unthreaded part at the left side of the box in Figure 1) coincides with the plane of the vanishing point of the thread runout of the pin. Depending on the tolerances this should correspond with between 1 and 3 make-up turns. As will be shown in paragraph 3.1.2 the number of make-up turns to be used in the models should be lower than the specified number since a certain rotation is necessary to settle the connection. For this reason the number of make-up turns was varied from 0.25 to 3 (see Figure 4). The tooth load at the LET of the pin with an external stress of 150 MPa does not

change significantly with the number of make-up turns. For an external tensile stress of 100 MPa, the tooth load at the LET of the pin increases linearly from 47% to 53% for 1 to 3 make-up turns, but for a lower number of make-up turns the tooth load moves to the values obtained for the higher stress of 150 MPa. The thread opening decreases with increasing number of make-up turns, but saturates for 1.75 make-up turns or more. This is because the engaged body of the pin yields completely and plastic deformation appears for 1.75 make-up turns or more.
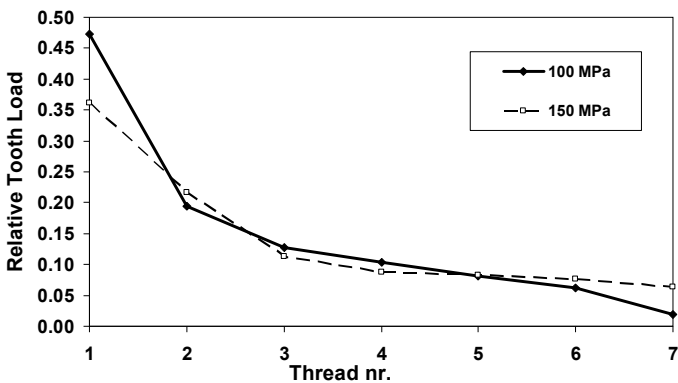
Figure 3:   Load distribution over the threads as a percentage of the total load.
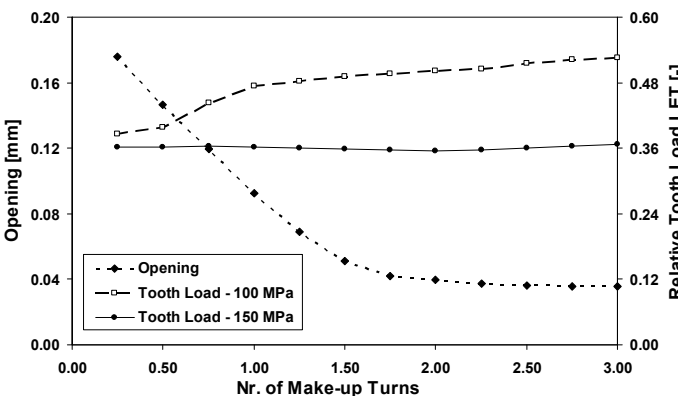
Figure 4:   Influence of make-up turns on thread opening and relative tooth load on the LET of the pin ($\mu = 0.12$).

2.2.4 Taper angle

The taper angle of both pin and box of the API Line Pipe connection has a nominal value of 3.576° and can be maximum 3.873° or minimum 3.428°. By changing the taper of both pin and box between these tolerances, it was found

that the taper difference Δt is the defining parameter for the behaviour of the connection. Where:

$$\Delta t = taper_{box} - taper_{pin} \; [°] \tag{3}$$

It can be seen in Figure 5 that both tooth load at the LET of the pin and thread opening decrease with increasing taper difference, however, the influence of the taper difference is much smaller than the influence of the number of make-up turns.
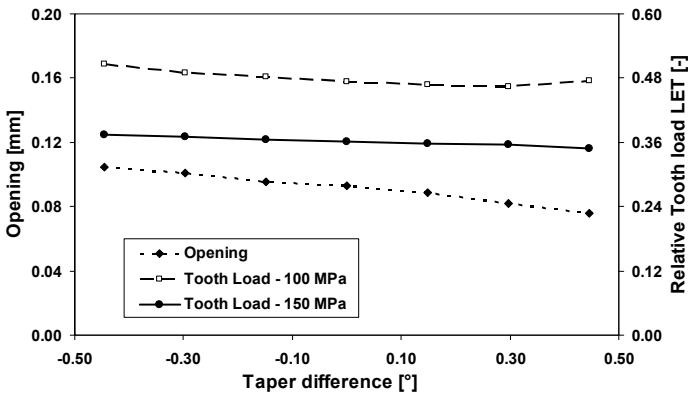
Figure 5:   Influence of taper angle on thread opening and relative tooth load on the LET of the pin (μ = 0.12, number of make-up turns = 1).

3   Experimental validation

To validate the results of the finite element simulations two different types of tests were carried out on standard 4" API Line Pipe connections. To validate the modelling of the make-up and to obtain a value for the COF between the threads the make-up of the connection was performed on a torque machine. A fatigue test was carried out on a four-point bending fatigue test setup using a coupled pipeline segment with a total length of 3 m.

3.1 Make-up tests

3.1.1 Torque machine description

During the make-up it is necessary to accurately control the rotation and to measure the resulting torque. In order to do this, a setup was made by modifying an old torque machine. The new setup is presented in Figure 6a. The test specimen (1), consisting of a pin and box, is mounted in the torque machine by the use of flanges that are welded to pin and box. Drive wheel (2) rotates a worm which drives the gear (3). This causes the pin of the test specimen (1) to rotate with respect to the stationary box. The resulting torque is transmitted to the lever arm (5) which is connected to the loadcell (4). The measured load multiplied by the length of the lever arm (1.00 m) equals the acting torque. To allow an axial motion during make-up, a linear guiding system (6) is present. The torque

machine has a capacity of 2500 Nm, and the maximum test specimen length is 400 mm.

3.1.2 Determination of the coefficient of friction

Two torque tests were performed; the resulting torque-turn graph of one of the tests is shown in Figure 7. The number of rotations was put to zero at the point where the torque started to increase, the so-called 'hand-tight' situation. The total number of make-up turns is 1.09, which lies within the area of the specified 1 to 3 make-up turns (see paragraph 2.2.3).

a)   b)
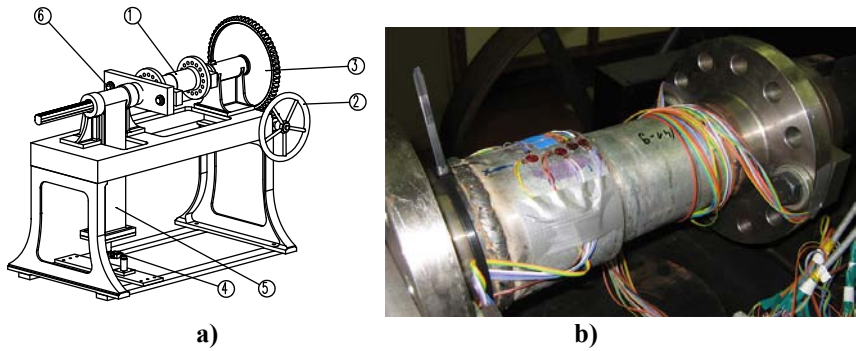
Figure 6:   a) Schematic view of the torque machine; b) instrumented test specimen mounted in the setup.
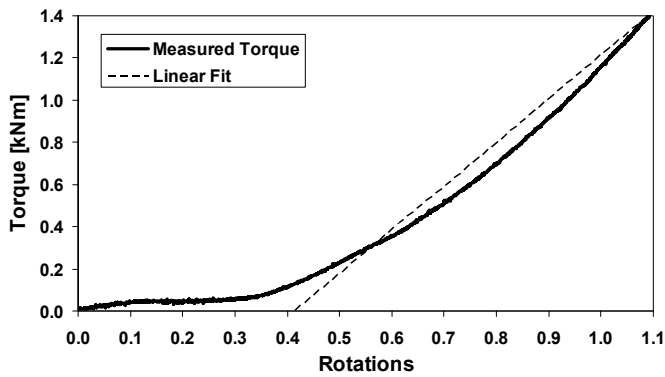
Figure 7:   Torque vs. number of turns.

The measured make-up torque was 1401 Nm, which conforms API 5C3 [15], that specifies the make-up torque should be between 850 Nm and 1430 Nm. From the torque-turn data, a coefficient of friction can be calculated. This is done by finding the best linear fit that coincides with the final value of make-up torque and number of rotations. From the slope of this line, the COF can be calculated. For the two torque tests a value of $\mu = 0.11$ and $\mu = 0.15$ was found.

As can be seen in Figure 7, the torque increases first to a value of about 50 Nm and stays constant for about 0.35 rotations. This is because all connections have some geometrical deviations and the connection needs to settle before the threads of pin and box are completely in contact with each other. Once the threads are fully contacting, the torque builds up, following the path of the linear fit. The linear fit becomes zero at a value of 0.42 rotations, so from this point of view, the number of final make-up turns is only $1.09 - 0.42 = 0.67$. This shifted value should be used as input for the finite element models since there is a perfect match between the geometry of pin and box in the models. In a previous study of Assanelli *et al.* [4] an analogue shift was observed for an API 8-round threaded connection.

3.1.3 Strain measurements during make-up

As can be seen in Figure 6b strain gauges were attached to the test specimens to measure strains during make-up. They were attached at different locations over the outside wall of the box and the inside wall of the pin. The measured strain values at the final torque of 1401 Nm were compared to the modelled strains. As input for the finite element model, a COF of 0.13, 0.67 make-up turns and the measured value for the taper difference was used.

The results are shown in Figure 8 for axial strain Exx and in Figure 9 for hoop strain Ezz. The distance is measured along the pipe axis, starting from the vanishing point of the thread runout of the pin. The RMS deviation between the measured and simulated values was 117 με. When the number of make-up turns was changed to 0.60, the RMS deviation even decreased to 80 με. This situation would correspond to an experimental number of make-up turns of 1.02 and a torque of 1200 Nm. These values are still within the API specifications.
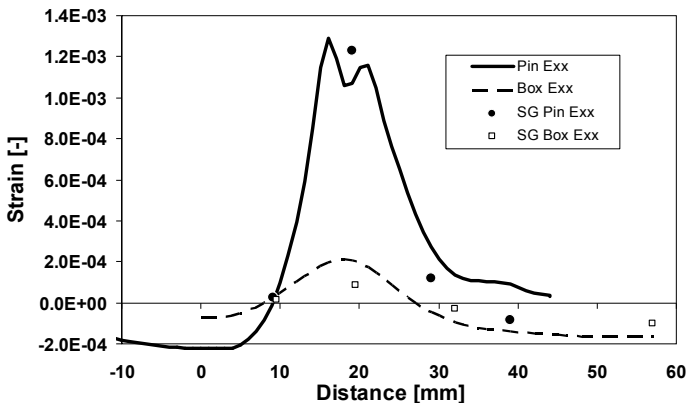
Figure 8:   Axial strain Exx: calculated (lines) vs. measured by strain gauges SG (points).

3.2 Fatigue test

On a four-point bending setup, a fatigue test was carried out on coupled pipeline segments with a 4" API Line Pipe connection and a total length of 3 m. The

applied stress amplitude at the outside wall of the pin was 75 MPa with an R-factor of 0.1 (σ_{max}= 167 MPa, σ_{min} = 17 MPa) and was fluctuated at a frequency of 1 Hz. From the analysis of the measured data it was found that a crack started to grow from the last engaged thread of the pin (indicated by the arrow in Figure 10a) after 18620 cycles.

At 20350 cycles, the test was stopped and the connection uncoupled. The grease that was used during assembly had turned black, which is an indication of fretting corrosion.

Fretting corrosion could be expected since the maximum applied stress of 167 MPa exceeds the limit stress S_L = 146 MPa which is found by substituting the value of $\mu = 0.13$ in equation (1).
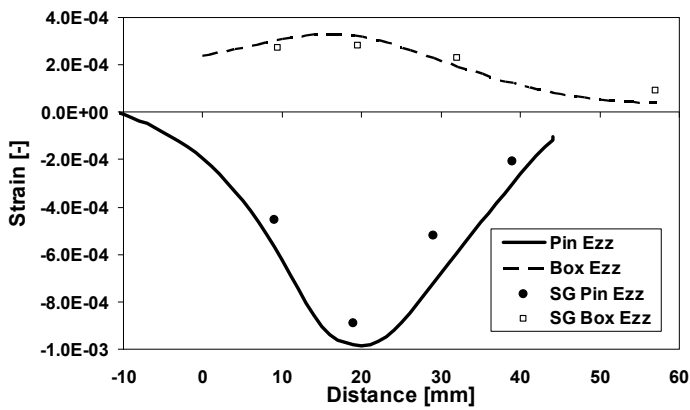
Figure 9: Hoop strain Ezz: calculated (lines) vs. measured by strain gauges SG (points).
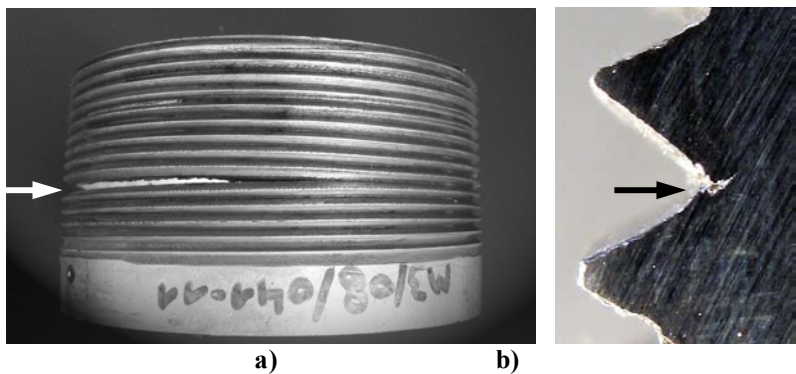
Figure 10: a) Fatigue crack emanating from LET pin; b) detail of the root of the LET of the pin.

Detailed examination of the fracture surface showed that the crack initiated in the root of the LET of the pin (see detail in Figure 10b), which is the location with the highest stress concentration in the finite element model.

4   Conclusions

A 2D axisymmetric finite element model of an API Line Pipe threaded connection has been. It was used to simulate and analyse the behaviour of this coupling type. Complementary experimental tests have been carried out as a validation. Following conclusions can be made:

- Small sliding of the thread contact surfaces appears under external loads, the magnitude of this sliding depends significantly on the coefficient of friction and the number of make-up turns. Under fatigue loads, this sliding can cause fretting fatigue.
- A value for the coefficient of friction was determined based on torque measurements. Strains measured during the make-up tests were in good agreement with the values obtained with the model.
- The number of make-up turns given in the API specifications should not be used as such for input in finite element models.
- During the fatigue test a crack emanated from the root of the LET of the pin, which is the region with the highest stress in the finite element model.

Acknowledgement

References

[1]   Vaisberg, O., Vincké, O., Perrin, G., Sarda, J.P. & Faÿ, J.B., Fatigue of Drillstring: State of the Art. *Oil & Gas Science and Technology – Rev. IFP*, 57(1), pp. 7–37, 2002.
[2]   Griffin, R.C., Kamruzzaman, S., Strickler, R.D., Casing Drilling Drill Collars Eliminate Downhole Failures. *Offshore Technology Conference*, Houston, Texas, USA, 3–6 May 2004.
[3]   Newport, A., Glinka, G., Concentration of Cyclic Stresses in Preloaded Threaded Connections. *Journal of Engineering Mechanics-ASCE*, 117(6), pp. 1257–1273, 1991.
[4]   Assanelli, A.P., Xu, Q., Benedetto, F., Johnson, D.H., Dvorkin, E.N., Numerical/experimental analysis of an API 8-round connection. *Journal of Energy Resources Technology-Transactions of the ASME*. 119(2), pp. 81–88, 1997.
[5]   Dvorkin, E.N., Toscano, R.G., Finite element models in the steel industry, Part II: Analyses of tubular products performance. *Computers & Structures*, 81(8–11), pp. 575–594, 2003.

[6]   Guangjie, Y., Zhenqiang, Y., Qinghua, W., Zhentong, T., Numerical and experimental distribution of temperature and stress fields in API round threaded connection. *Engineering Failure Analysis*, 13(8), pp. 1275–1284, 2006.

[7]   Chen, J.J., Shih, Y.S., A study of the helical effect on the thread connection by three dimensional finite element analysis. *Nuclear Engineering and Design*, 191(2), pp. 109–116, 1999.

[8]   Zhong, A., Thread Connection Response to Critical Pressures, *Abaqus Users' Conference*, pp. 690–706, Paris, France, May 2007.

[9]   Bahai, H., Glinka, G., Esat, I.I., Numerical and experimental evaluation of SIF for threaded connectors. *Engineering Fracture Mechanics*, 54(6), pp. 835–845, 1996.

[10]   ISO 10407-1, Petroleum and natural gas industries – Drilling and production equipment – Part 1: Drill stem design and operating limits, 2004.

[11]   Santus, C., Bertini, L., Beghini, M., Merlo, A., Baryshnikov, A., Torsional strength comparison between two assembling techniques for aluminium drill pipe to steel tool joint connection. *International Journal of Pressure Vessels and Piping*, doi:10.1016/j.ijpvp.2008.09.007, 2008.

[12]   API Specification 5B, Specification for Threading, Gauging and Thread Inspection of Casing, Tubing and Line Pipe Threads (U.S. Customary Units), *American Petroleum Institute*, fourteenth edition, 1996.

[13]   API Specification 5L, Specification for Line Pipe, *American Petroleum Institute*, forty-second edition, 2000.

[14]   Clinedinst, W.O., Joint Strength Formulas for API Threaded Line Pipe, *API Circular PS-1533*, 1976.

[15]   API Bulletin 5C3, Bulletin on Formulas and Calculations for Casing, Tubing, Drill Pipe and Line Pipe Properties, *American Petroleum Institute*, fifth edition, 1989.

Fatigue strength of a radical nitrided Ni-base super alloy

K. Morino[1], N. Kawagoishi[2], K. Yamane[3] & K. Fukada[3]
[1]Tokuyama College of Technology, Shunan, Japan
[2]Faculty of Engineering, Kagoshima University, Kagoshima, Japan
[3]Kohan Kogyo Co. Ltd., Kudamatsu, Japan

Abstract

Radical nitriding was applied to Ni-base super alloy, Alloy 718, which is difficult to nitride and the fatigue strength of the alloy was also investigated in comparison with the aged alloy under push-pull loading at room temperature and 500°C. By radical nitriding, compound layer of about 5 μm was formed and specimen surface was hardened over HV1300. Consequently, fatigue strength was increased in wide life region, especially beyond 10^6 cycles at room temperature. This was mainly caused by the suppression of crack initiation due to formation of hard compound layer. There was no or little difference in fatigue strengths between specimen removed nitrided layer by electro-polishing and aged specimen. That is, radical nitriding method is effective to improve the fatigue strength at room temperature without the damage of matrix.

Keywords: fatigue, alloy 718 steel, nitriding, aging, elevated temperature, compound layer, crack initiation.

1   Introduction

Ni-base super alloys are used under severe conditions like a high temperature or severe corrosive environment because of their superior properties on corrosion, creep, static strength at high temperature and so on [1–3]. Therefore these alloys have been used as a major material of gas turbine, jet engine and so on. However the alloy is inferior to wear resistance. To improve the wear performance and fatigue properties, surface modifications are applied. Radical nitriding is one of superior surface treatment methods, because the method can apply to nitriding of metals like an austenitic stainless steel with passive film, control the formation of

compounds, keep surface smoother and especially minimize the damage of matrix because of its low treatment temperature. However, it is difficult to nitride Ni-base super alloy, except for high temperature treatment like an ion nitriding.

In the present study, radical nitriding was applied to Ni-base super alloy, Alloy 718, and the fatigue strength of the alloy was also investigated in comparison with the aged alloy at room temperature and 500°C under push-pull loading.

2 Materials and experimental procedure

The material used was a Ni-base super alloy, Alloy 718, with a chemical composition (in wt. %) of 0.02C, 0.11Si, 0.12Mn, 0.009P, 0.001S, 18.67Cr, 3.09Mo, 0.09Co, 0.01Cu, 0.66Al, 0.90Ti, 18.67Fe, 0.004B, 5.12 Nb and Ta, and balance Ni. The material was solution treated at 982°C for 1 hr and then water quenched. After solution treatment, the material was aged at 720°C for 8 hr, then furnace cooled to 621°C and aged at 621°C for 8 hr followed by air-cooling. The mean grain size of the material was about 18 μm. Mechanical properties of aged alloy at room temperature and 500°C were 0.2% proof stresses of 1147 MPa and 1050 MPa, tensile strengths of 1372 MPa and 1235 MPa and reduction of areas of 38.1 % and 40.9 %, respectively.

Figure 1 shows shape and dimensions of specimen. All of the specimens were electro-polished by ~40 μm in diameter from the surface after machining and emery paper grinding in order to remove the worked layer and to make the observation of surface damage easier. Moreover, parts of aged specimen were nitrided under the conditions shown in fig. 2.
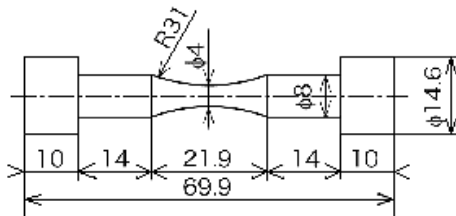
Figure 1:   Shape and dimensions of specimen.
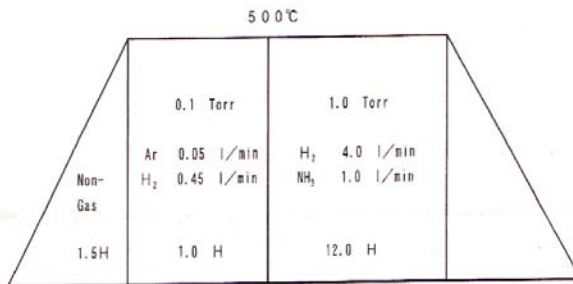
Figure 2:   Nitriding conditions.

Surface   Compound layer

表面   化合物層
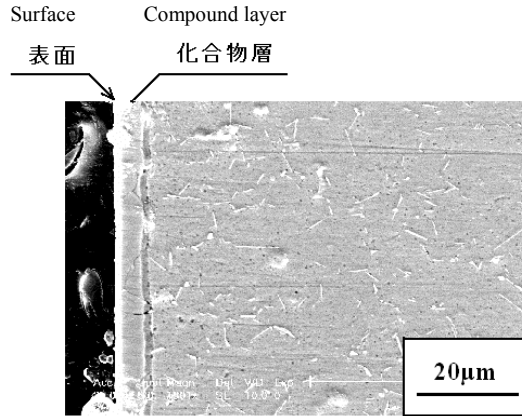
Figure 3:   Microstructure of nitrided alloy.
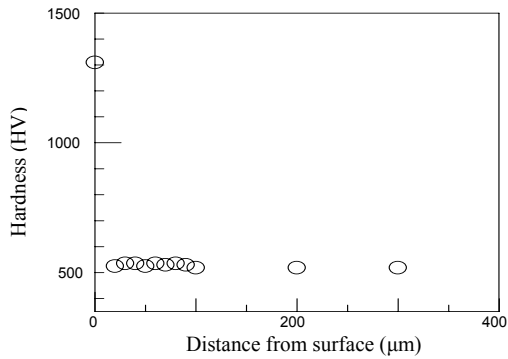
Figure 4:   Hardness distribution.

Figure 3 shows microstructure of nitrided alloy. Compound layer with about 5 μm in thickness is confirmed.

Figure 4 shows hardness distribution of cross section of specimen. Hardness of compound layer is about HV1300.

The measurement of surface damage and fracture surface were examined by using an optical microscope through plastic replica or a scanning electron microscope (SEM) directly. Fatigue tests were carried out using a push-pull fatigue testing machine at room temperature and 500°C in ambient atmosphere under stress ratio of -1. The loading frequency was 5Hz.

3   Results and discussion

3.1 Fatigue strength of nitrided alloy at room temperature

Figure 5 shows S-N curves of nitrided and aged specimens at room temperature. Fatigue strength was increased by nitriding, especially at low stress levels. All of
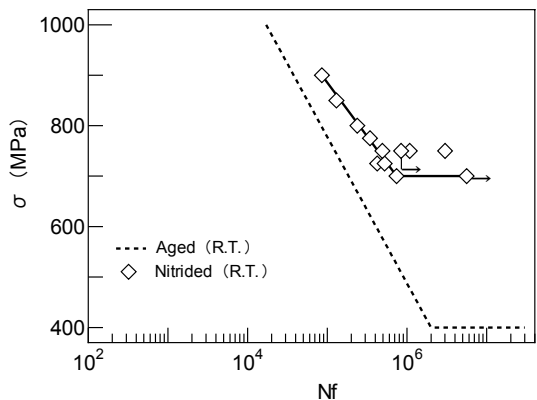
Figure 5:   S-N curves of nitrided and aged specimens at room temperature.
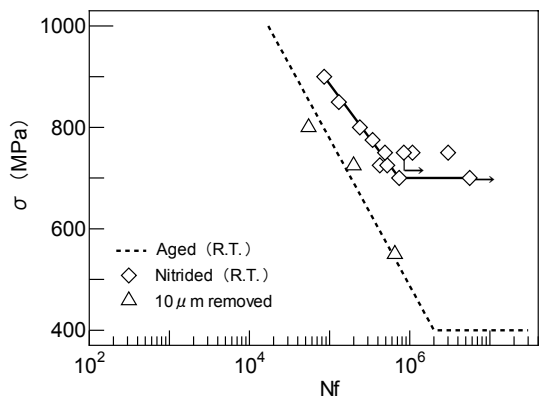
Figure 6:   Fatigue strength of specimen removed nitrided layer.

fractures occurred from specimen surface, though subsurface fracture occurred in many surface treated metals [4–6].

Figure 6 shows fatigue strength of specimen removed nitrided layer by electro-polishing from the surface of nitrided specimen. The fatigue strength of nitrided layer removed specimen is the same as that of aged specimen. This means that radical nitriding did not give any damage. This may be attributed to its low nitriding temperature.

Figure 7 shows crack morphologies observed at specimen surfaces in both alloys. The crack of aged alloy propagates in zigzag manner, while the crack morphology of nitrided alloy is straight, meaning that a brittle crack propagated.

Figure 8 shows fracture surfaces of both alloys. As seen from the surface observation of a crack, there is thin and flat layer corresponding thickness to compound layer near the specimen surface which means that a crack propagates in brittle manner in nitrided alloy, while fracture surface of aged alloy is ductile.
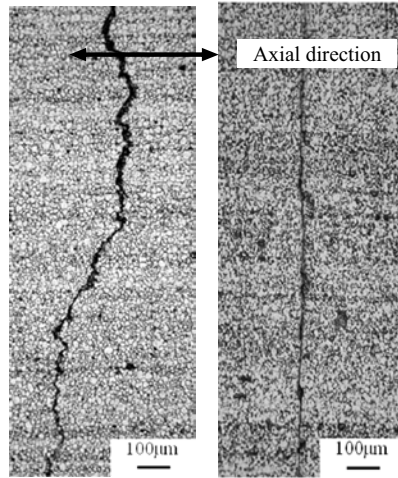
(a) Aged alloy   (b) Nitrided alloy

(Nf=6.82$\times10^4$)   (Nf=1.84$\times10^5$)

Figure 7:   Crack morphology at room temperature.
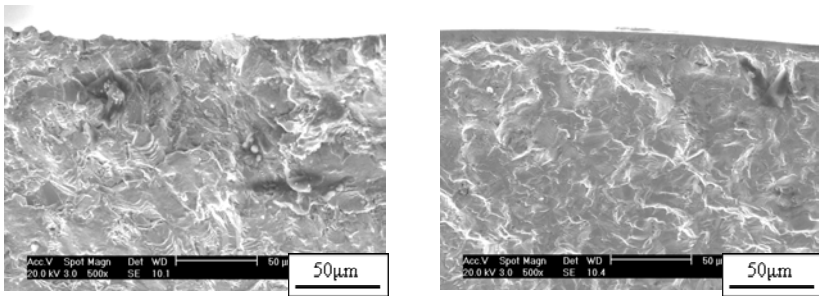
(a) Aged alloy   (b) Nitrided alloy

(σ a=500MPa, Nf=9.23$\times10^5$)   (σ a=750MPa, Nf=3.0$\times10^6$)

Figure 8:   Fracture surfaces at room temperature.

From the results mentioned above, it can be understood that the increase in fatigue strength by nitriding was caused by suppression of a crack initiation and the effect on the propagation of a crack was small. Moreover, small increase in fatigue strength at high stress level can be explained from the propagation of a brittle crack yielded by the large difference in Young's modulus between compound layer and matrix under large deformation.
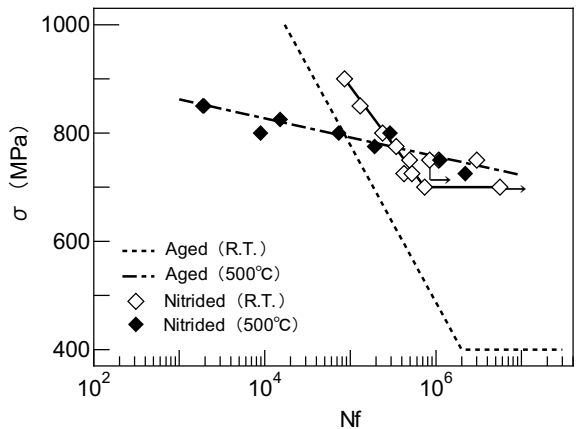
Figure 9:   S-N curves of nitrided and aged specimens at 500.

3.2 Fatigue strength of nitrided alloy at 500

Figure 9 shows S-N curves of nitrided and aged specimens at 500°C. In the figure, the results at room temperature are also drawn by lines only. Fatigue strength was not increased by nitriding, the increase in fatigue strength is almost the same in comparison with the results at room temperature. However, fatigue strength at 500°C is higher than that at room temperature under low stress levels, and it is converse under high stress levels.

Figure 10 shows crack morphologies observed at specimen surfaces of nitrided alloys at high stress. All of fracture at high stress occurred from specimen surface. There are many brittle cracks on the surface. These brittle cracks did not observe at specimen surface of aged specimen.
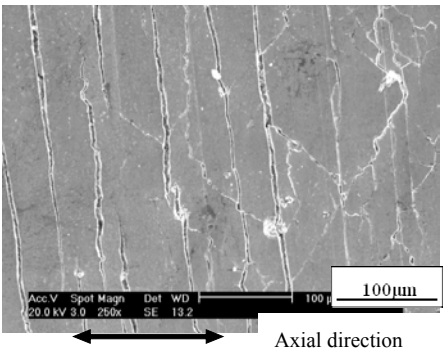
Figure 10:   Crack morphology of nitrided alloy at 500°C.

Figure 11 shows fracture surfaces of both alloys. As understood from the surface observation of a crack, the feature of fracture surfaces of both alloys is similar to the results at room temperature. However, fracture surface near the

(a) Aged alloy

(σ a=700MPa, Nf=3.27×10^6)

(b) Nitrided alloy

(σ a=750MPa, Nf=1.11×10^6)
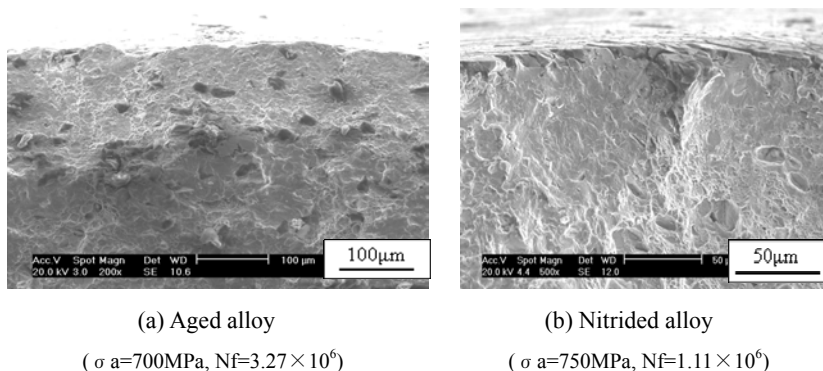
Figure 11: Fracture surfaces at 500°C.

surface of nitrided alloy is more brittle at 500°C than at room temperature. This tendency was marked at high stress levels. The difference in brittlement between room temperature and 500°C is a reason for the difference in nitriding effect on fatigue strength at both temperatures. That is, the difference in Young's modulus between compound layer and matrix is large at high temperature, because the effect of temperature on hardness is smaller in compound layer than in matrix.

4 Conclusions

Radical nitriding was applied to Ni-base super alloy, Alloy 718, and the fatigue strength of the alloy was also investigated in comparison with the aged material under push-pull loading at room temperature and 500°C. By radical nitriding, compound layer of about 5 μm was formed and specimen surface was hardened over HV1300. Fatigue strength was increased in wide life region, especially beyond 10^6 cycles at room temperature. This was mainly caused by the suppression of crack initiation due to formation of hard compound layer. There was no or little difference in fatigue strengths between specimen removed nitrided layer by electro-polishing and aged specimen. That is, this method is effective to improve the fatigue strength without the damage of matrix.

References

[1] Hwang, S.K., Lee, H.N. & Yoon, H.H., *Metallurgical Transaction A*, **20A**, pp.2793-2801, 1975.
[2] Grabowski, L. & Yates, J.R., *Int. J. Fatigue*, **14**, pp. 227-232, 1992.
[3] Anderson, H., Persson, C. & Hansson, T., *Int. J. Fatigue,* **23**, pp.817- 827, 2001.
[4] Kawagoishi, N., Morino, K., Fukada, K., Chen, Q. &Kondo, E., *Surface Treatment V*, WIT Press, pp.209-217, 2001.

[5] Shiozawa, K., Tao, L. & Ishihara, S., *J. Soc. Mater. Sci., Japan,* **48**, pp.1095-1100, 1999.

[6] Nakajima, M., Sakai, T. & Shimazu, T., *Trans. Japan Soc. Mech. Eng. A*, **65**, pp. 2504-2510, 1999.

The effect of Friction Stir Processing on the fatigue life of MIG-Laser hybrid welded joints as compared to conventional FSW 6082-T6 aluminium joints

A. Els-Botes, D. G. Hattingh & K. V. Mjali
Department of Mechanical Engineering,
Nelson Mandela Metropolitan University, South Africa

Abstract

From previous research, Friction Stir Processing (FSP) was identified as a unique processing method that could be applied to improve the microstructure of welded non-ferrous alloys. FSP is similar to Friction Stir Welding (FSW) in that the material is processed below the melting point of the material, but the emphasis is not to produce a joint as in the case of FSW, but to improve mechanical performance. The difference between the two processes is that FSP is used to improve an existing weld's mechanical properties through microstructure refinement. This investigation was conducted on an aluminium alloy due to the relative difficulty with which defect free welds can be produced using conventional fusion welding processes. The aluminium alloy sections were joined using a MIG-laser hybrid process with varying gap widths between the adjoining plates. Similarly, a number of plates were also prepared using a conventional FSW process for comparative purposes. After fabrication, samples were sectioned from the welded plates for mechanical testing in order to evaluate the integrity of the welds. Mechanical properties were evaluated by tensile, fatigue and microhardness testing. Based on comparative results between the FSP MIG-laser hybrid (FSPMLH), the MIG-laser hybrid (MLH) and FSW for the three different gap widths evaluated, several general trends could be observed: weld efficiency (based on tensile strength) was the highest for the 0mm gap MIG-laser hybrid welded plates; FSP had a negligible effect on the tensile strength of the MIG-laser hybrid welded plates, but the percentage elongation values increased significantly. The effect of FSP on fatigue life became more noticeable as the width of the gap between adjoining plates increased. Microstructure evaluation revealed that FSP resulted in a refinement of the as-welded dendritic structure as well as eliminating porosity in the weld.
Keywords: friction stir processing, friction stir welding, fatigue testing, weld integrity, aluminium alloy, MIG-laser hybrid welding.

1   Introduction

Friction Stir Processing (FSP) is closely related to Friction Stir Welding (FSW). The original process development concentrated on the FSW process, which was developed by TWI (UK) in the early 1990s. The basic principle of FSW involves a non-consumable rotating weld tool, which generates frictional heat and plasticizes the weld location, leading to the formation of a joint while the material is in the semi-solid state. The main characteristics of such a joint are low distortion, the absence of melt-related defects and improved joint strength (even in alloys considered non-weldable by conventional fusion welding processes) [1]. The main purpose of FSP on the other hand is to modify the microstructure/profile of either an existing weld or solid material. FSP are done to induce superplasticity, casting modification (FTMP – friction thermomechanical processing) and processing for low temperature formability to name but a few documented processes. The importance of studying FSP as a possible industrial process has been driven by the recent emphasis on the development of ultrafine and nanocrystalline microstructures through severe plastic deformation (SPD). FSP involves SPD, but under conditions that include rapid transients and steep strain gradients and temperature [2]. A good understanding of the process and the associated microstructure evolution is required in order to develop FSP into a viable production process/stage.

2   Material and processing parameters

2.1 Material

The material used for this study was 6082-T6 aluminium alloy plate of 6mm thickness. This is a heat treatable alloy which shows improved mechanical properties in the heat treated/aged condition due to the formation of beta double prime (Mg_5Si_6) particles in the matrix [1]. The typical chemical composition and various properties of the parent plate are given in Table 1.

Table 1:   Material properties: 6082-T6 aluminium alloy.

Element	Al	Cr	Cu	Fe	Mg	Mn	Si	Ti	Zn
Wt%	95.2-98.3	0,25 max	0,1 max	0,5 max	0,6-1,2	0,4-1,0	0,7-1,3	0,1 max	0,2 max
Tensile strength: 310MPa			**Yield strength:** 260MPa			**Melting point:** 660°C			

2.2 MIG-Laser hybrid weld parameters

MIG-laser hybrid (MLH) welded plates were produced by the National Laser Centre (SA) using the settings as given in Table 2. AWS ER 4043 filler wire was used during the welding process and the shielding gas was at a constant flow of 22 l/min for all the welds.

Table 2:   MIG-laser hybrid welding parameters.

Power, kW	Welding speed, mm/min	Current, A	Voltage, V	Gap width, mm
4	2000	170	21	0
4	2000	180	21	0,5
3	1500	180	21	1

Table 3:   Energy values associated with the MIG-laser hybrid welding process.

Power, kW	Line Energy – Laser, kJ/m	Heat input – MIG, kJ/m	Gap width, mm
4	2	96,4	0
4	2	102,1	0,5
3	2	136,1	1

The energy associated with the MIG-laser hybrid weld can be divided into the two processes i.e. laser weld and MIG weld. For the laser weld part the associated line energy can be calculated using the following equation:

$$E_l = \frac{P}{v} \tag{1}$$

where:
E_l = Line energy (J/m), P = laser power (W) and v = welding speed (m/min).

Heat input for the MIG part of the hybrid weld was calculated using the following general formula:

$$Q = \left(\frac{V.I.60}{s.1000} (efficiency) \right) \tag{2}$$

where: Q = heat input (kJ/mm), V = Voltage, I = Current, s = welding speed (mm/min) and efficiency = 0,9 for MIG processes.

The resulting energy values for the two parts of the hybrid welding process are given in Table 3. From this data it is evident that the main source of heat input was the MIG process.

It has been determined from previous studies that in order to obtain a weld of acceptable quality there need to be an increase in heat input as the gap width between plates increase.

2.3 Friction Stir Processing (FSP)

The tool designed for the FSP procedure differ from conventional FSW tools in that the emphasis for this application is to improve the weld microstructure and reduce stress concentration at the weld root bead. The main design difference relates to the smaller shoulder and pin geometry. Figure 1 shows the tool used for the FSP process. The tool was manufactured from H13 tool steel, which proved to be good quality material to use during the FSW of aluminium alloys. FSP was done using a rotational speed of 450rpm with a feed rate of 120mm/min. As only partial penetration was needed, the pin length was considerably shorter than the plate thickness.

Tool dimensions:
Shoulder diameter = 15mm
Pin diameter = 6mm
Pin length = 3mm

Figure 1:   Friction stir processing tool.

Tool dimensions:
Shoulder diameter = 25mm
Pin diameter = 10mm
Pin length = 5,8mm

Figure 2:   Friction stir welding tool.

2.4 Friction stir welding

The FSW tool used to join the aluminium alloy plates have been designed to weld 6mm thick plate successfully. The pin consists of a threaded profile with on flute running parallel to the pin on one side. The flute improves the flow path of material during welding and also assists in the mixing of material of the plates being welded. The tool appearance as well as dimensions is given in Figure 2. The process used a rotational speed of 500rpm and a feed rate of 80mm/min.

2.5 Mechanical testing

All samples for evaluation were removed from the stable region of the welded / processed plate. The stable region is defined as that region where the process variables, mainly temperature are stable, see Figure 3.

Fatigue and tensile samples were machined to dimensions according to ASTM E466 and E8 respectively. Fatigue samples were tested in the polished condition.
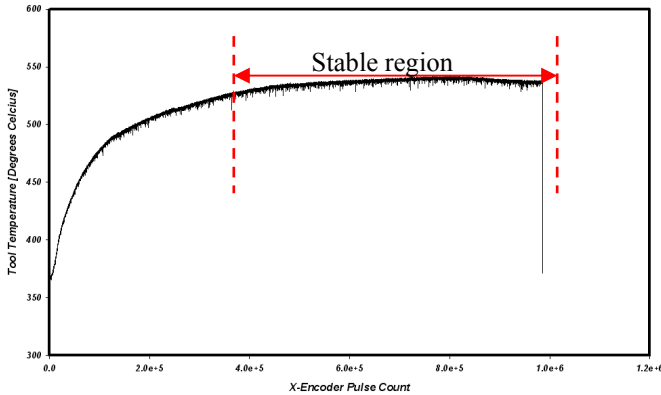
Figure 3:   Temperature profile showing the stable temperature region.

Table 4:   Average tensile results.

Process	Gap width, mm	0,2% Proof stress, MPa	Tensile strength, MPa	Elongation, %	Weld Efficiency, %
Parent plate	-	294	326	14,1	100
MLH	0,0	190	247	3,2	76
	0,5	150	221	3,0	68
	1,0	150	228	3,2	75
FSP	0,0	153	237	6,4	73
	0,5	160	222	5,2	66
	1,0	141	219	6,4	67
FSW	0,0	140	223	7,2	68
	0,5	120	226	7,1	69
	1,0	120	228	7,2	70

3 Results

3.1 Tensile tests

The average tensile results of three specimens are given in Table 3 for the three processes and three gap width variations. Weld efficiency (WE) is measured by the relationship as shown by equation 3.

$$WE = \frac{UTS_{weld}}{UTS_{original}} x100 \tag{3}$$

Measuring joint quality in terms of weld efficiency indicates that FSP did not lead to an improvement in the strength of the weld. However, the percentage elongation values indicate an increase in ductility of the weld (up to 50% increase). The area under the stress-strain curve also increased for the FSP samples which signify an increase in toughness of the weld. The conventional FSW samples showed the highest ductility and their strength values corresponded to those of the FSP samples.
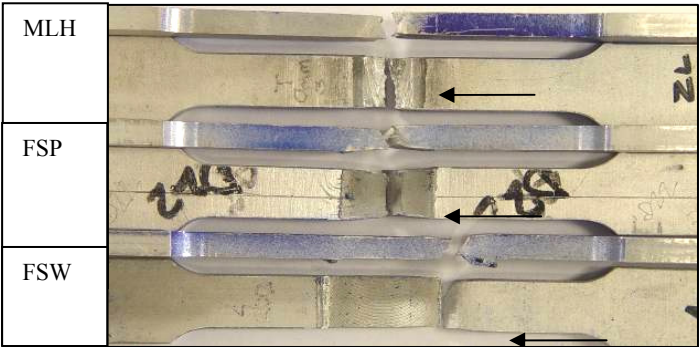
Figure 4:   Fracture locations observed after tensile testing.
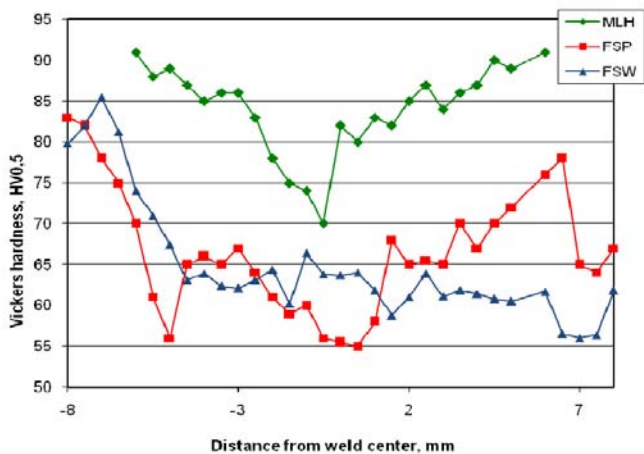
Figure 5:   Vickers microhardness profiles of processed/weld regions.

The fracture location for the MLH and FSP samples corresponded to the centre of the sample whereas the fracture location of the FSW sample was observed to be in the heat affected zone (HAZ) of the sample. The fracture positions are indicated in Figure 4 by arrows.

3.2 Vickers microhardness profiles

Vickers microhardness measurements were taken at a distance of 3mm below the weld root. The resultant hardness profiles are shown in Figure 5. From these profiles it is evident that the area with the lowest hardness corresponds to the tensile failure position. For the FSP and MLH samples the region of lowest hardness corresponds with approximately to the centre of the sample whereas the lowest hardness for the FSW samples was observed in the HAZ.

Since there is a direct relationship between hardness and strength, failure during tensile loading conditions can be expected in these regions. FSP and FSW samples indicate lower hardness values than the MLH samples.

3.3 Fatigue tests

Single load fatigue tests were conducted for comparative studies.   After preliminary testing, a stress amplitude of 170MPa was chosen with R=0,1 and a frequency of 40Hz. Five samples were tested for each process and gap width. The results of comparative fatigue testing are given in Table 4.

3.4 Fracture surface analysis

The fracture positions observed during fatigue testing are shown in Figure 6. The MLH and FSP samples' fracture path approximately followed the centre of the weld whereas the FSW samples failed in the HAZ of the material similar to the fracture positions observed during tensile testing.

Evaluation of the fracture surfaces revealed that for the FSP samples, fracture initiated on the MLH side of the weld with final fracture on the FSP side.

Further evaluation revealed that there is quite a large number of gas porosity as well as shrinkage porosity present in the MLH weld. Other defects observed include inclusions which were rich in iron and from analysis these inclusions can be classified as iron oxide particles in the weld. Fracture surface appearance of the MLH samples are shown in Figure 7.

The FSP samples showed similar defects on the MLH side of the specimen with a fine granular fracture appearance on the FSP side. Only void type defects were observed on the FSP side of the weld. These void types of defects did not

Table 5:   Single load (170MPa) fatigue results.

Process	Gap width, mm	Average cycles to failure
MLH	0	181 908
	0,5	106 349
	1,0	136 731
FSP	0	150 750
	0,5	253 645
	1,0	243 555
FSW	0	295 358
	0,5	202 376
	1,0	175 445
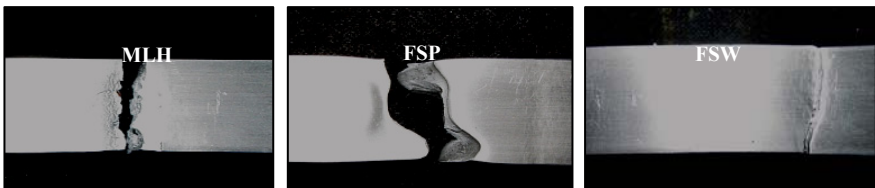
Figure 6:   Fracture positions of fatigue samples.
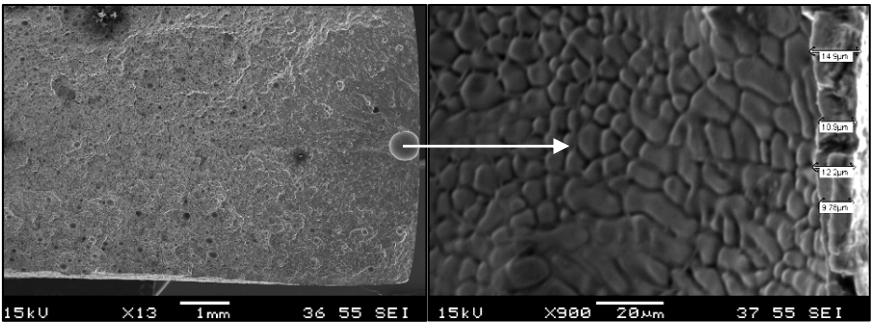
Figure 7:   Fracture surface appearance in fatigue zone of MLH welded samples.
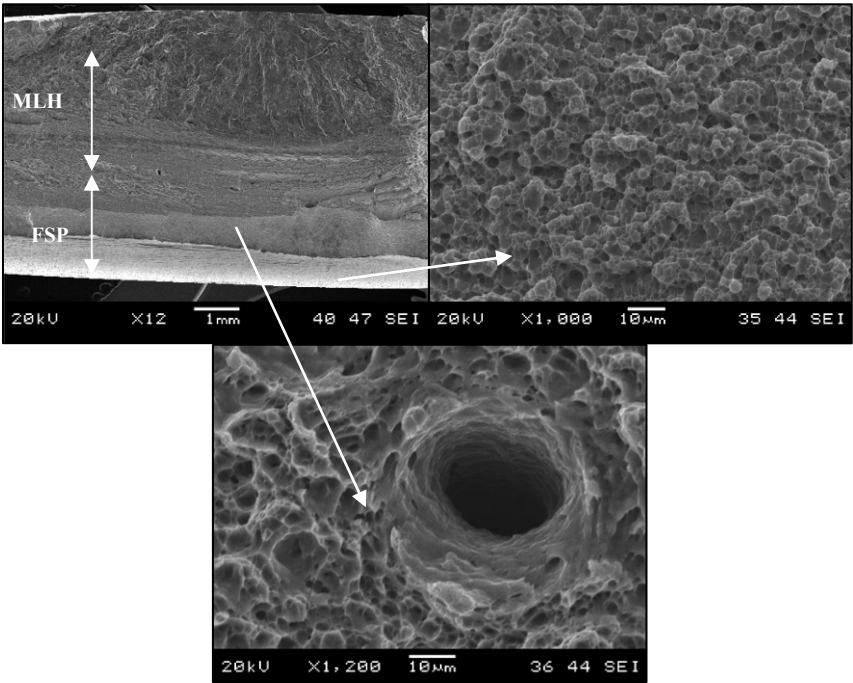
Figure 8:   Fracture surface appearance in fatigue zone of FSP samples.

contribute to crack initiation.   Figure 8 shows the typical fracture surface appearance of a FSP sample. The defects observed on the FSP side correspond to defects documented by other researches studying FSW of aluminium alloys [3].

The fracture surface appearance of the FSW samples showed a typical smooth featureless surface resembling the Friction Processed section as shown in Figure 8.
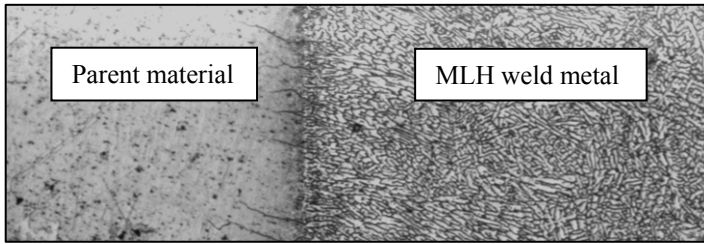
Figure 9:   MLH weld zone microstructure (x100).
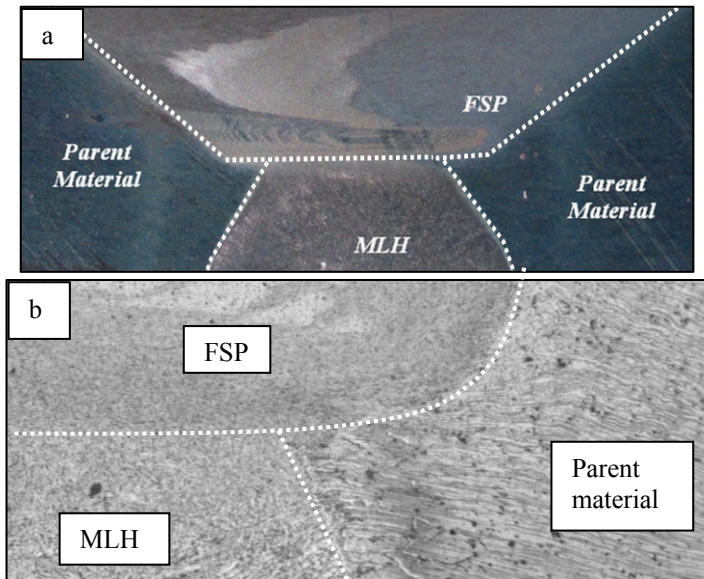
Figure 10:   Appearance of friction stir processed (FSP) sample: (a) macro; and (b) microscopic appearance showing the various zones observed (x100)

3.5 Microstructure

The microstructure in the region of the fusion line of the MHL welded samples are shown in Figure 9. The weld metal shows a typical dendritic structure with a narrow heat affected zone adjacent to the fusion line.

The FSP samples exhibited various zones which are directly associated with the procedure / process experienced by the sample. The various zones observed are shown in Figure 10(a) and (b).

The samples joined by the FSW process exhibited a microstructure similar to that observed on the FSP side of the sample as shown in Figure 10.

4 Discussion and conclusions

Friction Stir Processing is as a complex process as the FSW process. Tool design and selection of process parameters is of critical importance as it influences the maximum temperature reached by the stirred zone and as a consequence influence the resultant modified zone's properties. Process parameter selection is different to that of the FSW process in that the aim of the process is not to create a joint but to refine the microstructure in a specific region. From the results obtained the following general conclusions can be made:

- Friction stir processing of the MIG-laser hybrid welded samples did not lead to an increase in static strength (tensile and yield),
- FSP of the surface of the MLH samples did lead to an increase in weld ductility and toughness of the samples as observed from tensile testing,
- Fracture position of tensile and fatigue samples were the same i.e. in the centre for FSP and MLH samples and in the HAZ for the FSW samples. This fracture location coincided with the region of lowest hardness of the samples,
- Fatigue testing revealed that FSP of MIG-laser hybrid samples lead to an increased number of cycles to failure for the 0,5mm and 1,0mm gap width samples,
- Fatigue fracture initiation started on the MLH side of the friction stir processed samples,
- Fatigue fracture initiation of the MLH samples coincided with near surface gas porosity and / or inclusions in the weld metal,
- Friction stir processing refined the MLH weld metal and HAZ microstructure and eliminated gas and shrinkage porosity that were formed during the MIG-laser welding process

Acknowledgements

References

[1] Khaled, T., *An outsider look at friction stir welding,* Federal Aviation Administration (FAA), Report # ANM-112N-05-06, pp.7-15, 2005.

[2]   McNelly, T.R., et al., Recrystallization mechanisms during friction stir welding/processing of aluminium alloys. *Scripta Materialia,* **58**, pp. 349-354, 2008.

[3]   James, MN., Hattingh, DG. & Bradley, GR., Weld tool travel speed effects on fatigue life of friction stir welds in 5083 aluminium. *International Journal of Fatigue*, **25**, pp1389-1398, 2003.

This page intentionally left blank

Effect of humidity on fatigue strength of shot peened maraging steel

N. Kawagoishi[1], T. Nagano[2], M. Goto[3], Y. Maeda[1]
& M. Moriyama[4]
[1]Department of Mechanical Engineering, Kagoshima University, Japan
[2]Miyakonojo National College of Technology, Japan
[3]OitaUniversity, Japan
[4]Dai-ichi University College of Technology, Japan

Abstract

Rotating bending fatigue tests were carried out for maraging steels using shot peened and electro-polished specimens with various hardness of HV550~HV750 in atmosphere and controlled humidity to investigate the effects of hardness and humidity on the fatigue strength. Fracture occurred from specimen surface in short life region and from inclusion of specimen subsurface in long life one in shot peened specimen, while only surface fracture occurred in electro-polished specimen in wide life range. Hardness dependence of fatigue strength was different between surface fracture and internal one. That is, fatigue strength for internal fracture increased with increase in hardness within the tested hardness, while there was the peak of fatigue strength around HV600 and then fatigue strength decreased with increase in hardness in the relation between hardness and fatigue strength for surface fracture. These results were discussed from the sensitivities of fatigue strength for notch and humidity.
Keywords: fatigue, maraging steel, shot-peening, hardness dependence, humidity, fracture mechanism.

1   Introduction

Maraging steel has the highest static strength among steels for practical use. However, the fatigue strength is very low in comparison with its high static strength [1]. Therefore many studies on fatigue mechanism of the steel have been conducted to improve the fatigue strength. Authors reported that surface treatments like a nitriding and shot peening and formation of reverted austenite

were effective to improve the fatigue strength of the steel [2–4]. On the other hand, fatigue strength of high strength steels are sensitive not only for notch but also for humidity [5, 6]. The sensitivies of fatigue strength for notch and humidity increase with increasing hardness.

In the present study, rotating bending fatigue tests were carried out for maraging steels using shot peened and electro-polished specimens with various hardness of HV550~HV695 in atmosphere and controlled humidity to investigate the hardness dependence of fatigue strength and the effect of humidity on the fatigue strength.

2 Material and experimental procedures

The materials used were two kinds of 18% Ni maraging steels (300 grade and 350 grade) whose chemical compositions in mass % were shown in table 1. The materials were solution treated for 5.4ks at 1123K in vacuum, followed by air cooling and age hardened at different conditions shown in table 2 in a salt bath to change the hardness. The mechanical properties of aged specimen were also shown in table 2.

Table 1: Chemical composition.

Grade	Composition , mass%									
	C	Si	Mn	P	S	Ni	Mo	Co	Ti	Al	Fe
300	0.01	0.05	0.03	0.002	0.002	18.7	5.0	8.94	0.92	0.12	Bal
350	0.001	0.01	0.01	0.001	0.001	17.89	4.27	12.36	1.30	0.08	Bal

Table 2: Aging conditions and mechanical properties.

		Hardness HV	0.2% proof stress $\sigma_{0.2}$(MPa)	Tensile strength σ_B(MPa)	Elongation δ (%)
300grade	753K− 2.8ks	550	1730	1833	11.3
	753K− 6ks	570	1835	1890	7.3
	753K− 11ks	604	1730	1833	11.3
	753K− 48ks	634	2073	2156	8.5
350grade	743K−320ks	670	2201	2257	−
	753K−150ks	695	2272	2310	−
	753K−150ks + 673K−3.6ks	750	−	−	−

Figure 1 shows shape and dimensions of specimen. After machining the specimens, the parts of the specimens were electro-polished by about 20μm from the surface layer and the rest were shot peened under the conditions shown in table 3. Distributions of hardness and residual stress were measured by using a micro Vickers hardness tester (1.97N) and an X ray diffraction device (Cr-Kα), respectively. Fatigue tests were carried out using a rotating bending fatigue

testing machine with a capacity of 15 Nm operating at about 50Hz in ambient atmosphere, where relative humidity (RH) was about 60-80% and controlled humidity of 25% and 85%. The humidity was controlled by setting the testing machine in a cabin and using a humidifier or a dehumidifier.

Table 3:   Shot peening conditions.

Blasting equipment				Air type	
	Material	Size (mm)		Hardness	Specific gravity
Shot	Steel	Φ0.3, Φ0.6, Φ1.1		HV=700	7.5
	Cemented carbide	Φ0.05		HV=1400	14
Blasting			Single shot		Double shot
	Shot size(mm)	Φ0.05	Φ0.3	Φ0.6	Φ1.1	Φ1.1 Φ0.05
	Arc hight (mm A)	0.075	0.230	0.430	0.730	0.730 0.075
	Time (sec)	6	6	6	6	12 6
	Pressure (MPa)	0.3	0.3	0.3	0.3	0.3 0.3
	Distance (mm)	180				
	Coverage (%)	300				
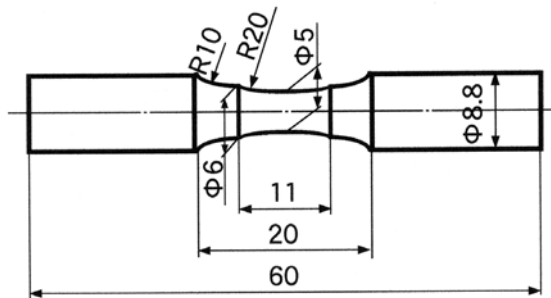
Figure 1:   Shape and dimensions of specimen.

3   Results and discussion

Figure 2 shows distributions of hardness and residual stress in shot-peened specimens. Marked hardening was generated in all materials. The harder material is, the larger the surface hardness is. And the hardened depth is smaller in harder

material. On the other hand, although compressive residual stress was generated by shot peening in all of the shot peened specimens, the maximum values and depths of stressed layer of these materials are nearly the same.

Figure 3 shows surface roughness of shot peened specimen. The surface roughness was decreased with increase in hardness of material.
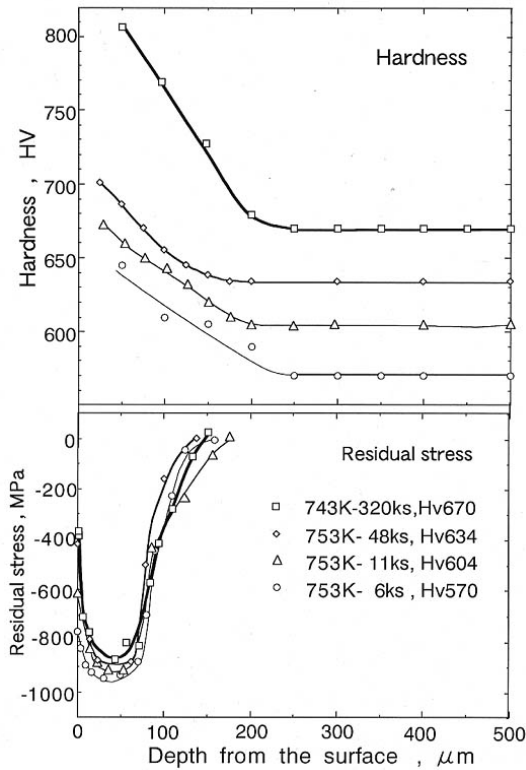
Figure 2:   Distributions of hardness and residual stress.
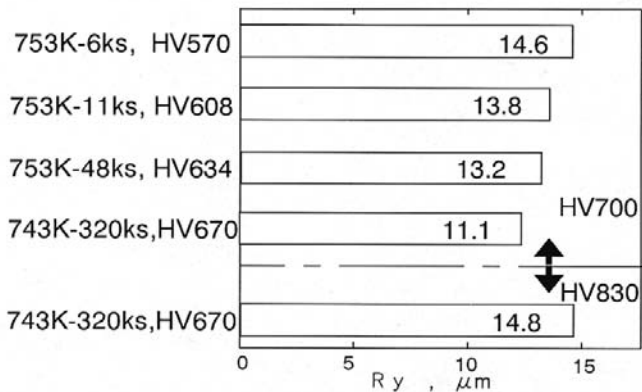
Figure 3:   Surface roughness of shot peened specimen.
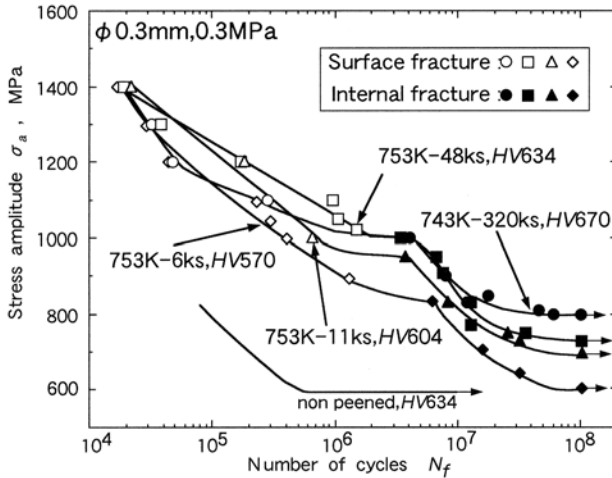
Figure 4:   *S-N* curves of shot peened specimen.
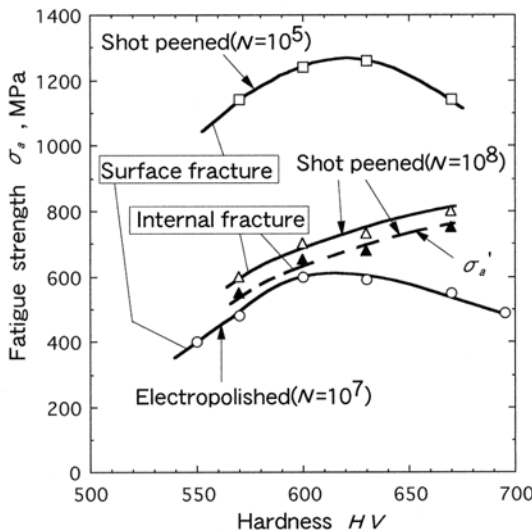
Figure 5:   Relation between fatigue strength and hardness.

Figure 4 shows *S-N* curves of shot-peened specimens. In the figures, open marks and solid ones mean a surface fracture and an internal one, respectively. In all of shot-peened specimens, fracture initiated from the specimen surface in the short life region and an internal fracture occurred from the subsurface in the long life region, while only surface fracture occurred from specimen surface in electro-polished specimens in wide life range. Fatigue strength was increased markedly by shot peening, while the increase in fatigue strength was small in long life region. *S-N* curves of shot peened specimens show duplex *S-N* shape

similar to the ones of many high strength steels and surface treated steels [7-9]. However, the horizontal line in *S-N* curve, which corresponds to the fatigue limit for surface fracture, is not clear.

(a) HV634

(b) HV670
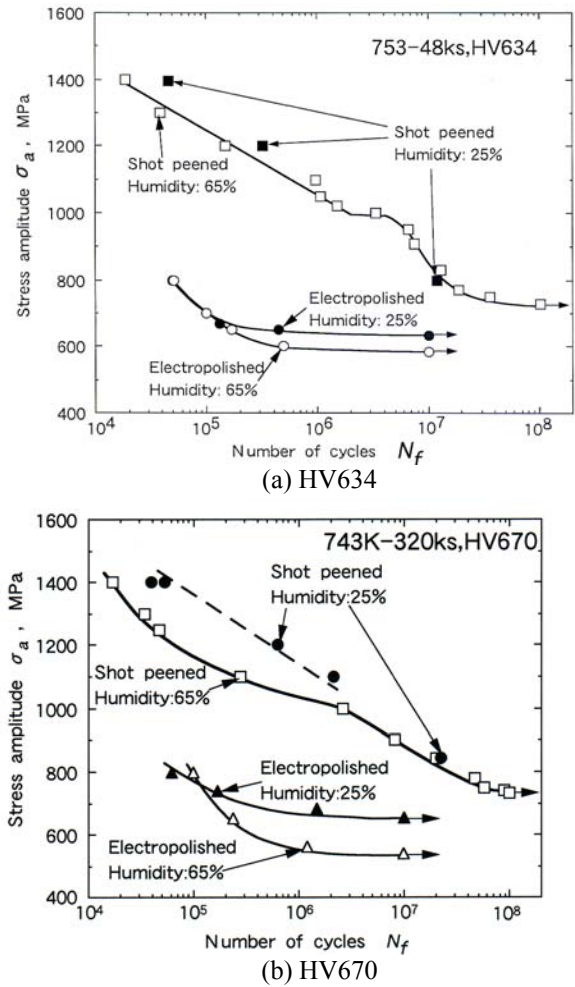
Figure 6:   *S-N* curves of shot peened specimen in humidity of 25%.

Figure 5 shows hardness dependence of fatigue strength of shot-peened specimens. In the figure, fatigue strengths at 10^5 and 10^8 are indicated as ones for surface fracture and internal one, respectively. Although fatigue strength for internal fracture increases with increasing hardness, one for surface fracture shows peak value around HV600 and then decreases with increasing hardness. In general, linier relation between fatigue strength and hardness holds until around HV400 and beyond the hardness, fatigue strength decreases in high strength steels [10, 11]. The reason for this breakdown in the relation was explained by

the high notch sensitivity of high strength steel [5, 6]. From this standpoint, the effect of hardness on fatigue strength should be the same regardless of fracture type. Moreover, surface roughness decreased with increase in hardness in this study as shown in fig.3. Therefore, it is difficult to explain the difference in hardness dependence between fatigue strengths for surface fracture and internal one from viewpoint of notch sensitivity. On the other hand, fatigue strength of high strength steel is affected by environment even in an ambient air. Therefore, in the following, the results mentioned above will be investigated from viewpoint of effect of humidity.

(a) HV550   (b) HV750
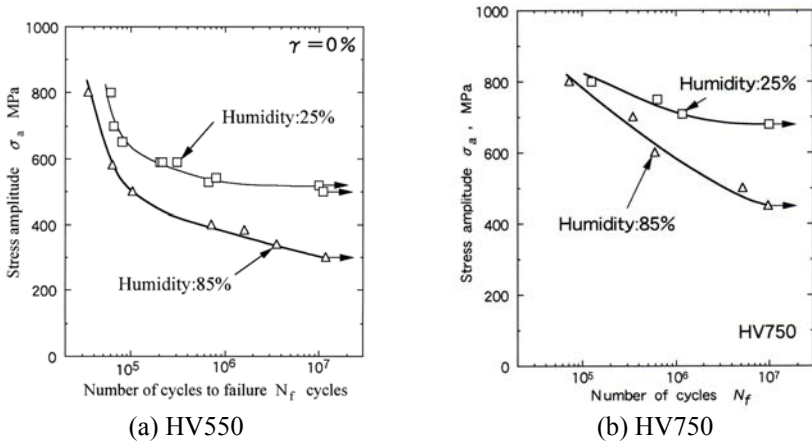
Figure 7:   S-N curves of electro-polished specimen in humidity of 25% and 85%.
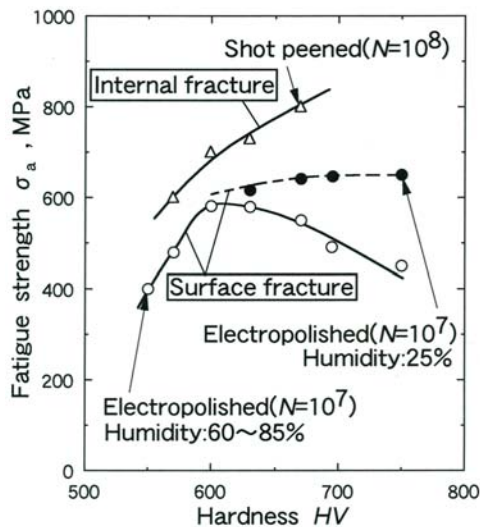
Figure 8:   Relation between fatigue strength and hardness.

Figure 6 is *S-N* curves of shot-peened specimens showing the effect of humidity in cases of materials of HV634 and 695. Fatigue strength in humidity of 25% increases in the surface fracture region in comparison with the results in ambient air, though fatigue strength for internal fracture does not change.

Figure 7 shows *S-N* curves of electro-polished specimens in humidity of 25% and 85%. In electro-polished specimens, all of fractures occurred from specimen surface. Large decrease in fatigue strength for surface fracture is confirmed in high humidity.

Figure 8 shows relation between fatigue strength of shot peened specimen and hardness in low humidity in addition to the results in fig. 5. Linear relation between fatigue strength and hardness holds beyond HV600 even in fatigue strength for surface fracture. That is, hardness dependence of fatigue strength for surface fracture is nearly the same as the one for internal fracture.

Figure 9 shows fracture surfaces in case of the specimen of HV670. Intergranular cracks are observed on fracture surface as indicated arrow mark in high humidity, while there is no intergranular crack in low humidity. That is, a main reason for lower fatigue strength in high humidity is an acceleration of crack growth by intergranular crack.

σ_a=570MPa, *N*=1.29×10^6 σ_a=700MPa, *N*=1.62×10^6

(a) In high humidity   (b) In low humidity
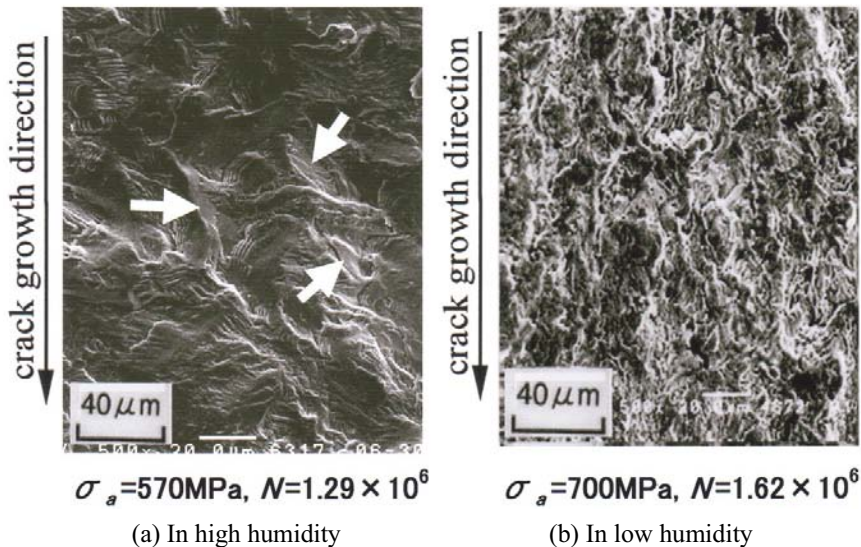
Figure 9:   Fracture surfaces of electro-polished specimen (HV670).

From mentioned above, in considering the hardness dependence of fatigue strength in high strength steel, we must notice not only about notch sensitivity but also about humidity-sensitive. Especially an attention to the effect of humidity on fatigue strength of maraging steel should be paid, because the range of humidity from 25% to 85% is not special case as ambient air in practical use.

4   Conclusions

Hardness dependence of fatigue strengths for surface fracture and internal one of maraging steel was investigated using shot peened specimens under rotating bending. Fatigue strength for surface fracture was evaluated by the fatigue strength at 10^5 cycles and that for internal fracture was by the one at 10^8 cycles. Both of fatigue strengths for surface fracture and internal one increased with increase in hardness. However, the proportional relationship between fatigue strength and hardness existed till higher hardness in the fatigue strength for internal fracture than in the one for surface fracture. The difference in the hardness dependence of fatigue strength was explained from the influence of humidity.

References

[1] Zackey, V. F., Parker, E. R. & Wood, W. E. Proc. of the 3rd Inter. Conference on the Strength of Metals and Alloys, 25, pp. 175-179, 1973.
[2] Fukada, K., Kawagoishi, N., Morino, K. & Nisitani, H., Steel, Surface Treatment V, pp.203-208, 2001.
[3] Kawagoishi, N., Nagano, T., Moriyama, M. & Kondo, E., Key Engineering, Vols 348-349, pp.537-540, 2007.
[4] Kawagoishi, N. Nagano, T., Moriyama, M. Ohzono, Y. & Kondo, E., Jour. of Soc. of Mater. Sci., Japan, Vol. 55, pp.843-848, 2006.
[5] Murakami, Y. & Shimizu, M., Trans. Jpn. Soc. Mech. Eng. A. Vol.54, pp.413-425, 1983.
[6] Endo, K,. Komai, K. Fujimoto, T. & Matsuda, Y., Trans. Jpn. Soc. Mech. Eng. A., Vol.45, pp.1152-1159, 1979.
[7] Kawagoishi, N., Morino, K. Fukada, K, Chen, Q. &Kondo, E., Steel, Surface Treatment V, pp.209-217, 2001.
[8] Shiozawa, K. Tao, L. & Ishihara, S., Jour. of Soc. of Mater. Sci., Japan, Vol. 48, pp.1095-1100, 1999.
[9] Nakajima, M., Sakai, T. & Shimazu, T., Trans. Jpn. Soc. Mech. Eng. A., Vol.65, pp. 2504-2510, 1999.
[10] Masuda, C. Nishijima, S. & Tanaka, Y., Trans. Jpn. Soc. Mech. Eng. A. Vol.52, pp.847-852, 1986.
[11] Sawai, T., Kimura, Y., Tusaki, K., Takeuchi, E. & Matsuoka, S., Trans. Jpn. Soc. Mech. Eng. A., Vol.68, pp49-56, 2002.

This page intentionally left blank

Section 7
Numerical analysis

This page intentionally left blank

New method of determination of the tool rake angle on the basis of the crack angle of the specimen in tensile tests and numerical simulations

L. Kukielka[1], J. Chodor[1] & B. Storch[2]
*[1]Department of Mechanical Engineering,
Koszalin University of Technology, Poland*
*[2]Department of Processes Monitoring,
Koszalin University of Technology, Poland*

Abstract

Turning is a very complicated technological process. To increase the quality of the product and minimize the cost of turning, we should know the physical phenomena that exist during the process. In some of the literature the thermo-mechanical models and other dependencies between the shape of the tool and the shape of the chip are presented. This paper is a continuation of previous issues and focuses on proper determination of active cutter geometry. A new method of determination of tool rake angle γ in two steps is presented. In the first step the basic angle γ is determined on the basis of the crack angle of the specimen in a tensile test. In the second step the optimal angle γ is determined using numerical simulations. The influence of the cutter geometry in the active part and the tool rake angle γ on the states of strain and stress in the surface layer during turning is explained. The phenomena on a typical incremental step were described using a step-by-step incremental procedure, with an updated Lagrangian formulation. The turning process is considered as a geometrical and physical non-linear initial and boundary problem. The finite element method (FEM) and the dynamic explicit method (DEM) were used to obtain the solution. The application was developed in the ANSYS/LS-DYNA system, which makes possible a complex time analysis of the physical phenomena: states of displacements, strains and stresses. Numerical computations of the strain have been conducted with the use of methodology, which requires a proper definition of the contact zone, without the necessity to introduce boundary conditions. Examples of calculations are presented.
Keywords: turning, chip creation, tensile test, yield stress, FEM, numerical analysis, state of strain, state of stress.

1   Introduction

In order to improve metal cutting processes, e.g. lower the part cost, it is necessary to model metal cutting processes at the system level. A necessary requirement of such is the ability to model interactions at the tool–chip interface and thus, predict cutter performance. Some model of testing for model development, either material, machining, or both, is required for all. However, the ability to model cutting tool performance with a minimum amount of testing is of great value, reducing costly processes and tooling iterations.

The process of the chip creation proves to have a substantial influence on the turning process, together with the geometrical and kinematics' dependencies in the contact zone of the cutter – the object machined. It has a significant impact on the wear of the cutter, the value of the components of the turning force, the temperature and the quality of the surface machined.

During the turning process, there occur large and fast plastic strains, which occur only in the part of the object machined. Under the influence of these strains in the material, its physical properties are subject to change: the hardness and strength increase. There occurs the so-called consolidation phenomenon of the material. The geometry of the zone of the chip creation during machining allows one to accept an assumption that in the area in question there is a plate state of strains.

For the correct modelling and analysis of the turning process, knowledge of the course of the physical phenomena occurring in the machining zone in real conditions (i.e. the geometry of the cutter and the technological parameters) proves to be necessary. For this purpose, an analysis of the process of turning with a cutter was conducted. The object is considered as the elastic/visco-plastic body and it rotates with the rate of turning of ω around its own axis (Fig. 1).

In papers [1, 2], a thermal and mechanic model of the process of the grain displacement on the elastic/visco-plastic body was developed and the distribution of temperatures were determined together with the intensities of strain in the material machined in the initial chip creation phase.

This paper shows how to properly create the surface layer of the product. The finite element method (FEM) is used to calculate chip geometry, its formation and separation from the body. A new method of determination of the tool rake angle γ in two steps is presented. Initially, the basic tool rake angle γ was determined from a tensile test. Then, using numerical simulation, the optimal angle γ was established. This ensures the best durability of the cutter, i.e. the lowest power of material deformation. For this case the states of stress and strains in the surface layer of the object at any time of the process were calculated.

2   Basic cutter rake angel

2.1   Method of determination

An analogy of physical phenomena was used during the turning and tensile test. According to the literature [6], necking, which is made in specimen in the tensile
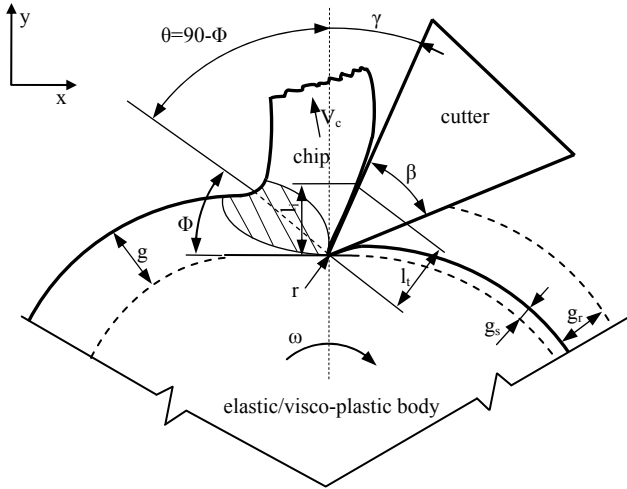
Figure 1:   Diagram of the considered issue of the elastic/visco–plastic body with rate of turning ω using a 2D model (g is the depth of cut, g_r is the real depth of cut, g_s is the elastic deformation of material, β is the cutter angle in active part, r is the corner radius, ω is the rate of turning, Φ is the cutting angle, γ is the tool rake angle, V_c is the chip velocity).
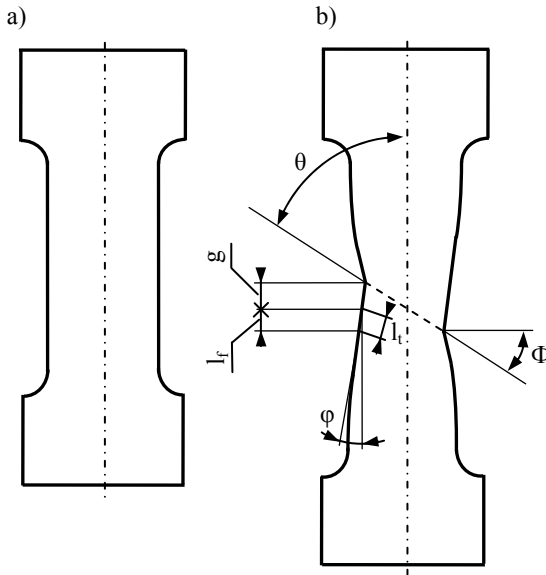
Figure 2:   View of specimen: a) before tensile test, b) after tensile test.

test (Fig. 2), is similar for every kind of material (crack angle $\Phi \sim 45°$). Many numerical calculations and their verification in real conditions do not overlap with the above statement.

In this section the first step to determinate a basic tool rake angle γ is shown. An analogy of physical phenomena was used during the turning and tensile test. The cutting angle Φ and crack angle Φ are similar. During the tensile test, the elongation of specimen and necking angle φ depend on the plasticity of the material. The tool rake angle γ, which is necessary for separating the material, can be described using the necking angle φ and the parameter of elongation ξ defined as (Fig. 2):

$$\xi = (l_t - l_i)/l_i. \tag{1}$$

From Fig. 1, we have:

$$\cos \gamma = l_i/l_t, \tag{2}$$

and from Fig. 2:

$$\cos \varphi = l_f/l_t. \tag{3}$$

Using l_f determined from formula (2) and (3), we obtain:

$$\cos \gamma = l_i \cos \varphi /l_f, \tag{4}$$

and then the value of the rake:

$$\gamma = \arccos(l_i \cdot \cos \varphi /l_f) = \arccos[l_t \cdot \cos \varphi)/l_f \cdot (\xi + 1)]. \tag{5}$$

The necessary angle φ and parameter ξ are determined from the tensile test.

2.2 Experimental results

Tensile tests were made on a testing machine ZD20 (200 kN) to determine the angle φ and parameter ξ, required to determine the basic tool rake angle γ.

Many experiments were carried out on four different materials: stainless steel 303, 4340 steel, AISI 1042 steel and titanium alloy Ti6AI4V. Fig. 3 shows the sample after the tensile test on universal testing machine ZD 20.
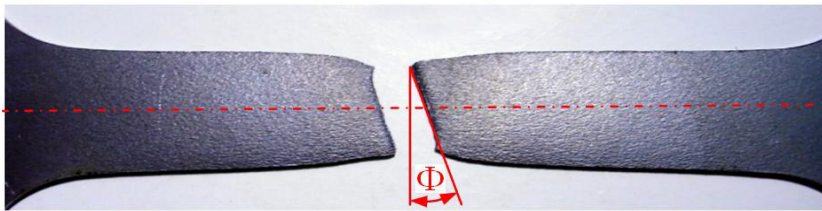
Figure 3:   View of specimen after tensile test with marked crack angle Φ for stainless steel 303.

After research we obtained the following tool rake γ angles: stainless steel 303 is $\gamma = 46^0$, AISI 4340 steel is $\gamma = 40^0$, 1042 steel is $\gamma = 44^0$, and titanium alloy Ti6Al4V is $\gamma = 33^0$. Then, using the above cutters, the turning process was carried out. Experiments were made on the same machining centre - NEF400 (FANUC MANUAL GUIDE) with traverse $f = 0.1$ [mm] and depth of cut $g = 1.9$ [mm]. The velocity of machining was different and depended on the type of material. The shapes of the chips after machining were different and were characteristic for every type of material. The original tool, used for comparison, had the same tool rake angle $\gamma = -7^0$.
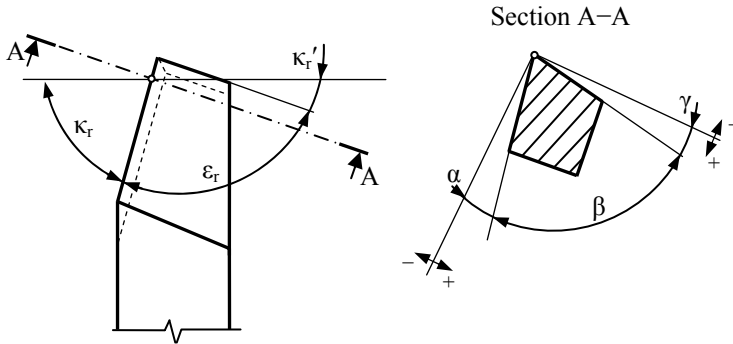
Figure 4:   Main angles of the cutter [7].

Experiment 1: Material machined – stainless steel 303.
Parameters of new geometry tool: $\gamma = 46^0$, $\kappa_r = 46^0$, and width of chip: $X = 0{,}127 \ [mm]$. The main angles of the cutter are shown in Fig. 4, where ε_r is the apex angle of the cutter and κ_r and $\kappa_r{'}$ are the main and auxiliary tool cutting edge angles, respectively.

Experiment 2: Material machined – AISI 4340 steel.
Parameters of new geometry tool: $\gamma = 40^0$, $\kappa_r = 40^0$ and $X = 0{,}254 \ [mm]$.
Five experiments were carried out using the base geometry of the tool and four experiments were carried out with the new geometry of the cutter. The tool with the original geometry allowed one to machine about 504 [mm] of material, whereas the new geometry tool allowed one to machine about 820 [mm] of material.

Experiment 3: Material machined – 1042 steel.
Parameters of new geometry tool: $\gamma = 44^0$, $\kappa_r = 44^0$ and $X = 0{,}127$ [mm].
Four experiments were carried out using the base geometry of the tool and four experiments were carried out with the new geometry of the cutter. The durability of the new geometry tool was much higher than the old one.

Experiment 4: Material machined – titanium alloy Ti6AI4V.
Parameters of new geometry tool: $\gamma = 33^0$, $\kappa_r = 33^0$ and $X = 0{,}127$ [mm].
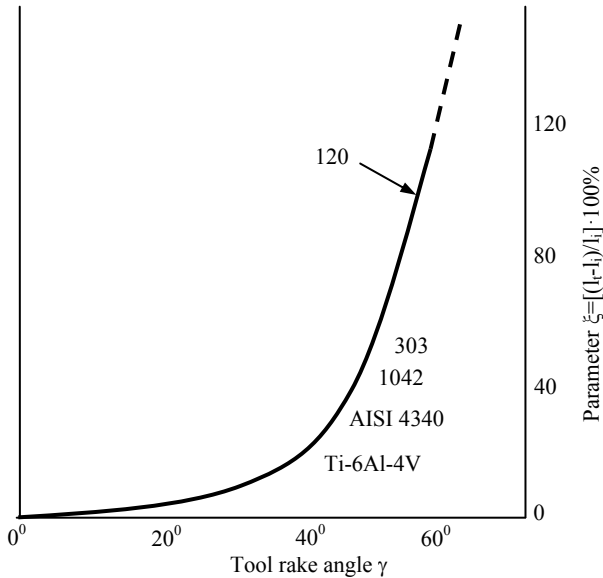
Figure 5: Dependence between tool rake angle γ and decreasing parameter of machining resistance ξ.

Three experiments were carried out using the base geometry of the tool and four experiments were carried out with the new geometry of the cutter. The durability of the new geometry tool was higher than the old one.

Fig. 5 shows the visual results of the experiments. Curve number 120 shows dependence between tool rake angle γ and parameter ξ. The angle changes between 0° and 24° for fragile materials (e.g. cast iron) and for materials that have unit elongation of about 10% (e.g. constructional steels, stainless steels, non-ferrous metals, aluminium, titanium).

The optimal tool rake angle γ is in situation when the turning power, which is dependent (for set-up turning feed and velocity) on the deformation power of the turned material, is low. If the turning power is lower than the durability of the cutter, the tool rake angle is larger. The static tensile test takes place during low strain rates of about $\dot{\varepsilon}_i = 10^{-4}$ s^{-1}, but real strain rates of material during turning are much higher and equal about $\dot{\varepsilon}_i = 10^4 \div 10^5$ s^{-1}, so modification of angle γ seems to be necessary. To solve this problem and to determine the optimal angle γ, numerical simulations of the turning process were conducted.

3 Numerical calculations

3.1 Numerical algorithm

Turning is considered as a geometrical and physical nonlinear initial and boundary problem. The analytic solution of this problem, such as the

determination of states of deformations and stresses in any moment of duration of the process, is impossible. Therefore this problem was solved by the FEM. An application was developed in the Ansys/LS-Dyna programme, which makes a complex time analysis of the states of deformation (displacements and strain) and stress in the surface layer of the object at/after turning possible.

For the purpose of the solution of the problem, the Dynamic Explicit Method (DEM), also known as the Method of Central Differences, was used. In this method, the equation that describes the movement and deformation of the object investigated on the typical step time, in updated Lagrangian formulation, has the following form:

$$\mathbf{M} \cdot \Delta \ddot{\mathbf{r}} + \mathbf{C}_T \cdot \Delta \dot{\mathbf{r}} + (\mathbf{K}_T + \Delta \mathbf{K}_T) \cdot \Delta \mathbf{r} = \Delta \mathbf{R}_T + \Delta \mathbf{F} + \mathbf{F}_T \tag{6}$$

where $\mathbf{M}$ is the global system-mass matrix at time t, $\mathbf{C}_T$ is the global system-damping matrix at time t, $\mathbf{K}_T$ is the global system stiffness matrix at time t, $\Delta \mathbf{K}_T$ is the global system stiffness-increment matrix at the step Δt, $\mathbf{F}_T$ is the global system internal and external load vector at time t, $\Delta \mathbf{F}$ is the global system internal load increment vector at the step Δt, $\Delta \mathbf{R}_T$ is the global system external load increment vector at step time Δt, $\Delta \mathbf{r}$ is the global system displacement increment vector at step time Δt, $\Delta \dot{\mathbf{r}}$ is the global system velocity increment vector at step time Δt and $\Delta \ddot{\mathbf{r}}$ is the global system acceleration increment vector at step time Δt. This equation is not solvable due to the number of unknowns exceeding the number of equations. An approximation by the central difference method has been applied to express $\dot{\mathbf{r}}$ and $\ddot{\mathbf{r}}$ vectors using the displacement vectors at moments: $t - \Delta t, t, t + \Delta t$:

$$\dot{\mathbf{r}}^t = \frac{1}{2\Delta t} \cdot (\mathbf{r}^{t+\Delta t} - \mathbf{r}^{t-\Delta t}), \text{ and } \ddot{\mathbf{r}}^t = \frac{1}{\Delta t^2} \cdot (\mathbf{r}^{t+\Delta t} - 2\mathbf{r}^t + \mathbf{r}^{t-\Delta t}).$$

It was accepted in the simulations that the cutter (Fig. 6) is a non-deformable body, but it can also be an elastic body for precise calculations, while the object is an elastic/visco-plastic body described with the aid of the Cowper–Symonds model. The Huber–Mises–Hencky plasticity model is used together with the associated flow right. The model takes into consideration the line–isotropic ($\eta = 1$) kinematic ($\eta = 0$) or mixed ($0 < \eta < 1$) plastic hardening, as well as the influence of the intensity of the plastic strain rate, according to the involution dependence:

$$\sigma_Y = \left(\sigma_0 + \eta \cdot E_{tan} \cdot \varepsilon_i^{(p)} \right) \cdot [1 + (\dot{\varepsilon}_i^{(p)}/C]^m \quad [MPa] \tag{7}$$

where σ_Y is the yield stress, $\sigma_0 \, [MPa]$ is the initial yield stress point, $\varepsilon_i^{(p)} \, [-], \dot{\varepsilon}_i^{(p)} \, [s^{-1}]$ is the intensity of true strain and plastic true strain rate respectively, $C \, [s^{-1}]$ is the material parameter to determine the influence of the intensity of the plastic strain rate, $m = 1/P$ is the material constant determining the sensitiveness of material on the plastic strain rate and $E_{tan} = E_T E/(E - E_T)$ is the material parameter dependent on the module of plastic hardening $E_T =$

$\partial\sigma_Y/\partial\varepsilon_i^{(p)}$ and of Young's elasticity module E. The parameters used in numerical calculations depended on the material, as each one was different.

3.2 Optimal tool rake angle

In order to determine the optimal tool rake angle γ for the chosen material, numerical simulations were conducted. Angle γ was changed every $0^030'$ (increasing and decreasing), starting from angle γ, which was determined from the tensile test (section 2).

The chosen results of the numerical simulations of the states of stress and strain during turning stainless steel 303 with $\beta = 50^0$ and $\gamma = 20^0$ are shown in Fig. 6.
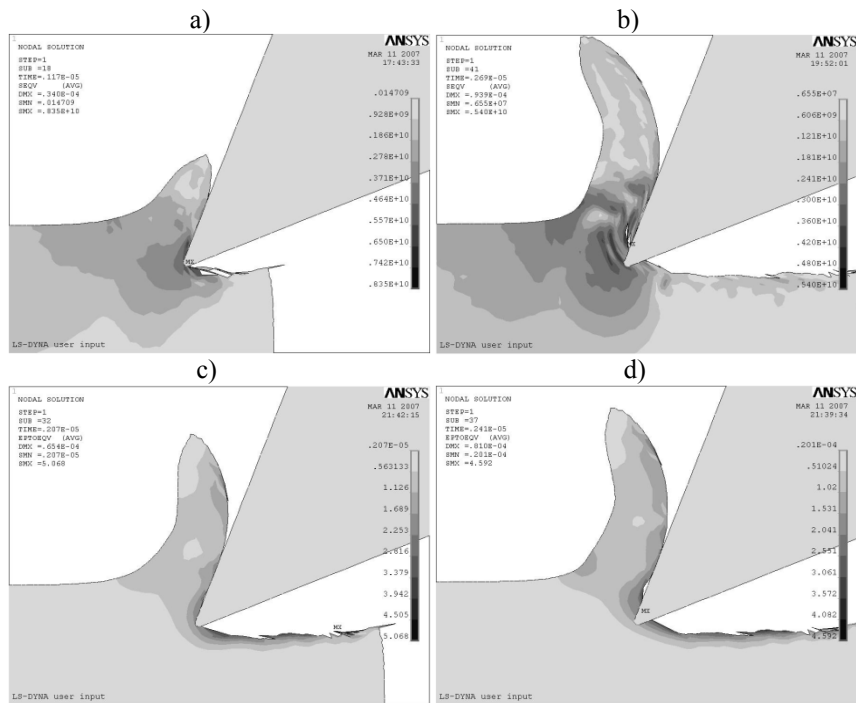
Figure 6:   View of 2D turning with example chip shapes and marked stress (a,b) and strain (c,d) distribution.

In Fig. 6 we can observe high values of stress intensities (b), especially in the plane of shear and in the contact zone of the cutter with the chip. The high value of strain is in the surface layer of material machined (d).

Fig. 7 shows turning of the AISI 4340 steel with $\beta = 70^0$ and $\gamma = 10^0$. We can notice the strip chip, which is curling in the direction of the foundation. This is characteristic for high velocity machining.
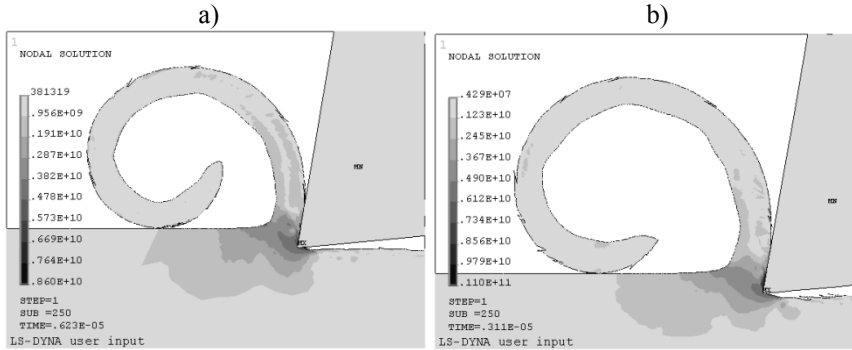
Figure 7:   View of 2D turning with example chip shapes and marked stress distribution (a,b).
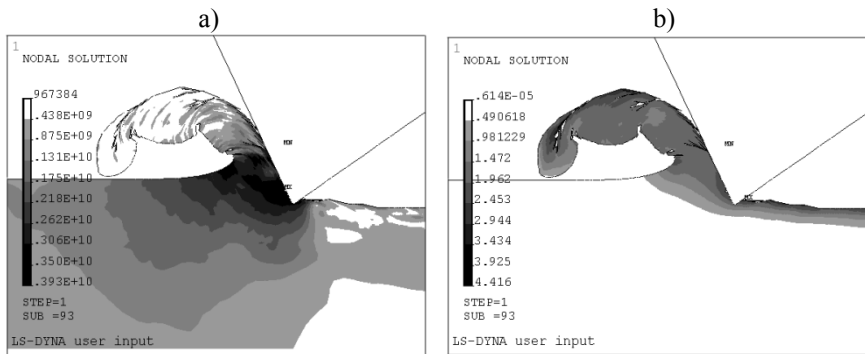
Figure 8:   View of 2D turning with example chip shapes and marked stress (a) and strain (b) distribution.

In Fig. 8 we can observe the turning process of 1042 steel with $\beta = 80°$ and $\gamma = -25°$. The chip that is created is a step chip. The maximum value of stress is in the plane of shear and equals about $\varepsilon = 3900$ [MPa].

From the above figures it can be seen that the smaller value of angel γ causes much better strain distribution in the material machined, especially in the surface layer. However, the growth of angel γ causes much less machining resistance and stress distribution.

4   Conclusions

Experiments shows us that the real cutting angle changes between 33° and 46° or between 39° and 53°. The geometry of the tool that is presented in this paper is the result of many numerical calculations and experiments in real conditions. It allows machining materials with a minimum loss of energy, minimum heat transfer and much greater strength of the tool material.

An application of modern numerical methods and computing systems allows an analysis of the complex physical phenomena occurring in the process under investigation. The application developed in the ANSYS/LS-DYNA system enables a time analysis of the process of machining with a cutter, with the consideration of the changeability of the cutter's apex angle and the tool rake angle.

The distribution of stresses and strains obtained for different cutter geometries and action angles, in particular the phases of the deformation process, can be made use of while designing machining: making a selection of the machining conditions and their optimisation in the aspect of the technological quality of the product.

The material flashes obtained before the cutting edge and the shape of the chips are similar to the results of experiential investigations, confirming the justifiability of the use of computer simulations and their reliability.

References

[1] Kukielka L., Kustra J.: Numerical analysis of thermal phenomena and deformations in processing zone in the centreless continuous grinding process. *Surface Treatment VI Computation Methods and Experimental Measurements for Surface Treatment Effects*. Ed. C.A. Brebbia, J.T.M. de Hosson, S-I. Nishida WIT Press, Southampton, Boston, 2003, pp.109-118.

[2] Kukielka L., Kustra J., Kukielka K.: Numerical analysis of states of strain and stress of material during machining with a single abrasive grain. *Computer Methods and Experimental Measurements for Surface Effects and Contact Mechanics VII*. WIT Press Southampton, Boston 2005, pp. 57-66.

[3] Kukielka L., Chodor J.: Numerical analysis of the influence of abrasive grain geometry and cutting angle on states of strain and stress in the surface layer of object. *Surface/Contact 2007 Conference*, Wessex Institute, Ed. J.T.M. De Hosson, C.A. Brebbia, S-I.Nishida, WIT Press Southampton, Southampton 2007, UK, pp.183-193.

[4] Kukielka L., Chodor J.: *Numerical analysis of chip formation during machining for different value of failure strain*. PAMM, Volume 7, Issue 1, p. 4030031-4030032. Zürich 2007, Switzerland.

[5] Kukielka L. Chodor J.: Numerical analysis of micromachining of C45 steel with single abrasive grain, *79th Annual Meeting of the International Association of Applied Mathematics and Mechanics*, Bremen 2008, Germany.

[6] Mundy William L.: *Cutting tool for the continuous machining of metals and the method of making same*, O'Fallon Investment. Co., Express Information, Moscow 1975.

[7] Storch B.: *Phenomena on cutting edge and monitoring of surface roughness after one-egde machining*. Monograph of Faculty Engineering, Nr 124, Publisher of Koszalin University of Technology.

Finite element method numerical simulation and ductile capacity analysis of bond-slip between epoxy coated plain steel bars and concrete

K. Kazakov[1] & A. Yanakieva[2]
[1]*Structural Mechanics Department, Higher School of Civil Engineering, Bulgaria*
[2]*Institute of Mechanics, Bulgarian Academy of Science, Bulgaria*

Abstract

This research is devoted to a finite element method (FEM) numerical simulation of the bond-slip between epoxy coated plain steel bars and concrete and the ductile capacity of the mechanical process of extracting the steel bars. In this case the cured epoxy coating is assumed to be mid-layer, located between the steel bar and the concrete. This layer leads to a change of the ductile capacity of the bond and to some differences in the nonlinear bond-slip relation in comparison with the bond-slip relation in the case of non-insulated steel bars. The aim of the research is the generation of an adequate numerical model for extracting the bond-slip relation. For that purpose, a more realistic concrete material model is assumed in the proposed computational model, by means of development of dispersion micro cracks. The pull-out force is compared with the force recorded in an experiment.

   The ductile capacity of the bond is also analyzed and discussed in detail. The analysis is performed by the FEM.

Keywords: FEM contact problems, bond-slip relation, ductile capacity, epoxy coated plane steel bars.

1   Introduction

A good bond between the steel reinforcing bar and concrete in concrete structures is decisive for structural and durable performance. If this bond is

inadequate, the behaviour and failure development can be altered. Very often in engineering practice, the steel used in the reinforced concrete elements is isolated by epoxy coating. Such a coating influences the bond-slip relation and pull-out force, i.e. the ultimate force, during the extraction process.

In the last three decades, many papers have been reported in this research area. In 1988 Gustafson [1] founds that coated deformable bars developed approximately 66% of the bond strength of the uncoated bars. The tests showed that the epoxy coating, whatever its thickness, is essentially the bond breaker of the adhesion bond. Choi *et al.* [2] consider the effect of various factors including coating thickness, bar size and deformation pattern. The effect of epoxy coating thickness on bond strength is also evaluated by Miller *et al.* [3]. In their experimental study, Cleary and Ramirez [4] compared the effect of repeated loading on the service behaviour and ultimate bond strength of reinforced concrete members containing epoxy-coated reinforcement to that of members with uncoated reinforcement. Kayyali and Yeomans [5] report the results of investigation into the bond of epoxy coated reinforcement in concrete beams acting in flexure, compared to that using pullout testing. Hamad [6] and Ldun and Darwin [7] assess the effect of rib geometry/rib angle, rib spacing, rib height and concrete strength on the relative bond-slip characteristics of coated and uncoated deformed bars. The value of bar-friction coefficient has been obtained (Prostatio [8]) by testing a concrete tension strut reinforced with a manually applied epoxy coated steel bar. In conclusion, there are many studies that take into account and discuss the parameters that influence bond behaviour, but these are mainly from test procedures [9, 10]. Besides, more of these investigations are assigned to deformable bars. The joineries in the precast concrete structures are prepared by plain steel bars welded to some built-in reinforcement. Placing the plain rebars along either side of the joint will strengthen its resistance and provide greater ductility. Therefore, the bond properties of plain bars in concrete need to be understood (Mo and Chan [11]).

In this paper two computational models are proposed. The results corresponding to the pull-out process bond-slip relations are excerpted and the ultimate extraction forces are obtained. The simulations are based on a step-by-step extraction of an isolated steel bar from a concrete body and strictly adhere to the experimental settings, reported in [12]. The first model, called Model A, is based on the précised multi-linear stress-strain concrete relation. This model is compared with a computational model, reported by the authors in [13]. In the second model, called Model B, in addition to Model A, the development of dispersion micro cracks is included.

The components, those that significantly influence the bond-slip behaviour, are discussed in detail. The so-called ductility capacity of the bond is also investigated.

2 Finite element method contact technology

Finite element method (FEM) contact technology requires a fine step-by-step increment to assure a smooth transfer of contact forces and iteration stability. If

the interaction area is a surface, the corresponding adequate computational model should be generated by surface-to-surface contact elements [14]. Such a model recognizes possible contact pairs by the presence of specific finite contact elements. These contact elements are overlaid on the part or parts of the model areas that are being analyzed for interaction.

2.1 Contact pair finite elements

The contact pairs contain two finite elements – contact and target elements with the same real constants as penetration, friction constant, maximum friction stress, contact surface offset, contact cohesion, tangent penalty stiffness factor, pinball region and etc.

Target elements are used to represent the body surface, in the present research it is the surface of the concrete block hole. In this paper, the so-called concrete solid finite element (CSFE) is used the concrete body to be discretized, see fig. 3. The solid is capable of cracking in tension and crushing in compression. The element is defined by four nodes and isotropic material properties. Target volume can be assumed as rigid or deformable. In the Model A and Model B, it is chosen as deformable, for the Poisson effect to be taken into account. Target elements are generated with an external surface that has the same shape and mesh as the underling solid elements. These elements have 4 nodes and 12 DOFs. Generally, in the FEM concept, target elements impose kinematic constrains which prevent penetration of one body through another. However, the computational models, discussed in the paper, are built in such a way that the contact of the steel surface and the concrete is taken as an initial. The contact can be closed only on some subareas of the contact zone due to the Poisson ratio. Some details, related to the theoretical aspects of the contact status, are discussed below.

Contact elements are used the steel bar surface to be discretized and to represent the contact and sliding between the 3D contact surfaces. Such an element overlies the solid elements describing the boundary of a deformable body, in the present research the steel bar, and is potentially in contact with the target surface. It has the same geometric characteristics as the solid with which it is connected. The rebar is discretized, see fig.3, by the so-called steel solid finite elements (SSFE).

Generally, contact occurs when the contact element surface penetrates one of the target segment elements on the specified target surface. In the present models, the contact and penetration are assumed as initial. The FEM module preliminary evaluates the model to detect the initial contact conditions. The target and contact elements are attached to the hollow radius of the concrete body and to the outer radius of the rebar, respectively. These elements are nonlinear and require a full Newton-Raphson iterative solution, regardless of whether large or small displacements are specified. The iterations detect the contact status of the nodes. In the present study large sliding and large displacement applications are involved. Each contact pair has a pair-based depth which is obtained by averaging the depth of each contact element across all the contact elements.

2.2 Contact status

In the present study the contact of the steel bar and the concrete is taken as open on the initial stage. The contact can be closed only on some subareas of the contact zone due to the Poisson effect, affecting as a reduction of the rebar radius. The contact status, opened or closed, is monitored by the gap, calculated for the upper nodes as

$$g = z_2^c - z_2^s = \left[Z_2^c - u_2^c\right] - \left[Z_2^s - u_2^s\right], \tag{1}$$

where z_2^c and Z_2^c denote respectively the current and reference coordinate of a node from the concrete contact surface, z_2^s and Z_2^s denote respectively the current and the reference coordinates of a node from the steel contact surface, and u_2^c and u_2^s are the displacements of the concrete and the steel bar contact nodes, respectively, perpendicularly to the contact surface. The subscript 2 means the contact surface, described by the functions of the form of the steel bar elements.

The location of the contact detection points coincides with the location of the Gauss integration points. In alternation, the nodal point can be used.

2.3 Contact calculation method

In the basic Coulomb friction model, two contacting surfaces can carry shear stress up to a certain magnitude across their interface before they start to slide relative each other. This stage is known as *sticking* stage. The Coulomb friction model defines an equivalent shear stress $\bar{\tau}$ ($\bar{\tau} = \mu p + c$), at which sliding on the surface begins as a fraction of the contact pressure. Once the equivalent shear stress is exceeded, the two surfaces will slide relative to each other. This stage is known as *sliding* stage. The calculations determine when a point transition from sticking to sliding or vice versa. By default, Coulomb and shear stress friction are allowed as isotropic or orthotropic. The contact stiffness is assumed to be updated on each load step. In the models one extension of the classical Coulomb friction is used. The real constant $\bar{\tau}$ is the maximum contact friction with units of stress. This maximum contact friction stress can be introduced so that, regardless of the magnitude of normal contact pressure, sliding will occur if the friction stress reaches this value.

For surface-to-surface contacts five algorithms can be applied. Such algorithms are: Penalty method, Augmented Lagrangian method, Lagrange multiplier on contact normal and penalty on tangent, Pure Lagrange multiplier on contact normal and tangent and Internal multipoint constrained method. In the present study the Augmented Lagrangian method with gradient-base algorithm is used. This method can be interpreted as series of penalty methods, usually leads to better conditioning and is less sensitive to the magnitude of the contact stiffness. For Augmented Lagrangian method, normal and tangential contact stiffnesses are required. The penetration between the contact and the target

surfaces depends on normal stiffness. The Augmented Lagrangian method can be written symbolically in the form

$$\begin{bmatrix} k & -k \\ -k & k \end{bmatrix} \begin{Bmatrix} du_2^c \\ du_2^s \end{Bmatrix} = \begin{Bmatrix} -\lambda_k & -kg \\ \lambda & +kg \end{Bmatrix}, \tag{2}$$

or if the contact is non-sliding

$$\begin{bmatrix} k & -k \\ -k & k \end{bmatrix} \begin{Bmatrix} du_2^c \\ du_2^s \end{Bmatrix} = \begin{Bmatrix} -\lambda_k & -p \\ \lambda_k & +p \end{Bmatrix}. \tag{3}$$

In eqn. (2) k is a penalty parameter, λ_k is a Lagrange multiplier, identified here as "force" and $\lambda_{k+1} = \lambda_k + kg$. The components du_2^c and du_2^s give the ramp increment of the displacements. This method can be treated as compromise between the Penalty method and the Lagrange multiplier method. In the penalty approach the final gap must be non zero. On the other hand, for any Lagrange multiplier approach the equations are not positive defined and indeed have a zero diagonal for each multiplier term (Lagrange multiplier methods introduce zero diagonal terms in the stiffness matrix and any iterative solver will encounter a preconditioning matrix singularity with these methods). These computational difficulties are ignored in the concept of the Augmented Lagrangian method, the matrix $[k]$ is symmetric and positive defined.

2.4 Surface-to-surface contact

The surface-to-surface contact concept investigates the contact through the shape functions of the elements. After every iteration the value of τ stresses is checked and constitutes the states of the contact: if $\tau < \bar{\tau}$ then sticking stage is in being, or if $\tau > \bar{\tau}$, then sliding stage is observed.

This technique has some advantages in the case of different forms of the contact and target surfaces and anisotropic materials. To prevent rigid body motion the initial geometry must be checked and appropriate initial conditions must be defined. The adjustment of the initial contact conditions is important stage in the case of similar geometry and coordinates of the contact and target surfaces. In other words, the model must be built so that the contact pairs are in initial contact, i.e. open contact. The normal and tangential stiffness can be updated during the course of the analysis. In the computational models, presented in the paper, this option is used so that the stiffnesses to be automatically updated.

2.5 Concrete crack determination

The presence of a crack at an integration point is represented through modification of the stress-strain relations by introducing a plane of weakness in a

direction normal to the crack face. Also, a shear transfer coefficient β_t is introduced which represents a shear strength reduction factor for those subsequent loads which induce sliding across the crack face. If the cracks are developed in one direction only the stress-strain relation in based on the matrix

$$
\left[D^{cr}\right] = \frac{E}{(1+v)}
\begin{bmatrix}
\dfrac{R^t(1+v)}{E} & 0 & 0 & 0 & 0 & 0 \\[2mm]
0 & \dfrac{1}{1-v} & \dfrac{v}{1-v} & 0 & 0 & 0 \\[2mm]
0 & \dfrac{v}{1-v} & \dfrac{1}{1-v} & 0 & 0 & 0 \\[2mm]
0 & 0 & 0 & \beta_t & 0 & 0 \\[2mm]
0 & 0 & 0 & 0 & \dfrac{1}{2} & 0 \\[2mm]
0 & 0 & 0 & 0 & 0 & \dfrac{\beta_t}{2}
\end{bmatrix} . \quad (4)
$$

In eqn. (4) the superscript *ck* signifies that the stress strain relations refer to a coordinate system parallel to principal stress directions. R^t is the slope, illustrated in fig.1,
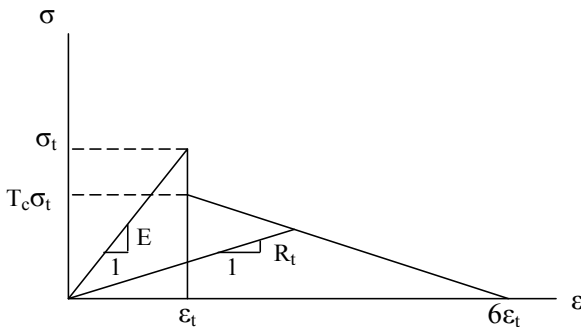
Figure 1:   Strength of cracked condition.

where σ_t is uniaxial tensile cracking stress and T_c - multiplier for amount of tensile stress relaxation.

3   Generation of the computational model

The steel bar material model is assumed to be totally linear. It has good reasons for such an acceptation, because the ultimate normal stresses, obtained in the steel bar, are less than the yielding stress (yield point of the strain-stress curve) for the grade of the steel, used in the experiment.
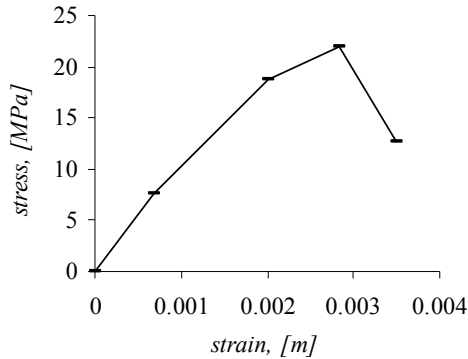
Figure 2:   Assumed multi-linear strain-stress relation.
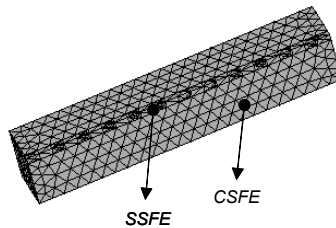
Figure 3:   FEM model.

The coordinates of the characteristic points from the graph, fig. 2, shows the assumed multi-linear strain-stress relation for the concrete elements (CSFEs).

Geometrical characteristics correspond to experimental test entirely [12] and the boundary conditions applied to the model are constraining the displacements of the concrete nodes, the position of which is on the front area of the concrete solid. The load is transformed to a step-by-step displacement of the front area of the steel bar. The displacement of the reinforcement increases up to the moment of the contact failure. By reason of symmetry of the setting only quarter of the geometry is used. The discretization mesh is illustrated in fig. 3.

4   Numerical results and ductile capacity analysis

4.1 Numerical results

In the present research two models are generated. The first one, called Model A, is based on the multi-linear strain-stress relation, illustrated on fig.2. The bond-relative slip relation is juxtaposed with the relation, reported in [13], where the concrete material model is assumed as bi-linear. In addition, in the second model, called Model B, the aim of which is to simulate more adequately the concrete behaviour in a region close to the contact surface, a special option of the CSFEs is used. Such an option allows development of dispersed micro cracks in the volume of the concrete.

The value of ultimate force reported in [13] is $F_{pullout}^{sim} = 31.36\,kN$. The force, obtained by the experiment is $F_{pullout}^{exp} = 22.12\,kN$. The relative difference between the two values is about 30%. In fig.4 can be seen the development of the bond stress-slip relation, in these two cases.

The ultimate forces during the extraction process obtained from Model A and Model B are respectively $F_{pullout}^{A} = 26.68\,kN$ and $F_{pullout}^{B} = 24.20\,kN$. Here, the relative differences in comparison with the test are 19% and 8%. The bond stress-slip relations concerning Model A and Model B are juxtaposed in fig.5.
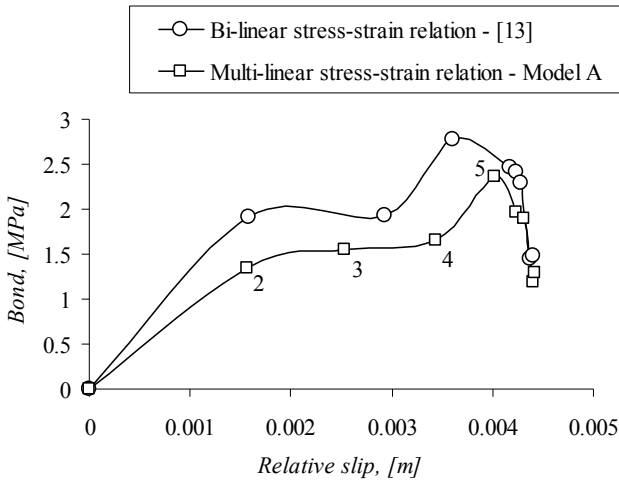
Figure 4:   Bond-relative slip relations (Model, given in [13] vs. Model A).

There are two possible ways for the global failure to be achieved. The first way is the case where the tensile stresses exceed the tensile strength of the concrete. This failure mode can be called *splitting failure mode* and dominates in cases where the concrete is well penetrated in the isolated steel bar concavities. The mode like this is peculiar to deformed steel bars. Due to the Poisson effect the change of the steel bar radius leads to decreasing the normal contact stress between the bar and the concrete. In the case of a surrounding concrete, well-confining the isolated steel bar, the failure mode can be called *pullout failure mode*. Such failure mode is typical for plane bars.

The Model A can be classified as splitting failure model, similar to the model reported in [13], by reason of the softening, observed between the second and the third points, given on the relation bond stress-relative slip, see fig.4, and the following increase of the contact capacity. The global failure begins once the ultimate pullout force is reached. On this stage all the contact status of the pull-out process is sliding, despite of some local increase of the force, observed probably because of the specific non-smooth geometry of the contact.

4.2 Ductility capacity of the bond

The bond stress-slip relation, related to Model B, can be classified as ductile contact behaviour. This leads to the need to give a new meaning to the failure modes and pull-out process as a whole. The region of the curve, limited between the points (point 4 and point 6) determines the ductile capacity of the bond. The length of the section presents the ductile capacity of the mechanical bond.
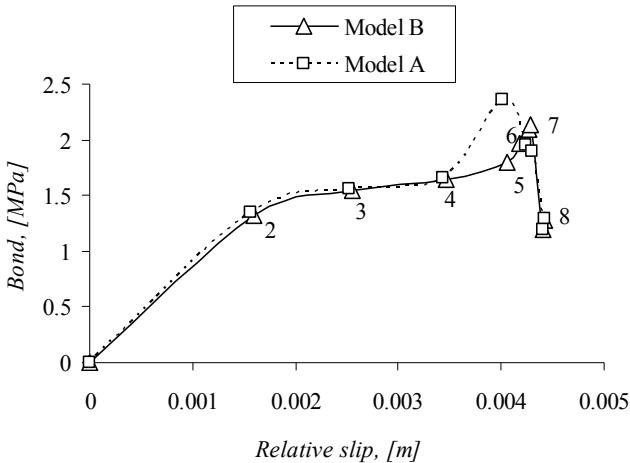
Figure 5:   Bond-relative slip relations, (Model A vs. Model B).

5   Conclusions

It can be concluded, that the proposed in this paper FEM models adequately simulate the pull-out process of the isolated steel bar from the concrete body. The multi-linear idealization of the stress-strain relation, concerning the concrete, leads to ultimate force closer to the experiment. An additional reduction of the ultimate force is observed due to the dispersion micro crack option introduced to the near to the contact surface concrete elements. More realistic modelling of the non-linear behaviour of the concrete obviously leads to reduction of the value of the ultimate pull-out force.

The ductile capacity of the bond can be treated as an important part of the ductile capacity of the entire structure. The real ductile capacity of the bond is more than the capacity, obtained by proposed models, because the steel bar and the cured epoxy coating are assumed as a solid with material parameters equivalent to the steel as a material. This assumption underrates the real deformations, which have arisen in the mid-layer, and neglects the reciprocally displacements between the points on the steel surface and the points on surface of the epoxy coating. Despite of that, the thickness of the so-called mid-layer (the epoxy coating) is insignificant from geometrical point of view. In that layer can be accumulated additional energy of deformation and the length of the section between points (point 4 and point 6), see fig. 5, to be increased.

Acknowledgement

References

[1] Gustafson P. David, Epoxy Update. *Concrete Reinforcing Steel Institute, Civ. Eng., ASCE,* **(58)10**, pp. 38-41, 1988.

[2] Choi, O. C., Hadje-Ghaffari, H. Darwin, D. & McCabe, S. L., Bond of epoxy-coated reinforcement: bar parameters. *ACI Materials Journal*, **88(2)**, pp. 207-217, 1991.

[3] Miller Gerald, K. Jennifer, and D. Darwin, Effect of Epoxy Coating Thickness on Bond Strength of Reinforcing Bars. *ACI Structural Journal*, **100(3)**, pp. 314-320, 2003.

[4] Cleary D. and J. Ramirez, Bond Strength of Epoxy-Coated Reinforcement. *ACI Materials Journal*, **88(2)**, pp. 146-149, 1991.

[5] Kayyali O. A. and S. R. Yeomans, Bond and slip of coated reinforcement in concrete. *Construction and Building Materials*, **9(4)**, pp. 219-226, 1995.

[6] Hamad S., Comparative Bond Strength of Coated and Uncoated Bars with Different Rib Geometry. *ACI Material Journal*, **92(6)**, pp. 579-590, 1995.

[7] Ldun E. and D. Darwin, Bond of Epoxy-Coated Reinforcement: Coefficient of Friction and Rib Face Angle. *ACI Structural Journal*, **96(4)**, pp. 609-615, 1999.

[8] Protasio F., Influence of Coatings on Bar-Concrete Bond. *Journal of Materials in Civ. Eng.*, **8(4)**, pp. 212-214, 1996.

[9] Cairns J. and R. Abdullah, Fundamental Test on the Effect of an Epoxy Coating on Bond Strength. *ACI Materials Journal*, **91(4)**, pp. 331-338, 1994.

[10] Cusens, A. R., Z. Yu, Pullout Tests of Epoxy-Coated Reinforcement in Concrete. *Cement & Concrete Composites*, Vol.**14**, pp. 269-276, 1992.

[11] Mo Y., and J. Chan, Bond and Slip of Plain Rebars in Concrete, *Journal of Materials in Civil Engineering*, **8(4)**, pp. 208-211, 1996.

[12] Yanakieva A., Bonding between protected steel reinforcement and concrete, *Proc. of the IX National Congress on Theoretical and Applied Mechanics*: Varna, Bulgaria, pp.627-632, 2001.

[13] Yanakieva A. & Kazakov K., FEM numerical simulation of bond-slip behaviour between epoxy coated plain steel bars and concrete, *Proc. of the Int. Conf. Of FCE STU*, Bratislava, Slovakia, 2008.

[14] Kazakov K., *The finite element method for structural modelling*: VSU publishing house, Sofia, 2006.

Section 8
Applications and case studies

This page intentionally left blank

Durability of domestic scroll compressor systems

I. Tzanakis, M. Hadfield & Z. Khan
School of Design Engineering and Computing,
Bournemouth University, UK

Abstract

A thorough surface examination of the main components of a scroll compressor after part uses was conducted. This was performed in order to identify the possible tribo-mechanical effects (abrasion, cavitation, erosion etc) which occur on the substrate of these components. Three dimensional interferometer surface scanning and scanning electron microscopy (SEM) were used for surface analyses. Subsequently the parts were used to perform sliding tribological tests using a special purpose built modified microfriction machine to clearly identify their wear and friction mechanisms.

The main interacting material parts of the scroll were identified and used for bench tests. The experimental conditions were adjusted to those of the industrial applications. The critical components for durability were identified on the tip seal and the plate of the scroll compressor. These components are manufactured from high performance fluoroelastomer and high carbon steel materials.

The rational behind these tests is to assess the durability and performance of the scroll compressor system. This specific scroll compressor consists of two involute scrolls; the one orbits eccentrically in respect to the other, compressing various refrigerants. The scroll was under operational conditions for more than 300 hours within a CHP system.

The microscopic and the sliding results showed that cavitation on the steel plate is an issue to be taken into consideration. Two and three body abrasive wear dominates and can considerably affect the durability and the performance of the scroll.

Keywords: compressor, scroll, abrasion, cavitation, fluoroelastomer, steel.

1 Introduction

A scroll compressor is an innovative machine which was invented in 1905 by Creux and was used for compressing air or refrigerant. Around the mid 1970s this inefficient technology was interpreted properly and the first working pair of scrolls with very small tolerances was a fact. Since that time the scroll compressor has gained popularity and during the last 10 years it has been the main part of many domestic appliances (CHP systems, air-conditions, heat pumps etc) [1].

A scroll is a device that uses two interleaved spiral shaped scrolls to compress or to expand mainly refrigerants which are used as the working fluid for these systems. In this case it is used as an expander. One of the scrolls is fixed whilst the other orbits eccentrically without rotating, thereby the working fluid is trapped and simultaneously expands into the gas pockets between the scrolls [2,3].

The scroll compressor which was used for this report is a small volumetric positive displacement device and it operates in a high pressure ratio between the suction and the discharge valve. The operation of the scroll expander is based on the organic ranking cycle (ORC). The ORC is similar to the cycle of a conventional steam turbine, except for the fluid that drives the turbine, which is a high molecular mass organic fluid. In this case the working fluid was a hydrocarbon refrigerant. The specific scroll was under operational conditions for more than 300 hundred hours as a main part of a small domestic combine heat and power (CHP) system. The role of this compressor is to expand the working fluid instead of compressing it [4,5].
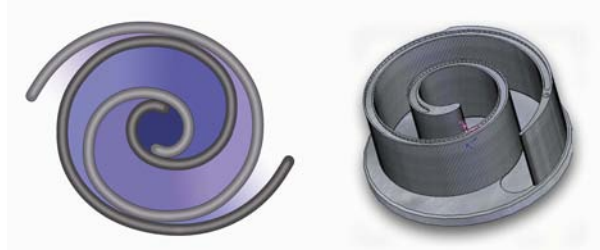
Figure 1:   Scroll compressor operation process.

During the operation process of the scroll (fig1), the working fluid after coming through the evaporator and reaching the gas state enters into the central chamber of the scroll at a pressure of about 12 bar and temperature of $150^{\circ}C$. At the end of a complete cycle of the scroll the working fluid leaves the compressor at a pressure of 2-3 bar and temperature of about $110^{\circ}C$. The scroll rotates eccentrically with a rotation speed of 3000rpm.

There are many complications regarding the scroll's performance. As reviewed by Cristian Cuevas higher rotation speeds or pressure ratio can steeply increase the working fluid's exhaust temperature which can chemically degrade the lubricant and the working fluid leading the scroll system to a thermally

mechanical failure. Moreover according to Leonid Paramonov high pressure ratio results to a high start up friction torque while the high pressures will introduce more efficiency losses. Apparently the biggest problem is the leakage of the gas which is responsible for the reduction of the volumetric efficiency of the working fluid. Typically the gap between the bottom or the top plate and the scrolls is around 1 micron (μm) across which the leakage is strangled. This may be significantly increased by wear and other tribological effects and it is known that if it reaches around 8 microns (μm), the scroll becomes useless [6–8].

The main interactive parts at the leakage points between the bottom plate and the scrolls are the high carbon steel (HCS) plate and the tip seal made by high performance fluoroelastomer (HPF). This is why the experimental wear tests will be focused on the performance of these two materials in order to evaluate the durability of the scroll.

Initially in this study a thorough surface examination of the main components of a scroll compressor was made. The interpretation of their wear mechanisms was completed. Then the wear and the possible cavitation mechanisms were identified while an effort was made to check the tribological behaviour of the actual interacting parts of the scroll, with the use of the special purpose modified pressurised microfriction machine TE 57.

2   Experimental procedure

The movement of the involute scrolls of the compressor is eccentric with a 10 mm diameter at a constant frequency of 50Hz. In the TE 57 machine, the sample follows a sinusoidal movement as it is produced by an electric rotary motor. The stroke was set at 5 mm in total and the speed was constant at 25Hz. This model was thought to approach the scroll's movement. Both movements caused sliding wear. Thus an effective evaluation of the wear effects inside the scroll during its operation can be estimated.
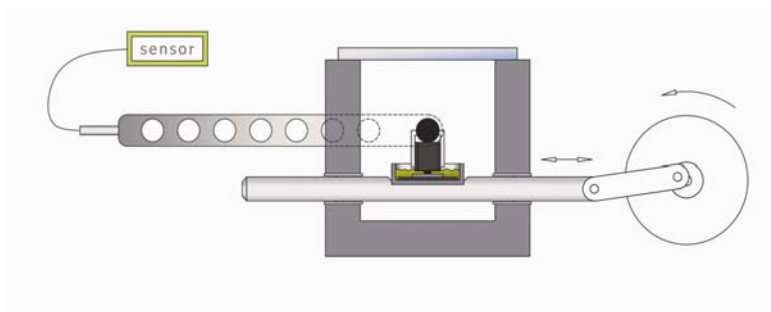

Figure 2:   Wear bench test-system schematic.

Figure 2 shows a schematic of the wear bench-test machine. The equipment is based upon a standard set-up from Phoenix Ltd model TE77 micro-friction machine. A modification allows for control of' the environmental conditions

surrounding the contact to simulate those found within the scroll compressor. The resultant micro-friction machine operates by sliding a lower-plate sample in a reciprocating motion against a fixed sample pin or ball. The plate is mounted in a bath to constrain a lubricant whilst the pin is connected via a feedback mechanism to a transducer to provide friction force feedback and hence friction co-efficient [9].

3 Experimental methodology

3.1 Overview

The main components of a scroll compressor after part uses were thorough examined. Three different types of microscopes were used. Those were an optical microscope (Olympus), a surface interferometer microscope (ZYGO) and a scanning electronic microscope (SEM). The results that show the wear failure mechanisms of the scroll are focused on the tip seal and the steel plate. Then an effort was made in order to evaluate the wear results and to understand the tribological behaviour of HPF tip seal against the HCS plate.

The tip seal is in a continuous contact with the counterface steel plate during the operation of the scroll. The tip seal reduces the leakage between the different crescent shaped gas pockets of the scroll. Despite the fact that the tip seal has excellent wear behaviour, still the high carbon steel plate is much harder and stronger so that it can cause wear failure to the fluoroelastomer tip seal.

Thus the tip seal and the steel plate were tested in the TE57 pressurised micro friction machine. The operating environment of the micro friction machine was adjusted as closely as possible to that of the scroll's compressor.

3.2 Chemical properties

The chemical properties of the steel plate and the tip seal were determined (table 1). Initially the steel sample was etched in a solution of 2% Nital in order for its grain structure to be determined. Then with the help of an optical emission spectrometer (OES) the steel sample was effectively distinguished in its elements. The steel plate structure comprises of isolated spheroidal carbides in a matrix of tempered martensite.

Table 1:   Chemical analysis of the scroll's main interacting components.

Steel Plate	%C	%Mn	%Si	%S	%P	%Cu	%Ni	%Cr	%Fe
Wt%	0.96	0.53	0.27	0.003	0.021	0.01	0.02	0.18	REM
Tip Seal			%F			%Si		%Ca	
Wt%			96.39			2.54		1.07	

The tip seal is a fluoroelastomer in a mixture of fluorine with other chemical elements. The chemical analysis of the fluoroelastomer was made with the use of a scanning electronic microscope (SEM).

3.3 Test specimens

Material test specimens were produced utilising the main parts of the scroll. The steel plate was cut in appropriate testing specimens. Then the specimens were stuck on the surface of other steel samples. The specimens from the tip seal were cut as well and implemented on the surface of enhancement rectangular steel samples. Special holders were constructed to hold the specimens.

The surface finish of the HCS plate was properly measured by the ZYGO interferometer microscope and found to be Ra=0.5μm. For the HPF samples the surface roughness was measured with the test surf machine using a sliding stylus across the surface. The Ra value was estimated to be 2μm. The hardness for the steel plate and for the tip seal is measured with a value of 530HV and 100HV respectively.

3.4 Test conditions

The test conditions inside the chamber of the TE 57 machine should match those found within the scroll compressor at the contact between the steel plate and the tip seal (table 2). Initially the contact load at the start up conditions of the scroll was estimated and it was found to be around 850N. This was achieved by measuring the friction torque and the static coefficient of the scroll during the start up conditions. Then with the use of the equation 1 assuming that the torque T (Nm) is equally distributed across the contact parts, the normal contact load L (N) was estimated

$$T = \mu \times L \times r \qquad \text{(eq1)}$$

where r (m) is the radius of the eccentricity and μ is the dimensionless static coefficient between the tip seal and the steel plate. Then the contact parameters were matched to those on the samples.

Three critical temperatures were chosen for the test processes. The temperature at the start up conditions (40°C) of the scroll. The temperature at its outlet port (100°C) where the working fluid leaves the scroll after it expands. The temperature at its inlet (150°C) port where the working fluid is introduced for expansion into the scroll.

Table 2:   Physical parameters for the scroll compressor and the test samples.

Physical Parameter	Scroll Compressor	Test Samples
Contact Load (N)	850	40
Contact Area (m^2)	2.3×10^{-3}	9×10^{-5}
Contact Stress (MPa)	0.37	0.4
Surface Velocity (m s^{-1})	1.57	0.25

3.5 Test procedure

The initial tests detailed in Table 3 were conducted using the TE 57 micro friction machine described previously. After the installation of the samples into

the holders of the TE 57 machine 3ml of lubricant were introduced into the bath. The lubricant which was used in these experiments is the actual lubricant of the scroll. Is a synthetic oil of a nominal viscosity 170cSt at 40°C. The load was set to be 40N for all the experiments and the speed was constant at 25Hz. Each of the tests was carried at a minimum of 4 times and the results were interpreted using the average values of these tests. Then the tests were run for 10 hours. In both the cases of the 100°C and the 150°C where the data could not provide sufficient results for comparison the tests duration was extended to 30 and 60 hours respectively.

Initially an estimation of the sliding friction coefficient was done using the samples into a non-lubricated environment while keeping the same conditions. The coefficient was found to be around 0.11 while after 5 hours was reduced to 0.03, because the HPF is probably melted. The idea behind it was to produce a reference point of the kinematic friction coefficient value. This will help for a better interpretation of the lubrication performance in all cases.

Table 3:   Wear bench test conditions.

Number of cases	Test regime	Temperature ($^{\circ}$C)	Time (sec)
1	No Lubrication	25	36.000
2	Synthetic Oil	40	36.000
3	Synthetic Oil	100	36.000
4	Synthetic Oil	150	36.000
5	Synthetic Oil	100	108.000
6	Synthetic Oil	150	216.000

4   Results and discussion

4.1 Surface analysis of the scroll's main parts

The surface analysis mainly focused on the HCS plate (fig 3). The process which was followed in order for the plate to be thoroughly analysed consisted of the use of the three different microscopes described previously. Moreover the investigation focused on two different regions of the scroll. These are the high pressure region (HP) and the low pressure region (LP).

The first interesting observation that was extracted was the different nature of the wear marks between the high and the low pressure region (fig 4). On the low pressure region the marks are more superficial and not so deep while on the high pressure one the marks are about 3 times wider and around 4 times deeper. This is a rough evidence of what is expected in the experiments with higher condition temperatures. Moreover the wear which is more obvious and prevails not only on those regions but across the whole scroll's plate surface can be determined as a two body abrasive wear.

Figure 3:   a) Circular wear marks on the steel plate after use 300 hours b) Tip seal.
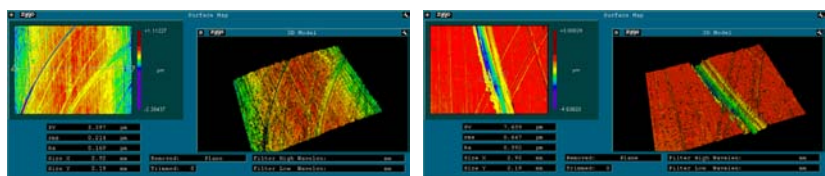

Figure 4:   a) Low Pressure Region average depth of the marks 0,5-1 μm- b) High Pressure Region average depth of the marks 2-4 μm.

   Apart from the two body abrasion, cavitation and three body abrasion wear were identified in many areas of the scroll's plate. Characteristically many cavities were found on different spots around the surface of the steel plate which implies the presence of random cavitation effects. On the low pressure region more detailed river marks (fig 5) where detected which were around 2mm long. What is more interesting is that they do not follow the path of the wear circular marks but have a totally different direction. The SEM showed that three body abrasion is the clue for these long rivers, let alone the fact that many cavities have been formed around these areas. These cavities, which in some cases may developed by cavitation impact, erode the surface of the steel plate while steel particles are released into the lubricant solution. These particles in their own way now produce three body abrasion during the contact of the two opposite surfaces during the scroll's operation.
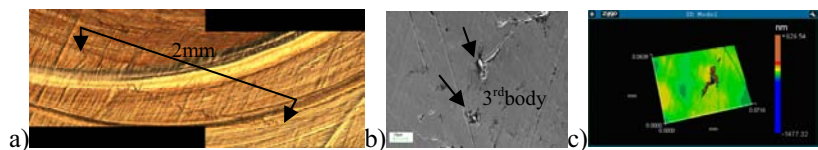

Figure 5:   a) The river marks across the steel plate b) Looking at the river marks c) Surface profile of the river marks.

In addition random points where identified with a cluster of elongated cavities in a much smaller size across many different areas around the scroll. Also evidence of isolated bigger size cavities were spotted at many different points, especially on the high pressure region (fig 6). SEM image shows how destructive the cavity can be while their characteristic geometries were defined with the interferometer microscope.
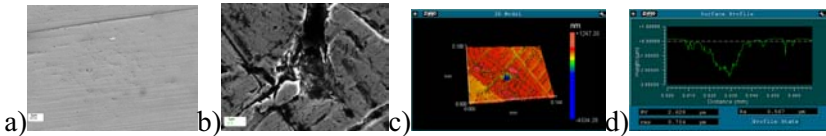

Figure 6: a) Cluster of cavities b) Cavity profile c) 3D-Cavity d) Surface profile.

Finally at the high pressure region many long river marks were observed but with slightly different nature from the previous one (fig 7). On these marks the effect of the three body abrasion wear is more obvious with a slight suspicion that cavities may have originated from cavitation. The result can be a more severe wear regime.
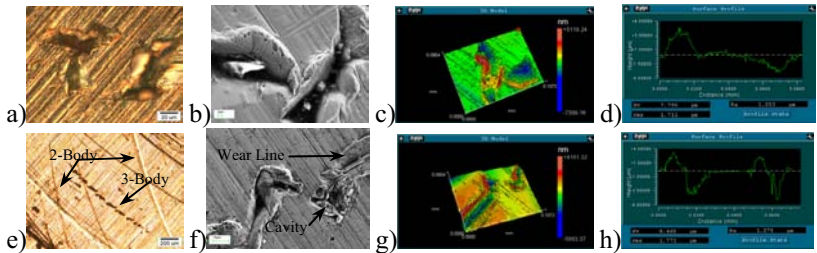

Figure 7: a) 3-Body wear marks b-f) Zooming the marks c-g) 3D profile d-h) Surface profile e) River marks.

For the HPF tip seal not many conclusions were drown from the initial surface investigation. The black colour and the high level of elasticity made the tribological investigation very harsh to be performed. Thus the experiments with the use of the TE 57 machine will show the wear mechanisms of this high efficient material against the steel plate.

4.2 Test results

Measurements coming from data acquisition have been used to plot friction coefficient over the time for the different temperature environments (fig 8). The results showed that at the temperature of 40°C friction coefficient starts from a value of 0.01 and after a 10 hour running it is stabilized in its minimum value of

0.006. More or less the same situation was observed in the case of the 100°C where the friction coefficient was stabilized at a similar value of 0.005-0.006 after running at douple the time (20 hours). This can easily be comprehended as the samples asperities are at a very close contact for the first couple of hours and then the lubricant shows its very good performance by gradually reducing the friction coefficient and providing excellent hydrodynamic lubrication.
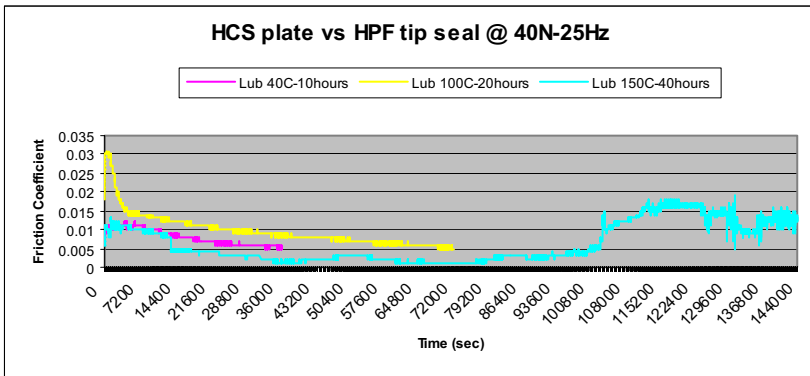

Figure 8:   Plot graph of friction coefficient over time for different cases.

In the case of 150°C the friction coefficient results are very interesting. What can be highlighted is the steep increase of the friction coefficient after 30 hours of running. During the first 30 hours the behaviour of the lubricant was similar to the previous cases but after that point probably a chemical degradation of the lubricant lead to the rise of the friction coefficient. Then for the remaining hours many irregular fluctuations were observed reaching even the highest friction coefficient value at nearly to 0.02.

After the evaluation of the samples in all cases, two body wear with evidence of plastic deformation were detected. Moreover a severe three body abrasion wear seriously damaged some parts of the samples. The wear scar dimensions at the plate were measured to provide further comparison between the different cases (fig 9). The wear is becoming more severe as the temperature increases.

Especially three body wear clearly appears in the high temperature cases. The particles are embedded in the surface of the HPF tip seal and they roll across the steel sample creating a series of indentations rather than linear grooves.

Furthermore material from the HPF tip seal was found onto the surface of the steel samples, explaining the adhesive wear mechanism. At lower temperature this phenomenon was more obvious than at the higher one. Probably the mechanical performance of the HPF is improved avoiding the transfer of particles. Another scenario is that the lubricant at these high temperatures can remove more easily the fluoroelastomer particles and clean the steel surface. The adhesion creates mountains with fluoroelastomer material on the surface of the steel with an average peak of 0.05-0.08 μm.

Looking at the tip seal samples after the friction/wear tests it can be said that at all occasions the HPF managed to trap the HCS particles and to create in that way a more rough and rigid surface. This could drastically affect the steel plate's structure and durability. Moreover the leakage is increased across the top of the seal. The wear mechanisms on the surface of the fluoroelastomer can be distinguished in 3 regimes: abrasive, adhesive, fatigue. Synoptically presented in the block diagram (fig 10).
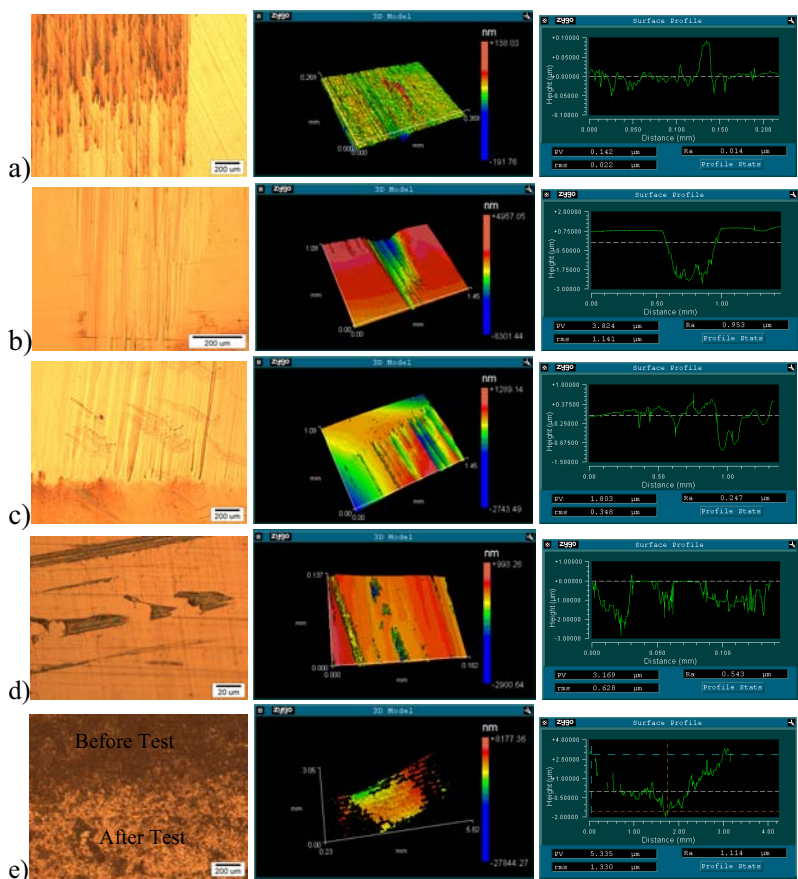

Figure 9:   a) HCS wear at 40°C-Layers of HPF with a max height of 0.1μm
b) HCS wear at 100°C-Max depth 2μm c) HCS wear at 150°C-Max depth 1μm d) 3-Body wear at 100°C-Max depth 2μm e) HPF wear at 150°C-Step of 4μm.

The surface analysis of the samples showed that abrasive wear is the one which dominates. In all cases abrasive wear was observed while high deposition of steel particles was found. The penetration of the steel particles onto the surface of the fluoroelastomer affects the sealing performance of the tip seal

since it cannot properly come in a full contact with the steel plate and effectively seal the gaps.

In addition adhesive wear appeared in many cases. This was expected since the steel samples had a very low roughness creating very smooth blunt asperities edges. Transfer of fluoroelastomer particles were found in all the cases. Finally fatigue wear was evident in some of the tested fluoroelastomer samples.
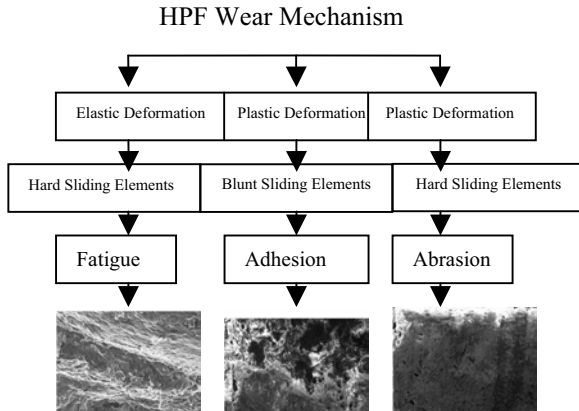
HPF Wear Mechanism

Figure 10:   Block diagram of the wear mechanisms found on the tip seal.

After time, both the seal and the counterface steel plate wear out and become thinner. This can seriously affect the performance of the scroll since the leakage can become catastrophic for the efficiency and the life of the scroll.

5   Conclusions

Abrasive wear derives from a two body contact in the interface of the tip seal and the steel plate. Moreover severe wear by a three body contact between the two interacting materials using the contaminated particles inside the lubricant/refrigerant mixture was identified.

According to the friction graphs, in the first few hours, the contact between the HCS plate and the HPF tip seal is quite rough. Afterwards the performance of the lubricant is improved, resulting to a lower friction coefficient. Eventually the presence of particles contaminates and degrades the lubricant. This, in turn, causes the enhancement of the friction and the wear rate of the samples especially at high temperatures (e.g. 150°C).

Finally another critical issue which has to be taken into consideration is the cavitation effects during the operation of the scroll. Cavitation can seriously damage the surface of the steel plate by contaminating the lubricant with ferrous particles. Once more, due to the three body wear abrasion the wear between the interacting materials can be increased.

References

[1] Wang, B., Li, X. &Shi, W. Q. 2007. A general geometrical model of scroll compressors based on discretional initial angels of involute. *International journal of refrigeration*, 28 (958- 966)

[2] Chen, Y., Halm, N.P., Braun, e. & Groll E.A. 2002. Mathematical modelling of scroll compressors – part I overall scroll compressor modelling. *International journal of refrigeration*, 25 (751-764)

[3] Tseng C.H. & Chang, Y.C. 2006. Family design of scroll compressors with optimization. *Applied thermal engineering*, 26 (1074-1086)

[4] Saleh, B., Koglbauer, G., Wendland, M. & Fischer, J. 2007. Working fluids for low – temperature organic Ranking Cycles. *Energy* 32(1210-1221)

[5] Yamamoto, T., Furuhata. T., Arai. N. & Mori, K. 2007. Design and testing of organic rankine cycle. *Energy* 26 (239-251)

[6] Cristian Cuevas, Jean Lebrun. 2009. Testing and modelling of a variable speed scroll compressor. *Applied thermal engineering*, 29 (469-478)

[7]   Leonid Paramonov. 2004. PhD Thesis: Simulation-based evaluation of scroll compressors for refrigeration applications. *University of Southern Denmark*

[8] Howell, P. 2004. *Fluid* mechanical modelling of scroll compressor. *Mathematical institute*, 131 (32-56)

[9] Nigel P. Garland, Mark Hadfield. 2005. Tribological Analysis of hydrocarbon refrigerants applied to the hermetic compressor. *Tribology International,* 38 (732-739)

Surface characterization of rotary-peeled eucalyptus veneers by confocal laser scanning microscopy and surface free energy and contact angle determination

G. Vázquez, J. González-Álvarez, M. S. Freire, J. Santos,
R. Uceira & G. Antorrena
Department of Chemical Engineering,
University of Santiago de Compostela, Spain

Abstract

Eucalyptus wood wettability was studied using aqueous solutions of chestnut shell and eucalyptus bark tannins as potential components of wood adhesives. The behaviour of both sides of rotary-peeled veneers, the tight and the loose sides, was analysed and lower equilibrium contact angles were found on the loose side, reflecting a higher wettability. In order to evaluate if rotary-peeling had provoked any surface modification responsible of the observed wettability behaviour, the free surface energy of the veneer tight and loose sides was determined using the Owens-Wendt and the van Oss-Chaudhury-Good models. The higher surface free energy values for the loose side justified the better wettability previously obtained. Confocal Laser Scanning Microscopy (CLSM) allowed obtaining topographical images of the material surface, without sample damage, and calculating the crack length and depth together with various roughness parameters. Significant differences between both sides of the veneers have not been found but CLSM has turned out to be a high resolution technique for material surface characterization.

Keywords: eucalyptus wood, rotary-peeled veneer, chestnut shell extract, eucalyptus bark extract, wettability, contact angle, surface free energy, confocal laser scanning microscopy.

1   Introduction

Wood-adhesive bond degree depends on several factors such as wood species, physico-chemical wood properties, surface treatments, adhesive properties and glue-line formation conditions.

Christiansen [1] summarised the mechanisms responsible for changes of wood surfaces that may influence wood bonding properties: a) migration of hydrophobic extractives during drying, 2) oxidation, 3) closure of micro-voids in the wood substance which reduces adhesive penetration, 4) acidity or reactivity of extractives affecting the curing time of adhesives and 5) molecular reorientation of functional groups at the surface.

Wettability and wood surface free energy are considered useful parameters to evaluate the bond degree, as provide information on the interaction between adhesives and wood surfaces. Contact angle measurement is the most common technique employed to determine the surface free energy of the solids. Once the contact angles with several probe liquids have been determined, there are various methods for determining the solid surface free energy. Among them, the Owens-Wendt and the van Oss-Chaudhury-Good (vOCG) methods have been selected in the present work.

Eucalyptus globulus is one of the main forest species in Galicia (NW of Spain), whose wood has a high mechanical resistance that makes it very appropriate for plywood manufacture. However, factories using this wood find serious difficulties due to the high level of rejects, attributed partly to eucalyptus wood characteristics but also to surface changes due to the rotary-peeling process, which affect the interaction with commercial phenolic resins.

In a previous work of the authors [2] the extraction of tannins from chestnut shell and eucalyptus bark extracts and their potential in the formulation of wood adhesives, which could substitute phenolic resins, have been studied.

The aim of this paper is to investigate the effect of rotary-peeling on the characteristics of both veneer surfaces, the tight and the loose sides, by means of contact angle measurement using aqueous solutions of the chestnut shell and eucalyptus bark extracts previously obtained, surface free energy determination and surface analysis by confocal laser scanning microscopy (CLSM). CLSM allows determining the crack length and depth, several roughness parameters and 3D imaging of thick and opaque specimens, such as wood surfaces, without damaging the samples.

2   Methods

2.1   Contact angle determination

Samples of *Eucalyptus globulus* rotary-peeled veneers with a humidity of 10% (wet basis) were used to prepare 2 cm (length) x 2 cm (width) x 1.5 mm (thickness) wood pieces for contact angle measurements. Contact angle determination was made in the grain direction of the wood according to the sessile drop method using a Dataphysics OCA 15 Plus (Filderstadt, Germany)

equipment with a video measuring system with a high-resolution CCD camera. The data were analyzed with the Dataphysics software SCA 20.

To compare the wettability of both sides of the eucalyptus veneers, the tight and the loose sides, 10% (by weight) aqueous solutions of chestnut shell and eucalyptus bark extracts, potential components of wood adhesives, were used. Ten μL drops were added and the variation of contact angle with time was registered till 240 s. For each solution, twelve measurements were done on each side of the veneer.

The surface tension of the extract aqueous solutions was determined by the pendant drop method (with 10 μL drops) and using the image analysis software SCA 20 from Dataphysics. Fifteen measurements were done for each solution.

2.2 Surface-free-energy determination

The surface free energy of both sides of eucalyptus veneers was determined using the following probe liquids: water, ethilenglycol, diiodomethane and formamide. Five μL drops were added and twelve measurements were carried out on each side of the veneer for each probe liquid.

The equilibrium contact angle used to determine the surface free energy was obtained using the method proposed by Nussbaum [3], based on the determination of the constant wetting rate angle (cwra), which is attained when the wetting rate or $d\theta/dt$, being θ the contact angle, become constant. From these data, the surface free energy was calculated according to the Owens-Wendt and the vOCG models.

Fowkes suggested that the surface free energy of materials (γ) could be considered as the sum of various components due to different intermolecular interactions [4]:

$$\gamma = \sum_i \gamma_i \qquad (1)$$

The Owens-Wendt model describes the surface free energy, γ_i, as the sum of two components, the dispersive component, γ_i^d, and the polar component, γ_i^p, according to eqn (2):

$$\gamma_i = \gamma_i^d + \gamma_i^p \qquad (2)$$

and eqn (3) allows one to calculate the dispersive and polar components of the surface free energy:

$$\gamma_L(1+\cos\theta) = 2\sqrt{\gamma_S^p \gamma_L^p} + 2\sqrt{\gamma_S^d \gamma_L^d} \qquad (3)$$

where the subscripts S and L represent the solid and the liquid, respectively, and θ, the contact angle. The surface tension and the free surface components for the four probe liquids employed are shown in table 1.

With respect to the vOCG model, the surface free energy is also considered as the sum of two components, the apolar or dispersive component, named the Lifshitz-van der Waals component, γ_i^{LW}, which is based on temporary forces of attraction and repellence due to the movement of electrons in molecules, and the Lewis acid-base or polar component, γ_i^{AB}. The polar component was further

divided into the Lewis acid, γ_i^+, and Lewis base, γ_i^-, component defined as given in eqn (4).

$$\gamma_i = \gamma_i^{LW} + \gamma_i^{AB} = \gamma_i^{LW} + 2\sqrt{\gamma_i^+ \gamma_i^-} \qquad (4)$$

To determine the total surface free energy of the solid and its components it is necessary to measure the contact angle of the solid versus at least three liquids according to eqn (5). The apolar and polar components of the surface free energy of the four probe liquids employed are shown in table 2.

$$\gamma_L \left(1 + \cos\theta\right) = 2\left(\sqrt{\gamma_S^{LW}\gamma_L^{LW}} + \sqrt{\gamma_S^+ \gamma_L^-} + \sqrt{\gamma_S^- \gamma_L^+}\right) \qquad (5)$$

Table 1:   Surface tension and surface free energy components for the probe liquids according to the Owens-Wendt model.

Probe liquid	γ_L (mN/m)	γ^P (mN/m)	γ^d (mN/m)
Water	72.8	21.8	51
Diiodometane	50.8	50.8	0
Ethylene glycol	48	29	19
Formamide	58	39	19

Table 2:   Surface free energy components for the probe liquids according to the vOCG model.

Probe liquid	γ^{LW} (mN/m)	γ^{AB} (mN/m)	γ^+ (mN/m)	γ^- (mN/m)
Water	21.8	51	25.5	25.5
Diiodomethane	50.8	0	0	0
Ethylene glycol	29	19	1.92	47
Formamide	39	19	2.28	39.6

2.3 Confocal laser scanning microscopy (CLSM)

Samples of the tight and loose sides of eucalyptus veneers, previously coated with gold using a Bio-Rad E5000 Sputted Coater (Hercules, USA) were analysed by confocal laser scanning microscopy using a TCS SP2 Leica microscopy (Mannheim, Germany) and a HC PL APO 10X/0.40 lens. Five random fields or xyz series of 1.5 mm (length) x 1.5 mm (width) x 0.5 mm (thickness) were analysed in each sample. Optical sections were obtained using 2.5 μm intervals in the z direction.

Results were analysed with the Leica Confocal software to obtain topographical images of the surface, 3D topographical surface reconstructions, a roughness profile along a path and the following parameters calculated according to the standard DIN EN ISO 4287:

The roughness index P_a calculated as follows:

$$P_a = \frac{1}{A}\int_0^A |Z(x,y)| dA \quad with \quad Z(x,y) = Z_i - \overline{Z} \qquad (6)$$

- The roughness index P_q (or RMS) calculated as follows:

$$P_q = \sqrt{\frac{1}{A}\int_0^A \left|Z^2(x,y)\right| dA} \quad with \quad Z(x,y) = Z_i - \overline{Z} \qquad (7)$$

- The height of highest peak of the profile (referred to the mean height), P_p.
- The depth of the deepest valley of the profile (referred to the mean height), P_v.

3   Results and discussion

3.1   Wettability of eucalyptus wood veneers

Fig. 1 shows, as an example, the images of a drop of chestnut shell extract on an eucalyptus veneer loose side at the initial a) and final b) stages of the wetting process. The variation o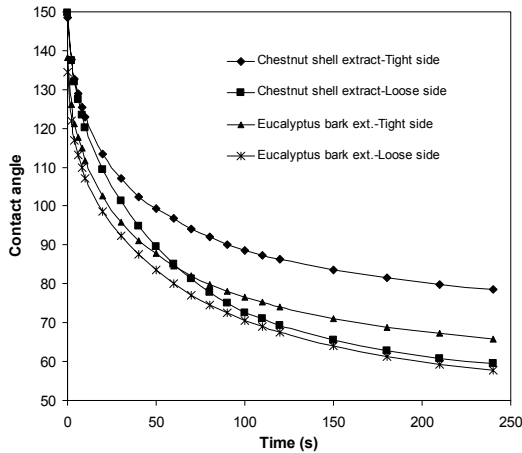f contact angle with time for the aqueous solutions of chestnut shell and eucalyptus bark extracts on the tight and loose sides of eucalyptus veneers is presented in fig. 2. The contact angles shown are the mean value of twelve measurements with each solution and veneer side. Surface tension of chestnut shell and eucalyptus bark extract solutions together with the initial (θ_0) and final (θ_f) contact angles on the tight and loose sides of eucalyptus veneers are given in table 3.
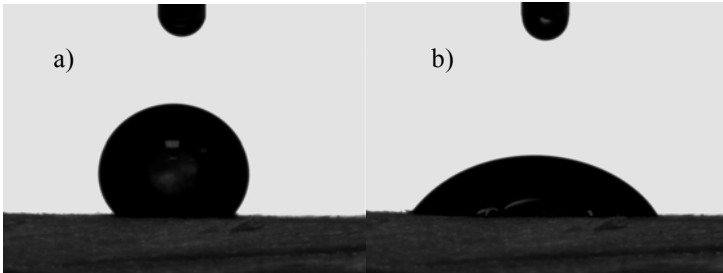
Figure 1:   Initial a) and final b) stages in the wetting process of an eucalyptus veneer loose side with a chestnut shell extract solution.

Initial and final contact angles were lower for the eucalyptus bark extract solution on both sides of the veneer, which could be attributed to its lower surface tension, and a better wetting was obtained. On the other hand, initial contact angle was hardly affected by the characteristics of the veneer surface. On the contrary, analysing the time course of contact angles and the final contact angles they are significantly lower on the loose side for both extract solutions. These results revealed that the rotary-peeling process has a marked effect on the wood surface characteristics influencing wood wetting. Shupe *et al.* [5] also found a better wetting on the loose side of *Pinus taeda* veneers using water as solvent, however no differences were detected for a phenolic resin due to its high surface tension.

Table 3:   Surface tension of chestnut shell and eucalyptus bark extract solutions and initial (θ_0) and final (θ_f) contact angles on the tight and loose sides of eucalyptus veneers.

Extract	Surface tension (mN/m)	Tight side		Loose side	
		θ_0	θ_f	θ_0	θ_f
Chestnut shell	60.85 (0.41)	148.48 (6.62)	78.66 (14.22)	149.68 (11.02)	59.44 (14.15)
Eucalyptus bark	51.21 (0.14)	138.14 (8.05)	65.85 (8.52)	134.45 (3.96)	57.68 (12.47)

Mean (Standard deviation)

Figure 2:   Contact angle versus time for aqueous solutions of chestnut shell and eucalyptus bark extracts on the tight and loose sides of eucalyptus veneers.

3.2 Surface free energy of eucalyptus wood veneers

Table 4 shows the constant wetting rate angle obtained on the tight and loose sides of eucalyptus veneers for the different probe liquids employed.

The results obtained for the surface free energy of eucalyptus wood according to the Owens-Wendt model are presented in table 5. The values obtained for the total surface free energy were comparable with those obtained for other hardwoods [6, 7]. On the other hand, it was higher for the loose side of the veneers than for the tight side, which is in accordance with the lower contact angles obtained for the former in the wetting study of eucalyptus veneers with tannin solutions. In both cases, although more significantly for the tight side, the dispersive component was higher than the polar one which is habitual in most polymers [6]. These differences in the surface free energy between both sides of the veneers indicated that the rotary-peeling process might have altered wood surfaces in different way influencing wettability.

Table 4:   Constant wetting rate angle for the different probe liquids on the tight and loose sides of eucalyptus veneers for the calculation of eucalyptus wood surface free energy.

Veneer side	Water	Diiodomethane	Ethylene glycol	Formamide
Tight	63.9 (8.75)	61.9 (5.32)	26.1 (1.87)	25.5 (4.15)
Loose	50.5 (12.42)	58.8 (7.65)	21.7 (3.46)	25.5 (4.15)

Mean (Standard deviation)

Table 5:   Surface free energy components (in mN/m) for eucalyptus veneers according to the Owens-Wendt model.

Veneer side	γ_S	γ_S^d	γ_S^p	R^2
Tight	45.20	29.41	15.80	0.9451
Loose	50.72	27.33	23.39	0.9754

The van Oss-Chaudhury-Good (vOCG) model led to the surface free energy data shown in table 6. The total surface free energy values for both sides of the veneers were slightly lower than those obtained by the Owens-Wendt model. Nevertheless, it was also higher for the loose side and the dispersive component, γ_s^{LW}, comparable with γ_S^d [4], was also higher than the polar one, γ_s^{AB}.

Table 6:   Surface free energy components (in mN/m) for eucalyptus veneers according to the vOCG model.

Veneer side	γ_S	γ_S^{LW}	γ_S^{AB}	γ_S^+	γ_S^-	R^2
Tight	42.51	27.51	14.99	6.88	8.17	0.9820
Loose	48.30	29.28	19.00	4.02	22.47	0.9868

With respect to the acid/base character of the wood surface, the basic component was higher than the acid component, which has been also found for other wood species [6]. However, the acid component of the eucalyptus wood is significantly higher than those found for those wood species In addition if the γ_s^+ / γ_s^- ratio is compared between both veneer sides, values of 0.17 and 0.84 were obtained for the tight and loose sides, respectively, which reflects a high significance of the acid component in the tight side with respect to the loose side that can condition wood wettability.

3.3 Confocal laser scanning microscopy of eucalyptus veneers surface

Figs. 3, 4 and 5 show, as an example, for one of the fields analyzed by CLSM of an eucalyptus veneer, a 3D topographical surface reconstruction, the topographical image of the surface and the depth profile along a path normal to the fibre length. Although qualitative differences have been found among the fields analysed in the same type of veneer side, the differences were more significant when the fields of tight and loose sides were compared. Tight sides showed smoother and less uneven fields than the loose sides.
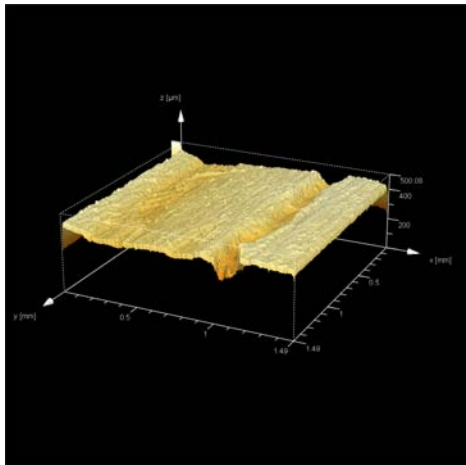
Figure 3:   3D topographical surface reconstruction for one of the fields of an eucalyptus veneer analyzed by CLSM.

Figure 4:   Topographical image of the surface for one of the fields of an eucalyptus veneer analyzed by CLSM.

The results obtained for the different roughness parameters analyzed are presented in table 7. As observed, no significant differences have been found between the values of the different parameters (P_a, P_q, P_p and P_v,) obtained for the tight and loose sides, in contrast with the qualitative analysis. Therefore, although tight and loose sides of the eucalyptus veneers showed differences in the wetting behaviour, it could not be attributed to differences in surface roughness, which suggests that other kind of analysis, such as analysis of surface composition, should be performed.
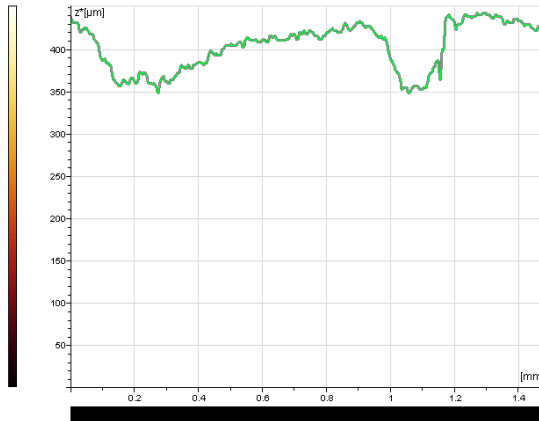
Figure 5:   Depth profile along a path normal to the fibre length for one of the fields of a eucalyptus veneer analysed by CLSM.

Table 7:   Roughness parameters for the tight and loose sides of eucalyptus veneers.

	Tight side	Loose side
$P_a\,(\mu m)$	29.87 (3.02)	30.11 (4.68)
$P_q\,(\mu m)$	39.02 (3.35)	36.18 (4.74)
$P_p\,(\mu m)$	114.45 (11.07)	114.29 (11.24)
$P_v\,(\mu m)$	385.54 (17.60)	388.80 (13.22)

Mean (Standard deviation)

References

[1] Christiansen, A.W., Effect of ovendrying of yellow-poplar veneer on physical properties and bonding. *Holz Roh- Werkstoff* , **52**, 139-149, 1994.
[2] Vázquez, G., González-Alvarez, J., Santos, J., Freire, M.S. & Antorrena, G., Evaluation of potential applications for chestnut (*Castanea sativa*) shell and eucalyptus (*Eucalyptus globulus*) bark extracts. *Ind. Crops Prod.,* in press, doi:10.1016/j.indcrop.2008.07.004., 2009.
[3] Nussbaum, R.M., Natural surface inactivation of Scots pine and Norway spruce evaluated by contact angle measurements. *Holz Roh- Werkstoff*, **57**, pp. 419-424, 1999.
[4] Etzler, F.M., Characterization of surface free energies and surface chemistry of solids. *Contact angle, wettability and adhesion Vol 3*, ed. K.L. Mittal, VSP: Utrecht and Boston, pp. 219-264, 2003.
[5] Shupe, T.E., Hse, C.Y., Choong, E.T. & Groom, L.H., Effect of wood grain and veneer side on loblolly pine veneer wettability. *Forest Prod. J.*, **48(6),** pp. 95-97, 1998.

[6] Gindl, M. & Tschegg, S., Significance of the acidity of wood to the surface free energy components of different wood species. *Langmuir,* **18**, pp. 3209-3212, 2002.

[7] Meijer, M., Surface energy determinations of wood: comparison of methods and wood species. *Langmuir,* **16**, pp. 9352-9359, 2000.

Generating behavior of whiskers on Pb free Sn plating and its control

Y. Kimura[1] & Y. Takeshita[2]
[1]*Department of Materials Science and Technology, Kogakuin University, Japan*
[2]*Graduate School, Kogakuin University, Japan*

Abstract

Until now, electronics materials have mainly been manufactured from Sn-Pb alloy plating. However, there is a problem in that Pb pollutes the environment. Therefore, Sn-Pb alloys are principally prohibited for use in electronic components by RoHS instruction. Therefore, the development of an alternative material to Pb is required from now on. However, whisker generation has become a problem when an alternative material to Sn-Pb alloy is used. In this study, various investigations are conducted employing Sn-Cu, Sn-Bi and Sn-Pb alloys on the basis of microstructure control for the best plating material to prevent whisker generation when used as an alternative material to Pb. As a result, the difference in crystal grain morphology was clarified between these three kinds of plating materials through conducting FIB processing and detailed SIM observation. Therefore, the residual and contact stresses generated by the process of putting the FPC into a connector cannot be easily be relieved in the case of Sn-Cu plating film, the microstructure of which has fine columnar grains. Increasing the Bi contents improved whisker generation and growth characteristics. Whisker generation and growth were suppressed in the case of applying a Sn-Bi alloy whose Bi content was larger than 2wt%. In this case, grain size was also increased with the increase of Bi content. Therefore, material selection and control of grain morphology are extremely important for suppressing whisker generation and growth.
Keywords: RoHS instruction, prevent whisker generation, an alternative material to Pb, Sn-Bi.

1   Introduction

The development of today's electronic industry is remarkable, as is the miniaturization and higher functionalization that have been achieved. In the plated parts, such as the circuit pattern used in IC and the print circuit board, the demand stemming from environmental issues concerning Pb free plating film has strongly increased [1]. It is not possible to solve this problem by using single metal plating, but a new functional usage of the alloy and compound plating based on peculiar characteristic of the metal is developed [2]. The considerations of environmental pollution and the environmental impact became indispensable, because there is a possibility of polluting the environment when electronic equipment containing Sn-Pb solder is abandoned. In addition, the promulgation of the RoHS instruction requested the material development of substitute alloys for the Sn-Pb alloy [1]. Therefore, an alternative material to Pb is required from now on. However, whisker generation has become a problem when an alternative material to the Sn-Pb alloy is used [3]. Therefore, in this study, various investigations are conducted employing Sn-Cu, Sn-Bi and Sn-Pb alloys on the basis of microstructure control for the best plating material to prevent whisker generation when using as an alternative material to Pb.

2   Experimental procedures

2.1 Plating species

The situation of connection of a connector with flexible substrate is schematically illustrated in Fig.1. Whiskers were generated from the contact part of the connector and this results in short circuit of the connector as shown Fig.2. The pitch of the connectors generally used is 0.3~0.5mm. Therefore, in cases where whisker length is 10 micrometers or less, the adjacent terminal can almost avoid the possibility of a short circuit.
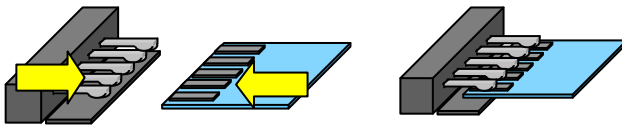
Figure 1:   Connection of connector with flexible substrate.
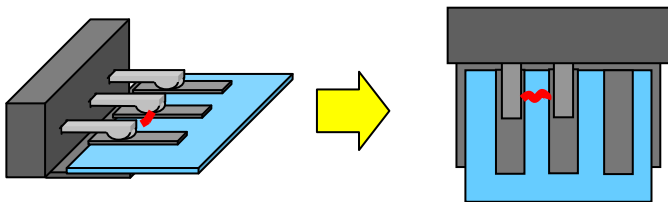
Figure 2:   Circumstance of short circuit.

Table 1:   Plating species.

Connector	FPC
Sn-1.5wt%Cu	Sn
Sn-2wt%Bi	Sn
Sn-10wt%Pb	Sn

At first, various investigations are conducted using the plating species shown in Table 1 to investigate the generation and growth characteristics of whiskers, because Sn-Pb has a suppressing effect on whisker generation and Sn-Cu easily generates whiskers. In addition, Sn-Bi is given attention as an alternative material to Sn-Pb plating. FPC is employed as the material that was put into the connector, because of its high degree of freedom of flexible elastic deformation.

2.2 Experimental procedures

In this study, external stress, generated internal stresses due to plastic deformation and recrystallization of plated film are considered as the governing factors for whisker generation, because some previous studies pointed out the importance of the external stress that was generated when flexible substrate was put in the connector [3]. Whiskers were generated under the connecting condition of flexible substrate and connector. The location where whiskers were generated was examined by SIM. Then, morphology and growth behavior of the whiskers [4] were examined in detail by SIM. In addition, the plating film was minutely process by FIB, and the crystal grain morphology [5] was examined by SIM. The test condition under which whiskers are generated easily is shown in Table 2. 100hrs or more time was needed for whisker generation. Therefore, it is observed by SIM from 100hrs after the connection, and the generation and the growth behavior of whiskers was examined.

Table 2:   Test condition.

Temperature	Humidity	Contact force	Time
295K	40%RH	Approximately 1.9N	100hrs~

3   Results and discussions

3.1 Dependence of generated whisker morphology upon plating species

The dependence of the whisker morphology upon plating species was investigated. As a result, the whisker morphology difference depended upon the plating species was recognized and shown in Fig.3. The whisker morphology of Sn-Cu alloy plating was needle. That of Sn-Pb alloy plating was nodule. In addition, that of Sn-Bi alloy plating was intermediate between needle and nodule. The whisker morphology and mean length are indicated in Table 3.

These results were obtained after 720hrs from the flexible substrate being put in. It was confirmed that the plastic deformation occurred on the plating part due to the insertion process of FPC into the connector, and then the whisker was generated from this part. Moreover, there is the possibility of a short circuit because the whisker from the Sn-Cu alloy plating grew longer than 30μm. On the contrary, it was recognized that the whisker of the Sn-Pb did not easily grow until 720hrs. It is reported that whisker growth begins at 100hrs or more after being put in. However, in this research the whisker generation was already recognized at 100hrs. Therefore, the initial growth behavior of the whisker depending upon the difference of the plating species was examined in detail through observing growth behavior every 24hrs with SIM.
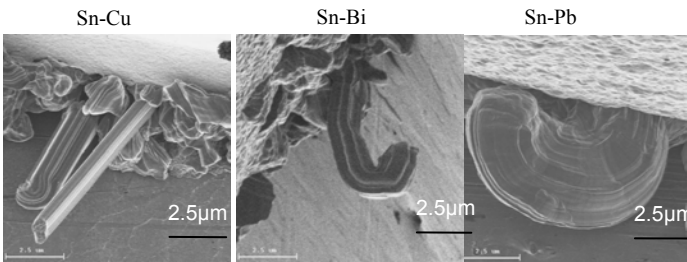
Figure 3:   Difference in whisker morphology.

Table 3:   Length and morphology of whiskers.

Plating species	Whisker morphology	Length	Time
Sn-Cu	Needle	32μm	720hrs
Sn-Bi	Intermediate	8μm	720hrs
Sn-Pb	Nodule	6μm	720hrs

3.2 Dependence of initial whisker growth rate upon plating species

Detailed observation of the growth behavior of the whiskers was conducted every 24hrs. Some examples of whisker morphology change with time, which in the case of the Sn-Cu alloy plating are shown in Fig.4. In Fig.5 the whisker length change [4] detected for the three kinds of plating species with time is indicated. The whisker growth of Sn-Cu and Sn-Bi alloy plating started 24hrs after the FPC was put in and the growth rate was gradually suppressed with time. Moreover, it was confirmed that the whisker grew up from its root. Therefore, the residual stress and contact stress generated when the FPC was put into the connecter plays a dominate role in whisker growth. In Fig.5, the remarkable whisker growth of Sn-Cu alloy plating with time was recognized. Next, the contact points of the connector and the FPC was uncoupled to confirm the part where whiskers had been generated through conducting detailed examination by SEM.

3.3 Details of whisker generating process

Detailed examination of the whisker generation process was conducted employing Sn-Cu alloy plating, which showed accelerated whisker growth. In Fig.6 it was confirmed that the plastic deformation occurred in the plating part due to the insertion under contact force between the connector and the FPC, and then the whisker was generated from this part.
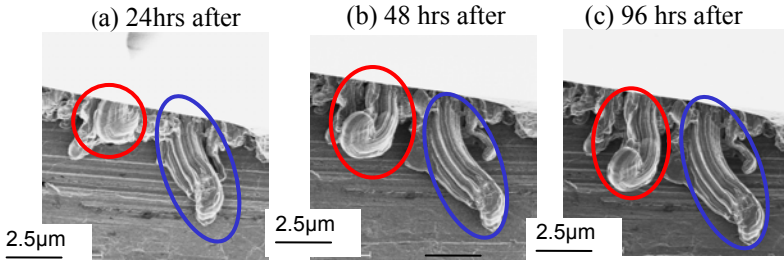
(a) 24hrs after   (b) 48 hrs after   (c) 96 hrs after

2.5μm   2.5μm   2.5μm

Figure 4:   Growth of Sn-Cu whisker from the contact part.
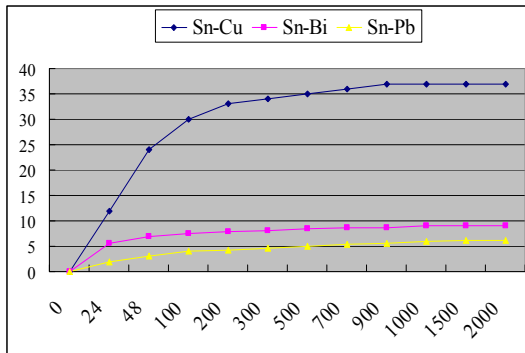
Figure 5:   Growth characteristics of whiskers.

50μm   20μm
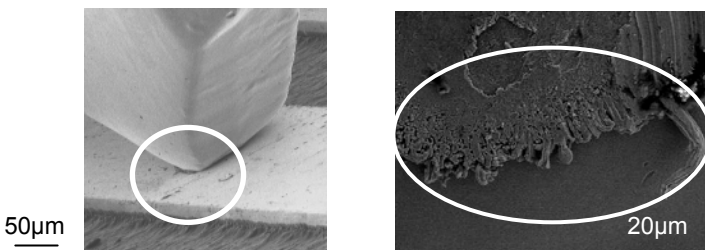
Figure 6:   Whisker generating parts.

These figures indicate the following whisker generation process. Plastic deformation of Sn-Cu plating film was generated by the contact force between the connector and the FPC when the FPC was inserted into the connector. From the above-mentioned detailed observation of plastic deformation recognized on plated Sn-Cu film, some amount of plastic deformation and also contact force being held after insertion of the FPC into the connector are considered as the governing factors of whisker generation. In the following, dependence of plastic deformation upon plating species was investigated. First of all, deference in plastically deformed morphology between Sn-Cu alloy plating, which showed accelerated whisker growth, and Sn-Pb alloy plating, which showed a suppressing effect for whisker generation, was examined by SIM observation and shown in Figs.7 and Fig.8.

(a) Outlook of contact parts

(b) Side part close up – cumulative deformation of plating film
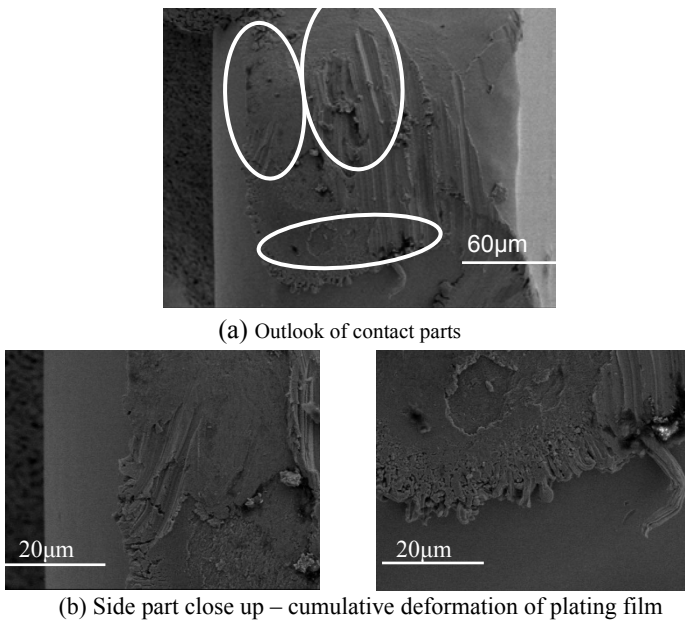
Figure 7:   Plastic deformation on Sn-Cu plating film.

From these observations, a lot of plastic deformation was generated in the case of Sn-Cu compared with Sn-Pb plated film. As a result, much plastic strain energy was stored in the Sn-Cu plated player. For this reason, whisker generation may be accelerated in the case of Sn-Cu plated layers compared with Sn-Pb. Just now authors have started evaluating the hardness of plated layers employing nano-indentation method and some results of micro-hardness measurement were obtained. As a result, hardness of Sn-Cu plating film showed relatively larger hardness compared with Sn-Pb plating film as shown in Table 4. For this reason, relief of residual stress was more suppressed in the case of Sn-Cu plating film compared with Sn-Pb plating film.

(a) Outlook of contact parts

(b) Side part close up

(c) Lower part close up
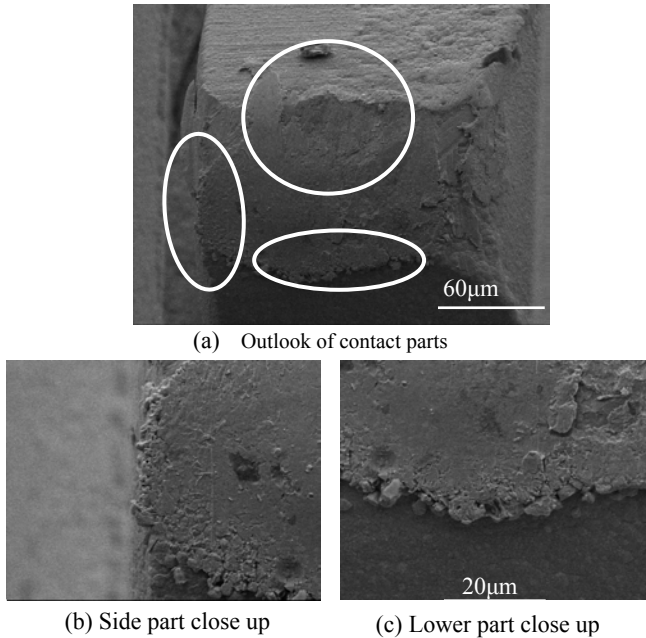
Figure 8:   Plastic deformation of Sn-Pb plating.

Table 4:   Hardness value of plating film.

Plating species	Hardness value
Sn-Cu	25.4
Sn-Pb	23.1

3.4 Dependence of crystal grain morphology upon plating species

Examination of detailed cross sectional crystal structure of plating film [5] was conducted by micro processing of each plated layer by FIB. Fig.8 (a)-(c), shows the observed result of this crystal grain morphology [6]. In Fig.9, a schematic illustration of crystal morphology whose SIM micrograph was shown in Fig.8 is indicated. It was understood from these observations that Sn-Bi had granular crystal grain morphology with random orientation. On the contrary, Sn-Pb and Sn-Cu showed columnar shaped crystal grain. However, Sn-Cu showed finer columnar shape compared with the crystal grain of Sn-Pb.

Therefore, plating film whose microstructure has a finer grain shows relatively higher yield stress. As a result, residual stress and contact stress, which were generated during the input process, were not easily relieved in this case compared with other plating film whose yield stress was relatively low. Whisker generation and growth preferentially occurred in the Sn-Cu plating for the above-mentioned reasons. As a result, generation and growth characteristics of the

whiskers shown in Table 3 and Fig.5 were understood from the viewpoint of residual and contact stress relief. These residual compressive and contact stresses may cause the generation of an inter-metallic compound then initiate Tin whiskers in the grain boundary [7].

(a) Sn-Cu (b) Sn-Bi (c) Sn-Pb
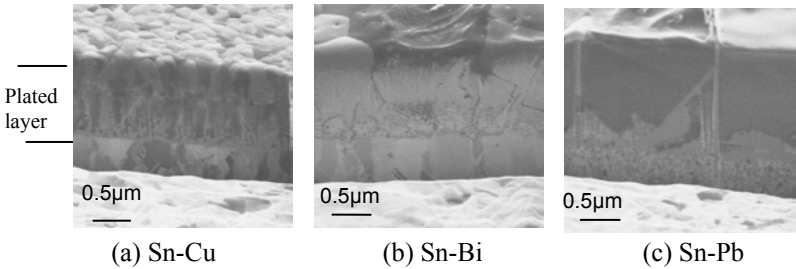
Figure 9:   Observation of crystal grain morphology after the FIB process.

(a) Sn-Cu (b) Sn-Bi (c) Sn-Pb
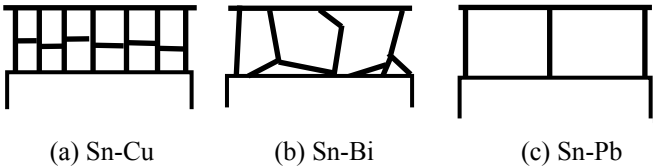
Figure 10:   Schematic illustration of crystal grain morphology of plated film.

3.5 Dependence of initial whisker growth rate upon Bi content of Sn-Bi plating

Sn-Bi plating showed relatively superior whisker growth suppressing characteristics compared with that of Sn-Cu plating. In this section, the content of Bi was changed from 1 to 4wt% and then the effect of the Bi content on the whisker generation characteristics were examined. Also in this case, various considerations were conducted from the viewpoints of both morphology of the whisker and whisker growth rate.

Growth characteristics of the maximum length whisker that were detected for the first time after 24hrs from the FPC being put in are shown in Fig.11. In Table 5, the morphology and maximum length of the whisker after 168hrs from the FPC being put in are indicated. Also in this table, the number of detected whiskers longer than 5μm is indicated. Judging from these data, the Sn-Bi alloy whose Bi contact is 1wt% showed preferential growth of whiskers whose length was around 20μm. On the contrary, in the case of Sn-4wt%Bi, the generation and growth of whiskers was relatively suppressed compared with Sn-1wt%Bi alloy plating. Therefore, a short circuit may be suppressed in the case when applying a Sn-Bi alloy whose Bi content is larger than 2wt% and also the evaluation of various properties such as wettability and so on necessary for plating process may be extremely important.
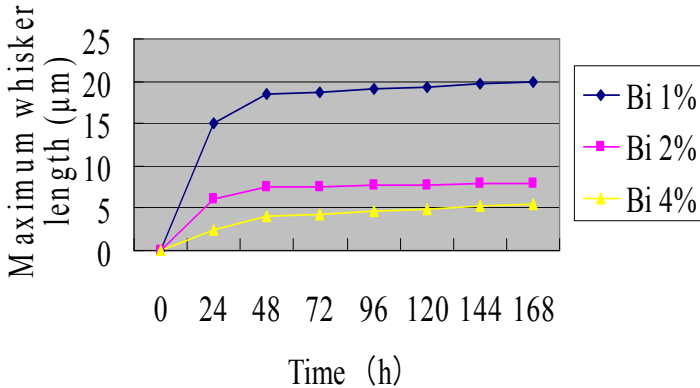
Figure 11:   Growth behavior of whisker in Sn-Bi plating.

Table 5:   Dependence of whisker morphology upon Bi content.

Plating species	Whisker morphology	Maximum length	Time	Number of whisker*
Sn-1wt%Bi	Needle	20μm	168h	14
Sn-2wt%Bi	Intermediate	8μm	168h	11
Sn-4wt%Bi	Intermediate	6μm	168h	7

*Number of whiskers longer than 5μm.

4   Conclusions

In this study the generation and growth characteristics of whiskers were investigated from the viewpoint of the micro structure of plating species of Sn-Cu and Sn-Bi(1%, 2% and 4%), which are notable as Pb free materials. In addition, Sn-Pb plating was used in this research. Then, the difference in the whisker morphology depending upon plating materials was investigated and the whisker growth rate was evaluated through the plating film being processed by FIB. In addition, the effects of additive elements such as Cu, Bi and Pb upon the physical properties of Sn plating and the morphology of generated whiskers were investigated through SIM observation of a cross sectional area processed by FIB.

The results obtained are summarized as follows;

1. In the case of Sn-Cu plating material, preferential generation and growth of whiskers were recognized compared with Sn-Bi and Sn-Pb.
2. Residual stress generated by the input process of the FPC into the connector and the contact force between the connector and the FPC is a governing factor in whisker generation and growth.
3. The difference in crystal grain morphology was clarified between these three kinds of plating materials through conducting FIB processing and detailed SIM observation. Therefore, the residual stress generated by the input process

of the FPC into the connector cannot easily be relieved in the case of Sn-Cu plating film, whose microstructure has fine grains.

4. Increasing Bi contents improved whisker generation and growth characteristics. Whisker generation and growth were suppressed in the case when applying Sn-Bi alloy whose Bi content is larger than 2wt%. In addition, in this case, grain size was increased with the increase of Bi content.

5. Therefore, the control of grain morphology is extremely important for suppressing whisker generation and growth.

References

[1] Minoru Shimada, Outline of European Directives, WEEE and RoHS, Ceramics, Vol.37(11), pp. 866-870, 2002.

[2] Yoshitou Hayashida, Yoshiyuki Takahashi, Takao Ohno and Ikuo Shohji, Whisker-Free Pb-Free Solder through Alloying, J. Japan Inst. Metals, Vol. 70(3), pp. 220-225, 2006.

[3] Shinobu Ohzone et al., Whisker of Sn system plating in connector, Technological report of Japan Aviation Electronics Industry, No.28, p. 19-29, 2005.

[4] Yuki Fukuda, Michael Osterman, and Michael Pecht, Length Distribution Analysis for Tin Whisker Growth, IEEE Transactions on Electronics Packaging Manufacturing, Vol. 30(1), pp.36-40, 2007.

[5] Asa Frye, George T. Galyon, and Larry Palmer, Crystallographic Texture and Whiskers in Electrodeposited Tin Films, IEEE Transactions on Electronics Packaging Manufacturing, Vol. 30(1), pp.2-10, 2007.

[6] Joe Smetana, Theory of Tin Whisker Growth: "The End Game", IEEE Transactions on Electronics Packaging Manufacturing, Vol. 30(1), pp.11-22, 2007.

[7] Katsuaki Suganuma and Masami Terauchi, Quantitative Analysis of Intermetallic Compound and TEM Specimen Preparation for Sn Whiskers, Proceeding of 2nd International Symposium on Tin Whiskers 2008, paper No.1-1-3, Japan Electronics and Information Technology Industries Association, 2008.

Determination of wheel/rail contact points in the simulation of railway vehicle dynamics

J. Auciello, S. Falomi, M. Malvezzi, E. Meli & P. Toni
Department of Energetics 'S. Stecco', University of Florence, Italy

Abstract

The numerical simulation of system dynamics is today a standard in the design of railway vehicles; their typical applications are the suspension kinematics, handling performance and ride comfort as well as the generation of load data for lifetime prediction. One of the key points in this type of simulation is the model of the wheel/rail interaction, in other words the definition of the forces exchanged between the wheels and the rail in the contact points. The direction and the magnitude of the contact forces depend on the number and the location of the contact points. The procedure that allows one to define the geometry of the contact then has a significant effect on the reliability of the simulation. The component of the normal contact force to the contact surfaces can be defined as a function of the relative indentation between the surfaces. The component of the contact force tangent to the contact surfaces depends on the relative speeds between the surfaces in the contact area (wheel sliding). The authors have been working on the definition of efficient and reliable models of the interactions between the wheels and the rails and in particular for the definition of the contact points. Different algorithms have been analyzed and compared, based on semi analytical approaches and on neural networks. The paper will summarize the proposed methods and the results obtained from the simulation of two different sceneries. Two different models have been used in this test: the first one was realized with a commercial software, while the second one was developed and implemented by the authors. There is a global agreement between the models, although some differences can be seen during the transients due to the different methods for the determination of the contact points for the integration.
Keywords: multibody simulation, wheel-rail contact, real time simulations.

1   Introduction

The numerical simulation of system dynamics is today a standard in the design of railway vehicles. The multibody analysis is applied, for example, to suspension kinematics and compliant kinematics, handling performance and ride comfort as well as to the generation of load data for lifetime prediction. These simulation tasks are usually carried out as off-line simulations performed by means of commercial or customized software.

In recent years Hardware in-the-Loop (HIL) simulation has been extensively introduced in the design of vehicle control systems and the testing of electronic control units, both in the automotive and in the railway fields. The reliability of this type of test is strictly related to the properties of the numerical model that simulates the condition that the tested device would meet in real operative conditions. The numerical model is a representation of the dynamics of the system in which the tested unit is inserted (single vehicle, entire train etc.). In order to obtain reliable results on this type of test rig, the availability of a realistic real time model of the system dynamics is necessary.

Over recent years the MBS (Multibody Simulation) method has then been established in the real-time simulation domain, typically for the design of vehicle control systems and the testing of electronic control units [1,2].

The numerical model described in this paper reproduces the complete three-dimensional dynamics of a railway vehicle running on a generic track. It has been developed with the objective of a real time implementation, in order use its results to control the actuators of HIL test rigs.

One of the key points in this study was the definition of a reliable and efficient model describing the forces arising in the wheel/rail interaction areas. The contact force vector is composed of a normal component, resulting from the weight of the vehicle, and by a tangential component resulting from the friction between the wheel and rail in the contact area. This component, named creep force, arises in the contact area when a traction or a braking torque is applied to the axle. These forces play an important role in the wheelset dynamics and their value depends on a number of parameters, including the position of the contact point between the bodies.

The introduction of a well-defined full three-dimensional wheel/rail interaction module in a standard multibody model is not easy and may sensibly increase the complexity and the computational burden of the numerical procedure [3–10].

In the model described in the following sections the wheelset is assumed to have six degrees of freedom with respect to the rails. The local deformation of the contact surface at the contact point is allowed and the normal contact forces are defined using Hertz's contact theory or in terms of assumed stiffness and damping coefficients. This type of approach allows the separation between the wheel and the rail and to manage multiple contact points. One of the main problems correlated with this approach is the definition of the contact point location on line. In most elastic force models, the three-dimensional contact

problem is reduced, for the sake of efficiency, to a two-dimensional problem when the location of the contact points is searched for.

In order to find a solution for the problem of contact mechanics, detailed descriptions of the surfaces in contact, as well as the kinematics of the bodies, are required. Because wheel and the rail profiled surfaces, the prediction of the location of the contact point on line is a not easy task, especially when the most general three-dimensional motion of a wheelset with respect to the rails is considered. In many cases, some simplifications are made in the geometric and/or the kinematic description. A common method used in many existing computer algorithms to find the location of the contact point is to interpolate some precalculated table entries. The location of the contact point is given as function of some coordinates that measure the relative position of the wheelset with respect to the rails. The degree of accuracy of such algorithms depends on the number of coordinates that are used to define this relative position.

The developed numerical procedure can be schematized as shown in Figure 1. The dynamics of each wheelset depends on the external actions (traction/braking torques) and on the contact forces. The solution of the differential equations describing the wheelset dynamics allows one to calculate the kinematical parameters (displacement and rotation) from which the position of the contact points can be identified. The creep forces are then calculated taking into account the position of the contact points and the wheel creepages, obtained from the wheelset kinematics.
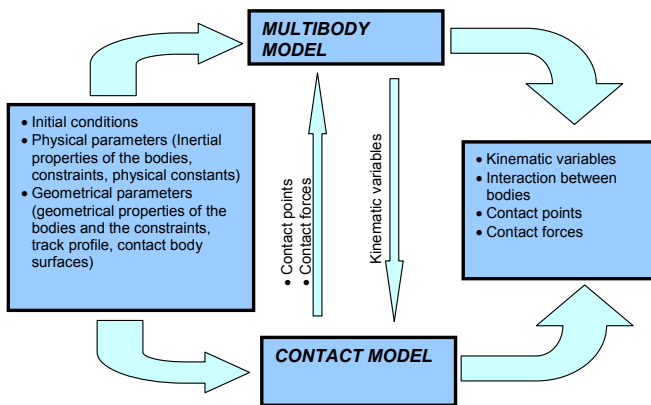
Figure 1:   Numerical procedure block diagram.

2   Definition of wheel/rail contact points

In Figure 2 the reference frames used to describe the wheel and rail profile geometries are shown. Concerning the rail coordinate system, x_b is parallel to the track direction, y_b is on the plane defined by the rails and normal to x_b, z_b

is consequently defined. The origin $\mathbf{O}_b$ is fixed on the track axis, in other words it is on the plane identified by the rails and is equally distant from both of them. The simulated vehicle can move on a generic track, defined by $\gamma(s)$, representing a generic three-dimensional curve defined by means of its parameter s. A second auxiliary coordinate system relative to the track is defined, its origin $O_{b'}$ is on the median railway curve $\gamma(s(t))$, it is not fixed, and depends on the wheelset motion on the track. The axis $x_{b'}$ is tangent to the track curve, the $z_{b'}$ axis is normal to the rail plane and $y_{b'}$ is consequently defined.

a)   b)
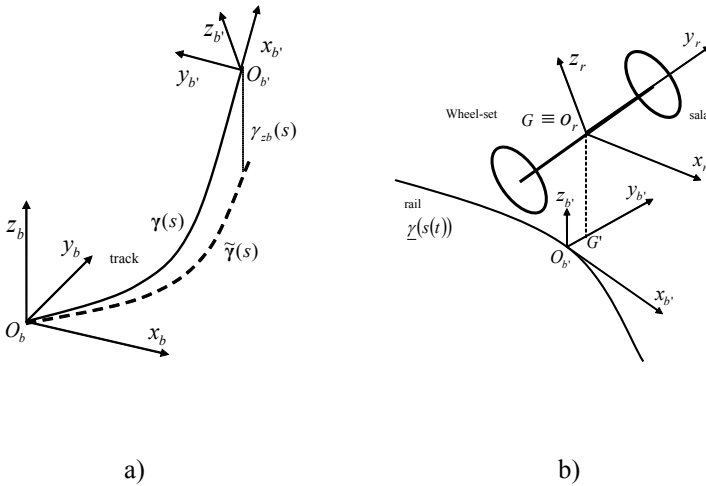
Figure 2:   a) Rail coordinate system, b) wheel coordinate system.

The origin O_r of the wheelset coordinate system is on the plane $y_{b'}, z_{b'}$, then:

$$[O_r(t) - O_{b'}(s(t))] \bullet \underline{\gamma}'(s(t)) = 0 \tag{1}$$

It is then evident that for any t value, $s(t)$ and then $O_{b'}$ can be calculated from the position of the wheelset center of mass.

The wheel is a revolution surface, the wheel radius depends on the y_r coordinate, the function $s = s(y_r)$ describes the wheel profile in the $y_r z_r$ plane, and the coordinates of a generic point on the wheel surface can be expressed, in the wheelset coordinate system, as follows:

$$\left(P_r - O_r\right)_r = \mathbf{s}_r(u, y_r) = \begin{pmatrix} -s(y_r)\sin u \\ y_r \\ s(y_r)\cos u \end{pmatrix} \tag{2}$$

where u is the angle between the radiuses that identify the generic point on the wheel and $-z_r$ direction.

The rail surface is an extrusion surface, the function $b = b(y_{b'})$ describes the rail profile in the plane $y_{b'}$, $z_{b'}$, and then the coordinates of a generic point on the rail surface can be expressed as:

$$\left(P_{b'} - O_{b'}\right)_{b'} = \begin{pmatrix} x_{b'} \\ y_{b'} \\ b(y_{b'}) \end{pmatrix} \tag{3}$$

the coordinates of a generic point on the wheel can then be expressed in the auxiliary coordinate system:

$$\left(P_{b'}^r - O_{b'}\right) = (O_r - O_{b'})_{b'} + \left[\mathbf{R}_2\right] \cdot O_r \tag{4}$$

The displacement $(O_r - O_{b'})$ and the rotation matrix $\left[R_2\right]$ between the wheelset and the track reference system depend on the relative displacement between the wheelset and the rail, then, for each wheelset configuration the wheel surface can be expressed with respect to the auxiliary reference frame as a function of the parameters u and y_r:

$$P_{b'}^r = \mathbf{s}_{b'}^r\left(u, y_r\right) \tag{5}$$

The point $P_{b'}$ corresponding to $P_{b'}^r$ on the rail surface is then given by:

$$P_{b'} = \begin{pmatrix} x_{b'}^r(u, y_r) \\ y_{b'}^r(u, y_r) \\ b(y_{b'}^r) \end{pmatrix} \tag{6}$$
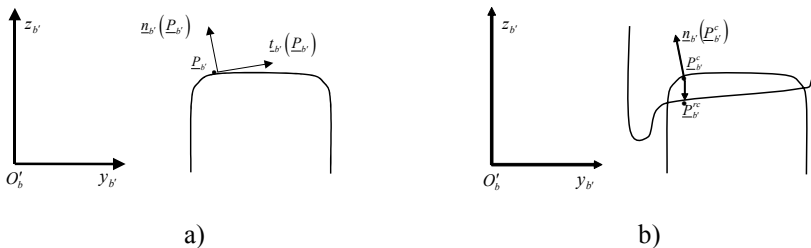
Figure 3:   a) Rail surface, normal and tangent directions, b) definition of the difference surface.

The *difference surface* is then defined as:

$$D(u, y_r) = \left(P_{b'}^r - P_{b'}\right) \bullet \mathbf{k}_{b'} \tag{7}$$

The contact points are located in the points in which this surface assumes a local minimum. Then, in order to find the contact points the local minima of this surface are searched.

$$\begin{cases} \min_{u,y_r} D(u,y_r) \rightarrow \left(u_i^{\ c}, y_{i,r}^{\ c}\right) \\ \quad i = 1,2,..,n \leq 4 \end{cases} \qquad (8)$$

The minima are calculated by a procedure that analytically reduces the problem dimension to a single equation that is numerically solved. This method is allows a good precision with low computational loads.

3 Contact forces between wheel and rail

Once the local minima have been identified, the indentation between the surfaces is conventionally defined in the direction normal to the rail:

$$p = \left(P_{b'}^{rc} - P_{b'}^{c}\right) \bullet \mathbf{n}_{b'}\left(P_{b'}^{c}\right) \qquad (9)$$

Where $\mathbf{n}_{b'}$ is the unitary vector normal to the rail in the contact point. The indentation value is used to calculate the normal component of the contact force, according to the elasto-viscous approach as sum of a term that depends on the normal penetration between the body (the elastic component), and a term proportional to the surface relative velocities in the contact point (the viscous term).

The magnitude of the tangential component of the contact forces is calculated on the basis of Kalker and Hertz theory [12,13]. The Hertz's theory is used to define the contact area dimensions and shape, which depend on the normal force magnitude, the material properties and the local profile geometry. The Kalker linear theory results are used to define the components of the creep forces as follows:

$$\begin{aligned} T_x &= -f_{11}\xi \\ T_y &= -f_{22}\eta - f_{23}\varphi \\ M_{sp} &= f_{23}\eta - f_{33}\varphi \end{aligned} \qquad (10)$$

where f_{11}, f_{22}, f_{33}, f_{23} are the linear creep coefficients, depending on the contact ellipse semi-axis and on the combined modulus of rigidity (their values are tabulated)[10]; ξ, η and φ are the values of the creepage components.

4 Vehicle multibody model

The multibody model is composed of seven rigid bodies (the car body, two bogies, four wheelsets) connected by three-dimensional non linear elastic-

viscous force elements modeling the connection elements between the bodies (for example the vehicle suspensions, dampers etc.).

On each wheelset the following force act:

- the creep forces in the contact area;
- the forces due to the interaction with the boogie;
- the external applied braking or traction torque;
- the weight.

The numerical model was realized in the Matlab/Simulink environment, which allows one to obtain a numerically efficient model, to test different types of integration algorithms, to manage singularities. The structure of the model is modular so different subsystems can be easily modeled and substituted in the main procedure. In this type of design environment different and complex systems can be modeled (electrical, pneumatic etc.), while a toolbox devoted to the multibody simulation allows to easily model mechanical systems with a high number of bodies and constraints.

The results of the simulations performed with the developed model were compared with those obtained with models of the same vehicle realized with Adams Rail and Simpack. The benchmark case is the Manchester wagon, whose features are known in the literature and whose Adams Rail model is available [14]. The validation process is necessary to evaluate the accuracy of the model and to verify the performance of the model in terms of computational burden, even if they are obtained using different software environments and different modeling approaches. The differences are particularly evident in the definition of the contact points and of the contact forces.

5 Results

In this section some the results obtained from the comparison with the Adams Rail model are briefly described. In tests the vehicle travels along a curve with a constant speed. The parameters that are varied in the first set of tests were:

- the curve radius values (500, 1200 and 2400 m);
- the rail angle was 1/40 and 1/20;
- the cant angles were 40/1435 rad and 90/1435 rad;
- the speed values were 15, 30 and 45 m/s.

The wheel/rail adhesion coefficient was 0.2 in all the tests. In this set of tests the displacements of the wheelset centers and the contact forces were analyzed and compared.

Figure 4 shows the parameters relative to one of the performed tests: the track curvature and the cant angle. Figure 5 shows the comparison between the results obtained by the Adams and Simulink multibody models, the time-history of the wheelset center of mass displacements is analyzed in the presented example. The results show a good agreement between the different models, a difference between the simulations can be noted in the transient, it is due to the differences in the contact force calculation.

Table 1 summarizes the hunting frequencies calculated through simulations performed imposing different vehicle speeds, a quite good agreement between

the results obtained with the Simulink and Adams models can be observed. The calculated critical speeds are 71 m/s with the Simulink model and 73 m/s with the Adams Rail model.

a)   b)
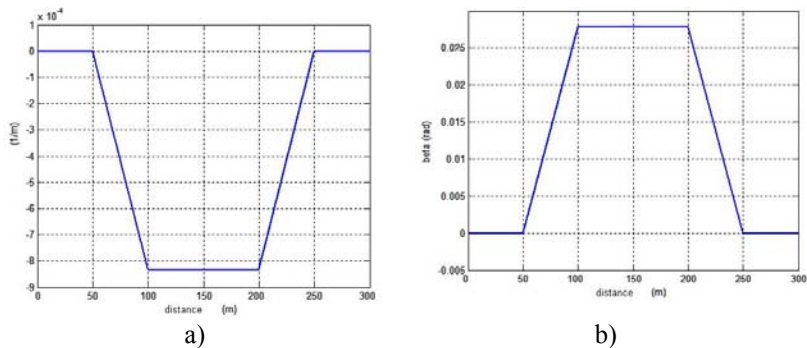
Figure 4: Test features: a) track curvature, b) cant angle ($R = 1200$ m, $\alpha_p = 1/40$rad, $\beta = 40/1435$rad, $V = 30$m/s).

a)   b)
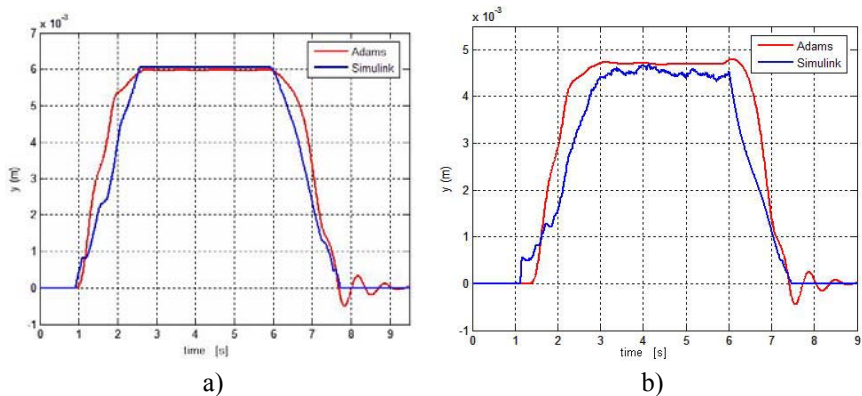
Figure 5: Wheelsets center of mass displacement: comparison between results obtained with Adams and Simulink models: a) First wheelset (front bogie, front wheelset), b) second wheelset (front bogie, rear wheelset).

The simulation results allow one to conclude that the Simulink and Adams multibody models give substantially comparable results. The time history analysis shows that the Simulink model is generally characterized by a higher transient damping, due to the different method for the calculation of the normal component of the contact force (in the Simulink model a nonlinear elasto-viscous approach is implemented).

Table 1:   Hunting frequencies, comparison between the results obtained through Adams and Simulink models.

Speed (m/s)	Hunting Frequencies (Hertz)	
	ADAMS	SIMULINK
25	1.7	1.6
40	2.5	2.6
55	3.3	3.5
70	4.6	4.4

6   Conclusions

The objective of the work presented in the paper is the development of a numerically efficient model describing the three-dimensional dynamics of a railway vehicle. The challenge is the realization of a real time implementation, to be used for example to control an HIL test rig. In this type of test rig the reliability of the realized tests depends on the accuracy of the simulation of the 'virtual' environment, on the other hand the real time constraint imposes limitations on the complexity of the numerical models and on their integration times. The development of such models has then to find a compromise between accuracy and efficiency.

This paper summarizes the main features of a railway vehicle multibody model realized in the Matlab-Simulink environment. The model was tuned in order to reproduce the dynamical behavior of a benchmark railway vehicle. The results of the simulations carried out with this model are compared with those obtained with the Adams Rail multibody model of the same vehicle. The comparison has shown a substantially good agreement between the models and the relative errors are acceptable. It has to be highlighted that the models evaluate the local deformation of the wheel and the rail in the contact zone by means of two different approaches. With respect to the existing and available railway multibody models, its features are then a more detailed modeling of the wheel/rail contact problems and the possibility to easily obtain an executable implementation that could run in real time conditions. In the developed model the aspects relative to the contact point definition and contact force calculation has been carefully investigated since they have a significant effect on the vehicle dynamics.

References

[1]   Wolfgang Rulka, Eli Pankiewicz, MBS Approach to Generate Equations of Motions for HiL-Simulations in Vehicle Dynamics Multibody System Dynamics (2005) n.14, pp 367–386.

[2] L. Pugi, M. Malvezzi, A. Tarasconi, A. Palazzolo, G. Cocci, M. Violani, "HIL Simulation of WSP Systems on MI-6 Test Rig", Proceedings of the XIX IAVSD 2005 - International Vehicle System Association, Milano 29 agosto-2 September 2005. Vehicle system Dynamics, Vol. 44, Supplement 2006 pp.843-852   ISBN 978-0-415-43616-8.

[3] A. A. Shabana, M. Tobaa, H. Sugiyama, K. E. Zaazaa, On the Computer Formulation of the Wheel/Rail Contact Problem, Nonlinear Dynamics, Springer 2005, vol. 40, pp. 169–193.

[4] Pombo, J. Ambrosio, Dynamics analysis of a railway vehicle in real operation conditions using a new wheel-rail contact detection model, "Int. J. of Vehicle Systems Modelling and Testing", 1, 2005

[5] De Pater, A. D., 'The geometric contact between track and wheelset', Vehicle System Dynamics 17, 1988, 127–140.

[6] L. Baeza, A. Roda, J. Carballeira, E. Giner, Railway Train-Track Dynamics for Wheelflats with Improved Contact Models, Nonlinear Dynamics, Springer 2006, vol. 45, pp. 385–397.

[7] T. G. Kolda, R. M. Lewis, V. Torczon, Optimization by direct search: new perspectives on some classical and modern methods, SIAM Review, Vol. 45, N. 3 (2003), pp. 385–482.

[8] M. W. J. C. Lagarias, J. A. reeds, P.E. Wright, convergence properties of the Nelder Mead simplex method in low dimensions, SIAM Journal on Optimization, No. 9 (1998), pp. 112–147.

[9] R. V. Dukkipati, J. R. Amyot, Computer aided simulation in railway dynamics, Marcel Dekker, 1988W. Schiehlen. Multibody system dynamics: Roots and perspectives. Multibody System Dynamics, 1, 149–188, 1997.

[10] J.J. Kalker, Three-Dimensional Elastic Bodies in Rolling Contact, Kluwer Academic Publishers, 1990.

[11] E.A.H. Vollebregt, J.J. Kalker, G. Wang, " CONTACT 93 Users Manual", VORtech Computing, Industrial and Scientific Computing, July 1992, revised March 1994.

[12] K.L. Johnson, Contact mechanics, Cambridge University Press, 1985.

[13] P.J. Vermeulen, K.L. Johnson, Contact of Nonspherical Elastic Bodies Transmitting Tangential Forces, Journal of Applied Mechanics, Transactions of the ASME, June 1964.

[14] Iwnicki S., 'The Manchester Benchmarks for Rail Vehicle Simulators' Swets & Zeitlinger B.V. Lisse 1999, (ISBN 90 265 1551 0)

Author Index